

THESE

présentée à

l'Université de Lille

par

Shuo CHEN

pour l'obtention du

TITRE DE DOCTEUR EN CHIMIE

Spécialité : Molécules et Matière Condensée

**EFFECT OF METAL DISPERSION ON THE CATALYTIC PERFORMANCE OF MONOMETALLIC
Ni/SBA-15 AND Cu/SBA-15 CATALYSTS IN THE HYDROCONVERSION OF HMF**

**EFFET DE LA DISPERSION DES MÉTAUX SUR LES PERFORMANCES CATALYTIQUES DES
CATALYSEURS MONOMÉTALLIQUES Ni/SBA-15 ET Cu/SBA-15 POUR
L' HYDROCONVERSION DE L'HMF**

Soutenance prévue le 9 Mai 2019 devant la commission d'examen :

Rapporteurs : **Mme Florence EPRON**, Directeur de Recherche, CNRS-Université de Poitiers

Mme Nadine ESSAYEM, Directeur de Recherche, CNRS-IRCELYON

Examineurs : **Mme Karine VIGIER**, Professeur, Université de Poitiers

Mme Hélène LAURON-PERNOT, Professeur, Sorbonne Université

Directeur : **M. Sébastien ROYER**, Professeur, Université de Lille

Co-directeur : **M. Eric MARCEAU**, Maître de Conférences, Université de Lille

Co-encadrant : **M. Robert WOJCIESZAK**, Chargé de Recherche, CNRS-Université de Lille

CONTENT

RÉSUMÉ	1
ABSTRACT	3
ACKNOWLEDGEMENT	5
INTRODUCTION	6
CHAPTER 1: LITERATURE REVIEW	15
1.1 Adsorption chemistry of furanic compounds on metal surfaces	16
1.2 The catalytic production of value-added chemicals from HMF: general trends....	19
1.3 The production of DMF from HMF	22
1.3.1 Catalytic performances of noble metal-based catalysts	24
1.3.2 Catalytic performances of non-noble metal based catalysts	29
1.4 The production of DMTHF from HMF	35
1.5 Conclusion	37
Reference	39
CHAPTER 2: MATERIALS AND METHODS	49
2.1 Introduction.....	50
2.2. Catalyst preparation	50
2.2.1. Preparation of the SBA-15 mesoporous silica support	50
2.2.2. Preparation of Cu/SBA-15 catalysts	51
2.2.3. Preparation of Ni/SBA-15 catalysts.....	52
2.3. Catalyst characterization.....	52

2.3.1. Nitrogen physisorption.....	52
2.3.2. X-ray diffraction	53
2.3.3. Hydrogen temperature-programmed reduction (H ₂ -TPR).....	54
2.3.4. High-resolution transmission electronic microscopy (HRTEM)	55
2.3.5. Fourier transform infrared resonance.....	55
2.4. Catalysis test	55
2.4.1. Catalyst activation.....	55
2.4.2. Catalysis test	55
2.4.3. Products identification and quantification	58
2.4.4. General calculation methods.....	60
Reference	61

CHAPTER 3: CATALYTIC PERFORMANCE OF MONOMETALLIC Ni/SBA-15 CATALYST FOR THE SELECTIVE HYDROCONVERSION OF HMF TO DMF AND DMTHF62

3.1 Introduction.....	63
3.2. Catalyst preparation	65
3.3. Results and discussion	66
3.3.1 Characterization of the calcined 15Ni/SBA-15_IWI-MD	66
3.3.2 Characterization of reduced 15Ni/SBA-15_IWI-MD.....	71
3.3.3 Catalytic performances of 15Ni/SBA-15_IWI-MD for HMF hydroconversion.....	73
3.3.4 Kinetic study	78

3.4 Conclusion	84
Reference	85

CHAPTER 4: TUNING THE DISPERSION AND CATALYTIC PERFORMANCES OF Ni PARTICLES BY CHANGING THE SECONDARY POROSITY OF SBA-15.....88

4.1 Introduction.....	89
4.2. Catalyst preparation	91
4.3. Results and discussion	92
4.3.1 Pore periodicity in SBA-15 supports and NiO/SBA-15 materials.....	92
4.3.2 Textural properties of SBA-15 supports and evolution in NiO/SBA-15 materials.....	93
4.3.3. Support morphology, localization and size of NiO NPs	96
4.3.4. Activation of the catalyst	102
4.3.5. Catalytic properties of Ni/SBA-15 materials for hydroconversion reactions	105
4.4 Conclusion	111
References.....	112

CHAPTER 5: EFFECT OF METAL DISPERSION ON THE CATALYTIC PERFORMANCE OF MONOMETALLIC Cu/SBA-15 CATALYSTS FOR THE SELECTIVE HYDROGENOLYSIS OF HMF TO DMF..... 119

5.1 Introduction.....	120
5.2. Catalyst preparation	123

5.3. Results and discussion	125
5.3.1 Characterization of the calcined catalysts	125
5.3.2 Characterization of the reduced catalysts	138
5.3.3 Preliminary exploration of reaction conditions.....	143
5.3.4 Effect of the HMF/Cu molar ratio	145
5.3.5 Effect of reaction temperature.....	147
5.3.6 Effect of metal dispersion on catalytic reactivity	151
5.3.6 Kinetic study	153
5.3.7 Recycling study.....	159
5.4 Conclusion	159
References.....	161

CHAPTER 6: GENERAL CONCLUSIONS AND PERSPECTIVES...170

RÉSUMÉ

La production d'additifs pour les carburants, d'indices d'octane élevés, à partir des molécules biosourcées telles que le 5-hydroxyméthylfurfural (HMF) est le sujet de nombreuses études. Les catalyseurs à base de Pt, de Pd et de Ru sont décrits comme particulièrement actifs dans la réaction de conversion du HMF en 2,5-diméthylfurane (DMF) et en 2,5-diméthyltétrahydrofurane (DMTHF). Cependant leur substitution dans les formulations catalytiques est souhaitable compte tenu de leur coût élevé et de leur faible disponibilité. Les éléments de substitution peuvent être certains métaux de transition (par exemple Cu ou Ni), plus abondants, mais généralement moins actifs. Mes travaux de recherche ont donc porté sur la préparation de catalyseurs, à base de métaux de transition, actifs et sélectifs pour l'hydrogénation du HMF en des molécules pouvant être incorporées dans les carburants. Les phases actives étudiées au cours de mon doctorat reposent sur les métaux de transition Ni et Cu. Ces phases actives ont été supportées sur des silices mésoporeuses de type SBA-15. L'étude est divisée en deux parties distinctes, en fonction du métal étudié.

La première partie du doctorat présente les résultats obtenus avec des catalyseurs monométalliques Ni supportés. Dans un premier temps, l'optimisation des paramètres de réaction pour l'hydroconversion sélective du HMF en DMF et en DMTHF a été réalisée en utilisant un catalyseur préparé par la méthode d'imprégnation à humidité naissante d'une solution du précurseur nitrate (Chapitre 3). Les paramètres de réaction optimisés incluent la température de réaction, la pression de dihydrogène, le rapport molaire HMF/Ni et le temps de réaction. Une étude cinétique préliminaire a également été réalisée. L'effet de la dispersion et de la taille des particules métalliques de Ni sur les performances catalytiques des catalyseurs Ni/SBA-15 a été étudié sur des matériaux préparés par la méthode d'infiltration à l'état fondu des précurseurs nitrates (Chapitre 4). Le niveau de dispersion du nickel a été modifié en utilisant des supports SBA-15 contenant des porosités d'interconnexion différentes et obtenues à différentes températures de synthèse. Les résultats montrent que le catalyseur Ni/SBA-15, préparé par la méthode simple IWI, permet d'atteindre des rendements élevés en DMF et DMTHF dans des conditions réactionnelles optimales. Le niveau de dispersion du Ni, tel qu'observé à partir des matériaux obtenus par infiltration des sels fondus, a quant à lui un effet significatif sur l'activité catalytique du catalyseur.

La deuxième partie de mes travaux de recherche porte sur les propriétés catalytiques des catalyseurs monométalliques à base de Cu/SBA-15 préparés par différentes méthodes, et présentant des états de division de la phase Cu différents (Chapitre 5). Les modes de synthèse appliqués incluent la méthode d'imprégnation à humidité naissante (IWI), la méthode d'autocombustion in situ (ISAC) et la méthode de déposition par précipitation (DP). La première partie de l'étude a donc portée sur l'optimisation des conditions de réaction pour l'hydroconversion sélective du HMF en DMF (avec le catalyseur Cu/SBA-15 préparé par la méthode ISAC). Les paramètres de réaction optimisés, comme dans le cadre de l'étude avec Ni/SBA-15, ont été la température de réaction, la pression de dihydrogène, le rapport molaire HMF/Cu et le temps de réaction. La réutilisation du catalyseur a également été étudiée, et une étude cinétique de la transformation du HMF sur Cu menée. Cette partie démontre que l'activité du Cu pour la conversion sélective du HMF en DMF dépend principalement de l'état de dispersion du Cu. L'utilisation de la méthode DP a conduit à un catalyseur Cu/SBA-15 hautement divisé, ce qui a permis d'atteindre des rendements élevés en DMF.

Mot clé : métaux de transition, imprégnation, hydrogénation, biomasse, mésoporeux, HMF

ABSTRACT

The production of fuel additives, having high octane numbers, from biosourced molecules such as 5-hydroxymethylfurfural (HMF), is the subject of many studies. The Pt, Pd and Ru-based catalysts are described as particularly active in the conversion reaction of HMF to 2,5-dimethylfuran (DMF) and to 2,5-dimethyltetrahydrofuran (DMTHF). However, their substitutions in the catalytic formulations are desirable in view of their high cost and low availability. The substitution elements can be transition metals (for example Cu or Ni), which are more abundant, but generally less active. My research has focused on the preparation of catalysts, based on transition metals, active and selective for the hydrogenation of HMF into molecules that can be incorporated into fuels. The active phases studied during my Ph.D. are based on Ni and Cu transition metals. These active phases were supported on mesoporous silica of SBA-15 type. The study is divided into two distinct parts, depending on the metal studied.

The first part of the Ph.D. presents the results obtained with Ni supported monometallic catalysts. In a first step, the optimization of the reaction parameters for the selective hydroconversion of HMF to DMF and DMTHF was carried out using a catalyst prepared by the incipient wetness impregnation (IWI) of the nitrate precursor solution (Chapter 3). Optimized reaction parameters include reaction temperature, hydrogen pressure, HMF/Ni molar ratio, and reaction time. A preliminary kinetic study was also performed. The effect of the dispersion and size of Ni metal particles on the catalytic performance of Ni/SBA-15 catalysts was studied on materials prepared by the melt infiltration (MI) method of nitrate precursors (Chapter 4). The level of dispersion of the nickel was modified using SBA-15 supports containing different interconnection porosities, obtained at different synthesis temperatures. The results show that the Ni/SBA-15 catalyst, prepared by the simple IWI method, achieves high yields of DMF and DMTHF under optimal reaction conditions. The level of Ni dispersion, as observed from the materials obtained by infiltration of molten salts, has a significant effect on the catalytic activity of the catalyst.

The second part of my research focuses on the catalytic properties of Cu/SBA-15 monometallic catalysts prepared by different methods, and having different Cu phase division degree (Chapter 5). The methods of preparation applied include the IWI method, the in situ autocombustion method (ISAC) and the deposition-precipitation method (DP). The first part of the study therefore focused on the optimization of the reaction conditions for the selective

hydroconversion of HMF to DMF (over the Cu/SBA-15 catalyst prepared by the ISAC method). Optimized reaction parameters, as for Ni/SBA-15, were reaction temperature, hydrogen pressure, HMF/Cu molar ratio, and reaction time. The reuse of the catalyst was also studied, and a kinetic study of the transformation of HMF on Cu/SBA-15 conducted. This part demonstrates that the activity of Cu for the selective conversion of HMF to DMF depends mainly on the state of dispersion of Cu. The use of the DP method led to a highly divided Cu/SBA-15 catalyst, which made it possible to achieve high yields of DMF.

Keywords: transition metal, impregnation, hydrogenation, biomass, mesoporous, HMF

ACKNOWLEDGEMENT

I would like to express my sincere gratitude to my supervisors Prof. Sebastien Royer and Dr. Eric Marceau for their continuous support and guidance of my PhD study, and for their patience, motivation, and encouragement. I would like to thank Prof. Karine Vigier and Dr. Robert Wojcieszak for their valuable discussions, advices and great help with my research work. I would also like to thank Prof. Frank Dumeignil for accepting me as a PhD student at the UCCS and for his help with the writing of my scientific article.

I would also like to thank the jury members of my thesis, Dr. Florence Epron, Dr. Nadine Essayem, Prof. Karine Vigier and Prof. H el ene Lauron-Pernot, for the reading and the examination of this manuscript.

I would like to thank the other past and present members of the MATCAT group, Carmen Ciotonea, Jean-Philippe Dacquin, J er emy Dhainaut, Jean-S ebastien Girardon, and Anne-Sophie Mamede, for their great help with my research work. I would especially like to thank Carmen, for her considerate help, from the first day of my PhD period, both in work and in life: thanks for the guidance in lab and all the wonderful memories of the coffee-time and selfie-time.

I would like to thank all my colleagues and the technical staff in UCCS, especially Svetlana Heyte, Olivier Gardoll, Jean-Charles Morin, Pardis Simon, Johann Jezequel, for their assistance in my work. I also would like to thank all my colleagues in IC2MP, especially Shi Jiang, Hang Hu, Gongming Peng, Jialu Li, Dimitri Wietthoff, Florent Boissou, Ayman Karam, for their great help and accompanying me during that short but precious staying-time.

I would like to thank my friends and colleagues, Dr. Zhiping Ye, Hao Hu, Dichao, Yin, Peixin, Bang, Xiang, Xuemei, Jin, Jianxiong, Nisrine, Grace, Danu, and all the PhD students, for their support and help during my PhD studies.

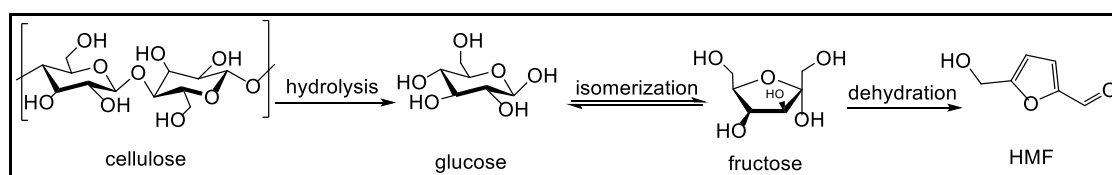
I am grateful to the China Scholarship Council (CSC) for the financial support of my PhD project.

A very special thanks to Mum, Dad and my brother for always being there and offering positive encouragement and endless support throughout.

INTRODUCTION

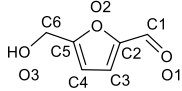
Fossil resources - petroleum, natural gas, coal - have been the main source for the production of transportation fuels and chemicals in the past century, and have thus played a crucial role in accelerating economic growth.^{1,2} However, these resources are limited, and the associated release of CO₂ in the atmosphere has been the source of climate change and global warming.^{3,4} For these reasons, abundant non-edible biomass such as lignocellulose has attracted attention in the last decades as a renewable alternative.⁵ Conversion of biomass can take place by pyrolysis, liquefaction or gasification under relatively harsh conditions,^{6,7} but a more appealing route is based on the hydrolysis of cellulose and hemicellulose, that can be transformed into platform molecules, and ultimately to second-generation biofuels.^{2,4} One of these platform molecules, 5-hydroxymethylfurfural (HMF) plays an important role in connecting biomass resources and the biofuel and chemicals industries.

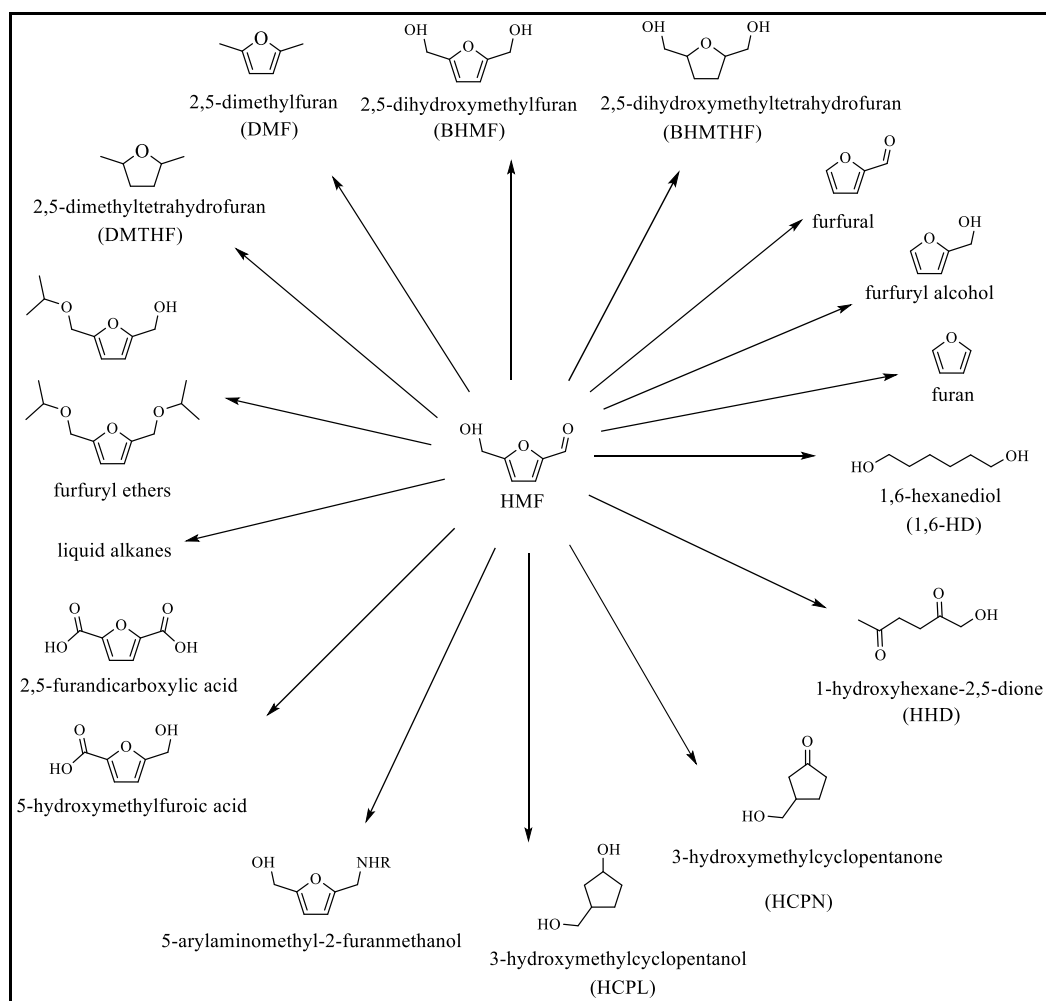
At room temperature, HMF appears as a white or light yellow solid. It is highly soluble in water and in organic solvents. Table 1 provides an overview of its physicochemical properties. It is generally synthesized by dehydration of glucose or fructose, or by hydrolysis/dehydration of cellulose in the presence of acid catalysts (*e.g.*, mineral acid/organic acid/solid acid).⁹⁻¹⁴ HMF was first reported at the end of the nineteenth century when, for the first time, Dull et al. produced it by heating inulin in a solution of oxalic acid under pressure.¹⁵ In the following decades, several new synthesis methods were reported in aqueous media, using either homogeneous or heterogeneous acid catalysts.^{16,17} A typical production route is shown in Scheme 1: cellulose is first converted into glucose/fructose by hydrolysis, and they are further transformed to HMF by dehydration. Currently, the production of HMF is at the stage of the pilot scale. The bottleneck for a scaled-up production is the manufacturing cost, about 2.0 \$/kg,¹⁸⁻²¹ twice the cost required to be competitive in large-scale applications compared to fossil resources.²² The production of HMF-derived molecules will become competitive if the plant size can be extended to over 100 kton/year.



Scheme 1 Production route of 5-hydroxymethylfurfural (HMF)⁸

Table 1 Chemical and physical properties of 5-hydroxymethylfurfural (HMF)

Chemical abstract name	5-(hydroxymethyl)-2-furaldehyde
Chemical formula	C ₆ H ₆ O ₃
Synonyms	5-hydroxymethylfurfural, 5-(hydroxymethyl)-2-furaldehyde, HMF, 5-(hydroxymethyl)-2-furancarbal, 5-(hydroxymethyl)-2-furfural, 5-oxymethylfurfurole, 5-hydroxymethyl-2-formylfuran, hydroxymethyl furfuraldehyde
Molecular structure	
Description	colorless to light yellow powder ²²
Boiling point	114-116 °C at 1 × 10 ⁻⁴ MPa ²²
Melting point	31.5 °C ²³
Solubility	freely soluble in water, methanol, ethanol, acetone, ethyl acetate, dimethylformamide; soluble in ether, benzene, chloroform; less soluble in carbon tetrachloride; sparingly soluble in petroleum ether ²³
UV-vis absorption maximum	282 nm ²⁴

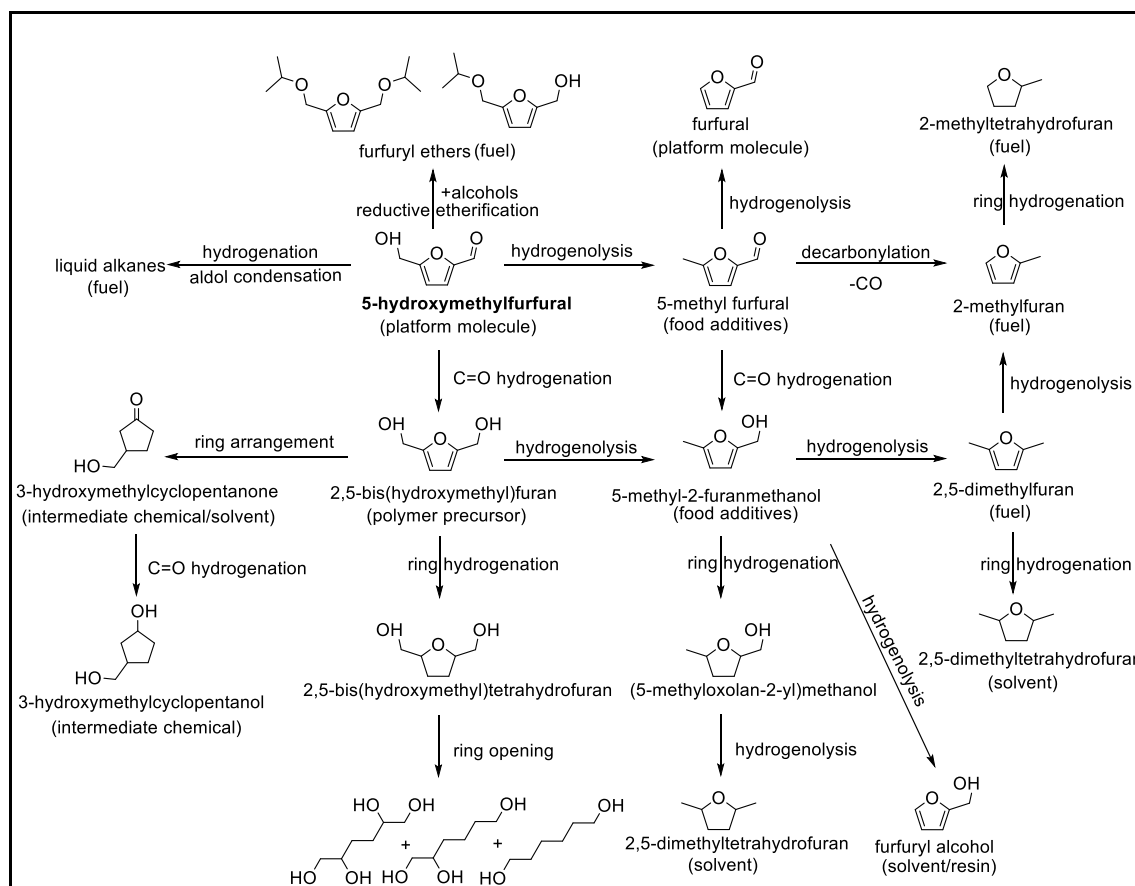


Scheme 2 HMF as a platform molecule

A summary of various derivatives from HMF, used as a platform molecule, is shown in Scheme 2. Chemically speaking, HMF is a heteroaromatic molecule with a pending aldehyde function and a hydroxymethyl group. The transformations of HMF derive from these functionalities. The typical reactions that the aldehyde group can undergo are: reduction to alcohols by H₂ or by hydrogen transfer (Meerwein-Ponndorf-Verley - MPV - reduction); decarbonylation; reductive amination to amines; oxidation to carboxylic acid; acetalisation; aldol and Knoevenagel condensations; acylation; and Grignard reactions. The hydroxyl group can undergo a hydrogenolysis of the C-O bond, oxidation to aldehyde or acid, etherification, acetalisation, esterification and halogenation reactions. The furan ring can be transformed by hydrogenation, ring-opening (by hydrogenolysis of the C-O-C bonds), alkylation, oxidation, halogenation, and nitration reactions.

As an oxygen-rich platform molecule, HMF is easily activated and transformed into valuable chemicals. But a high content of oxygen is a disadvantage when chemicals are used to produce fuels, as it means a lower heat capacity: a further step to decrease their oxygen content is needed. From HMF, this can be obtained by decarbonylation/decarboxylation, dehydration, or hydroconversion.^{22,25} Reductive transformations such as hydrogenation or hydrogenolysis are thus among the key routes for the conversion of HMF to fuels, and are routes in which heterogeneous catalysis plays a central role. However, HMF being a multifunctional compound, a wide variety of chemicals can be produced by reaction with H₂, as summarized in Scheme 3,²⁶⁻²⁹ and undesired reactions can occur during catalytic conversion. Therefore, it is crucial to design active, selective, and stable catalysts to orient the transformation of HMF towards the desired compounds.

Catalytic formulations for hydroconversion processes are based on noble metals, non-noble metals, or the combination of both. Noble metals such as ruthenium, palladium, platinum, gold and rhodium exhibit high intrinsic activities. But they suffer from high and fluctuating costs, and their resources are limited: some of them are expected to be depleted in the next twenty years. In contrast, non-noble metals such as copper, nickel, cobalt, iron and molybdenum are less active while possessing the advantages of a larger abundance and a lower price, and, for some of them, of a low toxicity.



Scheme 3 Summary of value-added chemicals and biofuels derived from HMF *via* hydroconversion⁸

Because of their lower activity, and in order to improve their selectivity and stability, non-noble metals are usually employed in combination with specific supports (TiO₂, Fe-containing supports) or with additives that modify the catalytic properties of the metal. Monometallic catalysts based on Ni or Cu, for example, are seldom reported as active or selective toward HMF hydroconversion reactions. However, one parameter is often not discussed in the literature: the dispersion of the non-noble metal particles. In fact, Ni or Cu particles are difficult to disperse efficiently on supports such as silica or alumina, especially when the preparation is carried out by the most common procedure, impregnation. One can thus wonder to what improvements to the catalytic properties a better control of the metal dispersion would lead, in the absence of further modifications of the catalyst.

This dissertation is divided into eight chapters. Chapter 1 describes the state of the art on the HMF catalytic hydroconversion, with a focus on catalytic formulations involving non-noble metals. Chapter 2 presents the experimental techniques and procedures used. Chapter 3 is devoted to the results obtained with the use of the high-surface area mesoporous SBA-15

silica support for Ni nanoparticles, prepared by an incipient wetness impregnation method. The reaction conditions for the conversion of HMF to alternative biofuels, 2,5-dimethylfuran (DMF) and 2,5-dimethyltetrahydrofuran (DMTHF), on this Ni/SBA-15 catalyst will be discussed. Chapter 4 further examines the properties and performances of another Ni/SBA-15 catalysts, here prepared by melting infiltration, and the effects of the dispersion of Ni NPs on the catalytic performances in HMF hydroconversion. Chapter 5 discusses the reaction condition optimization, the effects of dispersion of Cu nanoparticles (NPs) and the reaction mechanism of monometallic Cu/SBA-15 catalysts prepared by different methods (i.e. incipient wetness impregnation, in-situ auto-combustion, and deposition-precipitation). The manuscript will end with general conclusions and an outlook in this field. In the appendix chapter, additional research about the influence of basic sites in Cu/SBA-15 on the catalyst performances, and research on the preparation of mesoporous carbon materials and mesoporous carbon-supported monometallic Cu catalysts will be presented.

Reference

- (1) Chheda, J. N.; Dumesic, J. A. An Overview of Dehydration, Aldol-Condensation and Hydrogenation Processes for Production of Liquid Alkanes from Biomass-Derived Carbohydrates. *Catal. Today* **2007**, *123* (1–4), 59–70. <https://doi.org/10.1016/j.cattod.2006.12.006>.
- (2) Serrano-Ruiz, J. C.; West, R. M.; Dumesic, J. A. Catalytic Conversion of Renewable Biomass Resources to Fuels and Chemicals. *Annu. Rev. Chem. Biomol. Eng.* **2010**, *1* (1), 79–100. <https://doi.org/10.1146/annurev-chembioeng-073009-100935>.
- (3) Ravishankara, A. R.; Rudich, Y.; Pyle, J. A. Role of Chemistry in Earth's Climate. *Chem. Rev.* **2015**, *115* (10), 3679–3681. <https://doi.org/10.1021/acs.chemrev.5b00226>.
- (4) Huber, G. W.; Iborra, S.; Corma, A. Synthesis of Transportation Fuels from Biomass: Chemistry, Catalysts, and Engineering. *Chem. Rev.* **2006**, *106* (9), 4044–4098. <https://doi.org/10.1021/cr068360d>.
- (5) Elliott, D. C. Historical Developments in Hydroprocessing Bio-Oils. *Energy Fuels* **2007**, *21* (3), 1792–1815. <https://doi.org/10.1021/ef070044u>.
- (6) Lange, J. P. Lignocellulose Conversion: An Introduction to Chemistry, Process and Economics. *Biofuels Bioprod. Biorefining* **2007**, *1* (1), 39–48. <https://doi.org/10.1002/bbb.7>.
- (7) Mohan, D.; Pittman, Charles U.; Steele, P. H. Pyrolysis of Wood/Biomass for Bio-Oil: A Critical Review. *Energy Fuels* **2006**, *20* (3), 848–889. <https://doi.org/10.1021/ef0502397>.
- (8) Zakrzewska, M. E.; Bogel-Łukasik, E.; Bogel-Łukasik, R. Ionic Liquid-Mediated Formation of 5-Hydroxymethylfurfural—A Promising Biomass-Derived Building Block. *Chem. Rev.* **2011**, *111* (2), 397–417. <https://doi.org/10.1021/cr100171a>.
- (9) Zhao, H.; Holladay, J. E.; Brown, H.; Zhang, Z. C. Metal Chlorides in Ionic Liquid Solvents Convert Sugars to 5-Hydroxymethylfurfural. *Science* **2007**, *316* (5831), 1597–1600. <https://doi.org/10.1126/science.1141199>.
- (10) De, S.; Dutta, S.; Saha, B. Microwave Assisted Conversion of Carbohydrates and Biopolymers to 5-Hydroxymethylfurfural with Aluminium Chloride Catalyst in Water. *Green*

Chem. **2011**, *13* (10), 2859–2868. <https://doi.org/10.1039/C1GC15550D>.

(11) Climent, M. J.; Corma, A.; Iborra, S. Converting Carbohydrates to Bulk Chemicals and Fine Chemicals over Heterogeneous Catalysts. *Green Chem.* **2011**, *13* (3), 520–540. <https://doi.org/10.1039/C0GC00639D>.

(12) Dutta, S.; De, S.; Patra, A. K.; Sasidharan, M.; Bhaumik, A.; Saha, B. Microwave Assisted Rapid Conversion of Carbohydrates into 5-Hydroxymethylfurfural Catalyzed by Mesoporous TiO₂ Nanoparticles. *Appl. Catal. Gen.* **2011**, *409–410*, 133–139. <https://doi.org/10.1016/j.apcata.2011.09.037>.

(13) Karinen, R.; Vilonen, K.; Niemelä, M. Biorefining: Heterogeneously Catalyzed Reactions of Carbohydrates for the Production of Furfural and Hydroxymethylfurfural. *ChemSusChem* **2011**, *4* (8), 1002–1016. <https://doi.org/10.1002/cssc.201000375>.

(14) G. Dull. Action of Oxalic Acid on Inulin. *Chem Ztg* **1895**, 216.

(15) Fenton, H. J. H.; Mildre, G. Derivatives of Methylfurfural. *J. Chem. Soc.* **1901**, 807.

(16) Haworth, W. N.; W. G. M. Jones. The Conversion of Sucrose into Furanic Compounds. Part 1. 5-Hydroxymethylfurfuraldehyde and Some Derivatives. *J Chem Soc* **1944**, 667.

(17) Kazi, F. K.; Patel, A. D.; Serrano-Ruiz, J. C.; Dumesic, J. A.; Anex, R. P. Techno-Economic Analysis of Dimethylfuran (DMF) and Hydroxymethylfurfural (HMF) Production from Pure Fructose in Catalytic Processes. *Chem. Eng. J.* **2011**, *169* (1–3), 329–338. <https://doi.org/10.1016/j.cej.2011.03.018>.

(18) Daoutidis, P.; Marvin, W. A.; Rangarajan, S.; Torres, A. I. Engineering Biomass Conversion Processes: A Systems Perspective. *AIChE J.* **2013**, *59* (1), 3–18. <https://doi.org/10.1002/aic.13978>.

(19) Bicker, M.; Hirth, J.; Vogel, H. Dehydration of Fructose to 5-Hydroxymethylfurfural in Sub- and Supercritical Acetone. *Green Chem.* **2003**, *5* (2), 280–284. <https://doi.org/10.1039/B211468B>.

(20) Rapp, K. M. Process for Preparing Pure 5-Hydroxymethylfurfuraldehyde. US4740605 A, April 26, 1988.

(21) Van Putten, R. J.; Van der Waal, J. C.; De Jong, E.; Rasrendra, C. B.; Heeres, H. J.; de Vries, J. G. Hydroxymethylfurfural, a Versatile Platform Chemical Made from Renewable Resources. *Chem. Rev.* **2013**, *113* (3), 1499–1597. <https://doi.org/10.1021/cr300182k>.

(22) Budavari, S.; O'Neil, M. J.; Smith, A.; Heckelman, P. E. *The Merck Index*; Merck Rahway, NJ, 1989; Vol. 11.

(23) Boopathy, R.; Bokang, H.; Daniels, L. Biotransformation of Furfural and 5-Hydroxymethyl Furfural by Enteric Bacteria. *J. Ind. Microbiol.* *11* (3), 147–150. <https://doi.org/10.1007/BF01583715>.

(24) Chen, S.; Wojcieszak, R.; Dumeignil, F.; Marceau, E.; Royer, S. How Catalysts and Experimental Conditions Determine the Selective Hydroconversion of Furfural and 5-Hydroxymethylfurfural. *Chem. Rev.* **2018**, *118* (22), 11023–11117. <https://doi.org/10.1021/acs.chemrev.8b00134>.

(25) Nakagawa, Y.; Tamura, M.; Tomishige, K. Catalytic Reduction of Biomass-Derived Furanic Compounds with Hydrogen. *ACS Catal.* **2013**, *3* (12), 2655–2668. <https://doi.org/10.1021/cs400616p>.

(26) Gallezot, P. Conversion of Biomass to Selected Chemical Products. *Chem Soc Rev* **2012**, *41* (4), 1538–1558. <https://doi.org/10.1039/C1CS15147A>.

(27) Lange, J. P.; van der Heide, E.; van Buijtenen, J.; Price, R. Furfural-A Promising Platform for Lignocellulosic Biofuels. *ChemSusChem* **2012**, *5* (1), 150–166. <https://doi.org/10.1002/cssc.201100648>.

(28) Zeitsch, K. J. *The Chemistry and Technology of Furfural and Its Many By-Products*; Elsevier, 2000.

(29) Dautzenberg, G.; Gerhardt, M.; Kamm, B. Bio Based Fuels and Fuel Additives from Lignocellulose Feedstock via the Production of Levulinic Acid and Furfural. *Holzforschung* **2011**, *65* (4), 439–451. <https://doi.org/10.1515/hf.2011.081>.

CHAPTER 1: LITERATURE REVIEW

In the last decades, a substantial amount of publications has promoted the potential of replacing noble metal-based catalysts by non-noble metal-based catalysts for the hydroconversion of furanic compounds such as HMF. Nonetheless, the development of optimized catalytic formulations, especially based on non-noble metal-based catalysts, is complex. The development of original catalytic formulations and the enhancement of existing ones involve the study of a number of different impacts: the active metal(s); the support; the presence of metal additives or co-catalysts; the preparation procedure; the interplay between the catalyst and the solvent; the ability of the active phase to withstand the presence of poisons. The exploration of these parameters will be the subject of this chapter.

1.1 Adsorption chemistry of furanic compounds on metal surfaces

This section summarizes the knowledge on the adsorption chemistry of furanic compounds over different metal surfaces to reveal, to some extent, the nature of different active metals in the hydroconversion processes of HMF.

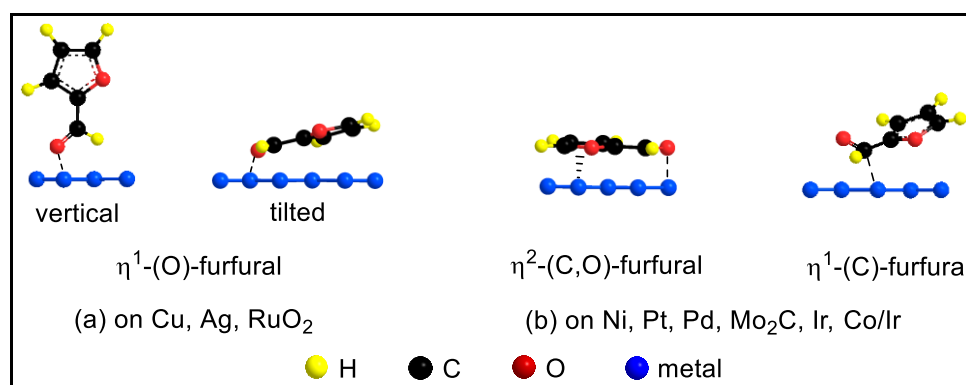


Figure 1.1 Preferential adsorption configurations of furfural over different surfaces, based on DFT calculations¹

The adsorption mode of furanic compounds onto the active metal determines to a large extent the pathway followed during its reductive transformation, and thus the product distribution. Most existing reports focus on the adsorption modes of furfural (FFR), a sister molecule of HMF, and of its hydrogenation/hydrogenolysis products: furfuryl alcohol (FOL), 2-methylfuran (MeF) and furan. Few reports are currently available on the adsorption of HMF on metals. The knowledge about the adsorption chemistry of FFR should help to understand the adsorption behaviors of HMF over different metal surfaces.

Density functional theory (DFT) calculations and surface science measurements have evidenced that multifunctional furanic compounds can adsorb onto a metal surface either *via* the furan ring, *via* the oxygenated pendant functions, or through multiple binding. The adsorption mode of furanic compounds is highly dependent on the nature of metals. Three typical adsorption modes have been proposed over metals active in the hydrogenation of FFR, as shown in Figure 1.1.

The interaction of FFR with a Cu surface involves the η^1 -(O) adsorption mode via the aldehyde function, as shown in Figure 1.1a. A tilted η^1 -(O) configuration is more stable than a perpendicular one.^{2,3} The strong repulsion of the furan ring with the Cu (111) surface results from the partial overlap of the 3d band of the Cu atoms with the anti-bonding orbitals of the furan ring.^{4,5} The flat adsorption mode of FFR on the Cu surface is thus not stable, and generally does not exist. A similar tilted adsorption mode of furanic compounds has also been reported on Ag (110).² The aldehyde function thus more likely reacts with adsorbed H atoms, and this adsorption mode limits the conversion of the furan ring, with consequently a less preferential formation of ring-hydrogenation or ring-opening products. Compared to Pt (111), Pd (111), Ni (111) and Ni/Cu (111), the binding energy of the furan ring on the Cu (111) surface is indeed low, indicating a lower hydrogenation ability of Cu-based catalysts for the furan ring hydrogenation.^{3,6} This all accounts for the high selectivity of Cu-based catalysts to alcohol products. The adsorption of FOL onto RuO₂ also adopts the tilted η^1 -(O)-aldehyde configuration, with the oxygen from the -OH group binding to a Ru coordinately unsaturated site. The interaction between the furan ring and the RuO₂ (110) surface is weak (-1.76 eV vs. -1.0 eV for FOL on metallic Pd).⁷ The stability of FOL on the RuO₂ (110) surface is attributed to the hydrogen bond formed between the -OH function from HMF and a neighboring O site. The Lewis basicity of the O site can improve the deprotonation of FOL on the way to MeF, giving to the RuO₂ phase a hydrogenolysis activity.

Unlike Cu, the furan ring can readily adsorb on Pt, Pd and Ni, because of a strong interaction between the metal and the π bonds in the molecule, originating from a sp^2 -to- sp^3 rehybridisation.^{2,8} On these metals, FFR tends to adopt an η^2 -(C,O)-aldehyde adsorption mode in which the furan ring lies onto the metal surface with both the C atom and the O atom of the carbonyl group also bonded to the surface (Figure 1.4b).^{9,10} The interaction strength of FFR with Ni, Pd, Pt and Cu follows the trend Ni > Pd > Pt >> Cu.^{11,12} Once FOL has been formed by hydrogenation of furfural, the hydroxymethyl group further favors the planar

adsorption on Ni, especially when surfaces are rough and exhibit edges or corner sites.¹³ Additionally, when the temperature increases, the η^2 -(C,O)-aldehyde adsorption mode converts into a η^1 -(C)-acyl species (Figure 1.1b).

Because in the η^2 -(C,O)-aldehyde adsorption mode, both the furan ring and the formyl group interact with the metal, hydrogenation reactions involve both the furan ring and the side function: hydrogenation of the furan ring to tetrahydrofuran (THF), hydrogenation of -CHO to -CH₂OH, or hydrogenation/hydrogenolysis of -CHO to -CH₃, even ring opening reactions. The η^1 -(C)-acyl species is rather the precursor for the decarbonylation of FFR to furan.

Like FFR, the differences in interaction strength between the different functional groups (e.g., the furan ring, the aldehyde group and the hydroxymethyl group) also lead to different adsorption geometries of HMF depending on the metal, as has been revealed by recent experimental and theoretical research.

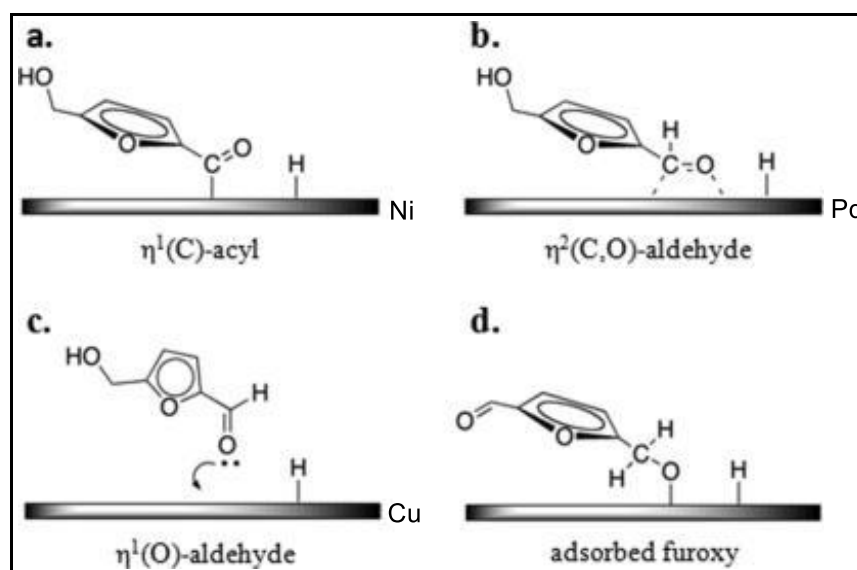


Figure 1.2 Proposed adsorption configurations of HMF on Ni, Pd and Cu metal surfaces¹⁴

In 2015, Duarte et al. reported an effect of the adsorption mode of HMF over alumina-supported Ni, Pd and Cu catalysts on the activity and selectivity in HMF hydrodeoxygenation.¹⁵ Adsorption geometries based on experimental data are presented in Figure 1.2. On Ni/alumina, FOL was the main product owing to the decarbonylation reaction of HMF through the η^1 -(C)-acyl intermediate (Figure 1.2a). On Pd/Al₂O₃ catalyst, the η^2 -(C,

O)-HMF configuration was preferred (Figure 1.2b), which led to a high activity both for decarbonylation and furan ring hydrogenation. On Cu/Al₂O₃ catalyst, HMF tended to adsorb in the η^1 -(O)-HMF configuration (Figure 1.2c), which allowed to abstract hydrogen from the hydroxyl group to give an adsorbed furoxy intermediate (Figure 1.2d). A later work by Luo et al. on the transformation of HMF over Pt₃Co₂, Pt₃Co, and Pt provided a theoretical insight into the catalyst composition effects on the adsorption mode of the molecule.¹⁶ The absence of covalent bonding of the ring with the metal surface (Pt₃Co₂) is critical to selectively favor the hydrogenolysis of the CH₂OH group and suppress ring-hydrogenation and ring-opening side reactions. In contrast, the strong interaction between the ring and Pt in both Pt and Pt₃Co nanocrystals promotes ring hydrogenation and ring opening, with barriers which are lower than for hydrogenolysis.

In conclusion, there tends to be a strong interaction between HMF, and Pt-group metal and Ni surfaces, especially through the furanic ring of the molecule, and a weaker interaction with Cu surfaces, on which the adsorption mode is limited to the side group, which leads to obvious differences in the products distribution.

1.2 The catalytic production of value-added chemicals from HMF: general trends

BHMF is the product of hydrogenation of the C=O bond of HMF. It is generally used as a six-carbon monomer for the synthesis of polymers: polyurethane foams, resins, artificial fibers.^{17,18} A wide series of heterogeneous catalysts (i.e., Pd-, Pt-, Ru-, Ir-, Au-, Cu-, Co-based catalysts and solid acid-base catalysts) have exhibited activities for BHMF production, as shown in Table 1.1. Relatively mild reaction conditions have been selected in order to avoid over-hydrogenation, especially for noble-metal based catalysts ($T \leq 130$ °C and $P \leq 6$ MPa for noble metal-based catalysts; $T \leq 220$ °C and $P < 7$ MPa for non-noble metal-based catalysts).¹ Pd-based catalysts are too active to exclusively form BHMF, even under very mild reaction conditions (e.g. $T \leq 60$ °C and $P \leq 1$ MPa). Monometallic Pt- and Ru-based catalysts are more appropriate when the reaction conditions are properly controlled ($T \leq 70$ °C and $P < 2$ MPa for Pt-based catalysts; $T \leq 130$ °C and $P < 3$ MPa for Ru-based catalysts). Au-based catalysts are intrinsically selective for C=O hydrogenation over C=C hydrogenation, which makes them potential candidates for the production of BHMF. Highly active Au catalysts have been supported on carriers with basic properties (e.g. La₂O₃ and CeO₂) and prepared with a good control of the particle size of Au clusters, obtained by

modulating the calcination conditions or by modifying the support surfaces (e.g., with FeO_x species). The hydrogenation ability of monometallic Ir-based catalysts is very limited, and ReO_x species have been used as promoters which, however, may face leaching problems in the reaction medium. Ni-based catalysts are considered to be too active in hydrogenation for the selective production of BHMF.

Table 1.1 Metals and reaction conditions generally used for the synthesis of the main HMF-derived chemicals

catalysts	BHMF			BHMTHF			DMF		
	T (°C)	P (MPa)	promoters	T (°C)	P (MPa)	promoters	T (°C)	P (MPa)	promoters
Pd-based	15-60	0.1-0.8	-	2-50	6-8	Ni, Ir	60-200	0.1-3	Au, Zn
Ru-based	25-130	0.5-2.8	Mg	130	2-4	Mg	150-220	0.7-2	Fe, Cu, Zn, MoO _x
Pt-based	35-70	0.8-2	Sn	-	-	-	120-200	1-3.3	Co, Cu, Zn, Ni
Rh-based	-	-	-	-	-	-	-	-	-
Ir-based	30-50	0.8-6	ReO _x	-	-	-	-	-	-
Au-based	80-120	3-6.5	Fe	-	-	-	-	-	-
Cu-based	100-220	1.5-5	Ru	-	-	-	180-220	1.5-6.8	Cr, Ru, Zn, Co, Ni
Ni-based	-	-	-	40- 120	0.4-9	Fe, Co	130-230	1.2-4	W ₂ C, Fe, Zn
Co-based	60-160	3-4	-	120	4	-	130-210	1-5	Ni, Cu, Zn, Ag, NGr
Fe-based	-	-	-	-	-	-	240	1-4	N
Acid cat.	150	0.1	-	-	-	-	-	-	-

Among non-noble metals, attention has been paid to the use of Cu- and Co-based catalysts, which exhibit high selectivities to BHMF, with hydrogenation activities that are relatively lower than those of noble metal-based catalysts. High metal loadings (≥ 15 wt %) and relatively higher reaction temperatures and H₂ pressures (> 100 °C and 1.5-5 MPa for Cu-based catalysts; 60-160 °C and 3-4 MPa for Co-based catalysts) are generally required to attain high hydrogenation activities. Besides, deactivation is still a tough problem troubling non-noble metal based catalysts. For example, Kumalaputri and co-workers reported a hydrotalcite-derived Cu and CuRu catalyst which afforded excellent activities, achieving near 100% BHMF yields. However, these catalysts experienced a severe loss of selectivity to BHMF ($> 30\%$) due to the deposition of carbon species onto the catalyst surface.^{19,20}

The formation of BHMTTHF results from the total hydrogenation of HMF (Scheme 3). As compared with the BHMF synthesis, higher reaction pressure and/or longer reaction time are generally needed. The high hydrogenation activity of Ni-based catalysts makes them the first choice for BHMTTHF production.¹ Commercial Raney Ni and Ni-Al-based catalysts have exhibited excellent catalytic performances under a wide range of reaction conditions (0.4-9 MPa and 60-120 °C). However, their efficiency is generally based on high Ni loadings (over 40 wt.%), and in some cases is troubled by deactivation caused by Ni leaching and carbon deposition. One potential method to decrease the Ni loading and at the same time to increase the catalyst stability may lie in the preparation of finely dispersed Ni NPs or in the use of bimetallic Ni-based catalysts (e.g., NiFe, NiCo). Co-based catalysts are another potential choice for BHMTTHF production.²¹ Ru- and Pd- based catalysts generally exhibit a higher stability and can be selective if the support bears basic sites or if a second metal is added (e.g., Ni and Ir).^{22,23}

Linear aldehydes (1-hydroxyhexane-2,5-dione, HHD) and alcohols (1,6-hexanediol (1,6-HD) and 1,2,6-hexanetriol (1,2,6-HT)) can be produced from HMF and from its derivatives (BHMF, BHMTTHF) via ring-opening reactions in reductive conditions. Bifunctional catalysts bear both the active metal sites catalyzing the hydrogenation of the C=O function, and the Brønsted acidic sites promoting the hydrolytic ring opening. Water is the most efficient reaction medium. A balance between the acidity and the hydrogenation activity should be found, since a too strong acidity may cause the degradation of HMF and of the reaction intermediates. Efficient systems include acidic M-M'Ox catalysts (M = Rh or Ir; M' = Re) which generally catalyze the conversion of BHMTTHF as starting reactant or intermediate, and some noble metal-based catalysts (Pd-, Pt- and Au-based catalysts) displaying Brønsted acidity, or combined with Brønsted acids. Recent progress in this field highlights the application of non-noble metal based catalysts, with a breakthrough made with Ni-Co-Al mixed metal oxides. But it is crucial for the large-scale industrialized production of HHD, 1,6-HD and 1,2,6-HT to enhance the catalyst stability in aqueous solution.¹

The reductive ring-rearrangement of HMF in aqueous phase affords 3-hydroxymethylcyclopentanone (HCPN) and 3-hydroxymethylcyclopentanol (HCPL). Typical catalytic systems include Pt supported on metal oxides (e.g., Ta₂O₅, ZrO₂ and Nb₂O₅), Pt/SiO₂ combined with metal oxides additives, and Ni-Co-Cu-Al₂O₃ mixed oxides. The acid-base properties of the catalyst must be moderate in order to facilitate intermediate steps of

aldolization and dehydration. The role of the metal sites in the ring-opening/closing steps, and the effect of the basic sites in the aldol-condensation reaction is still not completely clear. Furthermore, the reusability of non-noble metal based catalysts is currently limited by the catalyst deactivation caused by carbon deposition, the instability of the support (formation of hydrated boehmite $\text{AlO}(\text{OH})$ from Al_2O_3), and the transformation of the active phase (formation of Co_3O_4 from metallic cobalt). Catalysts presenting a high activity for the furan ring hydrogenation and for hydrogenolysis should be avoided, as they make it difficult to selectively produce the key intermediate, BHMF, and then target HCPN and HCPL.¹

The transformation of HMF to dimethylfuran (DMF) will be specifically presented in the next section.

1.3 The production of DMF from HMF

Table 1.2 Comparison of the physicochemical properties of DMF, bioethanol, gasoline and diesel^{17,24,25}

Properties	DMF	bioethanol	gasoline	diesel
molecular formula	$\text{C}_6\text{H}_8\text{O}$	$\text{C}_2\text{H}_6\text{O}$	$\text{C}_4\text{-C}_{12}$	$\text{C}_8\text{-C}_{25}$
oxygen content (%)	16.67	34.78	0	0
energy density(MJ/L)	31.5	23	35	35.8
research octane number	119	110	95.8	-
latent heat vaporization (kJ/kg, 25 °C)	389.1	919.6	351	270-301
relative vapor density	3.31	1.59	3-4	-
water solubility (wt.%, 20 °C)	0.26	miscible	negligible	-
boiling point (°C, 101 kPa)	92-94	78.4	27-225	180-370
liquid density (kg/m ³ , 20 °C)	889.7	790.9	744.6	820
kinematic viscosity (cSt, 20 °C)	0.57	1.5	0.37-0.44	-

Among the HMF-derived products, 2,5-dimethylfuran (DMF) is especially valuable is increasingly gaining attention. On the one hand, DMF is considered as a promising alternative fuel of new generation, which has the potential to relieve the global fossil fuel shortage and air pollution problems. As shown in Table 1.2, despite potential issues such as a lower energy density than gasoline and diesel,²⁶ DMF is attractive because of a higher energy density than bioethanol, higher octane number than bioethanol and gasoline, and lower volatility than gasoline and diesel. Besides, as compared with bioethanol, it is more difficult for DMF to absorb water from air.⁷⁷ DMF also exhibits good performances for direct-injection, spark-ignition type engines.^{27,28} On the other hand, DMF can directly serve as a solvent in the perfume and pharmaceutical industries.

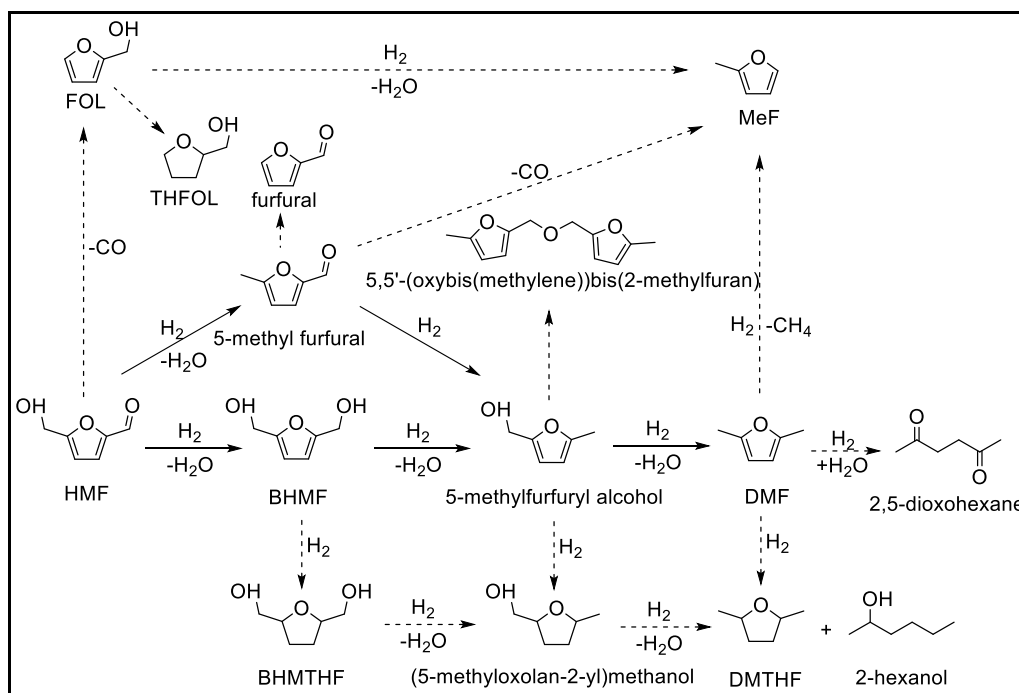


Figure 1.3 Reaction network for the transformation of HMF to DMF and possible side-reactions (dashed arrows)^{29,30}

The formation of DMF from HMF involves the hydrogenation and hydrogenolysis of both side groups of HMF. Two reaction routes have been well-established in the literature, both in the liquid phase.^{29,30} One starts with the hydrogenation of -CHO, first giving BHMF as intermediate, while the other one starts with the hydrogenolysis of -CH₂OH, first giving 5-methylfurfural (MFFR) as intermediate, both to be transformed to 5-methylfurfuryl alcohol (MFOL) by hydrogenolysis and hydrogenation respectively. MFOL is further converted to DMF through further hydrogenolysis of -CH₂OH. To achieve high DMF selectivities, one should thus target catalysts that are active both for the hydrogenation/hydrogenolysis of the -CHO and -CH₂OH functions, and at the same time inactive for reactions transforming DMF, in particular the furanic ring. Besides, reaction temperature is a key parameter for the selective formation of DMF. In most cases, this process requires high-temperature conditions, which unfortunately often induce undesired reactions (e.g., decarbonylation, ring hydrogenation, ring-opening reactions and condensation reactions), as shown in Figure 1.3. At low reaction temperatures, especially for non-noble metal based catalysts, the transformation of HMF may mainly stop at the formation of BHMF, while the hydrogenolysis activity may not be adequate to form DMF.³¹

Most of the catalyst formulations screened for the hydrogenolysis of HMF to DMF during the last decades are based on noble metals.^{22,32} Palladium, platinum and ruthenium exhibit high intrinsic hydrogenation activities. Non-noble metals such as copper, nickel, cobalt and iron stand as promising alternatives provided that their activity, selectivity and stability are efficiently improved. Optimization of non-noble metal-based systems can be performed through combination with other metals, and through the choice of proper support, and/or co-catalysts (*e.g.*, mineral acids). As a consequence, the preparation of active and stable non-noble metal catalysts has been highly sought-after in the selective hydrogenolysis of HMF to DMF, where the dispersion of non-noble metal NPs and the interaction between the metal and the support could act as key factors. The following sections will summarize the current progress on heterogeneous catalysis for the production of DMF from HMF. The different catalysts characteristics (especially of non-noble metals) and the strategies to improve the selectivity will be highlighted.

1.3.1 Catalytic performances of noble metal-based catalysts

For noble metal-based catalysts, the relatively strong interaction between the furan ring, the aldehyde group, the hydroxymethyl group, and the metal surface, leads to a broad distribution of products. In order to increase the yield of DMF, strategies involve the use of proper metal additives and supports.

Ru has been playing an important role, either as an additive or as the active metal, in the hydrogenolysis of HMF to DMF. Table 1.3 summarizes the performances of Ru-based catalysts for the DMF synthesis from HMF and fructose. Reaction temperatures vary from 50 to 260 °C and reaction pressures range between 0.8 and 6 MPa. The Dumesic group used CuRu/C as a catalyst in a pioneering work on the two-step conversion of fructose to DMF (71% yield), with HMF as an intermediate (Table 1.3, Entry 1).³³ Later, Saha et al. reported on a Ru/C catalyst giving a maximum of 32% DMF yield in 1 h from fructose (Table 1.3, Entry 7).³⁷ However, formic acid and sulfuric acid were required as hydrogen source and deoxygenating agent. The Ru/C catalyst used by Hu et al. gave a DMF yield of 95% at complete conversion of HMF at 180 °C under 2 MPa of H₂, but experienced deactivation after 3 cycles (Table 1.3, Entry 2).²⁹ Back to bimetallic systems, a recent work by Yang et al. showed that bi-functional 5wt.%Ru-MoO_x/C afforded a DMF yield of 79.5% at complete conversion at 180 °C under 1.5 MPa. Ru species acted as hydrogenation sites, while MoO_x assisted hydrogenolysis (Table 1.3, Entry 5).³⁵

Table 1.3 Catalytic performances of Ru-based catalysts for the conversion of HMF and fructose to DMF

Entry	Catalyst	Feed condition	P (MPa)	T (°C)	t (h)	conv. (%)	yield (%)	ref
1	CuRu/C	5 wt.% HMF in 1-butanol	6.8	220	10	100	71	33
2	Ru/C	3.6 mmol HMF; 20 mL THF	2	180	2	100	95	29
3	40 wt% Ru/Co ₃ O ₄	2 mmol HMF; 10 mL THF; 0.1 g catalyst	0.7	130	24	99	93.4	34
4	Ru-doped hydrotalcite	1 mmol HMF; 25 mL 2-propanol; 0.05 g catalyst	1	220	4	100	58	35
5	Ru-MoO _x /C	4 mmol HMF; 40 mL n-butyl alcohol; 0.1 g catalyst	1.5	180	1	100	79.5	35
6	Ru/CoFe-LDO	2 mmol HMF; 10 mL THF; 0.1 g catalyst	1	180	6	100	98.2	36
7	Ru/C	step 1: 4 mmol fructose, 2 mL formic acid, 150 °C, 2 h; step 2: 8 mL THF, 0.028 mL concentrated H ₂ SO ₄ , 0.8 g Ru/C, 75 °C, 15 h	-	-	-	-	30	37

^a: hydrogen titration gives 0.01475 mol/g substrate; ^b: two-step DMF synthesis from fructose with HMF as an intermediate.

Apart from carbon, Ru has been loaded on a variety of supports that contribute to the conversion of HMF to DMF. Zu et al. reported that Ru/Co₃O₄, prepared by co-precipitation, achieved a DMF yield of 93.4% at a conversion of over 99% HMF at 130 °C under 0.7 MPa of H₂ (Table 1.3, Entry 3).³⁴ This catalyst could be recycled 5 times without loss of activity. It was proposed that Ru was responsible for hydrogenation while CoO_x allowed the adsorption of the hydrogenated intermediate and the subsequent C-O bond cleavage. Nagpure showed that a 0.56 wt.% Ru-containing hydrotalcite-derived catalyst, prepared by co-precipitation, provided a DMF yield of 58% at complete conversion at 220 °C in 2-propanol under 1 MPa after 4 h (Table 1.3, Entry 4).³⁵ The performances were retained after five cycles. A higher metal loading (1-1.7 wt.%) led to a lower yield of DMF due to a decreasing dispersion of Ru particles. A very recent work by Li et al. showed that a 5 wt.% Ru catalyst supported on a CoFe layered double oxide (CoFe-LDO) afforded a DMF yield of 98.2% at complete conversion in THF at 180 °C under 1 MPa after 6 h (Table 1.3, Entry 6).³⁶ The catalyst could be recycled three times without loss of activity. The size of Ru particles was less than 3 nm. The catalytic performance was attributed to the cooperation between the metallic Ru sites and the CoO-Fe₂O₃ composite phase.

Table 1.4 Catalytic performances of Pt-based catalysts for the conversion of HMF to DMF

Entry	Catalyst	Feed Conditions	P (MPa)	T (°C)	t (h)	conv. (%)	yield (%)	ref
1	Pt/C	1 wt.% HMF in 1-propanol; 0.05 g catalyst	3.3	180	0.5	100	27.2	39
2	Pt/C	8 mmol HMF; 100 mL 1-propanol; W/F = 25 g·min/g	3.3	180	-	83.4	53.1	31
3	Pt/C	8 mmol HMF; 100 mL ethanol; W/F = 50 g·min/g	3.3	180	-	95.3	68.5	40
4	Pt ₃ Co ₂ /C	8 mmol HMF; 100 mL 1-propanol; W/F = 1.0 g·min/g	3.3	160	-	100	98	41
5	Pt ₃ Ni/C	8 mmol HMF; 100 mL 1-propanol; W/F = 1.0 g·min/g	3.3	200	-	100	98	42
6	Pt ₂ Zn/C	8 mmol HMF; 100 mL 1-propanol; W/F = 1.0 g·min/g	3.3	200	-	100	98	42
7	PtCu/C	8 mmol HMF; 100 mL 1-propanol; W/F = 1.0 g·min/g	3.3	200	-	100	96	42
8	PtCo@HCS	2 mmol HMF; 5.9 mL 1-butanol; 0.05 g catalyst	1	180	2	100	98	39
9	Pt/AC	2 mmol HMF; 12 mL 1-butanol; 0.088 g catalyst	3	120	2	67.4	32.6	43
10	Pt/rGO	2 mmol HMF; 12 mL 1-butanol; 0.08 g catalyst	3	120	2	100	73.2	43
11	Pt/OMD1 ^a	2 mmol HMF; 20 mL water; 0.05 g catalyst	3	200	6	99	62.3	44

^a: Pt-OMD1, Pt supported on mesoporous nitrogen-rich carbon, prepared by organic matrix deposition method.

The catalytic performance of Pt/C systems in the synthesis of DMF from HMF is summarized in Table 1.4. Compared to pure active carbon, the incorporation of nitrogen atoms to the surface of carbon not only enhances its conductivity, polarity and basicity, but also increases the strength of the carbon-metal interaction.^{45,46} In the aqueous phase, Pt supported on a nitrogen-rich carbon material (Pt/OMD1) synthesized using SBA-15 as a hard template, afforded a DMF yield of 62.3% at 99% conversion (Table 1.4, Entry 11).⁴⁴ rGO can also contribute to the catalytic efficiency of Pt on four aspects: (i) the dispersion of Pt particles is improved, as both sides of rGO sheets are accessible to Pt particles and a strong interaction prevents their aggregation;⁴⁷ (ii) oxo-functional groups on the surface of rGO may accelerate the catalytic reaction;⁴⁸ (iii) the micropore-free structure of rGO favors the diffusion of HMF molecules; (iv) the selective adsorption of HMF may be favored.⁴³ Shi et al. reported that a Pt/rGO catalyst afforded a DMF yield of 73.2% at complete conversion of HMF in 1-butanol (Table 1.4, Entry 10).⁴³ Finally, the combination of hollow carbon spheres and of a metal additive brings the catalytic performance of Pt-based catalysts to a higher level. Wang et al. encapsulated Pt NPs in hollow polymer spheres using a soft-templating method, followed by introduction of cobalt ions into the polymer shells through ion-exchange with carboxylate groups.³⁹ Small, homogeneously alloyed PtCo NPs (3.6 ± 0.7 nm) were formed in the system pyrolyzed at 500 °C. Elemental mapping showed that PtCo NPs were located both in the hollow core and in the

carbon shell. The resulting catalyst afforded a DMF yield of 98% at complete conversion of HMF at 180 °C and 1 MPa in butanol after 2 h (Table 1.4, Entry 8).

Another strategy consists of performing the reaction in a flow reactor instead of a batch reactor. Luo et al. reported that the highest yield of DMF (27.2%) at full HMF conversion was reached within 30 min over Pt/C in a batch reactor (Table 1.4, Entry 1), but with the formation of several side-products, most of which originating from the over-hydrogenation of DMF.³⁹ When the reaction was performed in a flow reactor, the selectivity to DMF significantly increased due to the shorter contact time between the catalyst and the reactants (Table 1.4, Entry 2).³¹ A higher yield (68.5% DMF at 95.3% conversion) was obtained in the same conditions of temperature and pressure with a comparable catalyst (Table 1.4, Entry 3).⁴⁰ Recently, the same group reported a series of highly efficient Pt alloy catalysts. A yield of DMF as high as 98% was achieved over Pt₃Co₂/C, Pt₃Ni/C, Pt₂Zn/C and PtCu/C under flow conditions (Table 1.4, Entry 4-7).^{41,42} It was proposed that alloying the metals modified the bonding of DMF so as to prevent the furan ring from lying down on the catalyst surface, suppressing the over-hydrogenation of DMF. Bimetallic catalysts also presented a higher stability.

Table 1.5 Catalytic performances of Pd-based catalysts for the conversion of HMF to DMF

Entry	Catalyst	Feed conditions	P (MPa)	T (°C)	t (h)	conv. (%)	yield (%)	ref
1	Pd/C	1 mL water; Pd/HMF, 1/5 molar ratio	1 ^a	80	2	100	100	49
2	Pd/C	1 mmol HMF; 1.5 mL acetonitrile; 3 g EMIMCl; 0.002 g catalyst	6.2	120	1	47	16	38
3	Pd/C	0.5 mmol HMF; 10 mL THF; 0.06 g catalyst	0.1	60	6	99	99	50
4	PdAu/C	1 mmol HMF; 10 mL THF; 0.03 g catalyst	0.1	60	6	99	99	50
5	Pd/C	2 mmol HMF; 20 mL THF; 0.4 g catalyst	1.0	90	2	96	38	51
6 ^c	Pd/C	2 mmol HMF; 10 mL THF; 0.4 g catalyst	0.1	70	15	100	95	52
7	Pd/C	1 mmol HMF; 5 mL dioxane; 10 mmol formic acid; 0.1 g catalyst	0.1(air)	120	20	95	95	53
8	Pd/C	4 mmol HMF; 30 mL 1-propanol; 0.25 g catalyst	0.1	60	2.5	100	35.7	54
9 ^d	Pd/Al ₂ O ₃	4 mmol HMF; 30 mL 1-propanol; 0.25 g catalyst	0.1	60	2.5	100	28.3	54

^a: P_{H₂} = 1 MPa, P_{CO₂} = 10 MPa; ^b: Pd-OMD1, Pd supported on mesoporous nitrogen-rich carbon, prepared by organic matrix deposition method ^c: formic acid and H₂SO₄ used as co-catalysts; ^d: 6 μL HCl added.

The production of DMF from HMF over Pd-based catalysts has been widely studied. Table 1.5 summarizes the catalytic performances of typical Pd-based catalysts reported in the literature. Temperatures vary between 60 and 220 °C, while pressures range from atmospheric pressure to 6.2 MPa. The best performance was obtained with a Pd/C catalyst under supercritical conditions, achieving a total conversion of HMF to DMF in water at

80 °C, under 10 MPa CO₂ and 1 MPa H₂ after 2 h (Table 1.5, Entry 1). In such conditions, noble metals such as Pt and Ru, considered as highly active in hydrogenation, exhibit extremely low catalytic activities. Pd generally favors decarbonylation, ring hydrogenation and ring hydrogenolysis of HMF.¹ Different strategies have been attempted to suppress these side-reactions, such as using co-catalysts, metal additives, alloys, specific supports or solvents, or tuning the experimental conditions.

Acids such as HCOOH, HCl, and H₂SO₄ have proved to be effective co-catalysts to improve the yield of DMF from HMF with Pd-based catalysts in CTH processes.^{52, 53, 54} With HCOOH and H₂SO₄ in the reaction medium, a DMF yield of 95% was obtained from HMF with Pd/C in THF under mild experimental conditions (Table 1.5, Entry 6). Formic acid played three roles: (i) hydrogen source for the formation of BHMF as the intermediate (Figure 46); (ii) reagent for the deoxygenation of furanymethanols; (iii) inhibitor to the decarbonylation and furan ring hydrogenation routes.^{52, 53} H₂SO₄ was used to catalyze the etherification reaction of the intermediate products, which improved the efficiency of the hydrogenolysis steps. HCl also prevented the undesired furan ring hydrogenation, and enhanced the hydrogenolysis steps through a nucleophilic substitution of Cl⁻ onto the hydroxyl groups, forming a reactive chlorinated intermediate:⁵⁴ both the strong acidity of HCl and the presence of chloride ions were thus necessary to orientate the conversion of HMF to DMF with high efficiency. CH₃COOH, CO₂/H₂O and dimethyldicarbonate ([CH₃OC(O)]₂O) also exhibited co-catalytic effects.⁵³ However, acid co-catalysts cause the corrosion of the equipment and environmental pollution, which may restrict their practical applications.

In contrast to acidic co-catalysts discussed above, the use of the acidic supports led to negative effects for this transformation. Carbon is the most used support for Pd phase in the production of DMF from HMF (Table 1.5). Pd supported on SiO₂, β -zeolite, Amberlyst-15 and α -Al₂O₃ afforded no more than a DMF yield of 40% from HMF (1.0 mmol HMF, 10 mL THF, 0.17 mmol HCl, 31.3 mg catalyst, Pd = 0.47 mmol/g, 0.1 MPa H₂, 60 °C, 12 h), while a DMF yield of 66% could be obtained with Pd/C.⁵⁰ The support acidity could induce side-reactions such as the furan ring opening. Besides, when the conversion of HMF was performed in water, the hydrophobic/hydrophilic nature of the support also affected the catalytic performance. Pd loaded over hydrophilic supports, such as Al₂O₃ and MCM-41, exhibited lower catalytic activities than Pd/C.⁴⁹

The nature of the solvent has an important influence on the properties of Pd-based catalysts. The most commonly used solvent for the synthesis of DMF from HMF is THF. Water, alcohols, ionic liquids and dioxane have also been tried. The low solubility of H₂ in EMIMCl (an ionic liquid) was proposed to be responsible for the low conversion of HMF over Pd/C (Table 1.5, Entry 2).³⁸ Solvation influences the adsorption behavior of the substrates and intermediates. In non-polar solvents, polar

reactants tend to be less strongly solvated and thus adsorb more strongly onto the surface of the catalyst.⁵⁵ As BHMF is a more polar compound than DMF, less polar solvents such as THF and 1,4-dioxane favor its strong adsorption, and a higher selectivity in DMF is obtained than in more polar solvents such as n-butanol.⁵¹

However, the cost and availability of noble metals may limit their large-scale applications. Non-noble metal-based catalysts, such as Cu-, Ni- and Co- based catalysts, are more appealing, though harsher experimental conditions are generally required and a durability problem often occurs.

1.3.2 Catalytic performances of non-noble metal based catalysts

Monometallic Cu-based catalysts minimize side reactions of decarbonylation and ring hydrogenation, but suffer from a low activity for H₂ activation and from stronger interactions with BHMF than with DMF, which makes the second step of the conversion of HMF to DMF slow.¹ Under optimized reaction conditions (e.g., temperature, pressure and solvent), bimetallic Cu-based catalysts and active/modified carriers have been proposed to overcome this problem. Reaction temperatures generally range between 180 and 260 °C, and pressures span from 1.5 to 6.8 MPa. Solvents commonly used include alcohols (e.g., methanol, ethanol, 2-propanol, 1-butanol) and ethers (e.g. THF, CPME, 1,4-dioxane). The influence of solvents is mainly reflected in the product distribution.^{19,57,65} When methanol was used as solvent with a basic catalyst, large amounts of etherification products were observed.¹⁹ When water was the solvent or was present as impurity, the selectivity shifted from DMF to BHMF over Cu/ γ -Al₂O₃, due to the coverage by water of sites active for hydrogenolysis.⁶⁵

Common bimetallic combinations used for HMF hydrogenolysis include Cu-Ru, Cu-Zn, and Cu-Ni. Kumalaputri et al. reported that the addition of a small amount of Ru in copper-doped porous metal oxides (PMO) was beneficial to the yield of DMF, because of the high hydrogenolysis ability of Ru.¹⁹ However, the promoting effect was limited to high-temperature conditions (220 °C), and low reaction temperatures (100-140 °C) only led to BHMF as the main product, with the same yield of DMF as the unpromoted Cu catalyst. Later, the same group reported a higher catalytic performance of a commercially available Cu-Zn nanoalloy catalyst, which gave a combined yield of DMF and DMTHF of 94% (DMF/DMTHF = 18:1) at complete conversion in cyclopentyl methyl ether (CPME) at 200 °C under 2 MPa after 6 h.²⁰ Recycling tests showed that the CuZn nanoalloy was stable for the first and second cycles, and then deactivated due to morphological and element distribution changes, in addition to deposition of organics. The structural changes depended on the solvent used. In CPME, homogeneous Cu-Zn nanoalloys transformed into a core-shell structure in which Zn covered copper-rich cores, whereas acicular particles formed in methyl isobutyl carbinol. The activity of the catalyst could be recovered by calcination, suggesting that the structural changes were reversible. In a very

recent work, Guo et al. demonstrated that the combination of Cu with Co and graphene could achieve a high selectivity for DMF synthesis.⁵⁸ A CuCo catalyst, prepared from acetate and 1,10-phenanthroline precursors on N-doped reduced graphene oxide (NGr) supported on alumina, gave a near complete conversion of HMF to DMF in THF at 180 °C under 2 MPa after 16 h (Table 1.6, Entry 10). No Cu-Co alloy was detected in the catalyst, but a synergistic effect between Cu, Co and pyrrolic-N species over the NGr/ α -Al₂O₃ support was believed to explain the high activity of the catalyst. However, this catalyst was troubled with deactivation since a 13% decrease of DMF yield started from the second run.

Table 1.6 Catalytic performances of Cu-based catalysts for the conversion of HMF to DMF

Entry	Catalyst	Feed conditions	P (MPa)	T (°C)	t (h)	conv. (%)	yield (%)	ref
1	CuCrO ₄	5 wt.% HMF in 1-butanol	6.8	220	10	100	61	33
2	CuRu/C	5 wt.% HMF in 1-butanol	6.8	220	10	100	71	33
3	CuRu/C	10 wt.% HMF in 1-butanol; 1 g catalyst; H ₂ flow rate equals to 19 mL(STP)/min	1.7	220	- ^a	100	79	33
4	Cu ₂₀ -PMO ^b	4 mmol HMF; 20 mL ethanol; 0.1 g catalyst	5	220	12	100	51.7	19
5	Cu ₂₀ -Ru ₂ -PMO ^c	4 mmol HMF; 20 mL ethanol; 0.1 g catalyst	5	220	6	100	61	19
6 ^d	Cu/AlO _x	0.2 mol/L HMF; 0.6 mol/L 1,4-butanediol; 1.5 g catalyst	1.6	220	0.5	100	72	56
7	CuZn nanoalloy	13.6 mmol HMF; 20 mL CPME; 0.2 g catalyst	2	200	6	100	89.1	20
8	Cu/ZnO	11.9 mmol HMF; 35 mL 1,4-dioxane; 0.5 g catalyst	1.5	220	5	100	91.8	57
9	CuZrO _x	0.7 wt.% HMF in 1-butanol	1.5	200	2	99	60.6	30
10	CuCo [®] /NGr/ α Al ₂ O ₃	1 mmol HMF; 2 mL THF; 0.1 g catalyst	2	180	16	>99	>99	58
11	CuNi/Al ₂ O ₃	1.6 mmol HMF; 20 mL THF; 0.5 g catalyst	3	200	6	100	56	59
12	Cu ₃ Ni/C	8 mmol HMF; 100 mL 1-propanol; 0.05 g catalyst	3.3	180	- ^a	100	98.7	60
13	CuNi/TiO ₂	4 mmol HMF; 25 mL 1,4-dioxane; 0.3 g catalyst	2.5	200	8	100	84.3	61
14	Raney Cu	12 mmol HMF; 35 mL 1,4-dioxane; 0.5 g catalyst	1.5	180	15	25.1	10.5	62
15 ^e	Cu/PMO	0.8 mmol HMF; 3 mL methanol; 0.1 mg catalyst	-	260	3	100	48	63
16	"Cu ₃ Al" oxide	1.2 mmol HMF; 15 mL methanol; 0.1 g catalyst	1(N ₂)	240	1.5	>99	96.7	64

^a: continuous flow; ^b: Cu_{0.59}Mg_{2.34}Al_{1.00}O_{4.5}; ^c: Cu_{0.61}Mg_{2.33}Al_{0.98}Ru_{0.02}O_{4.84}; ^d: combined 1,4-butanediol lactonization and transfer hydrogenation/hydrogenolysis of HMF under continuous flow conditions; ^e: CTH conversion of HMF by supercritical methanol, Cu/PMO represents Cu-doped Mg-Al oxides.

CuNi catalysts prepared by impregnation display a low selectivity due to the presence of Ni-rich particles providing over-hydrogenation.^{59,60} Recent strategies have relied on innovative preparation methods or SMSI effects. Luo et al. showed that bimetallic carbon-supported NiCu₃ nanocrystals prepared by a solvothermal method, and consisting of a Cu-rich core and a 1:1 molar Ni:Cu shell, led to an excellent DMF yield of 98.7% at complete conversion at 180 °C under 3.3 MPa in a continuous flow reactor.⁶⁰ The homogeneity of the particles surface was considered as the key factor for high catalytic efficiency. Seemala et al. used TiO₂ as support to selectively form strong Ni-TiO₂ interactions in Cu-Ni/TiO₂, which resulted in a deficit of Ni at the particle surface and a promotion of Cu hydrogenation activity without compromising selectivity.⁶¹ As a result, Cu-Ni/TiO₂ gave a DMF yield of 84.3% at complete conversion at 200 °C under 2.5 MPa in 1,4-dioxane after 8 h. Besides, the strong Ni-TiO₂ interactions stabilized the bimetallic particles on the support, which improved the catalyst stability. In contrast, monometallic Cu or Ni, or bimetallic CuNi/Al₂O₃ showed inferior catalytic performances and poor stability.

As is the case for Cu-based catalysts, the product distribution of HMF hydrogenation over Ni-based catalysts is highly temperature-dependent. Increasing the reaction temperature (generally to 130-230 °C) shifts the reaction from BHMF to DMF. However, Ni alone does not provide a high selectivity to DMF due to its high hydrogenation ability, which induces the formation of by-products such as FOL, MFOL, DMTHF and BHMTHF.^{14,66} Three strategies have been reported so far to improve the selectivity of Ni to DMF.

Table 1.7 Catalytic performances of Ni-based catalysts for the conversion of HMF to DMF

Entry	Catalyst	Feed conditions	P (MPa)	T (°C)	t (h)	conv. (%)	yield (%)	ref
1	Raney Ni	12 mmol HMF; 35 mL 1,4-dioxane; 0.5 g catalyst	1.5	180	15	100	88.5	62
2	Ni-W ₂ C/AC	1 mmol HMF; 12 mL THF; 0.12 g catalyst	4	180	3	100	96	67
3	NiAl-850	12 mmol HMF; 35 mL 1,4-dioxane; 0.1 g catalyst	1.2	180	4	100	91.5	68
4	Ni ₂ -Fe ₁ /CNTs	4 mmol HMF; 20 mL n-butanol; 0.05 g catalyst	3	200	3	100	91.3	69
5	NiSi-PS ^a	12 mmol HMF; 38 mL 1,4-dioxane; 0.08 g catalyst	1.5	130	3	100	72.9	70
6	NiSi-IMP-20	12 mmol HMF; 38 mL 1,4-dioxane; 0.08 g catalyst prepared by impregnation	1.5	130	3	50.9	9	70
7	Ni-OMD3 ^b	2 mmol HMF; 20 mL water; 0.05 g catalyst	3	200	6	>99.9	>98.6	44
8	LaFeO ₃ supported Ni	1 mmol HMF; 12 mL ethanol; 0.1 g catalyst	5	230	6	>99	98.3	71
9	Ni/C	8 mmol HMF; 100 mL 1-propanol; W/F = 2 g·min/mL	3.3	180	- ^c	92	53	31
10	NiZnAl metal oxides	12 mmol HMF; 34 mL dioxane; 0.15 g catalyst; Ni/Zn molar ratio 1	1.5	180	15	100	93.6	72

^a: Ni NPs from nickel phyllosilicate; ^b: Ni-OMD3, Ni supported on mesoporous nitrogen-rich carbon, prepared by organic matrix deposition (OMD) method; ^c: continuous process

The first one consists of introducing a proper amount of Lewis acidic sites onto the catalyst surface as promoters for C-O hydrogenolysis. Huang et al. showed that a 7 wt.% Ni-30 wt.% W₂C/AC catalyst afforded a DMF yield as high as 96% at complete conversion of HMF at 180 °C under 4 MPa after 3 h in THF (Table 1.7, Entry 2).⁶⁷ The synergy between W₂C and Ni was the key to the success of this bifunctional catalyst, where W₂C acted as the source of Lewis acidity, offering deoxygenation sites while Ni offered the hydrogenation function. A slight deactivation attributed to the deposition of carbonaceous species on the metal sites occurred after 4 cycles. A modification of the catalyst preparation parameters could also supply acidic sites. Kong et al. reported on a Ni-Al mixed oxide catalyst (NiAl-850, Ni/Al atomic ratio = 3), with which a DMF yield of 91.5% at complete conversion of HMF was obtained in 1,4-dioxane at 180 °C under 1.2 MPa after 4 h.⁶⁸ Surface acidic sites were formed by dehydration of the hydrotalcite precursor during the calcination process. The key to the high selectivity of DMF was the use of a high calcination temperature (850 °C) followed by reduction at 500 °C for 2 h, resulting in a proper balance between hydrogenolysis (through surface acidic sites) and hydrogenation (on metallic Ni). When the reaction time was prolonged to 20 h, a DMTHF yield of 97.4% at complete HMF conversion could be obtained over NiAl-850 in the same reaction conditions. Finally, Kong et al. reported that there was a synergy between Ni NPs arising from nickel phyllosilicate reduction (average size = 3.3 nm) and Lewis acidity from coordinately unsaturated, unreduced Ni (II) sites.⁷⁰ This synergy was beneficial to hydrogenolysis at low temperature. The total yield of DMF and DMTHF was 83-90% (DMF: 64-73%) at a complete conversion of HMF at 130-150 °C under 1.5 MPa in 1,4-dioxane after 3 h. It was proposed that during hydrogenolysis, the C=O bond of HMF simultaneously adsorbed to a metallic Ni site via the C atom and to an acidic site via the O atom, forming the CH₂OH-(C₄H₃O)-CH= intermediate, which was then hydrogenated and hydrogenolyzed into DMF and DMTHF. As compared to phyllosilicate-derived Ni catalysts, using commercial silica sol, Al₂O₃ or ZrO₂ as support resulted in inferior catalytic performances due to the inadequate distance between metallic and acidic sites.

The second strategy is based on bimetallic catalysts. The addition of oxophilic Fe to form a Ni-Fe alloy favors the selective cleavage of the CH₂-OH bond.⁷³ Yu et al. showed that Ni-Fe alloys with a controlled Ni/Fe atomic ratio could be formed on the surface of carbon nanotubes by co-impregnation. This led to a high selectivity to DMF.⁶⁹ A NiFe/CNT catalyst (10 wt.% Ni, Ni/Fe atomic ratio = 2) afforded a DMF yield of 91.3% at complete conversion of HMF at 200 °C under 3 MPa in n-butanol after 3 h. The catalyst experienced a gradual loss of selectivity to DMF, though the conversion of HMF was maintained. This was explained by the deposition of carbonaceous species on the active centers.

Table 1.8 Catalytic performances of Co-based catalysts for the conversion of HMF to DMF

Entry	Catalyst	Feed conditions	P (MPa)	T (°C)	t (h)	conv. (%)	yield (%)	ref
1	Raney Co	12 mmol HMF; 35 mL 1,4-dioxane; 0.5 g catalyst	1.5	180	15	94.3	78.5	62
2	Co ₃ O ₄	2 mmol HMF; 10 mL THF; 0.1 g catalyst	1	130	24	>99	70	74
3	Ni-Co oxides	2 mmol HMF; 10 mL THF; 0.1 g catalyst	1	130	24	>99	76	74
4	Co/C	8 mmol HMF; 100 mL 1-propanol; W/F = 2 g·min/mL	3.3	180	-	98	54	31
5	Co@C	2 mmol HMF; 10 mL ethanol; 0.02 g catalyst	5	180	8	100	91.9	75
6	CoCu@C	2 mmol HMF; 10 mL ethanol; 0.02 g catalyst; Co/Cu molar ratio 3	5	180	8	100	99.4	75
7	CoNi@C	2 mmol HMF; 10 mL ethanol; 0.02 g catalyst; Co/Ni molar ratio 3	5	180	8	100	97.8	75
8	CoZn@C	2 mmol HMF; 10 mL ethanol; 0.02 g catalyst; Co/Zn molar ratio 3	5	180	8	100	91.5	75
9	CoAg@C	2 mmol HMF; 10 mL ethanol; 0.02 g catalyst; Co/Ag molar ratio 3	5	180	8	100	96.2	75
10	Co/NGr/ α -Al ₂ O ₃	1 mmol HMF; 2 mL THF; 0.1 g catalyst	2	180	16	97	65.5	58
11	CoCu/NGr/ α -Al ₂ O ₃	1 mmol HMF; 2 mL THF; 0.1 g catalyst; Cu/Co molar ratio 1	2	180	16	>99	>99	58
12	CoNi/C	2 mmol HMF; 10 mL THF; 0.2 g catalyst; 2 wt.% Ni; 20 wt.% Co	1.5	210	24	99	61	76
13	CoNi/C	2 mmol HMF; 10 mL THF; 20 mmol formic acid; 0.2 g catalyst; 2 wt.% Ni; 20 wt.% Co	-	210	24	99	90	76

The third strategy focuses on supports displaying strong interactions with Ni. Goyal et al. showed that a nitrogen-rich mesoporous carbon support helped to disperse Ni NPs (< 5 nm) and to stabilize them during the reaction.⁴⁴ The catalyst (Ni/OMD3, 3 wt.% Ni over N-containing carbon) gave a DMF yield of 98.6% at near complete conversion of HMF at 200 °C under 3 MPa in water after 6 h. Perovskite-type functional materials also exhibited good potential for the HMF hydrogenolysis process. In a very recent work by Chen et al., a LaFeO₃-supported Ni catalyst (20 wt.% Ni), prepared by a one-step citric acid-complexing method, provided a DMF yield of 98.3% at near complete conversion of HMF at 230 °C under 5 MPa in ethanol after 6 h.⁷¹ The DMF yield was maintained above 90% after 5 cycles.

Cobalt catalysts generally exhibit higher selectivities to DMF than Ni and higher hydrogenation activities than Cu. Successful Co-based catalysts feature bimetallic compositions (e.g., Co-Cu, Co-Ni, Co-Zn and Co-Ag) or the promoting effect of the support. Metal additives, Ni, Cu, and Ag, are used to enhance the hydrogenolysis activity of Co-based catalysts. A Ni-Co metal oxide catalyst prepared by a hydrothermal method could afford a DMF yield of 76% at near complete conversion of HMF under mild reaction conditions (130 °C, 1 MPa) in THF after 24 h. This catalyst could be recycled 6 times without loss of activity and selectivity.⁷⁰ Guo et al. showed that an N-graphene-modified α -Al₂O₃ supported Co catalyst (Co/NGr/ α -Al₂O₃) gave a DMF yield of 65.5% at 97.3% conversion of HMF at 180 °C under 2 MPa in THF after 16 h (Table 1.5, Entry 10).⁵² The addition of Cu (CuCo/NGr/ α -Al₂O₃) increased the DMF yield to almost 100%. The high efficiency of bimetallic Cu-Co catalysts was confirmed by Chen et al. in a very recent work, in which carbon-coated Cu-Co NPs (Cu-Co@C) afforded a DMF yield of 99.4% at 100% conversion of HMF at 180 °C under 5 MPa in ethanol after 8 h.⁷¹ Polyetheneglycol acted both as the carbon source and as the reductant for metal species. The high reactivity of Cu-Co@C was attributed to the high hydrogenolysis activity of Co@C and to a synergistic effect between metallic copper sites, Co⁰ and cobalt oxide species. The catalyst protected from oxidation by carbon layers was recycled for 6 runs, but the abrasion of the carbon coating resulted in a gradual deactivation of the catalysts in the next runs. Besides, it was shown that the addition of Ni and Ag could also improve the yield of DMF to 96-98%, as compared with monometallic cobalt catalyst.

Table 1.9 Catalytic performances of Fe-based catalysts for the conversion of HMF to DMF

Entry	Catalyst	Feed conditions	P (MPa)	T (°C)	t (h)	conv. (%)	yield (%)	ref
1	5 wt.% Fe-L1/C-800 ^a	0.5 mmol HMF; 20 mL n-butanol; 0.1 g catalyst	4	240	5	100	86	77
2	20 wt.% Fe-N/C	0.5 mmol HMF; 20 mL n-butanol; 0.1 g catalyst	4	240	6	100	86	78
3	5 wt.% Fe-L1/C-800 ^a	0.5 mmol HMF; 20 mL n-butanol; 0.1 g catalyst	1(N ₂)	240	12	100	67	77

^a: L1 represents 1,10-phenanthroline (nitrogen precursor), 800 is the pyrolysis temperature (°C).

Fe alone displays very limited hydrogenation/hydrogenolysis activity. For example, a BHMF yield of 96% and a DMF yield of 91% could be obtained with a bimetallic Ni-Fe/CNT catalyst at 110 °C and 200 °C respectively, while only very small amounts of HMF were converted over Fe/CNT in the same reaction conditions.⁶⁹ But with the help of additives and/or functional supports, the hydrogenation reactivity of Fe-based catalysts can be significantly improved.

The production of DMF over Fe-based catalysts has been realized at high reaction temperatures (i.e., 240 °C) using either H₂ or alcohols as hydrogen donor. The first example was reported recently by Li et al.⁷⁷ A Fe-based catalyst (Fe-L1/C-800) was prepared by simultaneous pyrolysis of Fe (II) acetate and 1,10-phenanthroline (L1) on activated carbon at 800 °C, leading to the formation of FeN_x species proposed as the active phase. The catalytic performance was sensitive to the nature of the nitrogen precursor, pyrolysis temperature and Fe/N molar ratio. A DMF yield of 67% at complete catalytic transfer hydrogenation (CTH) of HMF was obtained at 240 °C under 1 MPa N₂ in n-butanol after 12 h (Table 1.9, Entry 3). A H₂ pressure of 4 MPa further increased the DMF yield up to 86% (Table 1.9, Entry 1) and prevented a loss of activity and selectivity after 5 cycles. However, this Fe-based catalyst was troubled with a low carbon balance during the reaction (< 80 %), explained by the polymerization of furanic compounds on the Lewis acidic sites of the catalyst. A later publication by the same group reported on a similarly active Fe-based catalyst (Fe-N/C) prepared from a different iron precursor (Fe(III) acetylacetonate) and a different nitrogen precursor (melamine) (Table 1.9, Entry 2).⁷⁸ Iron particles appeared as encapsulated in nitrogen-doped carbon shells, which were considered to be crucial for the hydrogenolysis of HMF to DMF. Unfortunately, limited catalyst stability was observed. A gradual loss of activity was attributed to Fe leaching, iron oxidation to Fe₃O₄, and changes of the textural properties.

1.4 The production of DMTHF from HMF

The further hydrogenation of DMF gives DMTHF. DMTHF is similar to DMF in terms of energy density (3.2×10^6 J/L), volatility (boiling point 90-92 °C), and solubility (immiscible in water).⁷⁹ Besides, because DMTHF is a saturated molecule, it has good storage and transportation stability and is a better candidate for liquid fuel. Moreover, DMTHF is also a valuable organic solvent.

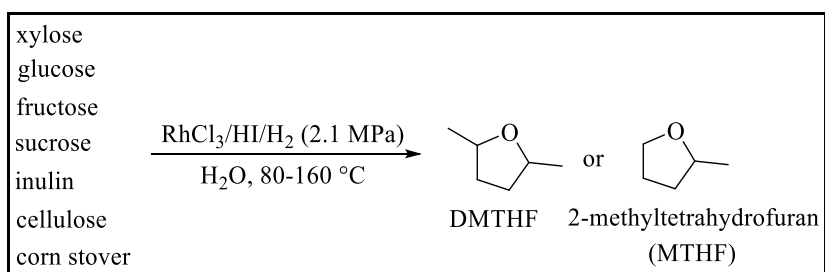


Figure 1.4 Production of DMTHF from carbohydrates and cellulosic biomass

The production of DMTHF is a newly-developing research field, with only a few works reported so far. Nevertheless, the synthesis of DMTHF using both biomass and HMF as reactants has been disclosed. A recent work by Sen and co-workers firstly revealed the feasibility to produce DMTHF from biomass-derived carbohydrates, cellulose and raw lignocellulose in one step with dual homogeneous catalyst system (Figure 1.7.).^{79,80} In their work, a homogeneous catalytic system composed of rhodium chloride and an acid under hydrogen atmosphere was applied, which could afford over 80% yield of DMTHF. However, the use of an expensive rhodium salt and the potentially corrosive acid clearly makes the process unsustainable. The production of DMTHF from fructose with heterogeneous catalysts was firstly explored by Jackson et al.⁸¹ In their work, a sulfur-modified Pt/C catalyst afforded a DMTHF yield of nearly 50% in a stirred reactor at 10.3 MPa H₂ and 175 °C in ethanol solution. However, the catalyst lost sulfur during the reaction and could not be reused.

Using HMF as reactant, Luo and co-workers tested the catalytic performances of a series of metal-based catalysts supported on activated carbon (i.e., Pd, Pt, Ir, Ru, Ni, Co) under flow reaction conditions (180 °C, 33 bar, space time in range of 0.25-10 g·min·mL⁻¹).³¹ Their work showed that it was easier for noble metal-based catalysts (i.e. Pd/C, Ir/C, Pt/C) to catalyze the formation of DMTHF especially at high space time (W/F = 1-4 g·min·mL⁻¹). Pd/C was the most active catalyst, affording a DMTHF yield of 55% at a space time of 4 g·min·mL⁻¹. In contrast, with non-noble metal-based catalysts (i.e., Ni/C, Co/C), DMTHF was much less apt to be produced, giving DMTHF yields lower than 10% even at high space time (i.e. W/F = 8 g·min·mL⁻¹). Bottari et al. reported work on commercial CuZn powder, which afforded a DMTHF yield of 25% (220 °C, 20 bar H₂, 0.5 g HMF, 0.1 g CuZn, 20 mL CPME in batch reactor) with DMF as the primary product.²⁰ Their study also showed that the nature of the solvent has a significant impact on the formation of DMTHF. The DMTHF yield increased as follows under the same reaction conditions: ethanol < isopropanol < methyl isobutyl carbinol (MIBC) < 2-methyltetrahydrofuran < cyclopentyl methyl ether (CPME).

Ni-based catalysts appear to be the most interesting non-noble metal-based catalysts for the production of DMTHF from HMF. Work by Kong et al. showed that a nickel catalyst supported on silica prepared by the ammonia evaporation method afforded a DMTHF yield of 26.1% (150 °C, 15 bar, 3 h, 1.5 g HMF, 38 mL 1,4-dioxane).⁷⁰ A breakthrough in highly efficient production of DMTHF was reported by the same group.⁶⁸ In their work, a Ni-Al mixed oxide catalyst (derived from a hydrotalcite-like precursor after calcination at 850 °C, Ni/Al atomic ratio = 3) was able to afford a DMTHF yield of 97.4% at complete conversion of HMF at 180 °C under 12 bar H₂ after 20 h. As mentioned in the former section, the key to the high selectivity to DMTHF was the use of a high calcination temperature (850 °C), followed by reduction at 500 °C for 2 h, resulting in a proper balance between hydrogenolysis aided by surface acidic sites and hydrogenation on metallic Ni, as well as of a long reaction time, as short reaction time led to the selective formation of DMF. However,

this catalyst was not stable during the stability tests, losing around 40% HMF conversion after 7 runs due to the deposition of carbon species on the active sites.

However, on the whole, the research in the production of DMTHF is still at its infancy at present. A more thorough exploration is expected in this field.

1.5 Conclusion

HMF plays an important role as a platform molecule in the valorization of lignocellulosic biomass into valuable chemicals and liquid fuels. Heterogeneous catalysis, based on both noble and non-noble metal-based catalysts, is central in reaching this objective. Due to advantages in terms of reserves and prices, the application of non-noble metal-based catalysts is increasingly attracting attention. Among the non-noble metal-based catalysts, bimetallic Cu-based and Ni-based catalysts, or catalysts based on functional supports, have shown great potential as alternatives to noble metal-based catalysts for the hydroconversion of HMF to valuable chemicals, in particular BHMF, DMF and DMTHF. However, at present, the exploration of these non-noble metal-based catalysts in HMF hydroconversion is still at an early stage, and a series of open problems still exist.

A more complete understanding of the fundamental aspects of the reaction, including kinetic modeling and the determination of the active sites and of the intermediates, is far from being reasonably accomplished for the production of most of the chemicals from HMF. Furthermore, avoiding side-reactions is still a complex issue, especially with monometallic systems that do not benefit from the introduction of additives, or from the adsorptive or acid-base properties of the support. On the one hand, the activity of non-noble metal based catalysts generally requires harsher reaction conditions than noble metals. On the other hand, the selectivity to the target product is highly sensitive to the reaction conditions (e.g., temperature, pressure, contact time and solvent). Overhydrogenation or polymerization reactions can be caused by a high reaction temperature.

Actually, in these conditions, a striking problem is the deactivation of the catalyst due to structure degradation (metal sintering), leaching, valence change of the metals, or carbon deposition. Deactivation by deposition of heavy by-products is a problem for most of the catalysts described herein. This is especially true for the transformation of HMF whose boiling point is high, making it difficult to devise gas-phase conversion. Polymerization and self-etherification reactions in the case of HMF hydroconversion have often been reported, when the mechanism involves steps catalyzed by acidic sites and when experimental conditions are severe. The mechanisms underlying the deterioration of the catalysts performances are still not fully understood.

Besides, the control and tunability of the chemical composition of non-noble bimetallic nanoparticles are still limited when catalysts are prepared with traditional methods such as co-precipitation or co-impregnation of metal nitrates. These procedures often result in a poor control of the average size and of the distribution of the particle sizes. It has been shown that the dispersion of the active NPs, and the chemical order within bimetallic NPs (alloys, core-shell), could have significant influences on the catalytic performances. However, research on the effects of the active metal NPs dispersion is still rare in the literature, both for monometallic and bimetallic systems. Studying the influence of the preparation method and of the particle size distribution on the catalytic performances is thus of prime importance to achieve optimized catalytic performances, before optimizing the local composition of multimetallic formulations.

In the current project, and because of the lack of systematic information on these systems, we have chosen to focus on the study of the impact of the dispersion of monometallic Ni and Cu NPs prepared on mesoporous supports, chosen for their high surface area. The preparation procedure of these monometallic Ni- and Cu-based catalysts was varied in order to change the metal particle size, provide different metal dispersion, and ultimately to:

1/ Evaluate their catalytic performances in the hydroconversion of HMF to DMF and DMTHF, and compare Ni and Cu-based catalysts;

2/ For a given metal, investigate the effects of the size and of the localization of the active metal NPs on the catalytic performances in the selective hydrogenation reactions;

3/ Reveal the sequence of reactions involved in the hydroconversion of HMF to DMF/DMTHF on Ni and Cu monometallic catalysts.

Reference

- (1) Chen, S.; Wojcieszak, R.; Dumeignil, F.; Marceau, E.; Royer, S. How Catalysts and Experimental Conditions Determine the Selective Hydroconversion of Furfural and 5-Hydroxymethylfurfural. *Chem. Rev.* **2018**, *118* (22), 11023–11117. <https://doi.org/10.1021/acs.chemrev.8b00134>.
- (2) Solomon, J. L.; Madix, R. J.; Stöhr, J. Orientation and Absolute Coverage of Furan and 2,5-dihydrofuran on Ag(110) Determined by near Edge X-ray Absorption Fine Structure and X-ray Photoelectron Spectroscopy. *J. Chem. Phys.* **1991**, *94* (5), 4012–4023. <https://doi.org/10.1063/1.460678>.
- (3) Xiong, K.; Wan, W.; Chen, J. G. Reaction Pathways of Furfural, Furfuryl Alcohol and 2-Methylfuran on Cu(111) and NiCu Bimetallic Surfaces. *Surf. Sci.* **2016**, *652*, 91–97. <https://doi.org/10.1016/j.susc.2016.02.011>.
- (4) Shi, Y.; Zhu, Y.; Yang, Y.; Li, Y.-W.; Jiao, H. Exploring Furfural Catalytic Conversion on Cu(111) from Computation. *ACS Catal.* **2015**, *5* (7), 4020–4032. <https://doi.org/10.1021/acscatal.5b00303>.
- (5) Sitthisa, S.; Sooknoi, T.; Ma, Y.; Balbuena, P. B.; Resasco, D. E. Kinetics and Mechanism of Hydrogenation of Furfural on Cu/SiO₂ Catalysts. *J. Catal.* **2011**, *277* (1), 1–13. <https://doi.org/10.1016/j.jcat.2010.10.005>.
- (6) Liu, B.; Cheng, L.; Curtiss, L.; Greeley, J. Effects of van Der Waals Density Functional Corrections on Trends in Furfural Adsorption and Hydrogenation on Close-Packed Transition Metal Surfaces. *Surf. Sci.* **2014**, *622*, 51–59. <https://doi.org/10.1016/j.susc.2013.12.001>.
- (7) Glen R. Jenness; Vlachos, D. G. DFT Study of the Conversion of Furfuryl Alcohol to 2-Methylfuran on RuO₂ (110). *J. Phys. Chem. C* **2015**, *119* (11), 5938–5945. <https://doi.org/10.1021/jp5109015>.
- (8) Bradley, M. K.; Robinson, J.; Woodruff, D. P. The Structure and Bonding of Furan on Pd(111). *Surf. Sci.* **2010**, *604* (11–12), 920–925. <https://doi.org/10.1016/j.susc.2010.02.021>.
- (9) Ni, Z. M.; Xia, M. Y.; Shi, W.; Qian, P. P. Adsorption and Decarbonylation Reaction

of Furfural on Pt(111) Surface. *Acta Phys.-Chim. Sin.* **2013**, *29* (9), 1916–1922. <https://doi.org/10.3866/PKU.WHXB201307101>.

(10) Sitthisa, S.; Pham, T.; Prasomsri, T.; Sooknoi, T.; Mallinson, R. G.; Resasco, D. E. Conversion of Furfural and 2-Methylpentanal on Pd/SiO₂ and Pd–Cu/SiO₂ Catalysts. *J. Catal.* **2011**, *280* (1), 17–27. <https://doi.org/10.1016/j.jcat.2011.02.006>.

(11) Ungureanu, A.; Dragoi, B.; Chirieac, A.; Royer, S.; Duprez, D.; Dumitriu, E. Synthesis of Highly Thermostable Copper-Nickel Nanoparticles Confined in the Channels of Ordered Mesoporous SBA-15 Silica. *J. Mater. Chem.* **2011**, *21* (33), 12529–12541. <https://doi.org/10.1039/C1JM10971E>.

(12) Sitthisa, S.; Resasco, D. E. Hydrodeoxygenation of Furfural Over Supported Metal Catalysts: A Comparative Study of Cu, Pd and Ni. *Catal. Lett.* **2011**, *141* (6), 784–791. <https://doi.org/10.1007/s10562-011-0581-7>.

(13) Nakagawa, Y.; Nakazawa, H.; Watanabe, H.; Tomishige, K. Total Hydrogenation of Furfural over a Silica-Supported Nickel Catalyst Prepared by the Reduction of a Nickel Nitrate Precursor. *ChemCatChem* **2012**, *4* (11), 1791–1797. <https://doi.org/10.1002/cctc.201200218>.

(14) Duarte, D. P.; Martínez, R.; Hoyos, L. J. Hydrodeoxygenation of 5-Hydroxymethylfurfural over Alumina-Supported Catalysts in Aqueous Medium. *Ind. Eng. Chem. Res.* **2016**, *55* (1), 54–63. <https://doi.org/10.1021/acs.iecr.5b02851>.

(15) Ferreira, L. R.; Lima, S.; Neves, P.; Antunes, M. M.; Rocha, S. M.; Pillinger, M.; Portugal, I.; Valente, A. A. Aqueous Phase Reactions of Pentoses in the Presence of Nanocrystalline Zeolite Beta: Identification of by-Products and Kinetic Modelling. *Chem. Eng. J.* **2013**, *215–216*, 772–783. <https://doi.org/10.1016/j.cej.2012.11.022>.

(16) Mehdi, H.; Fábos, V.; Tuba, R.; Bodor, A.; Mika, L. T.; Horváth, I. T. Integration of Homogeneous and Heterogeneous Catalytic Processes for a Multi-Step Conversion of Biomass: From Sucrose to Levulinic Acid, γ -Valerolactone, 1,4-Pentanediol, 2-Methyl-Tetrahydrofuran, and Alkanes. *Top. Catal.* **2008**, *48* (1–4), 49–54. <https://doi.org/10.1007/s11244-008-9047-6>.

(17) van Putten, R. J.; van der Waal, J. C.; de Jong, E.; Rasrendra, C. B.; Heeres, H. J.; de

Vries, J. G. Hydroxymethylfurfural, a Versatile Platform Chemical Made from Renewable Resources. *Chem. Rev.* **2013**, *113* (3), 1499–1597. <https://doi.org/10.1021/cr300182k>.

(18) Corma, A.; Iborra, S.; Velty, A. Chemical Routes for the Transformation of Biomass into Chemicals. *Chem. Rev.* **2007**, *107* (6), 2411–2502. <https://doi.org/10.1021/cr050989d>.

(19) Kumalaputri, A. J.; Bottari, G.; Erne, P. M.; Heeres, H. J.; Barta, K. Tunable and Selective Conversion of 5-HMF to 2,5-Furandimethanol and 2,5-Dimethylfuran over Copper-Doped Porous Metal Oxides. *ChemSusChem* **2014**, *7* (8), 2266–2275. <https://doi.org/10.1002/cssc.201402095>.

(20) Bottari, G.; Kumalaputri, A. J.; Krawczyk, K. K.; Feringa, B. L.; Heeres, H. J.; Barta, K. Copper–Zinc Alloy Nanopowder: A Robust Precious-Metal-Free Catalyst for the Conversion of 5-Hydroxymethylfurfural. *ChemSusChem* **2015**, *8* (8), 1323–1327. <https://doi.org/10.1002/cssc.201403453>.

(21) Yao, S.; Wang, X.; Jiang, Y.; Wu, F.; Chen, X.; Mu, X. One-Step Conversion of Biomass-Derived 5-Hydroxymethylfurfural to 1,2,6-Hexanetriol Over Ni–Co–Al Mixed Oxide Catalysts Under Mild Conditions. *ACS Sustain. Chem. Eng.* **2014**, *2* (2), 173–180. <https://doi.org/10.1021/sc4003714>.

(22) Alamillo, R.; Tucker, M.; Chia, M.; Pagán-Torres, Y.; Dumesic, J. The Selective Hydrogenation of Biomass-Derived 5-Hydroxymethylfurfural Using Heterogeneous Catalysts. *Green Chem.* **2012**, *14* (5), 1413–1419. <https://doi.org/10.1039/C2GC35039D>.

(23) Jain, A. B.; Vaidya, P. D. Kinetics of Catalytic Hydrogenation of 5-Hydroxymethylfurfural to 2,5-Bis-Hydroxymethylfuran in Aqueous Solution over Ru/C. *Int. J. Chem. Kinet.* **2016**, *48* (6), 318–328. <https://doi.org/10.1002/kin.20992>.

(24) Hu, L.; Lin, L.; Liu, S. Chemoselective Hydrogenation of Biomass-Derived 5-Hydroxymethylfurfural into the Liquid Biofuel 2,5-Dimethylfuran. *Ind. Eng. Chem. Res.* **2014**, *53* (24), 9969–9978. <https://doi.org/10.1021/ie5013807>.

(25) Qian, Y.; Zhu, L.; Wang, Y.; Lu, X. Recent Progress in the Development of Biofuel 2,5-Dimethylfuran. *Renew. Sustain. Energy Rev.* **2015**, *41*, 633–646. <https://doi.org/10.1016/j.rser.2014.08.085>.

(26) Fromowitz, M.; Shuga, J.; Wlassowsky, A. Y.; Ji, Z.; North, M.; Vulpe, C. D.; Smith, M. T.; Zhang, L. Bone Marrow Genotoxicity of 2,5-Dimethylfuran, a Green Biofuel Candidate. *Environ. Mol. Mutagen.* **2012**, *53* (6), 488–491. <https://doi.org/10.1002/em.21707>.

(27) Zhong, S.; Daniel, R.; Xu, H.; Zhang, J.; Turner, D.; Wyszynski, M. L.; Richards, P. Combustion and Emissions of 2,5-Dimethylfuran in a Direct-Injection Spark-Ignition Engine. *Energy Fuels* **2010**, *24* (5), 2891–2899. <https://doi.org/10.1021/ef901575a>.

(28) Daniel, R.; Tian, G.; Xu, H.; Wyszynski, M. L.; Wu, X.; Huang, Z. Effect of Spark Timing and Load on a DISI Engine Fuelled with 2,5-Dimethylfuran. *Fuel* **2011**, *90* (2), 449–458. <https://doi.org/10.1016/j.fuel.2010.10.008>.

(29) Hu, L.; Tang, X.; Xu, J.; Wu, Z.; Lin, L.; Liu, S. Selective Transformation of 5-Hydroxymethylfurfural into the Liquid Fuel 2,5-Dimethylfuran over Carbon-Supported Ruthenium. *Ind. Eng. Chem. Res.* **2014**, *53* (8), 3056–3064. <https://doi.org/10.1021/ie404441a>.

(30) Iriondo, A.; Mendiguren, A.; Güemez, M. B.; Requies, J.; Cambra, J. F. 2,5-DMF Production through Hydrogenation of Real and Synthetic 5-HMF over Transition Metal Catalysts Supported on Carriers with Different Nature. *Catal. Today* **2016**. <https://doi.org/10.1016/j.cattod.2016.02.019>.

(31) Luo, J.; Arroyo-Ramírez, L.; Wei, J.; Yun, H.; Murray, C. B.; Gorte, R. J. Comparison of HMF Hydrodeoxygenation over Different Metal Catalysts in a Continuous Flow Reactor. *Appl. Catal. Gen.* **2015**, *508*, 86–93. <https://doi.org/10.1016/j.apcata.2015.10.009>.

(32) Lee, J.; Xu, Y.; Huber, G. W. High-Throughput Screening of Monometallic Catalysts for Aqueous-Phase Hydrogenation of Biomass-Derived Oxygenates. *Appl. Catal. B Environ.* **2013**, *140–141*, 98–107. <https://doi.org/10.1016/j.apcatb.2013.03.031>.

(33) Román-Leshkov, Y.; Barrett, C. J.; Liu, Z. Y.; Dumesic, J. A. Production of Dimethylfuran for Liquid Fuels from Biomass-Derived Carbohydrates. *Nature* **2007**, *447* (7147), 982–985. <https://doi.org/10.1038/nature05923>.

(34) Zu, Y.; Yang, P.; Wang, J.; Liu, X.; Ren, J.; Lu, G.; Wang, Y. Efficient Production of the Liquid Fuel 2,5-Dimethylfuran from 5-Hydroxymethylfurfural over Ru/Co₃O₄ Catalyst. *Appl. Catal. B Environ.* **2014**, *146*, 244–248. <https://doi.org/10.1016/j.apcatb.2013.04.026>.

(35) Nagpure, A. S.; Venugopal, A. K.; Lucas, N.; Manikandan, M.; Thirumalaiswamy, R.; Chilukuri, S. Renewable Fuels from Biomass-Derived Compounds: Ru-Containing Hydrotalcites as Catalysts for Conversion of HMF to 2,5-Dimethylfuran. *Catal. Sci. Technol.* **2015**, *5* (3), 1463–1472. <https://doi.org/10.1039/C4CY01376J>.

(36) Li, Q.; Man, P.; Yuan, L.; Zhang, P.; Li, Y.; Ai, S. Ruthenium Supported on CoFe Layered Double Oxide for Selective Hydrogenation of 5-Hydroxymethylfurfural. *Mol. Catal.* **2017**, *431*, 32–38. <https://doi.org/10.1016/j.mcat.2017.01.011>.

(37) De, S.; Dutta, S.; Saha, B. One-Pot Conversions of Lignocellulosic and Algal Biomass into Liquid Fuels. *ChemSusChem* **2012**, *5* (9), 1826–1833. <https://doi.org/10.1002/cssc.201200031>.

(38) Chidambaram, M.; Bell, A. T. A Two-Step Approach for the Catalytic Conversion of Glucose to 2,5-Dimethylfuran in Ionic Liquids. *Green Chem.* **2010**, *12* (7), 1253–1262. <https://doi.org/10.1039/C004343E>.

(39) Wang, G. H.; Hilgert, J.; Richter, F. H.; Wang, F.; Bongard, H.-J.; Spliethoff, B.; Weidenthaler, C.; Schüth, F. Platinum–Cobalt Bimetallic Nanoparticles in Hollow Carbon Nanospheres for Hydrogenolysis of 5-Hydroxymethylfurfural. *Nat. Mater.* **2014**, *13* (3), 293–300. <https://doi.org/10.1038/nmat3872>.

(40) Luo, J.; Arroyo-Ramírez, L.; Gorte, R. J.; Tzoulaki, D.; Vlachos, D. G. Hydrodeoxygenation of HMF over Pt/C in a Continuous Flow Reactor. *AIChE J.* **2015**, *61* (2), 590–597. <https://doi.org/10.1002/aic.14660>.

(41) Luo, J.; Yun, H.; Mironenko, A. V.; Goulas, K.; Lee, J. D.; Monai, M.; Wang, C.; Vorotnikov, V.; Murray, C. B.; Vlachos, D. G.; et al. Mechanisms for High Selectivity in the Hydrodeoxygenation of 5-Hydroxymethylfurfural over PtCo Nanocrystals. *ACS Catal.* **2016**, 4095–4104. <https://doi.org/10.1021/acscatal.6b00750>.

(42) Luo, J.; Lee, J. D.; Yun, H.; Wang, C.; Monai, M.; Murray, C. B.; Fornasiero, P.; Gorte, R. J. Base Metal-Pt Alloys: A General Route to High Selectivity and Stability in the Production of Biofuels from HMF. *Appl. Catal. B Environ.* **2016**, *199*, 439–446. <https://doi.org/10.1016/j.apcatb.2016.06.051>.

(43) Shi, J.; Wang, Y.; Yu, X.; Du, W.; Hou, Z. Production of 2,5-Dimethylfuran from 5-

Hydroxymethylfurfural over Reduced Graphene Oxides Supported Pt Catalyst under Mild Conditions. *Fuel* **2016**, *163*, 74–79. <https://doi.org/10.1016/j.fuel.2015.09.047>.

(44) Goyal, R.; Sarkar, B.; Bag, A.; Siddiqui, N.; Dumbre, D.; Lucas, N.; Bhargava, S. K.; Bordoloi, A. Studies of Synergy between Metal–Support Interfaces and Selective Hydrogenation of HMF to DMF in Water. *J. Catal.* **2016**, *340*, 248–260. <https://doi.org/10.1016/j.jcat.2016.05.012>.

(45) Radkevich, V. Z.; Senko, T. L.; Wilson, K.; Grishenko, L. M.; Zaderko, A. N.; Diyuk, V. Y. The Influence of Surface Functionalization of Activated Carbon on Palladium Dispersion and Catalytic Activity in Hydrogen Oxidation. *Appl. Catal. Gen.* **2008**, *335* (2), 241–251. <https://doi.org/10.1016/j.apcata.2007.11.029>.

(46) Yang, S.; Feng, X.; Wang, X.; Müllen, K. Graphene-Based Carbon Nitride Nanosheets as Efficient Metal-Free Electrocatalysts for Oxygen Reduction Reactions. *Angew. Chem. Int. Ed.* **2011**, *50* (23), 5339–5343. <https://doi.org/10.1002/anie.201100170>.

(47) Li, Y.; Gao, W.; Ci, L.; Wang, C.; Ajayan, P. M. Catalytic Performance of Pt Nanoparticles on Reduced Graphene Oxide for Methanol Electro-Oxidation. *Carbon* **2010**, *48* (4), 1124–1130. <https://doi.org/10.1016/j.carbon.2009.11.034>.

(48) Wang, H.; Kong, Q.; Wang, Y.; Deng, T.; Chen, C.; Hou, X.; Zhu, Y. Graphene Oxide Catalyzed Dehydration of Fructose into 5-Hydroxymethylfurfural with Isopropanol as Cosolvent. *ChemCatChem* **2014**, *6* (3), 728–732. <https://doi.org/10.1002/cctc.201301067>.

(49) Chatterjee, M.; Ishizaka, T.; Kawanami, H. Hydrogenation of 5-Hydroxymethylfurfural in Supercritical Carbon Dioxide–Water: A Tunable Approach to Dimethylfuran Selectivity. *Green Chem.* **2014**, *16* (3), 1543–1551. <https://doi.org/10.1039/C3GC42145G>.

(50) Nishimura, S.; Ikeda, N.; Ebitani, K. Selective Hydrogenation of Biomass-Derived 5-Hydroxymethylfurfural (HMF) to 2,5-Dimethylfuran (DMF) under Atmospheric Hydrogen Pressure over Carbon Supported PdAu Bimetallic Catalyst. *Catal. Today* **2014**, *232*, 89–98. <https://doi.org/10.1016/j.cattod.2013.10.012>.

(51) Gawade, A. B.; Tiwari, M. S.; Yadav, G. D. Biobased Green Process: Selective Hydrogenation of 5-Hydroxymethylfurfural to 2,5-Dimethyl Furan under Mild Conditions

Using Pd-Cs_{2.5}H_{0.5}PW₁₂O₄₀/K-10 Clay. *ACS Sustain. Chem. Eng.* **2016**, *4* (8), 4113–4123. <https://doi.org/10.1021/acssuschemeng.6b00426>.

(52) Thananattananachon, T.; Rauchfuss, T. B. Efficient Production of the Liquid Fuel 2,5-Dimethylfuran from Fructose Using Formic Acid as a Reagent. *Angew. Chem. Int. Ed.* **2010**, *49* (37), 6616–6618. <https://doi.org/10.1002/anie.201002267>.

(53) Mitra, J.; Zhou, X.; Rauchfuss, T. Pd/C-Catalyzed Reactions of HMF: Decarbonylation, Hydrogenation, and Hydrogenolysis. *Green Chem.* **2014**, *17* (1), 307–313. <https://doi.org/10.1039/C4GC01520G>.

(54) Luijkx, G. C. A.; Huck, N. P. M.; Van, R.; Maat, L.; Van, B. Ether Formation in the Hydrogenolysis of Hydroxymethylfurfural over Palladium Catalysts in Alcoholic Solution. *Heterocycles* **2009**, *77* (2), 1037–1044. [https://doi.org/10.3987/COM-08-S\(F\)81](https://doi.org/10.3987/COM-08-S(F)81).

(55) Augustine, R. L.; Techasauvapak, P. Heterogeneous Catalysis in Organic Synthesis. Part 9. Specific Site Solvent Effects in Catalytic Hydrogenations. *J. Mol. Catal.* **1994**, *87* (1), 95–105. [https://doi.org/10.1016/0304-5102\(93\)E0215-3](https://doi.org/10.1016/0304-5102(93)E0215-3).

(56) Aellig, C.; Jenny, F.; Scholz, D.; Wolf, P.; Giovinazzo, I.; Kollhoff, F.; Hermans, I. Combined 1,4-Butanediol Lactonization and Transfer Hydrogenation/Hydrogenolysis of Furfural-Derivatives under Continuous Flow Conditions. *Catal. Sci. Technol.* **2014**, *4* (8), 2326–2331. <https://doi.org/10.1039/C4CY00213J>.

(57) Zhu, Y.; Kong, X.; Zheng, H.; Ding, G.; Zhu, Y.; Li, Y.-W. Efficient Synthesis of 2,5-Dihydroxymethylfuran and 2,5-Dimethylfuran from 5-Hydroxymethylfurfural Using Mineral-Derived Cu Catalysts as Versatile Catalysts. *Catal Sci Technol* **2015**, *5* (8), 4208–4217. <https://doi.org/10.1039/C5CY00700C>.

(58) Guo, W.; Liu, H.; Zhang, S.; Han, H.; Liu, H.; Jiang, T.; Han, B.; Wu, T. Efficient Hydrogenolysis of 5-Hydroxymethylfurfural to 2,5-Dimethylfuran over a Cobalt and Copper Bimetallic Catalyst on N-Graphene-Modified Al₂O₃. *Green Chem.* **2016**. <https://doi.org/10.1039/C6GC02630C>.

(59) Srivastava, S.; Jadeja, G. C.; Parikh, J. Synergism Studies on Alumina-Supported Copper-Nickel Catalysts towards Furfural and 5-Hydroxymethylfurfural Hydrogenation. *J. Mol. Catal. Chem.* **2017**, *426*, Part A, 244–256.

<https://doi.org/10.1016/j.molcata.2016.11.023>.

(60) Luo, J.; Monai, M.; Wang, C.; Lee, J. D.; Duchoň, T.; Dvořák, F.; Matolín, V.; Murray, C. B.; Fornasiero, P.; Gorte, R. J. Unraveling the Surface State and Composition of Highly Selective Nanocrystalline Ni–Cu Alloy Catalysts for Hydrodeoxygenation of HMF. *Catal. Sci. Technol.* **2017**, *7* (8), 1735–1743. <https://doi.org/10.1039/C6CY02647H>.

(61) Seemala, B.; Cai, C. M.; Wyman, C. E.; Christopher, P. Support Induced Control of Surface Composition in Cu–Ni/TiO₂ Catalysts Enables High Yield Co-Conversion of HMF and Furfural to Methylated Furans. *ACS Catal.* **2017**, 4070–4082. <https://doi.org/10.1021/acscatal.7b01095>.

(62) Kong, X.; Zhu, Y.; Zheng, H.; Dong, F.; Zhu, Y.; Li, Y.-W. Switchable Synthesis of 2,5-Dimethylfuran and 2,5-Dihydroxymethyltetrahydrofuran from 5-Hydroxymethylfurfural over Raney Ni Catalyst. *RSC Adv.* **2014**, *4* (105), 60467–60472. <https://doi.org/10.1039/C4RA09550B>.

(63) Hansen, T. S.; Barta, K.; Anastas, P. T.; Ford, P. C.; Riisager, A. One-Pot Reduction of 5-Hydroxymethylfurfural via Hydrogen Transfer from Supercritical Methanol. *Green Chem.* **2012**, *14* (9), 2457–2461. <https://doi.org/10.1039/C2GC35667H>.

(64) Zhang, J.; Chen, J. Selective Transfer Hydrogenation of Biomass-Based Furfural and 5-Hydroxymethylfurfural over Hydrotalcite-Derived Copper Catalysts Using Methanol as a Hydrogen Donor. *ACS Sustain. Chem. Eng.* **2017**, *5* (7), 5982–5993. <https://doi.org/10.1021/acssuschemeng.7b00778>.

(65) Liu, Y.; Mellmer, M. A.; Alonso, D. M.; Dumesic, J. A. Effects of Water on the Copper-Catalyzed Conversion of Hydroxymethylfurfural in Tetrahydrofuran. *ChemSusChem* **2015**, *8* (23), 3983–3986. <https://doi.org/10.1002/cssc.201501122>.

(66) Xiao, B.; Niu, Z.; Wang, Y. G.; Jia, W.; Shang, J.; Zhang, L.; Wang, D.; Fu, Y.; Zeng, J.; He, W.; et al. Copper Nanocrystal Plane Effect on Stereoselectivity of Catalytic Deoxygenation of Aromatic Epoxides. *J. Am. Chem. Soc.* **2015**, *137* (11), 3791–3794. <https://doi.org/10.1021/jacs.5b01391>.

(67) Huang, Y. B.; Chen, M. Y.; Yan, L.; Guo, Q. X.; Fu, Y. Nickel-Tungsten Carbide Catalysts for the Production of 2,5-Dimethylfuran from Biomass-Derived Molecules.

ChemSusChem **2014**, 7 (4), 1068–1072. <https://doi.org/10.1002/cssc.201301356>.

(68) Kong, X.; Zheng, R.; Zhu, Y.; Ding, G.; Zhu, Y.; Li, Y.-W. Rational Design of Ni-Based Catalysts Derived from Hydrotalcite for Selective Hydrogenation of 5-Hydroxymethylfurfural. *Green Chem.* **2015**, 17 (4), 2504–2514. <https://doi.org/10.1039/C5GC00062A>.

(69) Yu, L.; He, L.; Chen, J.; Zheng, J.; Ye, L.; Lin, H.; Yuan, Y. Robust and Recyclable Nonprecious Bimetallic Nanoparticles on Carbon Nanotubes for the Hydrogenation and Hydrogenolysis of 5-Hydroxymethylfurfural. *ChemCatChem* **2015**, 7 (11), 1701–1707. <https://doi.org/10.1002/cctc.201500097>.

(70) Kong, X.; Zhu, Y.; Zheng, H.; Li, X.; Zhu, Y.; Li, Y.-W. Ni Nanoparticles Inlaid Nickel Phyllosilicate as a Metal–Acid Bifunctional Catalyst for Low-Temperature Hydrogenolysis Reactions. *ACS Catal.* **2015**, 5 (10), 5914–5920. <https://doi.org/10.1021/acscatal.5b01080>.

(71) Chen, M. Y.; Chen, C. B.; Zada, B.; Fu, Y. Perovskite Type Oxide-Supported Ni Catalysts for the Production of 2,5-Dimethylfuran from Biomass-Derived 5-Hydroxymethylfurfural. *Green Chem.* **2016**, 18 (13), 3858–3866. <https://doi.org/10.1039/C6GC00432F>.

(72) Kong, X.; Zhu, Y.; Zheng, H.; Zhu, Y.; Fang, Z. Inclusion of Zn into Metallic Ni Enables Selective and Effective Synthesis of 2,5-Dimethylfuran from Bioderived 5-Hydroxymethylfurfural. *ACS Sustain. Chem. Eng.* **2017**, 5 (12), 11280–11289. <https://doi.org/10.1021/acssuschemeng.7b01813>.

(73) Sitthisa, S.; An, W.; Resasco, D. E. Selective Conversion of Furfural to Methylfuran over Silica-Supported NiFe Bimetallic Catalysts. *J. Catal.* **2011**, 284 (1), 90–101. <https://doi.org/10.1016/j.jcat.2011.09.005>.

(74) Yang, P.; Cui, Q.; Zu, Y.; Liu, X.; Lu, G.; Wang, Y. Catalytic Production of 2,5-Dimethylfuran from 5-Hydroxymethylfurfural over Ni/Co₃O₄ Catalyst. *Catal. Commun.* **2015**, 66, 55–59. <https://doi.org/10.1016/j.catcom.2015.02.014>.

(75) Chen, B.; Li, F.; Huang, Z.; Yuan, G. Carbon-Coated Cu-Co Bimetallic Nanoparticles as Selective and Recyclable Catalysts for Production of Biofuel 2,5-Dimethylfuran. *Appl.*

Catal. B Environ. **2017**, *200* (Supplement C), 192–199.
<https://doi.org/10.1016/j.apcatb.2016.07.004>.

(76) Yang, P.; Xia, Q.; Liu, X.; Wang, Y. Catalytic Transfer Hydrogenation/Hydrogenolysis of 5-Hydroxymethylfurfural to 2,5-Dimethylfuran over Ni-Co/C Catalyst. *Fuel* **2017**, *187*, 159–166. <https://doi.org/10.1016/j.fuel.2016.09.026>.

(77) Li, J.; Liu, J.; Liu, H.; Xu, G.; Zhang, J.; Liu, J.; Zhou, G.; Li, Q.; Xu, Z.; Fu, Y. Selective Hydrodeoxygenation of 5-Hydroxymethylfurfural to 2,5-Dimethylfuran over Heterogeneous Iron Catalysts. *ChemSusChem* **2017**, n/a-n/a.
<https://doi.org/10.1002/cssc.201700105>.

(78) Li, J.; Zhang, J.; Liu, H.; Liu, J.; Xu, G.; Liu, J.; Sun, H.; Fu, Y. Graphitic Carbon Nitride (g-C₃N₄)-Derived Fe-N-C Catalysts for Selective Hydrodeoxygenation of 5-Hydroxymethylfurfural to 2,5-Dimethylfuran. *ChemistrySelect* **2017**, *2* (34), 11062–11070.
<https://doi.org/10.1002/slct.201701966>.

(79) Yang, W.; Sen, A. One-Step Catalytic Transformation of Carbohydrates and Cellulosic Biomass to 2,5-Dimethyltetrahydrofuran for Liquid Fuels. *ChemSusChem* **2010**, *3* (5), 597–603. <https://doi.org/10.1002/cssc.200900285>.

(80) Grochowski, M. R.; Yang, W.; Sen, A. Mechanistic Study of a One-Step Catalytic Conversion of Fructose to 2,5-Dimethyltetrahydrofuran. *Chem. – Eur. J.* **2012**, *18* (39), 12363–12371. <https://doi.org/10.1002/chem.201201522>.

(81) Jackson, M. A.; Appell, M.; Blackburn, J. A. Hydrodeoxygenation of Fructose to 2,5-Dimethyltetrahydrofuran Using a Sulfur Poisoned Pt/C Catalyst. *Ind. Eng. Chem. Res.* **2015**, *54* (28), 7059–7066. <https://doi.org/10.1021/acs.iecr.5b00766>.

CHAPTER 2: MATERIALS AND METHODS

2.1 Introduction

Throughout this chapter, the materials, equipment and methods involved in the catalyst preparation, characterization and catalysis test are described. The first section is dedicated to the preparation of the support materials, including the preparation of SBA-15 silica. The second section focuses on the dispersion of the different metals (i.e., Ni, Co and Cu) on the support materials. The third section describes the instruments used for material characterizations. The last section involves description of the instruments used for the catalysis tests, and is followed by the building-up of the product analysis methods and the detailed setting parameters of the product analysis.

2.2. Catalyst preparation

2.2.1. Preparation of the SBA-15 mesoporous silica support

SBA-15 was prepared according to classical procedure, using Pluronic P123 (poly(ethyleneoxide)-block-poly(propyleneoxide)-blockpoly(ethyleneoxide)-block), PEO₂₀PPO₇₀PEO₂₀, molecular weight of 5800, BASF Corp.) as the template agent and tetraethylorthosilicate (Si(OC₂H₅)₄, TEOS, 98%, Sigma-Aldrich) as the source of silica. To obtain 2.4 g of SBA-15, 4 g of P123 was dissolved in 150 mL of hydrochloric acid (HCl, 37%, Sigma-Aldrich) aqueous solution (1.6 M). The mixture was kept under stirring at 40 °C for 24 h before adding 8.5 g TEOS. The suspension was transferred into a Teflon-lined autoclave, and aged at 100 °C for 48 h. After the synthesis, the resulting white solids was filtered, washed with distilled water and dried at 80 °C for 24 h. Finally, the sample was calcined at 550 °C for 6 h (heating rate: 1.5 °C/min) to remove the organic template.

Dried SBA-15 materials, aged at different temperatures (i.e. 60, 100 and 140 °C), were used for the melt infiltration procedure described in Chapter 4. The calcined SBA-15 material aged at 100 °C was used as support in all other studies (Cu-based catalysts in Chapter 5 and Ni/SBA-15 catalyst prepared by in-situ auto-combustion in Chapter 3).

2.2.2. Preparation of Cu/SBA-15 catalysts

Cu/SBA-15 catalysts were prepared by three different methods, namely, incipient wetness impregnation – mild drying (IWI-MD), in-situ automatic combustion (ISAC) and deposition-precipitation (DP). The metal loading for all the catalysts was fixed at 15 wt.%.

IWI-MD procedure: to prepare 1 g of Cu/SBA-15 catalyst, 1.02 mL of a copper nitrate aqueous solution (2.35 mmol/mL; $\text{Cu}(\text{NO}_3)_2 \cdot 2.5\text{H}_2\text{O}$, 98%, Sigma-Aldrich) was dropped into 0.85 g of SBA-15 powder (pore volume: 1.2 mL/g) and then mixed homogeneously. The wet mixture was put in an oven set at 25 °C and aged in static air conditions for five days. The calcination was thereafter performed at 500 °C for 6 h with a ramp of 1.5 °C/min. The calcined Cu/SBA-15 sample is denoted as 15Cu/SBA-15_IWIMD.

ISAC procedure: for the preparation of 1 g of 15 wt.% Cu/SBA-15, 50 mL of a copper nitrate aqueous solution (0.048 mmol/mL; $\text{Cu}(\text{NO}_3)_2 \cdot 2.5\text{H}_2\text{O}$, 98%, Sigma-Aldrich) and 50 mL of a glycine aqueous solution (0.448 mmol/mL; $\text{NH}_2\text{CH}_2\text{COOH}$, 99%, Sigma-Aldrich) were mixed together and stirring for 12 h at room temperature. The resulting solution was added dropwise to 0.85 g of SBA-15 powder, and then aged for 12 h. The blue gel was heated at 100 °C until water was evaporated. A white solid was obtained and combusted at 300 °C for 30 min in an open vessel in an oven under static air conditions. Finally, the sample was calcined at 500 °C for 6 h under static air conditions (temperature increase rate = 1 °C/min). The calcined catalyst is noted 15Cu/SBA-15_ISAC.

DP procedure: for the preparation of 1 g of 15 wt.% Cu/SBA-15, 0.85 g SBA-15 was added in 70 mL distilled water and stirred intensely to disperse the support. 35 mL of copper nitrate aqueous solution (0.069 mmol/mL; $\text{Cu}(\text{NO}_3)_2 \cdot 2.5\text{H}_2\text{O}$, 98%, Sigma-Aldrich) was added into the SBA-15 suspension. If necessary, few drops of nitric acid were added to adjust the pH value of the solution to 2.0. The temperature of the reactor was increased to 90 °C. Then, 35 mL of urea (0.8 mmol/mL; $\text{CO}(\text{NH}_2)_2$, 99%, Sigma-Aldrich) with the mass ratio of urea/copper nitrate equaling to 3 was added to the slurry solution. The slurry was stirred for 24 h, cooled down to room temperature, filtered and washed. The precipitates were dried at 80 °C overnight and then calcined at 500 °C for 6 h with a ramp of 1.5 °C/min. The as-made catalyst before calcination is noted 15Cu/SBA-15_DP_am. The calcined catalyst is noted 15Cu/SBA-15_DP.

2.2.3. Preparation of Ni/SBA-15 catalysts

Monometallic Ni-based catalysts were prepared using two different methods: IWI-MD, as previously described, and melt infiltration (MI).

IWI-MD procedure: to prepare 10 g of 15 wt.% Ni/SBA-15, 9.435 mL of an aqueous solution of nickel nitrate (2.77 mmol/mL; $\text{Ni}(\text{NO}_3)_2 \cdot 6\text{H}_2\text{O}$, 98% purity, Sigma-Aldrich) was dropped into 8.5 g of SBA-15 powder (pore volume = 1.1 mL/g) and then mixed homogeneously. The wet mixture was put in an oven set at 25 °C and aged under static conditions for five days. A calcination under static air was finally performed at 500 °C for 6 h with a ramp of 1.5 °C/min. The calcined Ni/SBA-15 sample is denoted as 15Ni/SBA-15_IWI-MD.

MI procedure: to prepare of 1 g catalyst, 0.5 g of nickel nitrate ($\text{Ni}(\text{NO}_3)_2 \cdot 6\text{H}_2\text{O}$, 99%, Sigma-Aldrich) was ground and mixed with 0.9 g of dried SBA-15. The mixture was heat-treated at 57 °C in an autoclave for 4 days in order to ensure the complete diffusion of the molten phase into the support porosity.³ Once the diffusion step was completed, the solid was calcined under static conditions at 500 °C for 5 h, using a heating rate of 1.5 °C/min⁻¹. The calcined materials (NiO/SBA-15) prepared using the different dried SBA-15 supports were named Ni_T, where T was the temperature at which the support was aged (60, 100 or 140 °C).

2.3. Catalyst characterization

2.3.1. Nitrogen physisorption

Textural properties of catalysts were determined by nitrogen physisorption at 77 K on a Micromeritics TriStar II Plus automated gas sorption system. The different samples were pretreated under vacuum (Micromeritics Vacprep 061) before physisorption experiments. SBA-15 supported samples were degassed at 90 °C for 15 min and then 350 °C for 3 h. The adsorption/desorption isotherms were obtained at -196 °C by allowing 4 min for equilibration between each successive point.

The specific areas of the catalysts were determined by the Brunauer-Emmett-Teller (BET) model. For SBA-15 and SBA-15 supported catalysts, the calculation of the surface area was

done using the adsorption-desorption points in the range of 0.05-0.3 P/P₀. For all of the catalysts, the pore size distribution was calculated from the desorption branches of the isotherms using the Barrett-Joyner-Halenda (BJH) model. The total pore volume was calculated by converting the adsorbed gaseous nitrogen quantity into liquid volume at a relative pressure of 0.99. The t-plot method was applied to quantitatively determine the micropore volume and to assess the micropore surface area.

2.3.2. X-ray diffraction

X-ray powder diffraction (XRD) was used to identify the crystalline phases and determine the crystallite size. The XRD patterns of all the calcined catalysts were recorded by a Bruker D8 Advance X-ray diffractometer, using a Cu K α radiation ($\lambda = 1.54184 \text{ \AA}$) as X-ray source. For the reduced catalysts, a Co radiation was used as X-ray source ($\lambda = 1.788965 \text{ \AA}$). High angle XRD record was carried out in the 2θ range of 10° to 80° . Low angle XRD scanning was carried out in the 2θ range of 0.5° to 5° . Both were recorded with 0.05° step size and 2 s step time. Crystallite phases were determined by comparing the diffraction patterns with those in the standard powder XRD files (JCPDS) published by the International Center for Diffraction Data (ICDD). The average crystallite size of CuO and NiO crystals were calculated according to the Scherrer equation (Equation 2-1).

$$d = 0.89\gamma/\beta\cos\theta \quad \text{Equation 2.1}$$

where d is the average crystallite diameter, γ is the X-ray wavelength, β is the line broadening at half the maximum intensity after correction for instrumental broadening (FWHM), θ is the Bragg angle.

According to the position of the diffraction peaks in the low angle pattern, the interplanar distance of d_{100} was calculated by the Bragg Law:

$$d_{100} = \lambda/2\sin\theta \quad \text{Equation 2.2}$$

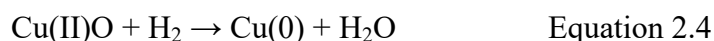
where d_{100} is interplanar distance of (100) plane, γ is the X-ray wavelength, θ is the Bragg angle.

Then the cell parameter a_0 was determined by:

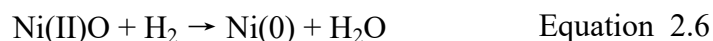
$$a_0 = 2 d_{100} / \sqrt{3} \quad \text{Equation 2.3}$$

2.3.3. Hydrogen temperature-programmed reduction (H₂-TPR)

H₂-TPR was used to measure the reducibility of active phases. H₂-TPR was performed on an Autochem analyzer (Micromeritics) equipped with a quartz U-shaped microreactor. Prior to reduction, the samples were pretreated under air flow (30 mL/min) at 500 °C for 1 h (heating ramp of 5 °C/min). Thereafter, 60 mg of sample was reduced under 5 vol.% H₂/Ar flow (50 mL/min) from RT to 900 °C (heating ramp of 5 °C/min). The practical hydrogenation consumptions of Cu and Ni oxides during the reduction processes were checked using the following equations.



$$n(\text{H}_2)_{\text{consumed}} = n(\text{Cu})_{\text{reduced}} \quad \text{Equation 2.5}$$



$$n(\text{H}_2)_{\text{consumed}} = n(\text{Ni})_{\text{reduced}} \quad \text{Equation 2.7}$$

Where $n(\text{H}_2)_{\text{consumed}}$ represents the quantity of H₂ consumed (mol) during the transition metal reduction, $n(\text{Ni})_{\text{reduced}}$ represents the quantity of Ni²⁺ (mol) reduced to metal, $n(\text{Cu})_{\text{reduced}}$ represents the quantity of Cu²⁺ (mol) reduced to metal.

2.3.4. High-resolution transmission electronic microscopy (HRTEM)

High-resolution transmission electronic microscopy (HRTEM) was used to characterize catalyst morphology and particle size distribution. A JEOL 2100 instrument with Filament LaB₆ having an acceleration voltage of 200 kV and equipped with a Gatan 832 CCD camera was used for visualizing the catalyst. Before analysis, the sample was included in a resin and cut into ~100 nm width samples using ultramicrotomy. The particle size distribution was measured by manual analysis of micrographs using Image J software.

2.3.5. Fourier transform infrared resonance

The functional groups of copper catalysts prepared by DP method were identified by an infrared spectrometer with total attenuation (IR-ATR) of Thermo scientific IS50. The spectra are recorded at room temperature in a wavenumber range of 4000-800 cm⁻¹ using a triglycine sulfate pyro-electric detector (DTGS). The samples are directly pressed between the detector window and a diamond tip.

2.4. Catalysis test

2.4.1. Catalyst activation

Before catalytic test, the samples were firstly reduced under H₂. The reduction conditions were determined according to the H₂-TPR results. For the Cu-based catalysts, reduction was performed at 300 °C for 2 h under pure H₂ flow condition. For the Ni-based catalysts, the catalyst reduction was performed at 550 °C for 2 h under the same conditions. These conditions ensure complete reduction of the Cu / Ni phases.

2.4.2. Catalysis test

2.4.2.1 Catalysis test for HMF hydro-conversion

The catalysis tests were performed using two different setups. The optimization of the reaction conditions for both Cu-based catalysts and Ni-based catalysts was performed on an

Autoplant-Chemspeed instrument available at the REALCAT platform in UCCS Laboratory. The Autoplant robot is equipped with 8 high-pressure batch reactors (100 mL) and is controlled using a dedicated software affording a control over the reaction parameters. Each reactor is equipped with a heater, a pressure regulator, a reflux system, a temperature probe and a mechanic stirrer. The Autoplant robot offers the possibility of working with 8 reactors under different temperature and pressure conditions in parallel. For a typical test, the required amounts of pre-reduced catalysts were put into reactors in glove box environment (to avoid the exposure of the catalyst to oxygen). 25 mL of HMF solution in 1,4-dioxane (0.15 mmol/mL) then was added to the reactor allowing to completely immerse the catalysts. The reactors were hermetically closed, moved out of the glove box and connected to the Autoplant robot. The Autoplant robot started running according to the pre-written program: (1) the reactors were purged under nitrogen (1 time) and with hydrogen (3 times), and the hydrogen pressure was stabilized at a specified hydrogen pressure (lower than the reaction pressure, e.g. 10 of 15 bar) at ambient temperature; (2) reactor temperatures were subsequently increased to the setting values; (3) the hydrogen pressures in each reactor were increased to the target values, this step corresponding to the zero time of the reaction. The reaction was performed for 8 h with mechanic stirring set at 700 rpm. When the reaction in each reactor was achieved, the reflux system in each reactor started to cool down the reactor to the room temperature. The H₂ pressure inside each reactor was decreased and the reactors were purged with N₂ gas. Finally, the samples, which contained both the liquid reaction mixture and the solid catalyst, were collected from the opened reactors and filtered.

The kinetic profiles of the selected Cu/SBA-15 and Ni/SBA-15 catalysts were performed in a 45 mL Parr reactor in IC2MP in University Poitiers. The detailed procedure is given taking the tests performed over Cu/SBA-15 catalysts (i.e. 15Cu/SBA-15_ISAC and 15Cu/SBA-15_DP) as example. 0.085 g catalyst was placed in the reactor and reduced at 300 °C under 10 bar of hydrogen pressure for 2 h. The reactor was opened after the reactor was cooled down to the room temperature. Then, 12.5 mL of 0.15 mmol/mL HMF solution in 1,4-dioxane was added to the reactor. The reactor was closed and purged with hydrogen gas for several times. A pressure of 6 bar of H₂ was applied, in order to obtain 15 bar of H₂ under the reaction condition (T = 210 °C). The pressure was monitored using a gauge connected to the reactor. The reactor was settled in the oven and heated to the target temperature (210 °C) and magnetic agitation was started. Samples of reaction medium were taken off at selected reaction times: 5 min, 10 min, 20 min, 30 min, 1 h, 2 h, 4 h, 6 h, 8 h and 10 h. When the reaction time was over, the reactor was put into ice to rapidly cool down the reactor and stop

the reaction. Then the reactor was opened and the sample was collected and filtered. The cycling tests were performed in a comparable Parr reactor in UCCS in University Lille. The manipulation details were comparable with the catalysis tests previously performed, except for: (1) 0.135 g catalyst and 25 mL of 0.15 mmol/mL HMF solution in 1,4-dioxane was added to the reactor; (2) the reactions were stopped after 3 h. After the reaction, the solution was separated from the spent catalyst by centrifugation. Between two successive runs, the spent catalyst was regenerated by calcination and reduction under the same conditions with the fresh catalysts.

2.4.2.2 Catalysis test for cinnamaldehyde hydro-conversion

The catalytic performances of Ni_T materials in the cinnamaldehyde (CNA) hydrogenation reaction were assessed in a Parr reactor in Laboratory of Chemical Engineering in Technical University of Iasi (RO). Catalyst is first activated at 500 °C for 10 h under H₂ flow. A series of preliminary tests were performed with different granulometric fractions, stirring rates and catalyst loadings, to determine conditions under which no diffusional limitations would occur: grain size lower than 0.126 mm, stirring rate of 750 rpm minimum, and 0.066 - 0.265 g catalyst are selected. A blank experiment was conducted under N₂ pressure (instead of H₂), in order to confirm the absence of hydrogenation product by hydrogen-transfer reaction with the solvent after 6 h of reaction. Finally, a blank experiment with calcined SBA-15_100 sample was performed to determine the support presence effect on the cinnamaldehyde concentration in solution. No modification of the concentration was observed after 6 h of reaction, leading to conclude on a low adsorption capacity of the silica support under the conditions of test. The catalytic experiments were performed at 60 °C under 10 bar H₂ with 0.133 g catalyst in 40 mL CNA solution in 2-propanol (0.2 mmol/mL).

2.4.3. Products identification and quantification

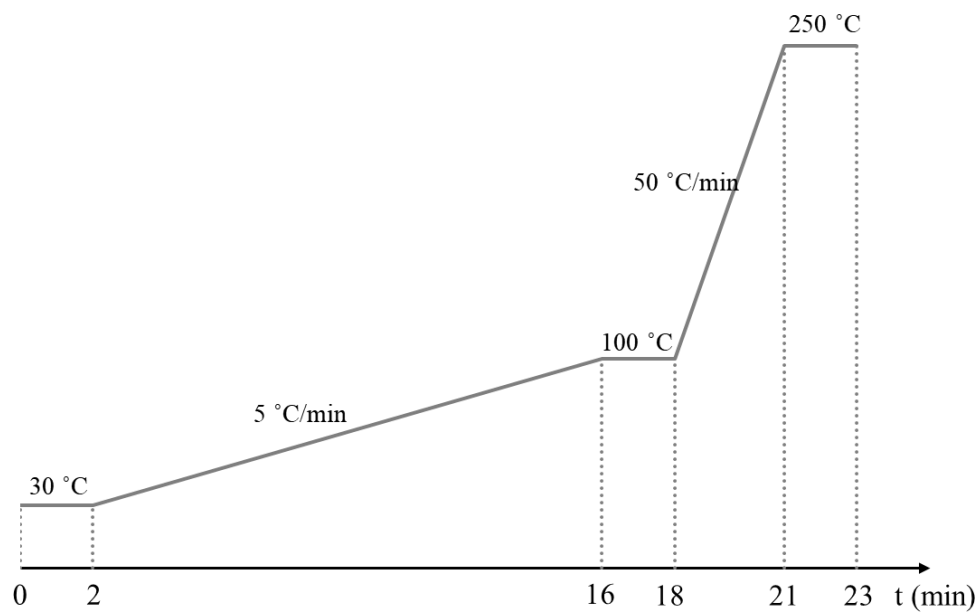


Fig. 2.1 Column oven temperature program of GC analysis in UCCS in University Lille

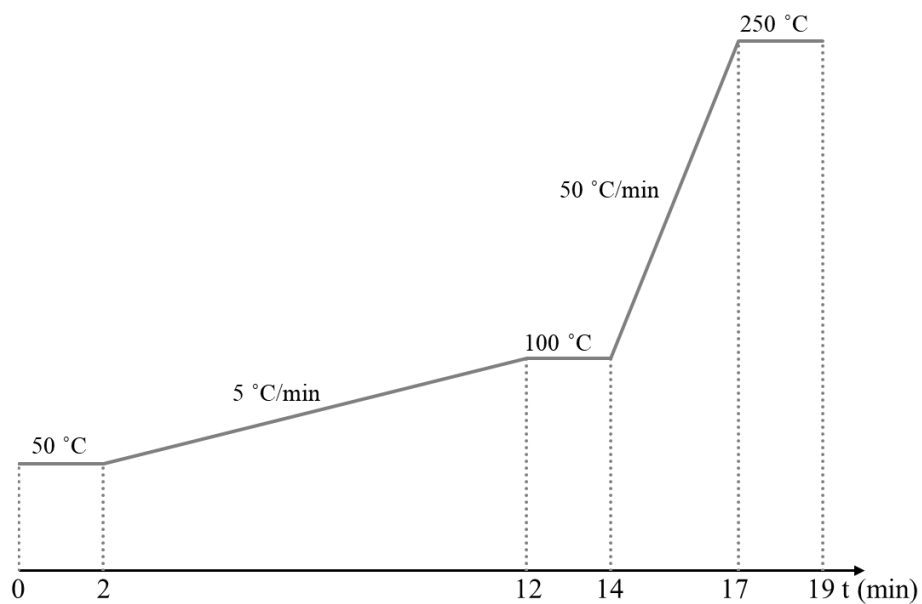


Fig. 2.2 Column oven temperature program of GC analysis in IC2MP in University Poitiers

After the reaction, the mixture of the products was collected from the reactor, diluted if necessary and analysed. For the catalysis tests performed in UCCS in University of Lille, the samples were analysed by GC (Shimadzu 2010 Plus) equipped with ZB-WAX Plus capillary column (30.0 m × 0.25 mm × 0.25 μm) and a flame ionization detector (FID). The analytical methods were adjusted for the product mixtures depending on the boiling point and polarity of the different compounds. The key analysis parameters deciding the residence time and the peak shape include the column oven temperature program, the split ratio and the flow rate of the carrier gas (H₂), the injector temperature, the detector temperature and the injection volume. The column oven temperature was programmed as shown in Fig. 2.1: the initial column temperature of 30 °C was held for 2 min, and then, the temperature was ramped at 5 °C/min until 100 °C was reached and held for 2 min; after that, the temperature was ramped at 50 °C/min until 250 °C was reached and held for 2 min. The injection volume was 1 μL, the injector temperature was 250 °C, the detector temperature was 270 °C, the carrier gas was H₂ with a split ratio of 100 and a flow rate of 1.7 mL/min.

For the catalysis tests performed in IC2MP in University of Poitiers, the samples were analyzed by a Varian Bruker 450 GC equipped with a flame ionization detector (FID) and a HP-5MS column (30.0 m × 0.25 mm × 0.25 μm). The oven temperature was programmed as shown in Fig. 2.2: the initial column temperature of 50 °C was held for 2 min, and then, the temperature was ramped at 5 °C/min until 100 °C was reached and held for 2 min; after that, the temperature was ramped at 50 °C/min until 250 °C was reached and held for 2 min. The injection volume was 2 μL, the injector temperature was 250 °C, the detector temperature was 300 °C, and the flow rate of carrier gas was 1.0 mL/min.

Identification of the unknown products was conducted using gas chromatography–mass spectrometry (GC-MS), which combines the features of gas chromatography and mass spectrometry. The analysis was carried out in UCCS in University of Lille on a Shimadzu QP2010 Ultra EI system equipped with a ZB-1XT capillary column (15.0 m × 0.53 mm × 0.25 μm) and a FID detector. The conditions used for separation were identical to those previously described for gas chromatography analysis.

2.4.4. General calculation methods

The conversion of the reactants and product yields were calculated using the following equations:

$$\text{Conversion} = (1 - n_r/n_0) \times 100\% \quad \text{Equation 2.8}$$

$$\text{Yield} = (n_i/n_0) \times 100\% \quad \text{Equation 2.9}$$

$$\text{Carbon balance} = (\sum n_i + n_r)/n_0 \times 100\% \quad \text{Equation 2.10}$$

Where n_r is the remaining molar amount of reactant after reaction, n_0 is the initial molar amount of reactant, n_i is the molar amount of product i obtained after reaction, $\sum n_i$ is the sum of the molar amount of all the known products.

Reference

- (1) Huwe, H.; Fröba, M. Synthesis and Characterization of Transition Metal and Metal Oxide Nanoparticles inside Mesoporous Carbon CMK-3. *Carbon* **2007**, *45* (2), 304–314.
- (2) Wu, H.; Zhou, S.; Wu, Y.; Song, W. Ultrafine CuO Nanoparticles Isolated by Ordered Mesoporous Carbon for Catalysis and Electroanalysis. *J. Mater. Chem. A* **2013**, *1* (45), 14198–14205.
- (3) Ciotonea, C.; Dragoi, B.; Ungureanu, A.; Catrinescu, C.; Petit, S.; Alamdari, H.; Marceau, E.; Dumitriu, E.; Royer, S. Improved Dispersion of Transition Metals in Mesoporous Materials through a Polymer-Assisted Melt Infiltration Method. *Catal. Sci. Technol.* **2017**, *7* (22), 5448–5456.

**CHAPTER 3: CATALYTIC PERFORMANCE
OF MONOMETALLIC Ni/SBA-15 CATALYST
FOR THE SELECTIVE HYDROCONVERSION
OF HMF TO DMF AND DMTHF**

3.1 Introduction

When supported on high-surface-area materials (e.g. mesoporous silica SBA, KIT, MCM, FDU and MSU families), non-noble metal NPs should be prepared as well-dispersed in order to favor the catalytic activity and/or the selectivity. Previous research indicates that the reactivity of metal NPs basically depends on: (i) the properties of the metal NPs; (ii) the properties of the host structure (i.e., pore architecture, surface area, surface properties); and (iii) the properties of particle/host system (i.e., loading, spatial distribution of NPs, and strength of interactions between the support and NPs).^{1,2} It is thus crucial to select suitable metals and supporting materials, and especially to choose proper preparation parameters to moderate these properties in order to obtain efficient catalysts for the targeted transformations.

There is a large diversity of methods for the preparation of supported non-noble metal NPs into the porosity of mesoporous supports, such as impregnation, sol-gel process, sonochemical methods, *in situ* glycine combustion, deposition-precipitation, chemical vapor deposition and one-pot processes (e.g. one-pot block-copolymer self-assembly strategy). Among them, impregnation (wet impregnation – WI, and incipient wetness impregnation – IWI) is by far the most used method, due to its simplicity, to the small amount of required solvent, to the availability of commercial metal precursors and to limited production of waste.³ An impregnation procedure generally involves several successive steps:⁴ (i) impregnation itself, putting into contact the porous support with the solution of metal precursors, such as nitrates, chlorides and acetates; (ii) maturation and solvent evaporation by drying of the impregnate, (iii) thermal decomposition of the precursor and stabilization of the material, and (iv) activation of the catalyst for the specific application. Each step has to be carefully optimized (concentration of precursor in the initial impregnation solution, temperature and duration of drying, heating rate and gas atmosphere for the stabilization/activation, etc.). It is noteworthy that the drying step is particularly important in order to reach a homogeneous repartition of metal NPs throughout the support surface. During drying the liquid solution is transported by capillary flow and diffusion, and the metal precursor may be redistributed by adsorption/desorption phenomena. Fast drying at high temperatures often result in poor redistribution of the metal precursors on the support surface and sintering of metal particles during the following calcination process.^{5,6} In contrast, mild drying condition facilitates good dispersion of metal particles.⁸ For example, when

performing the drying step at room temperature, a high and stable dispersion of NiO particles in the mesopores of SBA-15 via IWI method can be achieved.⁶ The stabilization of NPs in the mesopores of SBA-15 by confinement, and the strong interaction between NiO and silica via nickel phyllosilicate phases, play important roles in this result.

Beside the effect of the drying or calcination conditions after IWI preparations, the nature of support is another factor which matters for the control of the properties of supported metal (oxide) NPs. Ordered mesoporous silicas such as MCM-41 and SBA-15 are ideal host materials for guest NPs thanks to their large specific surface areas and well defined pore structures. Particularly interesting are the large-pore mesoporous SBA-15-type silica materials prepared using triblock copolymers (i.e. Pluronic P123) as structural directing agents.^{7,8} As compared to MCM-41, SBA-15 materials have improved framework cross-linking and thicker walls which results in a higher thermal and hydrothermal stability.⁹

Concerning the non-noble metals used for the hydroconversion of HMF, Ni-based catalysts are known for their excellent hydrogenation abilities, and also for some activity in the cracking of the C-O bonds under relatively mild conditions.¹⁰ Actually, efforts have been made for years to explore efficient Ni-based catalysts for the hydroconversion of HMF to biofuels. On one hand, successes have mostly been achieved with multifunctional catalysts bearing both hydrogenation and deoxygenation properties, e.g. Ni-W₂C/C, Ni-Fe/CNTs (carbon nanotubes), and Ni/LaFeO₃, which rely on the use of promoters and/or functional supports to increase activity/selectivity. On the other hand, the study of more simple monometallic Ni-based catalysts, which have been indicated as potential for the production of DMF as well as DMTHF by few reports as summarized in Chapter 1, is still lacking at present. In the literature, the high reactivity of monometallic Ni-based catalysts (e.g. Raney Ni, hydrotalcite-derived NiAl oxides) relied on the high Ni content. It's more appealing to use the dispersed monometallic Ni-based catalyst with less Ni loading. However, no related work in this field has been reported yet at present.

The topic of this chapter is thus to study the catalytic performances of the monometallic Ni/SBA-15 catalyst prepared by the simple IWI method, in the hydroconversion of HMF. The purpose is to explore the suitable reaction conditions for achieving high yields of DMF and DMTHF with this catalyst, and to identify intermediate products on the way to the formation of DMF and DMTHF. The catalyst was first studied by different characterization techniques, namely, nitrogen physisorption, X-ray diffraction (XRD), temperature programmed reduction

by hydrogen (H_2 -TPR) and transmission electron microscopy (TEM), in order to determine its structural properties. The catalytic performances were evaluated under varying reaction conditions (i.e., temperature, pressure, reaction time, HMF/Ni molar ratio) in order to determine optimum ranges of reaction parameters. A kinetic study was then performed to investigate the reaction routes. Reusability tests were performed to see the potential of the catalyst for the practical application.

3.2. Catalyst preparation

10 gram of 15 wt.% Ni/SBA-15 was prepared by the incipient wetness impregnation-mild drying (IWI-MD) method according to the following procedure: 9.435 mL nickel nitrate (7.59 g $Ni(NO_3)_2 \cdot 6H_2O$, 98% purity, Sigma-Aldrich) aqueous solution was dropped into 8.5 g SBA-15 powder (pore volume: 1.11 mL/g) and then mixed homogeneously. The wet mixture was put in an oven set at 25 °C and aged for five days. Thereafter, the calcination was performed at 500 °C for 6 h with a ramp of 1.5 °C/min to decompose the nickel nitrate into nickel oxide (NiO). The calcined Ni/SBA-15 sample is denoted as 15Ni/SBA-15_IWI-MD. Before the catalysis tests, the 15Ni/SBA-15_IWI-MD sample was reduced in a flow of pure H_2 at 550 °C for 2 h to obtain metallic Ni.

3.3. Results and discussion

3.3.1 Characterization of the calcined 15Ni/SBA-15_IWI-MD

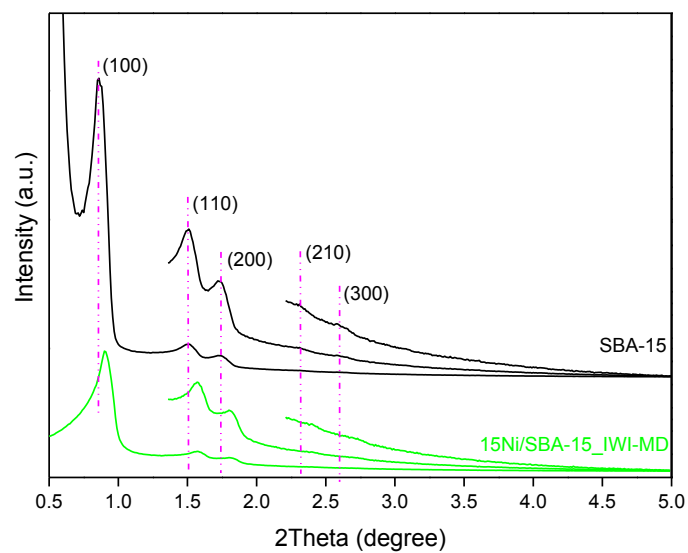


Fig. 3.1 Low angle XRD patterns for SBA-15 and 15Ni/SBA-15_IWI-MD

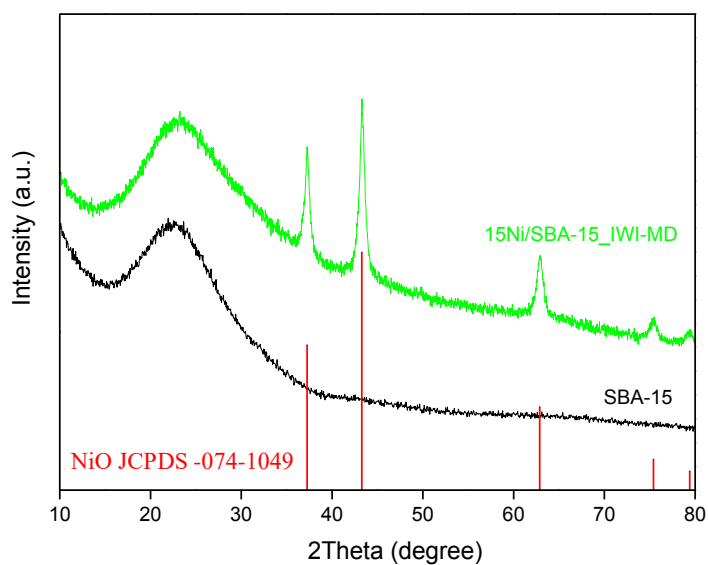


Fig. 3.2 High angle XRD patterns for SBA-15 and 15Ni/SBA-15_IWI-MD

Fig. 3.1 depicts the low angle X-ray diffraction domain for 15Ni/SBA-15_IWI-MD. Both the catalyst and the support exhibit one intense diffraction peak and four less intense diffraction peaks, indexed to the (100), (110), (200), (210) and (300) planes respectively, which indicate that the ordered hexagonal 2D structure of $p6mm$ symmetry in SBA-15 is well preserved after the formation of nickel oxide. Besides, the decrease of the diffraction peak intensity may also be explained by pore filling. The speciation of nickel was checked by high-angle XRD ($10-80^\circ$), as depicted in Fig. 3.2. The diffraction peaks at 37.2° , 43.3° , 62.9° , 75.4° and 79.4° indicate the presence of NiO particles (cubic symmetry, JCPDS 047-1049). The shape of the diffraction peaks with broad onsets topped by sharper lines suggests that both small and large NiO crystals exist in the catalyst. Accordingly, the crystal size calculated with the Scherrer equation at mid-height, in the sharper part of the peak, is 16.5 nm.

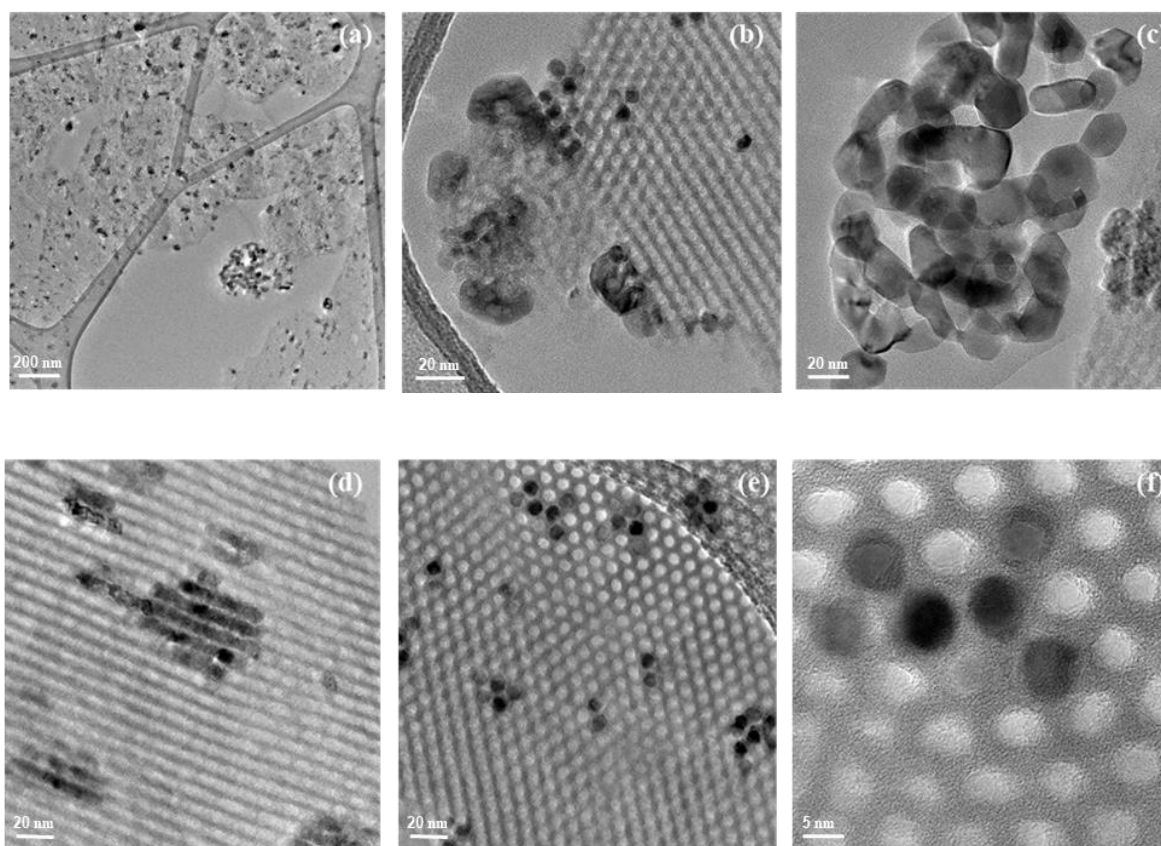


Fig. 3.3 Representative TEM images recorded for 15Ni/SBA-15_IWI-MD

The dispersion of nickel particles in the catalyst was further characterized by transmission electron microscopy. Representative TEM images taken on ultramicrotomed slices are shown in Fig. 3.3. The support shows the typical hexagonal SBA-15 mesoporous structure, with an excellent long-range order confirming the results obtained by XRD at low angles. Besides, both empty and full mesopores exist in the structure. Two kinds of metal oxide NPs with different morphologies can be observed. Part of the nickel oxide phase forms aggregates at the edge of the SBA-15 grains or recrystallized out of the support porosity (Fig. 3.3 a-c), and part is confined within the pores, generating nanorods (Fig. 3.3 d-f). The size of the NiO particles outside the pores is quite large, around 30-75 nm. The mean diameter of the NiO nanorods is 7.6 nm, which is close to the pore size of SBA-15, while their length varies from 14 to 115 nm. A careful observation shows that they actually consist of aggregates of small NiO particles. The existence of large particles explains the sharp diffraction peaks with small full width at half maxima as observed in the high angle XRD patterns.

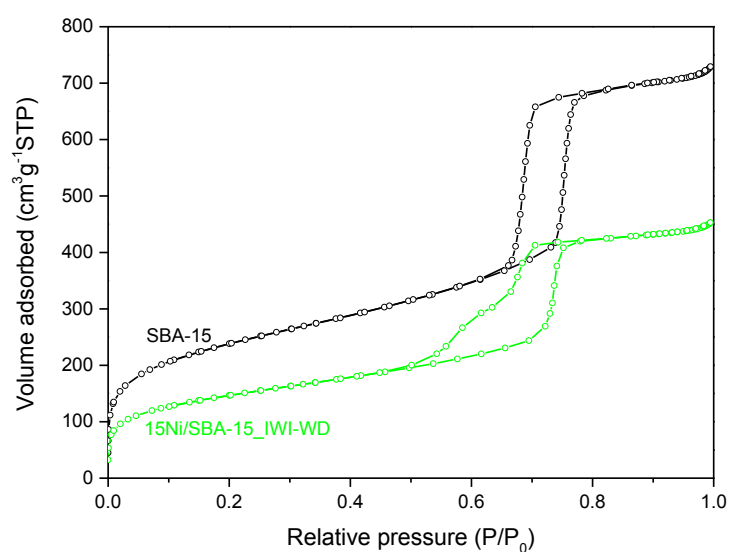


Fig. 3.4 N₂ physisorption isotherms for SBA-15 and 15Ni/SBA-15_IWI-MD

The textural properties of 15Ni/SBA-15_IWI-MD were determined by nitrogen physisorption. The nitrogen adsorption/desorption isotherms are presented in Fig. 3.4. The following features can be deduced: (1) the isotherm of type IV confirms the typical mesoporous SBA-15 structure; (2) a shift down along y-axis of the volume adsorbed in the P/P₀ range of 0.02-0.25 and of the volume adsorbed in the whole P/P₀ range indicates a

decrease of the pore volume of 15Ni/SBA-15_IWI-MD (as compared to SBA-15), as shown in Table 3.1, suggesting the partial filling of the mesopores by NiO particles, which is consistent with the XRD and TEM results; (3) the steep capillary condensation indicates that the mesopores have a uniform diameter; (4) the two-step desorption branch with a delayed closure at lower relative pressures ($P/P_0 = 0.46$ vs. 0.61) indicates that some pore have been partially blocked.^{11,12} In conclusion, the adsorption-desorption properties of 15Ni/SBA-15_IWI-MD reveal that the catalyst contains both open and blocked cylindrical mesopores, as shown by the TEM images. Fig. 3.5 displays the pore size distribution of the support and the catalyst. For 15Ni/SBA-15_IWI-MD, another kind of pore of 5.2 nm appeared and the diameter of the primary mesopores decreased to 6.6 nm as compared to the bare SBA-15 support, which could be ascribed to the fact that partial nickel loading into the cylindrical pores of SBA-15 decreased the pore size.

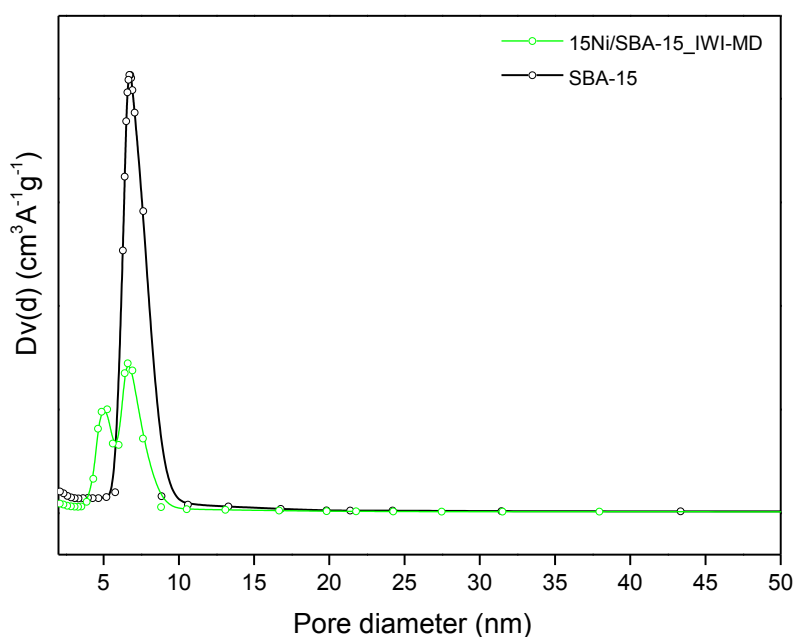


Fig. 3.5 Pore size distribution curves calculated using the desorption branch

Table 3.1 Physico-chemical properties of 15Ni/SBA-15_IWI-MD

Samples	$S_{\text{BET}},^a \text{ m}^2/\text{g}$	$V_t,^b \text{ cm}^3/\text{g}$	$D_p, \text{ nm}$
SBA-15	841	1.1	6.8
15Ni/SBA-15_IWI-MD	519	0.7	5.2, 6.6

^a: B.E.T. surface area per gram of SBA-15 support; ^b: total pore volume per gram of SBA-15 support.

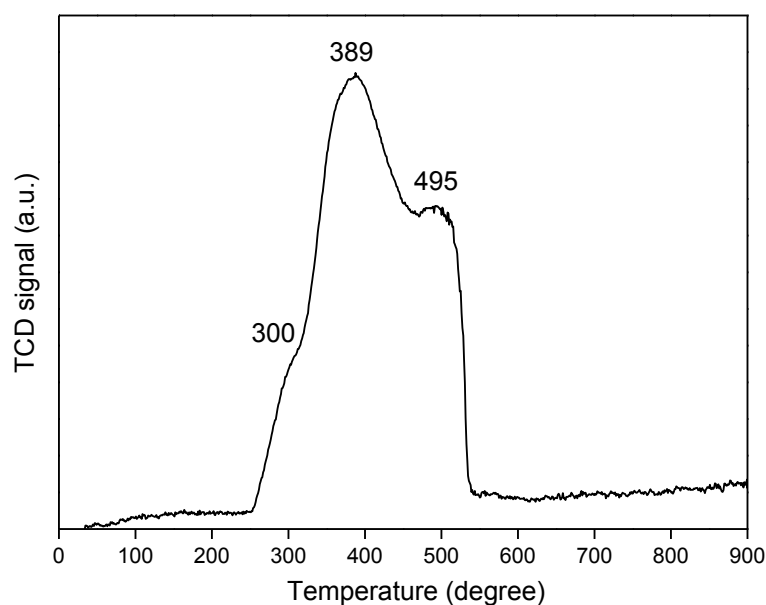


Fig. 3.6 H₂-TPR profile for calcined 15Ni/SBA-15_IWI-MD

The reducibility and characteristics of NiO species were investigated by H₂-TPR, as shown in Fig. 3.6. The H₂-TPR profile of 15Ni/SBA-15_IWI-MD presents two main peaks at 389 °C and 495 °C and one shoulder at around 300 °C. According to the literature, the reduction of bulk NiO generally takes place at temperatures below 420 °C.^{13,14} The reduction peak at 300 - 389 °C is associated to NiO NPs behaving like bulk NiO; and the peak at 495 °C to smaller, more difficult-to-reduce NiO NPs, in stronger interaction with the silica support.¹⁵

3.3.2 Characterization of reduced 15Ni/SBA-15_IWI-MD

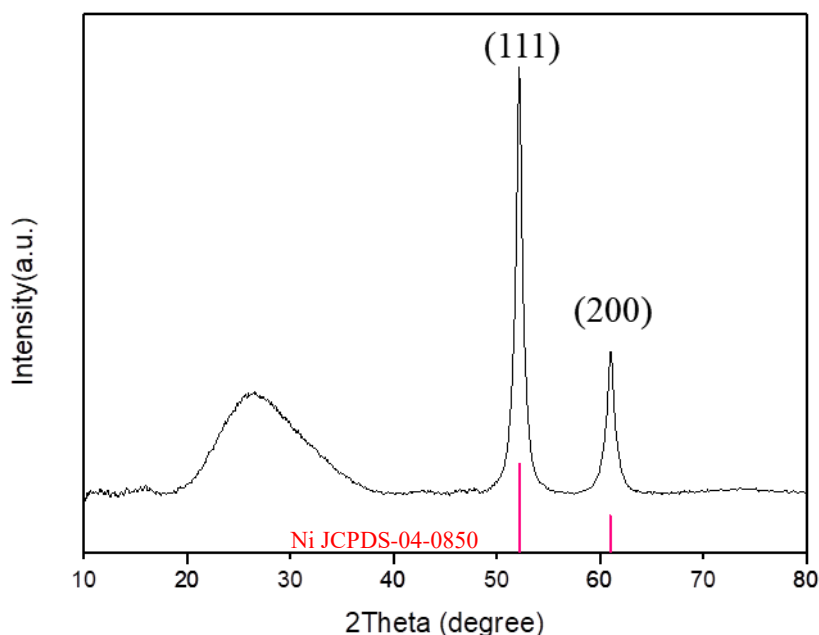


Fig. 3.7 High angle XRD pattern of reduced 15Ni/SBA-15_IWI-MD (Co-resource)

(Reduction condition: 550 °C for 2 h in pure hydrogen atmosphere at 50 mL min⁻¹)

The speciation of nickel after reduction (550 °C, 2 h) was determined using high-angle XRD as depicted in Fig. 3.7. The diffraction peaks at 52.2° and 61.0° as well as the corresponding interplanar spacing values ($d_{111} = 0.2035$ nm, $d_{200} = 0.1763$ nm) indicate the presence of the metallic nickel crystals (JCPDS 04-0850). The shape of these diffraction peaks is similar to that seen for calcined 15Ni/SBA-15_IWI-MD (see the especially sharp ends), implying the existence of both large and small Ni crystals in the catalyst. The mean crystal size calculated according to Scherrer equation is 15.5 nm, which is slightly lower than that of the oxide 15Ni/SBA-15_IWI-MD due to the removal of oxygen by reduction. As with the calcined sample, the value derives from the larger particles that provide the narrower component of the diffraction peaks.

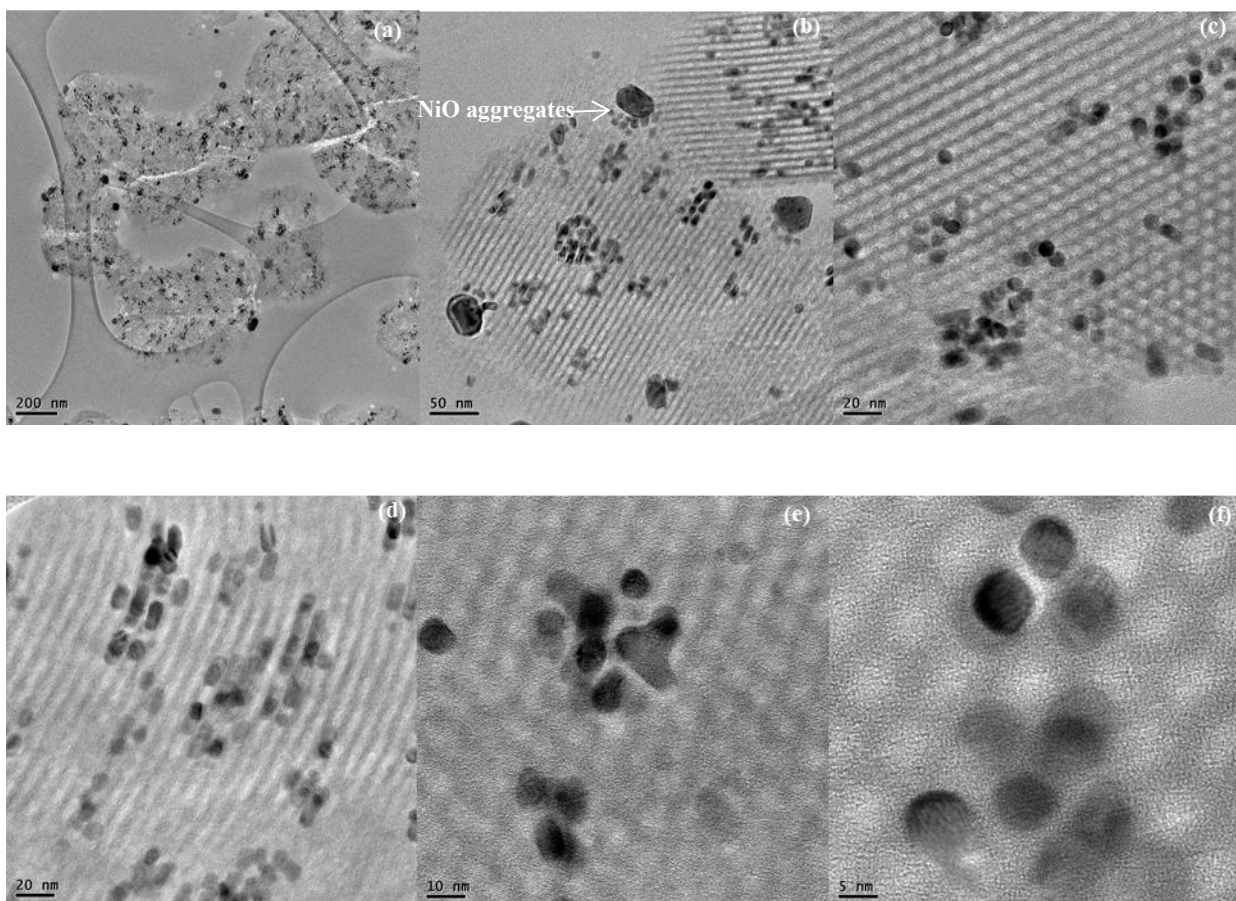


Fig. 3.8 Representative TEM images of the reduced $^{15}\text{Ni}/\text{SBA-15_IWI-MD}$

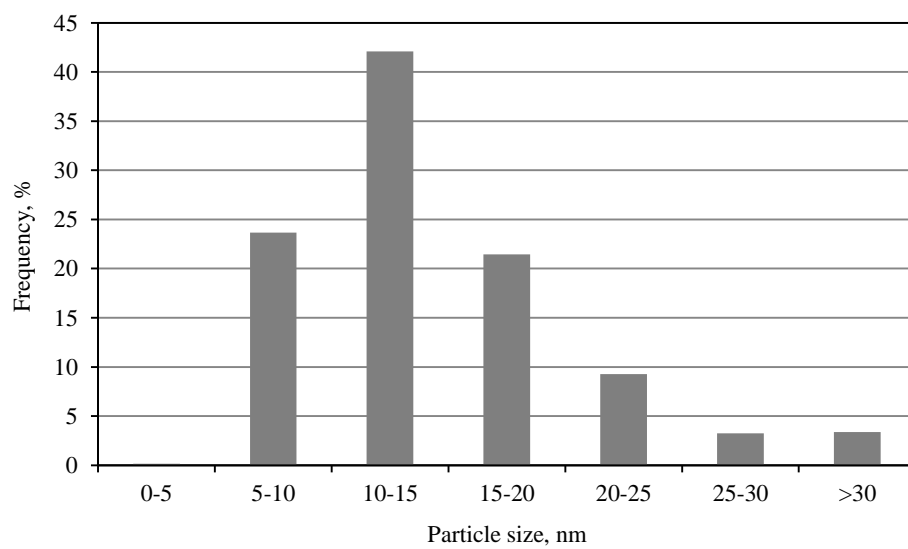


Fig. 3.9 NiO particle size distribution in the reduced $^{15}\text{Ni}/\text{SBA-15_IWI-MD}$

TEM images (Fig. 3.8 (a-f)) show that the pore system of the reduced catalyst is similar to that of the calcined catalyst, and that the dispersion of nickel particles in the support is non-uniform. Two types of nickel particles are always observed: large nickel particles recrystallized out of the support porosity (Fig. 3.8 a, b); small nickel nanoparticles confined within the support channels (Fig. 3.8 c-f). The size of the observed particles ranges from 5 to 50 nm. The value deduced from high-angle XRD lies in the middle of this range. As shown in the histogram of the particle size distribution of the reduced Ni NPs in Fig. 3.9, the size of most of the Ni particles were in the range of 10-15 nm. Notably, there exists a large population (~ 24%) of small Ni particles with a size less than 10 nm.

3.3.3 Catalytic performances of 15Ni/SBA-15_IWI-MD for HMF hydroconversion

15Ni/SBA-15_IWI-MD was used to determine reaction conditions that would lead to a significant production of DMF and DMTHF from HMF. The catalysis tests were performed in autoclaves in an Autoplant-Chemspeed instrument as described in Chapter 2. 1,4-Dioxane, a stable solvent under the hydrogenation reaction conditions, was selected as the reaction medium in order to avoid the solvent conversion which is normal when using other commonly used solvents (e.g. ethanol and 2-propanol).¹⁶ However, attention should be paid to safety during the operation with 1,4-dioxane due to its toxicity.

In order to find the proper reaction parameters for high DMF/DMTHF yield over 15Ni/SBA-15_IWI-MD, a set of orthogonal experiments were designed. The process parameters (*i.e.*, reaction temperature, H₂ pressure and HMF/Ni molar ratio) and their values were selected on the basis of preliminary studies.¹⁷⁻¹⁹ According to the literature, when the temperature is lower than 180 °C, the hydrogenolysis of the C-O bond leading to DMF/DMTHF becomes difficult. 180 °C was thus selected as the minimum temperature. The selectivity to DMF/DMTHF generally decreases with an increase of temperature, owing to the formation of by-products. When the temperature is above 240 °C, it has little influence on the yield of DMF/DMTHF. Hence, the reaction temperature was set in the range of 180-210-240 °C. The hydrogen pressure was chosen in the range 15-30-45 bar, considering that increasing hydrogen pressure increases the solubility of hydrogen in the solvent, which may benefit the conversion. Maximum DMF/DMTHF yields were obtained below 50 bar in the literature.²⁰ Hence, 45 bar was selected as the maximum pressure level. Besides, since the

conversion of HMF is directly proportional to the amount of active sites available in the reduced catalysts, the HMF/Ni molar ratio was varied in the range of 3-15-30, covering the range of the HMF/Ni molar ratios mentioned in the literature. Once reaction parameters determined, a L9 (3 (levels) ^ 3 (factors: T, P, HMF/Ni molar ratio)) orthogonal array was constructed according to Taguchi method using software Minitab 17. The corresponding parameters are presented in Table 3.2. Then catalysis experiments were then performed accordingly following an identical procedure as described in Chapter 2. The catalysis results of HMF conversion and distribution of main products under different reaction conditions in each catalysis test are summarized in Table 3.2.

Table 3.2 Catalysis conditions and corresponding conversions and product distributions^a

Expt. No.	T/°C	P/bar	HMF/Ni molar ratio	cat./g	conv./%	yield/%				Carbon balance /%
						DMF	DMTHF	MFFR	MFOL	
1	180	15	30	0.052	7.4	1.2	0	1.0	2.4	97
2	180	30	3	0.522	100	0.9	81.4	1.0	1.5	85
3	180	45	15	0.104	33.9	11.5	0	2.0	10.3	90
4	210	15	3	0.522	100	0.8	72.4	1.1	1.2	76
5	210	30	15	0.104	43.8	40.6	1.0	2.1	0	100
6	210	45	30	0.052	21.3	16.8	1.0	1.4	2.1	100
7	240	15	15	0.104	32.0	21.1	2.6	8.2	0	100
8	240	30	30	0.052	11.4	7.1	1.0	1.4	1.9	100
9	240	45	3	0.522	100	0	54.7	1.3	1.1	58

^a: all the catalysis tests were performed in autoclaves in a Autoplant-Chemspeed instrument with 0.15 mmol/mL HMF in 25 mL 1,4-dioxane solution in each reactor for 8 h.

The catalysis experimental results show that: (1) DMF, DMTHF, MFFR and MFOL were detected after reaction for 8 h over 15Ni/SBA-15_IWI-MD with DMTHF and/or DMF as the major products and MFFR and MFOL as the minor products in each test, indicating that the hydrogenolysis of C-OH and/or the furan ring hydrogenation are favored by 15Ni/SBA-15_IWI-MD; (2) low HMF/Ni molar ratios (≤ 15) or large catalyst quantity (≥ 0.052 g) is required for efficient conversion of HMF, indicating the limited activity of 15Ni/SBA-15_IWI-MD; (3) hydrogen pressure in the selected range (15-45 bar) shows weaker influence on the catalytic reactivity as compared to the HMF/Ni molar ratio and the reaction temperature; (4) poor carbon balance occurred on low HMF/Ni molar ratios at high reaction temperatures (Table 3.3, Entry 4 and 9) possibly due to the polymerization of the intermediate products (e.g. BHMF and MFOL).¹⁷

Two test results out of the nine tests are worthy of noting. In Expt. No. 5, a DMF yield of 40.6% at 43.8% HMF conversion was obtained at 210 °C under 30 bar H₂ with a HMF/Ni molar ratio of 15, giving a maximum DMF selectivity (93%) among the selected range of reaction conditions. However, the conversion of HMF is low under this reaction condition due to the low catalyst quantity. Increasing the catalyst quantity can promote the HMF conversion but may also result in decreasing of DMF selectivity at the same time. In Expt. No. 2, a DMTHF yield as high as 81.4% was achieved at 180 °C under 30 bar H₂ with a HMF/Ni molar ratio of 3, suggesting that this reaction condition is suitable for the selective production of DMTHF over 15Ni/SBA-15_IWI-MD. This is a quite interesting result considering that only one report in the literature exhibited similarly high DMTHF yield obtained with Ni-based catalysts.²¹ Moreover, the high DMTHF yield obtained here also indicates the possibility to achieve high yield of DMF under this reaction condition with decreased reaction time, which has not been explored as an affecting factor on HMF conversion and products distributions so far, considering that DMTHF is derived from the furan ring hydrogenation of DMF. Herein, in the next stage of catalysis study, the effect of reaction time on the catalytic performances of 15Ni/SBA-15_IWI-MD was explored.

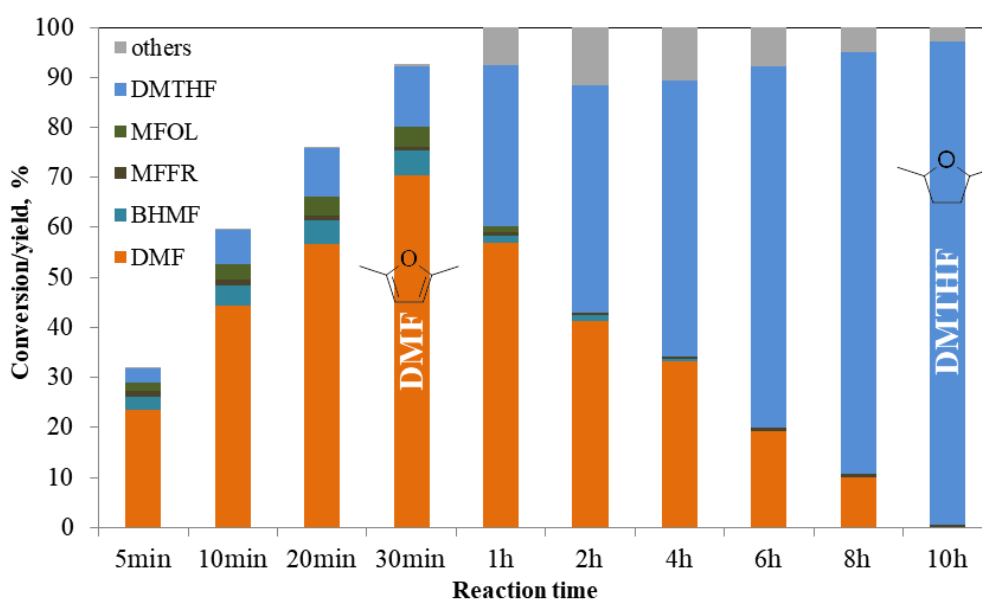
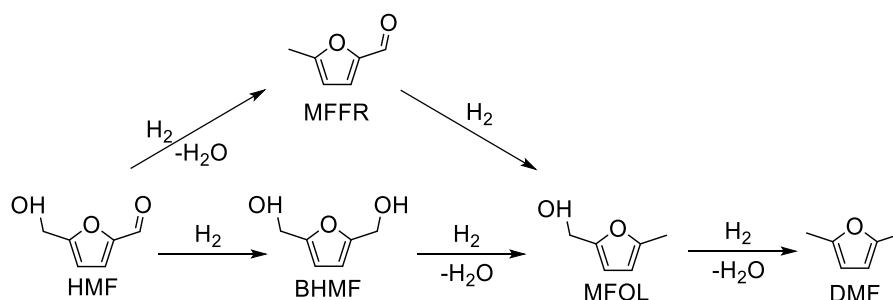


Fig. 3.9 Effect of reaction time on the conversion of HMF (reaction conditions: 0.144 mmol/mL HMF in 12.5 mL 1,4-dioxane, P(H₂) = 30 bar, T = 180 °C, HMF/Ni molar ratio of 3 (corresponding to 0.261 g catalyst))

The time course of HMF hydrogenation over 15Ni/SBA-15_IWI-MD at 180 °C under 30 bar H₂ with a HMF/Ni molar ratio of 3 was performed in a Parr batch reactor. Since the Parr reactor used here has a volume half of the batch reactor used in previous tests for reaction condition screening, the reactant solution volume was decreased by half to 12.5 mL correspondingly while keeping the other parameters unchanged. The detailed procedure of the catalysis tests is described in Chapter 2.



Scheme 3.1 Possible reaction pathways for the formation of DMF from HMF

The evolution of the product distribution with reaction time is shown in Fig. 3.9. It shows that at short reaction time (0.5 h), HMF was primarily converted into DMF (70.5% yield) in a fast way and the yield of DMTHF was just 12.2%. BHMF and MFOL were detected with a yield of 4.9% and a yield of 4.0%, respectively. Almost no MFFR was detected (only 0.8% MFFR yield). Since BHMF could be converted into MFOL and DMF through the selective cleavage of the C-O bond (Scheme 3.1), the conversion of BHMF to MFOL and the hydrogenolysis of MFOL to DMF were the dominating processes during this period. The other possible route for DMF formation via MFFR and MFOL (-CH₂OH hydrogenolysis before -CHO hydrogenation) is negligible. This DMF yield obtained at t = 0.5 h is quite comparable to the results obtained over monometallic Ni-based catalysts reported in the literature, especially considering that most catalytic performances rely on the use of functional supports (Table 3.3, Line 4-5). This suggests that the 15Ni/SBA-15_IWI-MD catalyst simply prepared by mild-drying IW1 using an inert SBA-15 support does own properties of fast hydrogenolysis, selectively forming DMF at short reaction time.

Table 3.4. Catalytic performances of Ni-based catalysts for the conversion of HMF to DMF

Entry	Catalyst	Feed conditions	P (MPa)	T (°C)	t (h)	conv. (%)	yield (%)	ref
1	Raney Ni	12 mmol HMF; 35 mL 1,4-dioxane; 0.5 g catalyst	1.5	180	15	100	88.5	22
2	NiSi-PS ^a	12 mmol HMF; 38 mL 1,4-dioxane; 0.08 g catalyst	1.5	130	3	100	72.9	23
3	NiSi-IMP-20 ^b	12 mmol HMF; 38 mL 1,4-dioxane; 0.08 g catalyst	1.5	130	3	50.9	9	23
4	Ni/CN ^b	2 mmol HMF; 20 mL water; 0.05 g catalyst	3	200	6	>99.9	>98.6	24
5	Ni/LaFeO ₃	1 mmol HMF; 12 mL ethanol; 0.1 g catalyst	5	230	6	>99	98.3	25
6	Ni/C	8 mmol HMF; 100 mL 1-propanol; W/F = 2 g·min/mL	3.3	180	- ^d	92	53	26
7	15Ni_IWI-MD	1.9 mmol HMF; 12.5 mL 1,4-dioxane; 0.052 g catalyst	3	210	8	43.8	40.6	this work
8	15Ni_IWI-MD	1.8 mmol HMF; 12.5 mL 1,4-dioxane; 0.261 g catalyst	3	180	0.5	92.8	70.5	this work

^a: Ni NPs from nickel phyllosilicate; ^b: catalyst prepared by impregnation; ^c: Ni/CN, Ni supported on mesoporous nitrogen-rich carbon; ^d: continuous process.

Prolonging the reaction time to 1 h led to fast decrease of the yield of DMF to 57% and fast increase of the yield of DMTHF to 32.1%. The concentration of BHMF and MFOL had decreased to a negligible level (yields less than 2%). During this period, the main transformation process was shifted to the hydrogenation of the furan ring of DMF to DMTHF. When reaction time was extended to 10 h, the yield of DMTHF continuously increased, reaching 96.6% at complete HMF conversion, at the cost of DMF yield though the reaction rate was slower. Overall, HMF was fast converted into DMF via hydrogenolysis with BHMF and MFOL as main intermediate products, followed by gradual furan ring hydrogenation of DMF to DMTHF. As compared to the reports in the literature, the DMTHF yield afforded here by the 15Ni/SBA-15_IWI-MD catalyst reaches to the top level.²⁰ Only one work reported by Kong et al. in the literature achieved similar result: a bifunctional Ni-Al₂O₃ catalyst (derived from the calcination of hydrotalcite-like precursor at high temperature (850 °C)) afforded a DMTHF yield of 97% at 180 °C under 12 bar with a HMF/Ni molar ratio of 11.²¹ However, the catalytic performance of their catalyst relied on a much longer reaction time (20 h). In total, our sample associating both fast hydrogenolysis of the C-O bonds and full hydrogenation of the furan ring can serve as a simple and efficient catalyst for the selective production of DMTHF from HMF, which is quite comparable with the best catalyst reported in the literature.

3.3.4 Kinetic study

In order to provide a more quantitative analysis of the kinetic curves, a simplified kinetic model was defined, lying on the following hypotheses:

(1) Order with respect to the organic molecules

Based on the related studies in the literature, we will suppose a first order with respect to the concentration of each reactant, and that all reactions are unidirectional.^{26,27} It is also supposed that no inhibition term involving adsorption constants is present in the rate laws.

(2) Order with respect to hydrogen

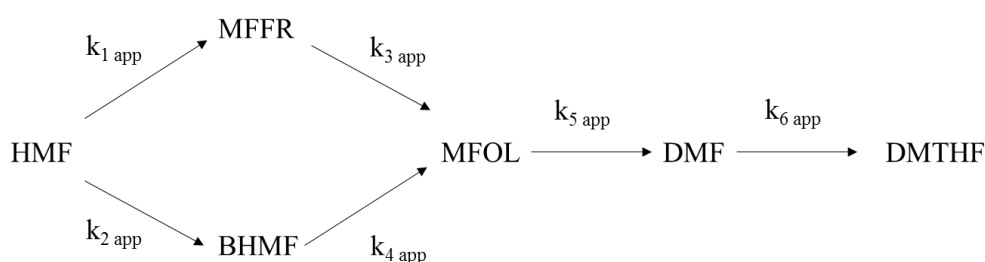
Madon et al. stated that if the rate-determining step involves the dissociative adsorption of H₂, the rate is first-order with respect to the H₂ concentration in the liquid phase.⁵² On the other hand, if the rate-determining step involves reactant species adsorbed on the catalyst surface, the rate should be half-order with respect to the partial pressure of H₂ in the gas phase. In fact, it has generally been supposed that the reaction rate is not expected to be dependent on the liquid-phase H₂ concentration, implying the existence of a zero-order.⁴⁸ In any case, H₂ was always in excess in the selected reaction conditions. The change of the H₂ pressure before and after reaction was measured as small, indicating that H₂ concentration in solution should not vary either. Even though the order is not 0, we will thus consider that the H₂ pressure term is constant and appears as included in the apparent rate constants.

If we suppose that the adsorption of each reactant is described by a Langmuir isotherm, and if the product between the adsorption constant K and of the concentration is small in front of 1, each reaction rate can thus be expressed as $r = k_{app} [\text{reactant}]$, with k_{app} an apparent rate constant being the product of the adsorption constant K, of the true kinetic constant k, and, if the reaction order with respect to H₂ is not 0, of a term containing the constant concentration [H₂].

Finally, the Weisz-Prater number ($N_{W,P}$) was estimated to confirm that the reaction was not affected by pore diffusion limitations. The Weisz-Prater criterion is given by Equation 3.1:²⁸

$$N_{W-P} = \frac{RR_p^2}{D_{eff}C_s} \leq 0.3 \quad \text{Equation 3.1}$$

Where R represents the reaction observed rate (per unit volume of catalyst, 1×10^{-3} mmol mL⁻¹ s⁻¹), R_p is the catalyst particle radius (< 150 μm),²⁹ C_s is the reactant concentration at the external surface of the particle (0.144 mmol/mL), supposed to be equal to the concentration in solution, and D_{eff} is the effective diffusivity in the pore. D_{eff} was estimated to be around 1×10^{-6} m²s⁻¹ which was derived from the pore diameter of the catalyst.²⁷ The Weisz-Prater number was calculated to be less than 1×10^{-4} , which was much smaller than 0.3 therefore verifying the absence of pore diffusion limitations.



Scheme 3.2 Kinetic scheme of the DMTHF production from HMF

The transformation of HMF to DMF and DMTHF is based on the formation of MFOL as an intermediate (Scheme 3.2). It is supposed that the two hydrogenolysis steps take place sequentially, and that the hydrogenolysis of the aldehyde group requires an initial step of hydrogenation to -CH₂OH.³⁰ MFOL itself can be produced following two routes:

- (1) Hydrogenolysis of HMF to MFFR, followed by the hydrogenation of the aldehyde function of MFFR to MFOL.
- (2) Hydrogenation of the aldehyde function of HMF to BHMF, followed by the hydrogenolysis of BHMF to MFOL.

As DMTHF appears in the last stage, once DMF has been produced, we will suppose that the hydrogenation of the furan ring does not take place to a large extent on the minor intermediate products.

When 15Ni/SBA-15_IWIMD is tested at 180 °C, both MFFR and BHMF are detected in small amounts at short reaction times. MFOL appears in parallel to BHMF, and not in a second stage as would be the case if it was produced only from BHMF. It is thus not possible to eliminate one of these two routes *a priori*.

A fitting of the kinetic curve was performed by least-square minimization, according to the following steps:

(1) HMF consumption was fitted using a first-rate law of rate constant ($k_{1\text{ app}} + k_{2\text{ app}}$):

$$[\text{HMF}] = [\text{HMF}]_0 \exp(-((k_{1\text{ app}} + k_{2\text{ app}})t)) \quad \text{Equation 3.2}$$

(2) As a primary intermediate product, MFFR neat production rate was defined as the difference between the production rate $k_{1\text{ app}} [\text{HMF}]$ (HMF being consumed by paths 1 and 2) and the consumption rate $k_{3\text{ app}} [\text{MFFR}]$, leading to

$$[\text{MFFR}] = \frac{k_{1\text{ app}}[\text{HMF}]_0}{k_{3\text{ app}} - (k_{1\text{ app}} + k_{2\text{ app}})} [\exp(-((k_{1\text{ app}} + k_{2\text{ app}})t)) - \exp(-k_{3\text{ app}}t)] \quad \text{Equation 3.3}$$

(3) As a primary intermediate product, BHMF neat production rate was defined as the difference between the production rate $k_{2\text{ app}} [\text{HMF}]$ and the consumption rate $k_{4\text{ app}} [\text{BHMF}]$, leading to:

$$[\text{BHMF}] = \frac{k_{2\text{ app}}[\text{HMF}]_0}{k_{4\text{ app}} - (k_{1\text{ app}} + k_{2\text{ app}})} [\exp(-((k_{1\text{ app}} + k_{2\text{ app}})t)) - \exp(-k_{4\text{ app}}t)] \quad \text{Equation 3.4}$$

A first fitting of HMF consumption, and of MFFR and BHMF neat productions, led to the determination of the 4 first apparent rate constants, from $k_{1\text{ app}}$ to $k_{4\text{ app}}$, and to the calculation of v_1 to v_4 . It appeared that $v_1 = 10 v_2$, and that v_3 was larger than v_4 by a factor 20 to 40. The main production path to MFOL was thus identified as the one involving MFFR.

(4) As a consequence, the neat production of the secondary intermediate, MFOL, was based on the $\text{HMF} \rightarrow \text{MFFR} \rightarrow \text{MFOL}$ pathway, of rate constants $k_{1\text{ app}}$ and $k_{3\text{ app}}$, for the production rate, and $k_{5\text{ app}}$ for the consumption rate, leading to the equation:

$$[\text{MFOL}] = (k_{1\text{ app}}k_{3\text{ app}})[\text{HMF}]_0 \left[\frac{\exp(-k_{1\text{ app}}t)}{(k_{3\text{ app}}-k_{1\text{ app}})(k_{5\text{ app}}-k_{1\text{ app}})} - \frac{\exp(-k_{3\text{ app}}t)}{(k_{1\text{ app}}-k_{3\text{ app}})(k_{5\text{ app}}-k_{3\text{ app}})} + \frac{\exp(-k_{5\text{ app}}t)}{(k_{1\text{ app}}-k_{5\text{ app}})(k_{3\text{ app}}-k_{5\text{ app}})} \right] \quad \text{Equation 3.5}$$

and to the fitting of constant $k_{5\text{ app}}$ along with $k_{1\text{ app}} - k_{4\text{ app}}$.

(5) As DMF is not the final product of reaction, it is not possible to model its production just by subtracting the concentrations of HMF, BHMF, MFFR and MFOL from $[\text{HMF}]_0$. However, BHMF, MFFR and MFOL being formed in very low amounts with respect to DMF and DMTHF, it can be attempted to apply the steady state approximation to these intermediates, and consider that the production rate of DMF is close to the consumption rate of HMF. DMF thus becomes an intermediate between HMF and DMTHF, and its concentration follows the law:

$$[\text{DMF}] = \frac{(k_{1\text{ app}}+k_{2\text{ app}})[\text{HMF}]_0}{k_{6\text{ app}}-(k_{1\text{ app}}+k_{2\text{ app}})} [\exp(-((k_{1\text{ app}}+k_{2\text{ app}})t) - \exp(-k_{6\text{ app}}t))] \quad \text{Equation 3.6}$$

making it possible to fit $k_{6\text{ app}}$ with the other constants.

(6) Finally, DMTHF is calculated as the difference between $[\text{HMF}]_0$, and the concentrations of all the other products, including the unknown ones (implicitly supposing that they derive from the last stages of the global reaction).

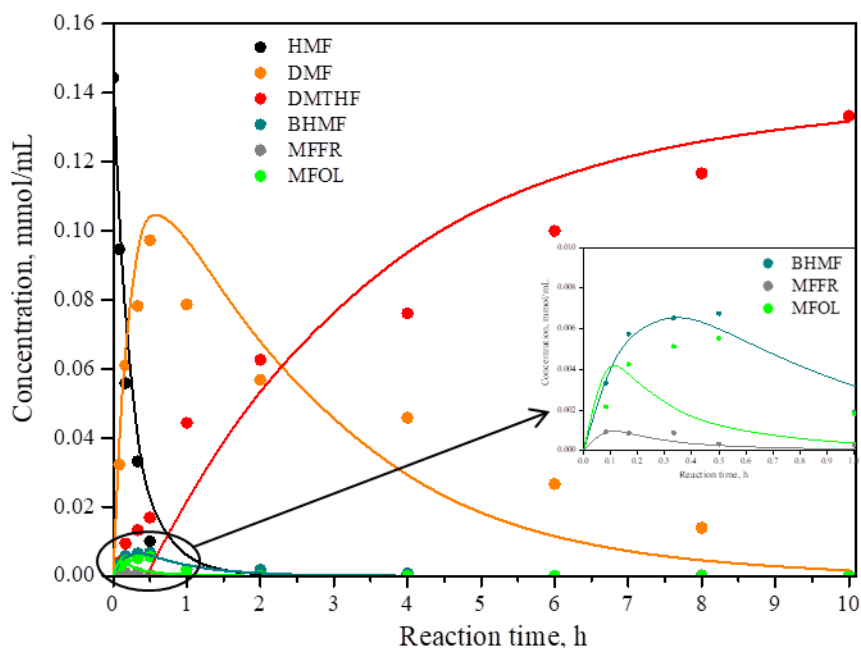


Fig. 3.9 Kinetic patterns of HMF conversion over 15Ni/SBA-15_IWI-MD simulated using KaleidaGraph software, reaction conditions: 0.144 mmol/mL HMF in 12.5 mL 1,4-dioxane, $P(H_2) = 30$ bar, $T = 180$ °C, HMF/Ni molar ratio of 3, data points and solid lines represent experimental data and model, respectively

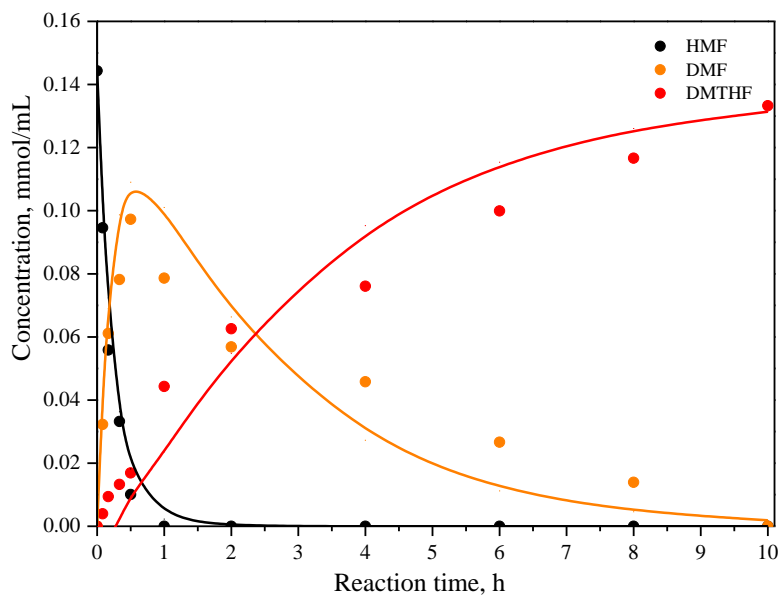


Fig. 3.10 Simulated kinetic patterns based on simplified kinetic model over 15Ni/SBA-15_IWI-MD reaction conditions: 0.144 mmol/mL HMF in 12.5 mL 1,4-dioxane, $P(H_2) = 30$ bar, $T = 180$ °C, HMF/Ni molar ratio of 3, data points and solid lines represent experimental data and model, respectively

After least-square minimization, the values of the six apparent reaction constants are determined as:

$$k_{1 \text{ app}} = 3.6 \text{ h}^{-1} \text{ (hydrogenolysis of } -\text{CH}_2\text{OH in HMF)}$$

$$k_{2 \text{ app}} = 0.4 \text{ h}^{-1} \text{ (hydrogenation of } -\text{CHO in HMF)}$$

$$k_{3 \text{ app}} = 326.9 \text{ h}^{-1} \text{ (hydrogenation of } -\text{CHO in MFFR)}$$

$$k_{4 \text{ app}} = 2.4 \text{ h}^{-1} \text{ (hydrogenolysis of } -\text{CH}_2\text{OH in BHMF)}$$

$$k_{5 \text{ app}} = 82.8 \text{ h}^{-1} \text{ (hydrogenolysis of } -\text{CH}_2\text{OH in MFOL)}$$

$$k_{6 \text{ app}} = 0.5 \text{ h}^{-1} \text{ (hydrogenation of the furan ring of DMF)}$$

The stability of the complete model was tested on a simplified model based on the sole reactions $\text{HMF} \rightarrow \text{DMF} \rightarrow \text{DMTHF}$, in which only two rate constants, $k_{\text{HMF app}} (= k_{1 \text{ app}} + k_{2 \text{ app}})$ and $k_{6 \text{ app}}$ were fitted. The values obtained ($k_{\text{HMF app}} = 4.1 \text{ h}^{-1}$ and $k_{6 \text{ app}} = 0.4 \text{ h}^{-1}$) are in good agreement with those found in the more complex model.

A graphical comparison between the experimental and the modeled concentrations (Fig. 3.10 and 3.11) raises the following comments:

(1) HMF consumption, MFFR production and BHMF production are correctly modeled, in particular the position of the maximum of production of MFFR and BHMF.

(2) In contrast, the production of MFOL is poorly reproduced, as its consumption starts too early. Decreasing $k_{5 \text{ app}}$ shifts the maximum of production to longer times, but also increases considerably the amount of MFOL formed, which means that $k_{3 \text{ app}}$ would also need to be better adjusted. There is thus a large uncertainty on the values of $k_{3 \text{ app}}$ and $k_{5 \text{ app}}$ obtained by this model. A new fitting based only on the concentrations of the minor species led to a decrease of the two rate constants, but at the expense of the quality of the fitting for BHMF. In any case, $k_{3 \text{ app}}$ and $k_{5 \text{ app}}$ were still large compared to $k_{2 \text{ app}}$ and $k_{4 \text{ app}}$.

(3) The fits for DMF and DMTHF follow the same tendency as the experimental data, though at longer times the consumption of DMF and the production of DMTHF are overestimated. Some inhibition phenomena not taken into account in the model can be postulated.

In summary, this probably over-simplified model shows that, globally speaking, both C=O hydrogenation and hydrogenolysis steps are fast compared to the hydrogenation of the furan ring. C-O hydrogenolysis and C=O hydrogenation reactions are in competition. The MFFR route seems to be predominant, confirming the hydrogenolysis properties of Ni. The apparent rate constants of the hydrogenation and hydrogenolysis steps involving intermediates containing a methyl group (MFFR, MFOL) are found to be much larger than the others, suggesting a preferential adsorption of these molecules. However, uncertainties are large concerning the intermediates detected in low amounts and the larger values of k_{app} , so this conclusion should be confirmed by building a more precise kinetic model.

3.4 Conclusion

The use of the IWI-MD method resulted a monometallic 15(wt.%)Ni/SBA-15 catalyst bearing both external and a large population of mesopore-confined NiO particles. Despite the existence of the aggregated metal particles (10-50 nm) as well as some pore blocking by confined particles, the 15Ni/SBA-15_IWI-MD sample after activation is able to afford a DMF yield of 70.5% at short reaction time (0.5 h) and a DMTHF yield of 96.6% at long reaction time (10 h) under optimized reaction conditions (180 °C, 30 bar), exhibiting a fast hydrogenolysis ability and a high ability of the furan ring hydrogenation. The kinetic study implied that HMF was probably converted via the route with MFFR as an intermediate product. The competitive reactions, i.e. C-O hydrogenolysis and C=O hydrogenation, are fast as compared to the furan ring hydrogenation.

Reference

1. Sietsma, J. R. A. *et al.* Ordered Mesoporous Silica to Study the Preparation of Ni/SiO₂ ex Nitrate Catalysts: Impregnation, Drying, and Thermal Treatments. (2008). doi:10.1021/cm702610h
2. Prieto, G., Zečević, J., Friedrich, H., Jong, K. P. de & Jongh, P. E. de. Towards stable catalysts by controlling collective properties of supported metal nanoparticles. *Nat. Mater.* **12**, 34–39 (2013).
3. Munnik, P., de Jongh, P. E. & de Jong, K. P. Recent Developments in the Synthesis of Supported Catalysts. *Chem. Rev.* **115**, 6687–6718 (2015).
4. Sietsma, J. R. A. *et al.* Ordered Mesoporous Silica to Study the Preparation of Ni/SiO₂ ex Nitrate Catalysts: Impregnation, Drying, and Thermal Treatments. *Chem. Mater.* **20**, 2921–2931 (2008).
5. Toupance, T., Kermarec, M. & Louis, C. Metal Particle Size in Silica-Supported Copper Catalysts. Influence of the Conditions of Preparation and of Thermal Pretreatments. *J. Phys. Chem. B* **104**, 965–972 (2000).
6. Ungureanu, A. *et al.* Synthesis of highly thermostable copper-nickel nanoparticles confined in the channels of ordered mesoporous SBA-15 silica. *J. Mater. Chem.* **21**, 12529–12541 (2011).
7. Soler-Illia, G. J. de A. A., Crepaldi, E. L., Grosso, D. & Sanchez, C. Block copolymer-templated mesoporous oxides. *Curr. Opin. Colloid Interface Sci.* **8**, 109–126 (2003).
8. Taguchi, A. & Schüth, F. Ordered mesoporous materials in catalysis. *Microporous Mesoporous Mater.* **77**, 1–45 (2005).
9. Cassiers, K. *et al.* A Detailed Study of Thermal, Hydrothermal, and Mechanical Stabilities of a Wide Range of Surfactant Assembled Mesoporous Silicas. *Chem. Mater.* **14**, 2317–2324 (2002).
10. Kong, X. *et al.* Ni Nanoparticles Inlaid Nickel Phyllosilicate as a Metal–Acid Bifunctional Catalyst for Low-Temperature Hydrogenolysis Reactions. *ACS Catal.* **5**, 5914–5920 (2015).

11. Thielemann, J., Girgsdies, F., Schlögl, R. & Hess, C. Pore structure and surface area of silica SBA-15: Influence of washing and scale-up. *Beilstein J. Nanotechnol.* **2**, 110–8 (2011).
12. Voort, P. V. D. *et al.* Plugged hexagonal templated silica: a unique micro- and mesoporous composite material with internal silica nanocapsules. *Chem. Commun.* **0**, 1010–1011 (2002).
13. Robertson, S. D., McNicol, B. D., De Baas, J. H., Kloet, S. C. & Jenkins, J. W. Determination of reducibility and identification of alloying in copper-nickel-on-silica catalysts by temperature-programmed reduction. *J. Catal.* **37**, 424–431 (1975).
14. Brown, R., Cooper, M. E. & Whan, D. A. Temperature programmed reduction of alumina-supported iron, cobalt and nickel bimetallic catalysts. *Appl. Catal.* **3**, 177–186 (1982).
15. Louis, C., Cheng, Z. X. & Che, M. Characterization of nickel/silica catalysts during impregnation and further thermal activation treatment leading to metal particles. *J. Phys. Chem.* **97**, 5703–5712 (1993).
16. Seemala, B., Cai, C. M., Wyman, C. E. & Christopher, P. Support Induced Control of Surface Composition in Cu–Ni/TiO₂ Catalysts Enables High Yield Co-Conversion of HMF and Furfural to Methylated Furans. *ACS Catal.* 4070–4082 (2017). doi:10.1021/acscatal.7b01095
17. Nakagawa, Y., Tamura, M. & Tomishige, K. Catalytic Reduction of Biomass-Derived Furanic Compounds with Hydrogen. *ACS Catal.* **3**, 2655–2668 (2013).
18. Hu, L., Lin, L. & Liu, S. Chemoselective Hydrogenation of Biomass-Derived 5-Hydroxymethylfurfural into the Liquid Biofuel 2,5-Dimethylfuran. *Ind. Eng. Chem. Res.* **53**, 9969–9978 (2014).
19. Hu, L. *et al.* Catalytic conversion of biomass-derived carbohydrates into fuels and chemicals via furanic aldehydes. *RSC Adv.* **2**, 11184–11206 (2012).
20. Chen, S., Wojcieszak, R., Dumeignil, F., Marceau, E. & Royer, S. How Catalysts and Experimental Conditions Determine the Selective Hydroconversion of Furfural and 5-

Hydroxymethylfurfural. *Chem. Rev.* **118**, 11023–11117 (2018).

21. Kong, X. *et al.* Rational design of Ni-based catalysts derived from hydrotalcite for selective hydrogenation of 5-hydroxymethylfurfural. *Green Chem.* **17**, 2504–2514 (2015).

22. Kong, X. *et al.* Switchable synthesis of 2,5-dimethylfuran and 2,5-dihydroxymethyltetrahydrofuran from 5-hydroxymethylfurfural over Raney Ni catalyst. *RSC Adv.* **4**, 60467–60472 (2014).

23. Kong, X. *et al.* Ni Nanoparticles Inlaid Nickel Phyllosilicate as a Metal–Acid Bifunctional Catalyst for Low-Temperature Hydrogenolysis Reactions. *ACS Catal.* **5**, 5914–5920 (2015).

24. Goyal, R. *et al.* Studies of synergy between metal–support interfaces and selective hydrogenation of HMF to DMF in water. *J. Catal.* **340**, 248–260 (2016).

25. Chen, M. Y., Chen, C.-B., Zada, B. & Fu, Y. Perovskite type oxide-supported Ni catalysts for the production of 2,5-dimethylfuran from biomass-derived 5-hydroxymethylfurfural. *Green Chem.* **18**, 3858–3866 (2016).

26. Luo, J. *et al.* Comparison of HMF hydrodeoxygenation over different metal catalysts in a continuous flow reactor. *Appl. Catal. Gen.* **508**, 86–93 (2015).

27. Liu, Y., Mellmer, M. A., Alonso, D. M. & Dumesic, J. A. Effects of Water on the Copper-Catalyzed Conversion of Hydroxymethylfurfural in Tetrahydrofuran. *ChemSusChem* **8**, 3983–3986 (2015).

28. Weisz, P. B. & Prater, C. D. Interpretation of Measurements in Experimental Catalysis. in *Advances in Catalysis* (eds. Frankenburg, W. G., Komarewsky, V. I. & Rideal, E. K.) **6**, 143–196 (Academic Press, 1954).

29. Data taken from the following:
<https://www.sigmaaldrich.com/catalog/product/aldrich/806854?lang=fr®ion=FR>
(accessed Jan 21, 2019).

30. Zhu, Y. *et al.* Efficient synthesis of 2,5-dihydroxymethylfuran and 2,5-dimethylfuran from 5-hydroxymethylfurfural using mineral-derived Cu catalysts as versatile catalysts. *Catal Sci Technol* **5**, 4208–4217 (2015).

**CHAPTER 4: TUNING THE DISPERSION
AND CATALYTIC PERFORMANCES OF Ni
PARTICLES BY CHANGING THE SECONDARY
POROSITY OF SBA-15**

4.1 Introduction

In order to prepare highly efficient and stable non-noble metal-based catalysts, one must pay attention to the dispersion of metal NPs and to their interaction with the supports. One of the most efficient and direct strategies to improve dispersion and thermal stability of NPs is to confine them inside the pore channels of mesoporous scaffolds, in order to mitigate particle growth.^{1,2} The mesoporous materials act as: *(i)* nanoreactors to spatially confine NPs and suppress their growth; *(ii)* modulators of the metal (oxide)-support interactions to suppress sintering. Such catalysts are renowned as superior catalytic systems regarding their catalytic activity, selectivity and reusability.³⁻⁵ This goal can be achieved via common catalyst preparation procedures, such as the impregnation method.⁶⁻⁸ However, as seen in the previous chapter, there are some limits when using impregnation: *(i)* NPs are still relatively large, because the size is close to the mesopore diameter (~8 nm in the case of SBA-15); *(ii)* some pore plugging occurs, that could result in inaccessible catalytic centers, decreased activity and significant mass-transfer resistances; *(iii)* in some cases, large aggregates are formed outside the mesopores, leading to a dispersion of metal particles poorer than expected.

Less often used for the preparation of pore-confined non-noble metal NPs is melt infiltration (MI).⁹ In contrast with impregnation, for which a solution of precursor is used and the solvent (usually water) can diffuse out of the porosity during drying, MI consists of blending the support and the precursor(s) in solid form, followed by a heating of the mixture in a closed vessel, during which the molten precursor diffuses into the porosity of the support.^{9,10,11-15} It is a solvent-free, green synthesis procedure, and MI is followed by calcination without the need for an intermediate drying step. The control of the final dispersion for MI-derived materials can be achieved by changing several parameters, such as the nature and structure of the support and the duration of infiltration.¹⁶ Ordered mesoporous silica scaffolds have been used as supports for MI (MCM-41, KIT-6, SBA-15), based on their high surface area and abundant surface silanol groups, which favor an improved wettability of the support by the molten phase.¹⁷⁻²⁰

Nevertheless, when confined in mesopores, the size of non-noble metal NPs remains close to that of the support pore diameter.²¹⁻²³ In contrast, the dispersion of non-noble metal NPs can be significantly improved when the infiltration is performed on the uncalcined SBA-15 support still containing the surfactant porogen in the pores (i.e. Pluronic P123 copolymer),

which reduces the available space inside the mesopores and forces the metal precursor to diffuse along the silica pore walls and to migrate into the microporosity.²³ Based on this strategy, homogeneously dispersed NiO particles could be formed in an uncalcined SBA-15 support, with a particle size lower than 2 nm.¹⁶ On the other hand, the infiltration of the molten phase is more difficult and slower into micropores/intra-wall pores than into large mesopores, which makes the infiltration time another important factor affecting the dispersion of the metal NPs. Long infiltration time will facilitate the complete infiltration of the molten phase into the intra-wall pores, and thus will increase the dispersion of metal particles.¹⁶

Indeed, one of the remarkable properties of SBA-15-type supports is the existence of a hierarchical microporous-mesoporous architecture, and the possibility to control the secondary intra-wall porosity (IWP) generated by the removal of ethyleneoxide segments from the Pluronic P123 surfactant, simply by changing the hydrothermal (aging) temperature, or by using swelling agents.²⁴⁻²⁸ In particular, playing on the temperature of aging is an effective way to change the secondary porosity from ultramicroporosity (pore size < 1 nm) to secondary mesoporosity, as well as the degree of pore interconnectivity.²⁴⁻²⁷ The IWP can significantly contribute to the total pore volume of the host material and provide a unique, *yet incompletely explored*, confinement space for encapsulating NPs of a very small size. In principle, interconnected micro-mesoporous channels in SBA-15 should facilitate the mass-transfer of molten precursors to the support internal surface, and of reactants toward the metal particles, and suppress the growth of metal particles during the thermal steps. In summary, IWP could thus determine: (i) the final dispersion of the metal phase, (ii) its thermal resistance to sintering, and as consequence (iii) the catalytic properties for hydrogenation reactions.

In this chapter, we investigate the impact of the secondary porosity of SBA-15 on the infiltration efficiency of molten nickel precursor in the pores occluded with the Pluronic P123 surfactant, and thus on the Ni dispersion over the SBA-15 supports bearing different secondary porosities due to different aging times of SBA-15. The purpose of this chapter is to obtain well-dispersed Ni/SBA-15 catalysts compared with the catalyst described in the former chapter, to correlate the properties of the secondary porosity of SBA-15 with Ni dispersion, and to study the application potential of the resulting monometallic Ni/SBA-15 catalysts in typical hydroconversion reactions. Three types of SBA-15 silica were synthesized in order to obtain different degrees of interconnectivity between the main mesopores. The

impact of the SBA-15 pore characteristics, *i.e.*, the interconnectivity of the pores, or the presence of a secondary intra-wall porosity, on the final nickel (oxide) NPs size and localization, has been investigated via various characterization methods such as nitrogen physisorption, X-ray diffraction (XRD), temperature programmed reduction by hydrogen (H_2 -TPR) and transmission electron microscopy (TEM). The obtained materials were tested, after reduction, in the hydrogenation of cinnamaldehyde (CNA) and HMF.

4.2. Catalyst preparation

Three supports were synthesized according to a classical procedure.²⁹ The aging temperature was varied in order to reach different secondary porosities.^{24,25} 4 g Pluronic P123 were dissolved into a 1.6 M solution of HCl at 40 °C, followed by adding 8.5 g of TEOS dropwise to the solution. The solution was then stirred for 24 h. The resulting gel was submitted for 48 h to hydrothermal aging, at 60, 100 or 140 °C. After recovering by filtration, the SBA-15 samples were washed with water, and dried at 100 °C for 24 h. *The dried SBA-15 samples were the materials used for the melt infiltration procedure.* However, for characterization purpose, parts of the different supports were calcined at 550 °C for 6 h in a muffle furnace, using a heating ramp of 1.5 °C·min⁻¹. The calcined supports were named SBA-15_T (T, aging temperature = 60, 100 or 140 °C).

The nickel catalysts were prepared by melt infiltration. In a typical preparation of 1 g catalyst, 0.5 g of nickel nitrate $Ni(NO_3)_2 \cdot 6H_2O$ (99%, Sigma-Aldrich) (mass calculated to obtain 10 wt.% of Ni in the final material) was ground and mixed with 0.9 g dried SBA-15. The mixture was heat-treated at 57 °C in a Teflon autoclave for 4 days in order to ensure the complete diffusion of the molten phase into the secondary porosity.¹⁶ Once the diffusion step was completed, the solid was calcined under static conditions at 500 °C for 5 h, using a heating rate of 1.5 °C·min⁻¹. The calcined materials (NiO/SBA-15) prepared using the different dried SBA-15 supports were named Ni_T, where T was the temperature at which the support was aged (60, 100 or 140 °C).

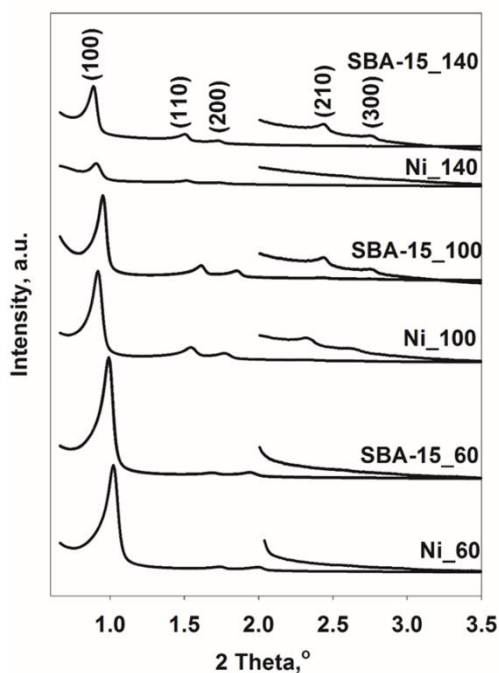


Fig. 4.1 Low-angle XRD patterns recorded for SBA-15_T supports and Ni_T materials in a calcined form (Cu K α source): SBA-15_T, SBA-15 aged at T = 60, 100, 140 °C; Ni_T – calcined NiO/SBA-15 using supports aged at T = 60, 100, 140 °C

4.3. Results and discussion

4.3.1 Pore periodicity in SBA-15 supports and NiO/SBA-15 materials

The low angle XRD patterns recorded for the SBA-15_T calcined supports are presented in Fig. 4.1. The three diffractograms show the main peaks associated to the (100), (110) and (200) lattice reflections of an ordered hexagonal pore structure with $P6mm$ symmetry. This indicates a regular mesostructure ordering for the three supports.^{30–32} The presence of (210) and (300) reflections at $2\theta > 2^\circ$, for materials synthesized at aging temperature above 100 °C, are evidence of an excellent textural uniformity in SBA-15_100 and SBA-15_140.

The evolution of the mesostructure geometric characteristics is directly reflected by the changes in the reflection positions, from which one can identify the modification of interplanar spacing “ d ”, of the cell parameter “ a ” = $2d/\sqrt{3}$, and of the wall thickness and main mesopore diameter. When the aging temperature was increased from 60 to 140 °C, the (100) reflection shifted to lower values of 2θ , giving a cell parameter increasing from 10.2 to 11.4 nm (Table 4.1). This increase mostly comes from the P123 micelle size dilatation with the increasing temperature of aging.²⁴

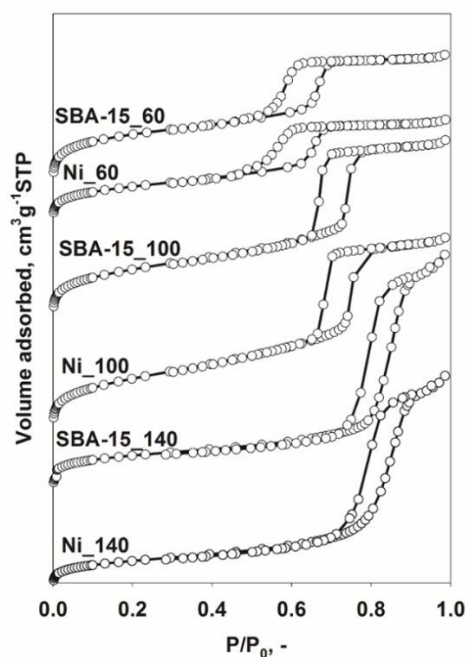


Fig. 4.2 N_2 physisorption isotherms recorded for SBA-15_T supports and Ni_T materials in calcined form: SBA-15_T, SBA-15 aged at $T = 60, 100, 140$ °C; Ni_T - calcined NiO/SBA-15 using supports aged at $T = 60, 100, 140$ °C

After introduction of the nickel oxide phase (Ni_T samples), only few modifications are visible on the diffractograms (Fig. 4.1). As a first remark, the persistence of the three major reflections confirms the maintaining of the pore ordering after melt infiltration and thermal decomposition of the precursor to form NiO. A decrease in the reflection intensities is observed, which could be explained by the specific localization of the NiO NPs inside the support pores that become filled, thus reducing the electron density contrast between the pores and silica walls.³³ Very small changes in cell parameter values are also measured between the calcined support and the corresponding calcined NiO material (Table 4.1). In fact, the ± 0.3 nm fluctuation of the values is in the experimental error range, which suggests that no significant modification of the hexagonal cell occurs when the MI procedure is performed, and that the materials prepared by the MI process possess structures comparable with those of the pristine SBA-15 supports.

4.3.2 Textural properties of SBA-15 supports and evolution in NiO/SBA-15 materials

The textural properties extracted from nitrogen physisorption experiments are gathered in Table 4.1, while the isotherms are presented in Fig. 4.2.

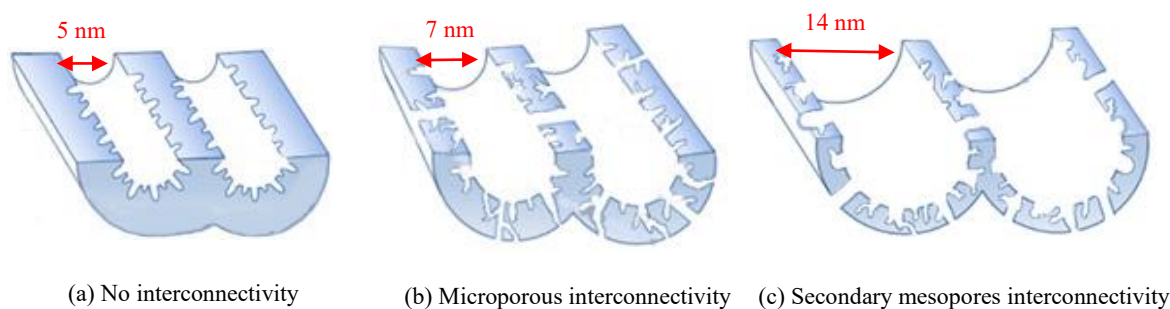
Table 4.1. Textural and structural properties of the synthesized materials

Sample	S_{BET}^a $m^2.g^{-1}$	S_{μ}^b $m^2.g^{-1}$	V_p^c $cm^3.g^{-1}$	V_{μ}^d $cm^3.g^{-1}$	D_p^e nm	a_0^f nm	d_{NiO} / nm	
							XRD	TEM
SBA-15_60	765	291	0.71	0.128	5.4	10.2	-	-
Ni_60	483	151	0.50	0.067	5.4	9.9	8.5	- ^g
SBA-15_100	673	116	0.91	0.050	6.8	10.6	-	-
Ni_100	589	59	0.82	0.020	6.3	10.9	n.d.	2.1
SBA-15_140	361	68	1.10	0.030	14.0	11.4	-	-
Ni_140	315	58	0.92	0.027	13.7	11.1	3.5	3.1

^a: B.E.T. surface area per gram of SBA-15 support; ^b: microporous surface area per gram of SBA-15 support; ^c: total pore volume per gram of SBA-15 support; ^d: micropore volume per gram of SBA-15 support; ^e: B.J.H. mean pore size; ^f: unit cell parameter; n.d.: not detectable; ^g: the average particle size is difficult to obtain since particles appear as aggregated.

For all samples, N₂ adsorption-desorption isotherms recorded on supports, as well as NiO/SBA-15 systems (Ni_T materials), are of type IV (Fig. 4.2), already described in the section dedicated to 15Ni/SBA-15_IWIMD (Chapter 3, Section 3.2.1). For the bare supports, the hysteresis position is significantly affected by the aging temperature: an increase from 60 to 140 °C leads to a marked shift of the hysteresis position to higher relative pressures (P/P₀). This evolution indicates a significant change in the pore diameter, as it can be confirmed following the evolution of the B.J.H. pore diameter (D_p, Table 4.1), which increases from 5.4 (SBA-15_60) to 14.0 nm (SBA-15_140). Comparing these values with those obtained for Ni_T materials, it appears that the MI process has very limited effect on the mesopore size, confirming data issued from low-angle XRD. A hysteresis of H1-type (parallel and vertical adsorption and desorption branches, Fig. 4.2) is still present between the adsorption and the desorption branches of the isotherms. Consequently, after MI and further calcination for NiO formation, the supports retain their ordered structure, whatever the aging temperature.

Besides the pore diameter, B.E.T. surface area, microporous surface area, and total pore volume are also significantly affected by the aging temperature (Table 4.1). As can be expected from the pore diameter increase at increased aging temperature, the pore volume also increases (from 0.71 to 1.10 cm³.g⁻¹), while the surface area decreases (from 765 to 361 m²/g). At the same time, some fluctuations of the microporous characteristics of the materials are observed, reflecting the changes in the properties of the secondary porosity.



Scheme 4.1 Porosity of SBA-15 supports aged: (a) at 60 °C; (b) at 100 °C; (c) at 140 °C³⁴

At low aging temperature (60 °C), a significant proportion of micropore forms, with a S_{μ} of 291 m²/g and a V_{μ} of 0.128 cm³/g. At this aging temperature, it was previously reported that SBA-15 presents small mesopores and thick walls (comparable to the distance between consecutive hydrated micelles in water, ~ 4 nm), and ultramicropores as well (see Scheme 4.1 (a)).^{35,36} The wall thickness obtained by comparing D_p and a (between 4.5 and 5 nm) is thus consistent with the values from the literature. As the silica walls may replicate the topology of the hydration shells of the PEO chains in water, at a temperature of aging of 60 °C, no micropores bridging the main mesopores are expected.²⁴

After aging at 100 °C, the P123 mesophase is modified since the temperature exceeds the cloud point of the surfactant (~ 90 °C).³⁷ Under such conditions, a decrease in the strength of interaction between the surfactant and the inorganic matter results in the densification of the walls. The resulting SBA-15_100 consequently presents larger mesopores and thinner silica walls (see Scheme 4.1 (b)). The wall thickness obtained by comparing D_p and a in Table 4.1 (between 3.8 and 4.5 nm) is smaller than the one calculated for the systems aged at 60 °C. The presence of a secondary porosity is the result of the collapse of the ultramicropores (decrease of S_{μ} and V_{μ} , Table 4.1). In this case, micropores and small mesopores connecting the adjacent mesopores are expected, with sizes in the range of 1.5-4 nm.^{24,25}

Finally, when the aging temperature is increased to 140 °C, the destabilization of the corona of PEO due to the loss of hydration H₂O at high temperature results in a decreased micelle surface/silica interaction.³⁷ Equally, densification of the silica walls brings about an important decrease in the wall thickness and microporous volume (Table 4.1 and Scheme 4.1 (c)). SBA-15_140 presents therefore large mesopores (in our case, 14.0 nm), separated by 2 nm-thick silica walls, and being crossed by a secondary porosity spanning from 1.5 to 5 nm.²⁴ The fact that the pore diameter appears as larger than the unit cell parameter in Table 4.1 may be due to uncertainties in the determination of a and does not allow calculating a wall thickness.

After the MI process, the NiO-containing materials exhibit slightly different textural properties. The most important differences are noticed between SBA-15_60 and Ni_60, with decreases of S_{BET} (-37%) and V_p (-30%), associated with important decreases in microporous surface area (-48%) and volume (-48%). Remarkably, in the case of the Ni_100 and Ni_140 samples, the variations of surface area and pore volume are overall below 10%. Only an important decrease of the microporous surface is measured between SBA-15_100 and Ni_100, of around 49 % (Table 4.1).

4.3.3. Support morphology, localization and size of NiO NPs

Representative micrographs obtained for Ni_60 are presented in Fig. 4.3. It is evident that most of the NiO NPs appear located around the silica grains (Fig. 4.3(a)), in the form of large aggregates of smaller particles (Fig. 4.3(c)). Analysis of the images allows one to plot a particle size histogram (Fig. 4.3(d)). Elementary particles constituting the external aggregates are of large size, most of them being larger than 10 nm. High magnification observation on the silica grain evidences the formation of some small NPs located inside the pores, with a size below 5 nm (Fig. 4.3(b) and (c)). The fraction of this small-size particle population amounts to approximately 15%, confirming that most of NiO is present as external phases. Consequently, these results show that melt infiltration does not allow obtaining NPs homogeneously dispersed inside the silica grains when the SBA-15_60 support is used.

Low magnification images of the Ni_100 sample (Fig. 4.4(a)-(c)) are completely different from those acquired on Ni_60. Indeed, no extra-porous oxide phases can be detected, despite the similar nickel loading. Increasing the magnification allows distinguishing the mesopores (Fig. 4.4(b), (c)) which are free of NPs, as usually observed when classical IWI or MI procedures are applied for the preparation (see the former chapter, ~10 nm in size, and cited references).^{16,17,33,38,39} Remarkably, very small NPs are observed inside the silica walls (Fig. 4.4(b), (c)). The statistical measurements (Fig. 4.4(d)) show that NiO particles are exclusively below 3 nm in size, 90 % of them being 2 nm large (average size of 2.1 nm, Table 4.1). Consequently, for the support obtained at 100 °C, the MI approach is highly efficient to encapsulate small NiO NPs inside the pores of SBA-15, with a very homogeneous distribution, in contrast with SBA-15_60.

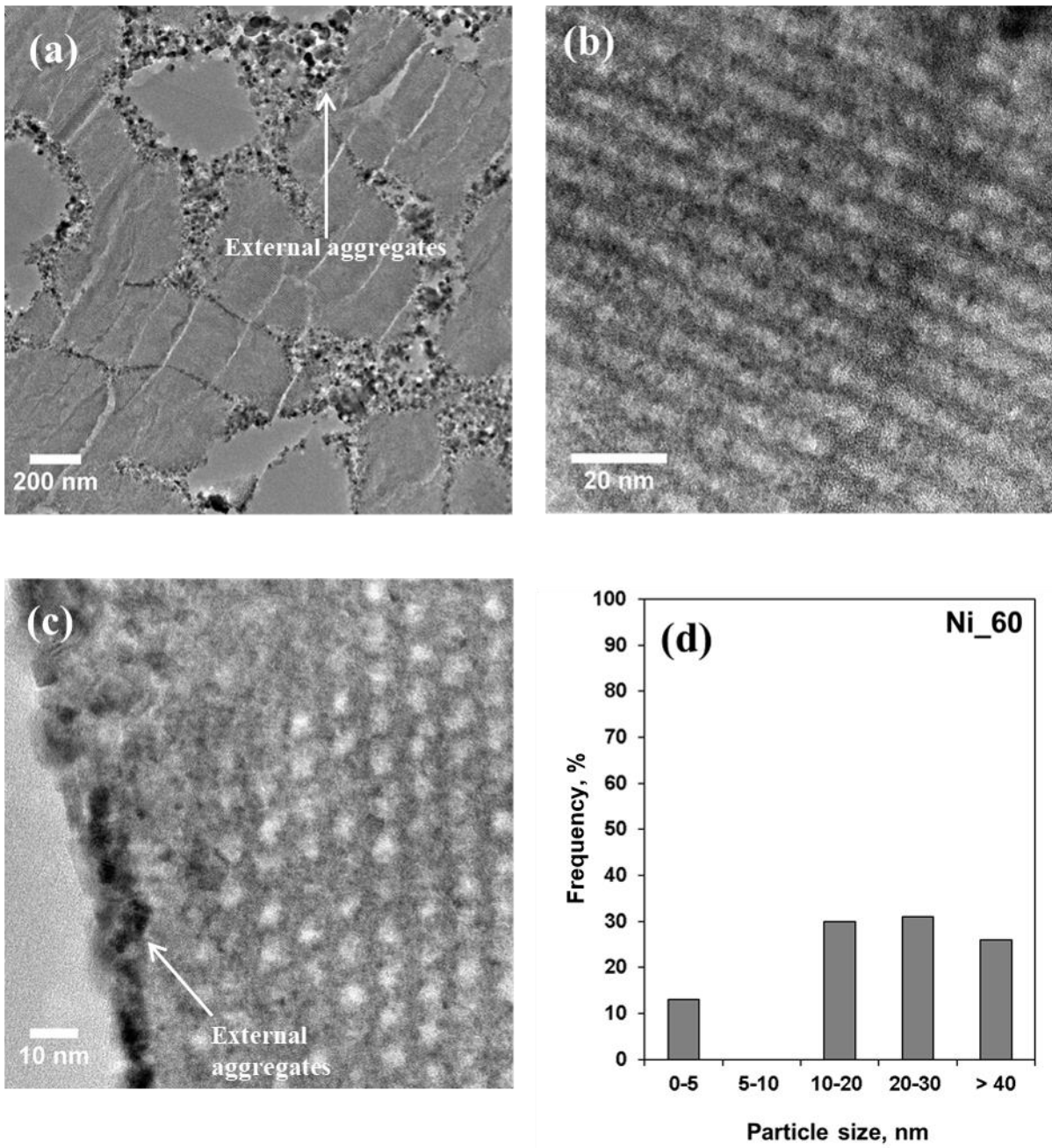


Fig. 4.3 (a)-(c): Selected TEM images obtained for Ni-60 (Ni_60, calcined NiO/SBA-15 using supports aged at 60 °C);
 (d): NiO Particle size distribution in Ni_60

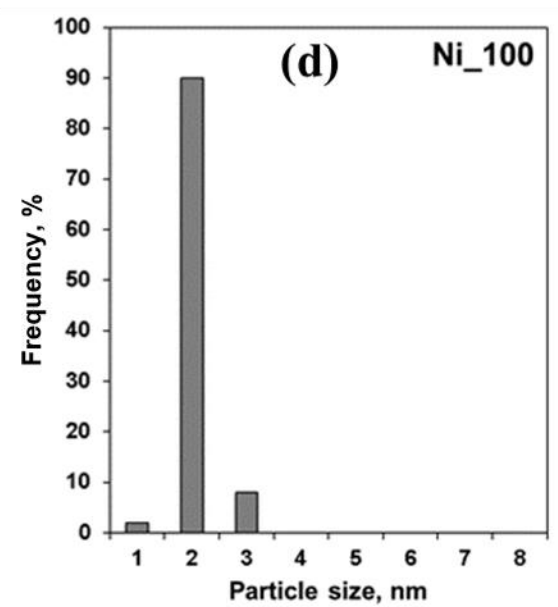
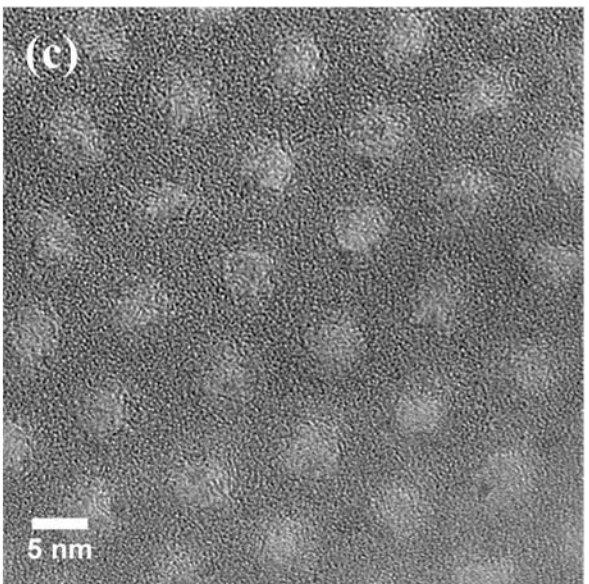
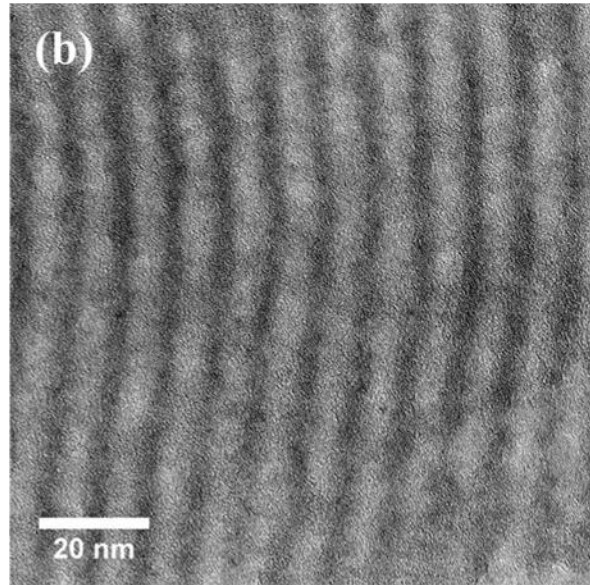
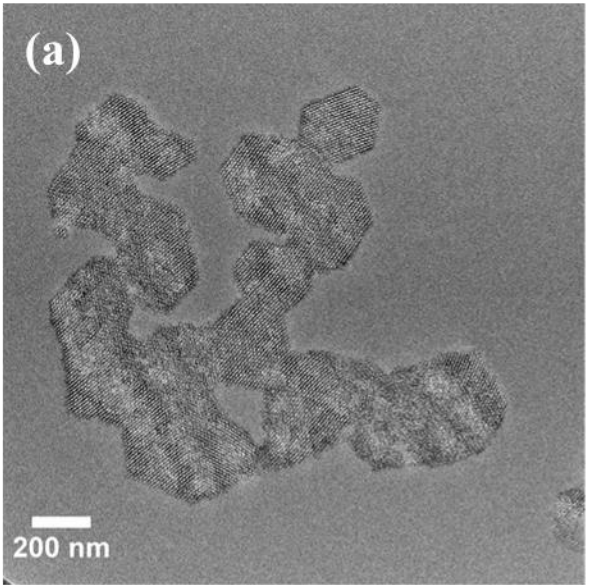


Fig. 4.4 (a)-(c): Selected TEM images for Ni₁₀₀ (Ni₁₀₀, calcined NiO/SBA-15 using supports aged at 100 °C);
(d) NiO Particle size distribution in Ni₁₀₀

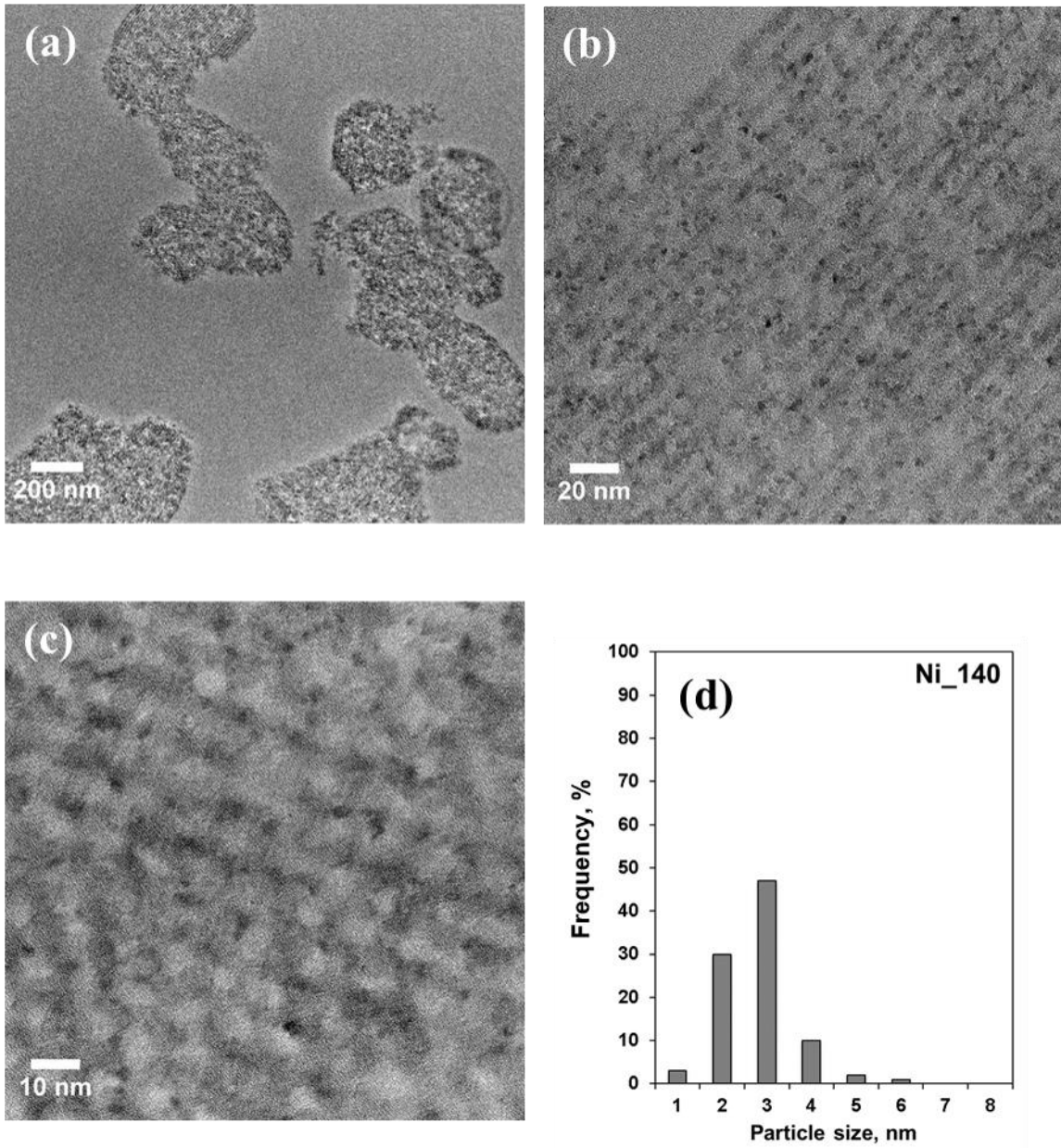


Fig. 4.5 Selected TEM images for Ni_140 materials (calcined NiO/SBA-15 using supports aged at 140 °C);

(d) NiO Particle size distribution in Ni_140

Finally, Fig. 4.5 shows the results obtained for Ni_140. Low magnification image (Fig. 4.5(a)) and high magnification images (Fig. 4.5(b), (c)) evidence a morphology comparable with that of Ni_100: *(i)* absence of external NiO NPs, *(ii)* absence of plugging by mesopore-confined NiO NPs, and *(iii)* formation of small NPs with a size largely below the main mesopore size, and relatively homogeneously distributed throughout the silica grains. The main difference between Ni_140 and Ni_100 resides in the size of the NPs produced, which are observed to be non-uniform (Fig. 4.5(d), with an average size measured at 3.1 nm (Table 4.1). It can be concluded that, similarly to SBA-15_100, the MI approach is efficient to disperse NiO in SBA-15_140 support, and that the particle size is essentially controlled by the intra-wall pore dimensions.

These results clearly show the lack of dispersion efficiency in the case of SBA-15_60, and the difference in NiO NPs size obtained over SBA_100 and SBA_140 supports. They can be rationalized by taking into consideration the different textural properties and pore architectures for the distinct SBA-15 host materials. SBA-15_60 is the only support in the series showing non-interconnected mesoporosity,⁴⁰ and we have observed that the diffusion of the molten precursor is not efficient. Such problem is not encountered for the other two SBA-15 supports synthesized at higher aging temperature, which display interconnected mesoporosity. In these cases, the infiltration of the molten phase inside the pores of the scaffolds is efficient and complete (Ni_100 and Ni_140, Fig. 4.4 and 4.5).

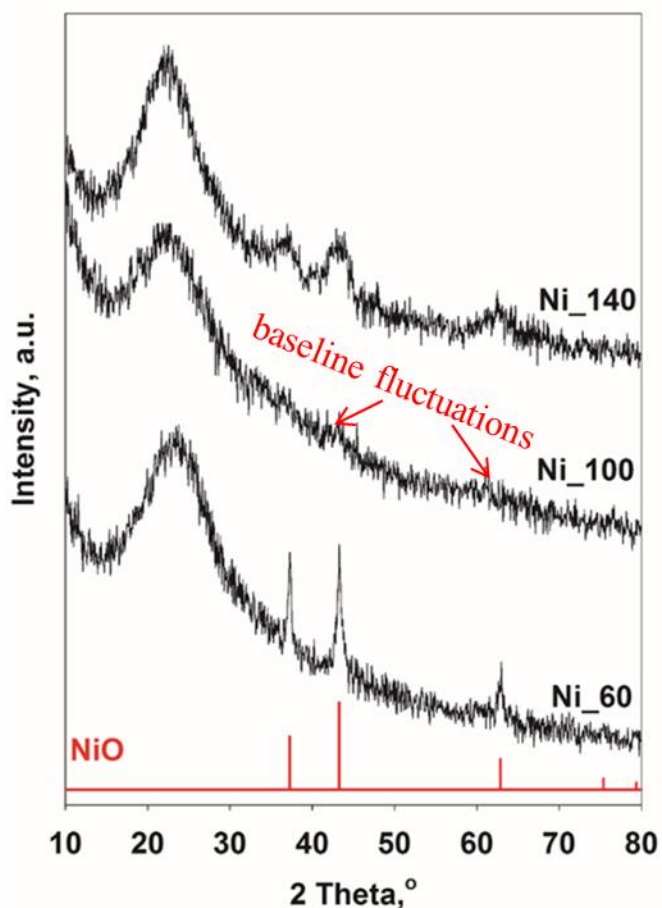


Fig. 4.7 Wide-angle X-ray diffraction patterns obtained for Ni_T materials (Ni_T, calcined NiO/SBA-15 using supports aged at T = 60, 100, 140 °C; Bottom: NiO, JCPDS file n°47-1049)

At the same time, as the support of Ni₁₄₀ was aged at a higher temperature than Ni₁₀₀, the secondary pores have increased in size, and evolved from micropores to small mesopores. The parallel evolution of the mean NiO NPs size deduced from Fig. 4.7 (high-angle X-ray diffraction) follows this trend, which is in line with the fact that NiO NPs are confined inside the intra-wall porosity. Reflections ascribed to the NiO phase are only observed for Ni₆₀ and Ni₁₄₀. The average crystal domain size calculated by the Scherrer equation is 8.5 and 3.5 nm, respectively. For Ni₁₀₀, NiO is not detected by XRD, yet some fluctuations in the baseline are observed at positions corresponding to NiO. This might confirm that in this case NPs are highly dispersed, in agreement with TEM analysis (Fig. 4.4).

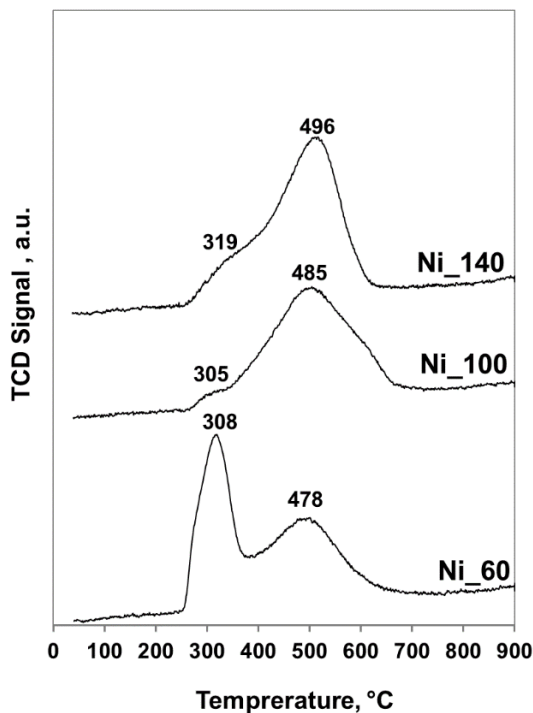


Fig. 4.8 H₂-TPR profiles recorded for the MI-derived materials (Ni_T, calcined NiO/SBA-15 using supports aged at T = 60, 100, 140 °C)

4.3.4. Activation of the catalyst

Considering the application in hydrogenation reactions, the reducibility of the nickel oxide phases in the different materials was investigated by H₂-TPR (Fig. 4.8). First, the hydrogen consumed during the H₂-TPR process was evaluated to correspond to the theoretical quantity necessary to fully reduce NiO into Ni⁰ (8.7 mmol/g for Ni₆₀, 8.5 mmol/g for Ni₁₀₀ and 9.2 mmol/g for Ni₁₄₀, ±5 % of the theoretical value). These data indicate the accessibility of the NiO NPs to hydrogen, even if they are located in the intra-wall pores.

Reduction of NiO in Ni₆₀ occurs in two distinct steps: (1) first hydrogen consumption, being the major step, centered at 308 °C; (2) second hydrogen consumption centered at 478 °C. For the other two materials, Ni-100 and Ni₁₄₀, the first hydrogen consumption is significantly depressed and most of the hydrogen consumption (> 90%) occurs during the second step, with the reduction maximum at ~490 °C.

In light of previous discussions concerning the size and distribution of NiO NPs, it seems reasonable to assume that: (1) the reduction of bulk NiO, located at the external surface of the silica (observed only for Ni_60) occurs at the lowest temperatures, $T_{max} \approx 310$ °C; (2) the reduction of smaller NiO particles, located in the intra-wall porosity of the mesoporous host, occurs at a higher temperature, $T_{max} \approx 485$ °C.^{17,37} The presence of minor hydrogen consumptions at $T \sim 310$ °C for Ni_100 and Ni_140, the proportion of which for Ni_100 is approximately 6% and for Ni_140 being 19%, suggests the presence of a low fraction of NiO external particles in these two materials, whereas not found on TEM micrographs. The H₂-TPR profile of 15Ni/SBA-15_IWIMD as discussed in the previous chapter exhibited three reduction peaks centered at 300, 389 (main peak) and 495 °C, respectively. As compared to the Ni_T materials, the majority of the hydrogen consumption (> 60%) for 15Ni/SBA-15_IWIMD occurred during the second step, indicating that the dispersion of NiO NPs is at an intermediate level between Ni_60 and Ni_140.

Always in view of possible practical applications, the stability of the materials under reducing atmosphere was evaluated by TEM for Ni_100 and Ni_140, in order to determine if Ni NPs are thermally stable or suffer from sintering during activation under hydrogen at 900 °C. Representative images are presented in Fig. 4.9.

For Ni_100, no visible modification of the NPs size takes place upon activation under reducing conditions at high temperature (Fig. 4.9a). Ni⁰ NPs exhibit sizes always below or equal to 3 nm, close to what was observed for NiO before activation. This result supports our previous interpretation consisting in a selective localization of the NPs inside the intra-wall pores of the support, and confirms their stabilization. A completely different behavior is obtained over Ni_140 materials. The NPs population is centered at 4-5 nm, with an average NPs size calculated at 5.1 nm, but some Ni⁰ NPs are much larger than the initial NiO NPs (11 nm) (Fig. 4.9 b, c). Considering the textural features of the support synthesized at 140 °C, the thin silica walls have not been robust enough to withstand this severe thermal treatment, resulting in the destruction of the pore network periodicity (Fig. 4.9b) and to some visible Ni NPs sintering.

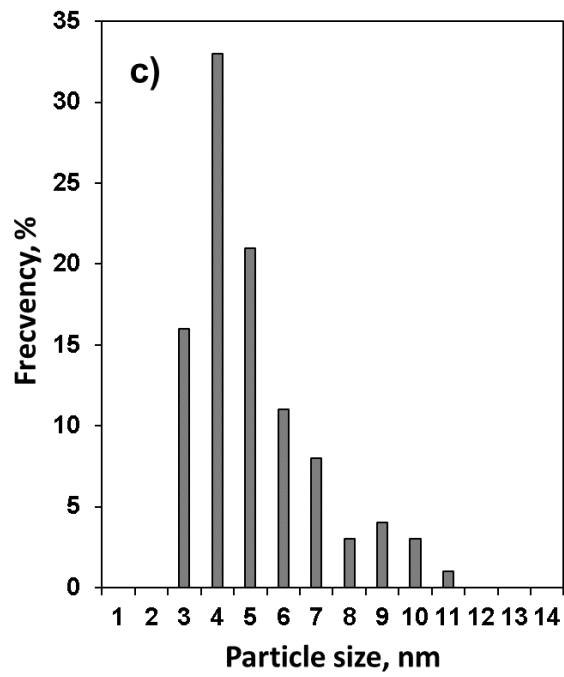
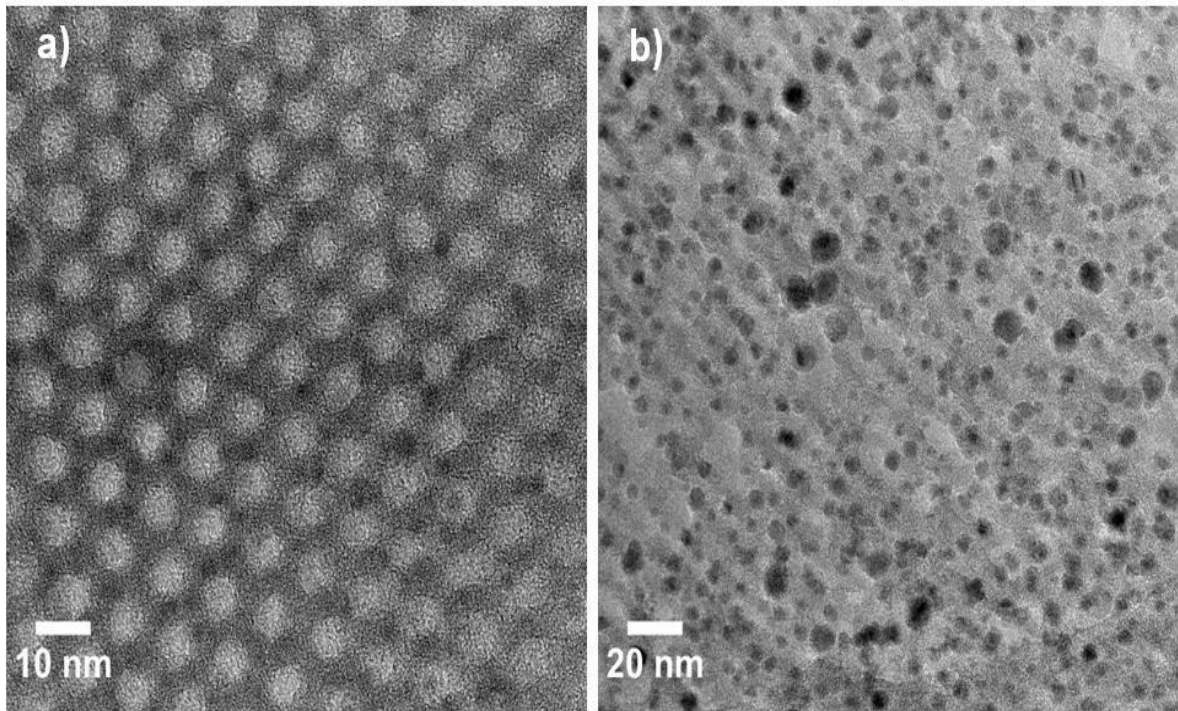
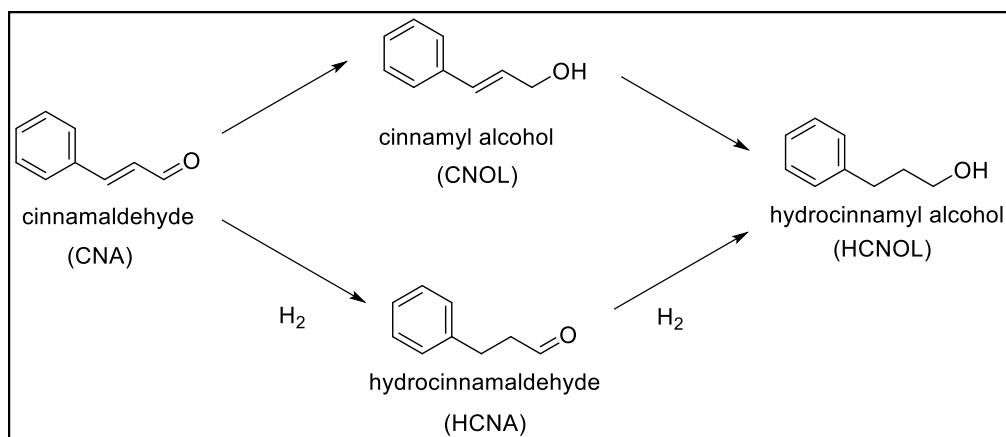


Fig. 4.9 TEM images obtained for Ni_T materials reduced *ex-situ* at 900 °C: a) Ni₁₀₀; b) Ni₁₄₀; c) particle size distribution of Ni₁₄₀



Scheme 4.2 Reaction pathways for the hydrogenation of cinnamaldehyde⁴³

4.3.5. Catalytic properties of Ni/SBA-15 materials for hydroconversion reactions

For a first evaluation, Ni_T catalysts were tested in a reaction in the liquid phase that was studied on similar MI-derived systems, the hydrogenation of cinnamaldehyde (CNA), under mild reaction temperature conditions.^{16,17} CNA is an unsaturated aldehyde, which can undergo hydrogenation of both the C=C and C=O bonds (Scheme 4.2). Over Ni-based catalysts, only hydrocinnamaldehyde (HCNA, by C=C bond hydrogenation) and hydrocinnamyl alcohol (HCNOL, by hydrogenation of HCNA) are usually formed, with a selectivity towards HCNA higher than 80 % at all conversion levels.¹⁶

The catalytic performances of Ni_T materials in CNA hydrogenation were assessed at the Gheorghe Asachi Technical University of Iasi, in a Parr reactor, after an activation step at 500 °C for 10 h under H₂ flow. The reaction was performed under the following conditions: 1 mL CNA, 0.133 g catalyst, 40 mL 2-propanol, 60 °C, 10 bar H₂. Preliminary tests were performed with different granulometric fractions, stirring rates and catalyst loadings, *to determine conditions under which no diffusional limitations would occur*: grain size lower than 0.126 mm, stirring rate of 750 rpm, 0.066 - 0.265 g catalyst. In addition, a blank experiment was conducted under N₂ pressure instead of H₂, in order to confirm the absence of hydrogenation product by hydrogen-transfer after 6 h of reaction. Finally, a blank experiment with calcined SBA-15_100 sample was performed to determine the support impact on the cinnamaldehyde concentration in solution. No modification of the concentration was observed after 6 h of reaction.

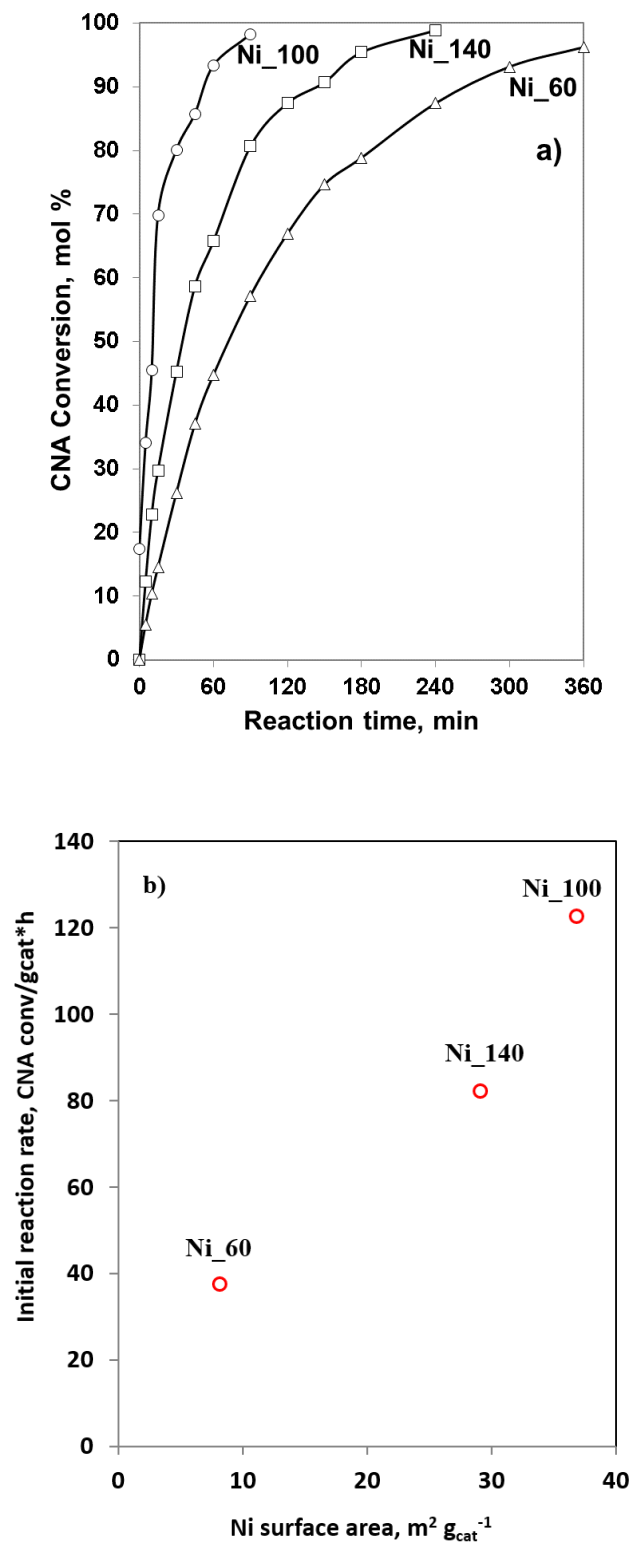


Fig. 4.10 CNA conversion evolution with reaction time (a), and initial reaction rate as a function of Ni surface area exposed per gram of catalyst (calculated using the particle size histogram data from TEM) for the MI-derived materials (b). Reaction conditions: 1 mL CNA, 0.133 g catalyst, 40 mL 2-propanol, P(H₂) = 10 bar, T = 60 °C, stirring rate = 750 rpm

Table 4.2 CAN hydrogenation rate, fraction of exposed Ni atoms and Ni surface area

Sample	hydrogenation rate ^a , mmolCNA g _{cata.} ⁻¹ h ⁻¹	% atoms exposed on the NPs surface ^b	Ni surface area ^c , m ² g _{cat} ⁻¹
Ni_60	37.5	13	8
Ni_100	122.8	57	37
Ni_140	82.2	45	29

^a: calculated on the initial slope of the conversion curve, at CNA conversion < 40%; ^b: % of atoms exposed on the surface, calculated using the particle sizes determined by TEM statistical analysis, considering that $d_{Ni} = d_{NiO} \times 0.84$ based on differences of molar mass and density, and that for each particle, Ni dispersion (%) = $97.1/d_{Ni}$ (nm);⁴¹ ^c: using the fraction of Ni atoms exposed at the NPs surface and assuming that one Ni atom occupies $6.3 \times 10^{-2} \text{ nm}^2$.⁴²

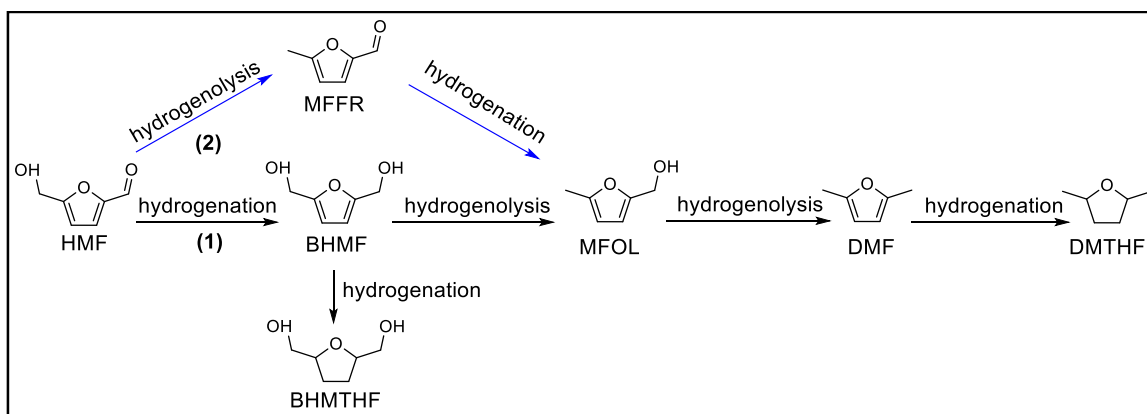
The three Ni_T materials exhibited the same selectivity $\geq 98\%$ to HCNA. The difference in the catalytic performances mainly lied in the catalytic activity. The evolutions of the conversion of CNA with reaction time, obtained for Ni₆₀, Ni₁₀₀ and Ni₁₄₀ catalysts, are presented in Fig. 4.10a. For Ni₆₀ (large particle size - Fig. 4.3), the complete CNA conversion was not achieved after 360 min, and a hydrogenation initial rate of $37.5 \text{ mmolCNA g}_{\text{cat}}^{-1}\text{h}^{-1}$ was measured (Fig. 4.10b). Ni₁₄₀ sample showed a nearly complete CNA conversion after 240 min and an initial reaction rate of $82.2 \text{ mmolCNA g}_{\text{cat}}^{-1}\text{h}^{-1}$. In contrast, when small Ni NPs were highly dispersed on the silica support and presented a high dispersion (Ni₁₀₀), the complete CNA conversion was obtained within 90 min, with an initial reaction rate of $122.8 \text{ mmol CNA g}_{\text{cat}}^{-1}\text{h}^{-1}$, which is the highest reaction rate in the series. Ni₁₀₀ thus shows a superior catalytic activity, which is about 1.5 times higher than that of Ni₁₄₀ and 3 times higher than that of Ni₆₀. In addition, as compared with the reaction rate afforded by Ni-based catalysts from the literature (Table 4.3), the monometallic Ni₁₀₀ catalyst also exhibited a catalytic activity at the top level and at a lower reaction temperature, indicating the high catalytic efficiency of this catalyst for the selective hydrogenation of CNA to HCNA.

Table 4.3 Catalytic performances of nickel-based catalysts for the conversion of CNA to HCNA

Entry	Catalyst	Feed conditions	P (bar)	T (°C)	t (h)	conv. (%)	yield (%)	reaction rate ^a	ref
1	Ni/TiO ₂	3 mmol CNA; 10 mL 2-propanol; 0.05 g catalyst	20	80	1	66	65	40	43
2	Ni-Ir/TiO ₂	3 mmol CNA; 10 mL 2-propanol; 0.05 g catalyst	20	80	0.3	98	93	175	43
3	NiCu/SBA-15	8 mmol CNA; 25 mL propylene carbonate; 0.265 g catalyst	-	150	3	99	89	9.9	33
4	Ni/SBA-15	8 mmol CNA; 25 mL propylene carbonate; 0.265 g catalyst	-	150	3	86	81	8.6	33
5	Ni/TiO ₂	9 mmol CNA; 16 mL methanol; 0.15 g catalyst	1	100	1	73	39	44.2	44
6	NiCo/TiO ₂	9 mmol CNA; 19 mL 2-propanol + 1.65 mL water; 0.15 g catalyst	20	120	1	84	83	50	45
7	Ni/SBA-15	7 mmol CNA; 40 mL isopropanol; 0.265 g catalyst	10	60	0.7	100	100	131	46
8	Ni_100	7 mmol CNA; 40 mL isopropanol; 0.133 g catalyst	10	60	1.5	100	99	122.8	<i>this work</i>

^a: unit, mmolCNA g_{cat}⁻¹h⁻¹.

Hydrogenation rates have been plotted in Fig 4.10b as a function of the Ni surface area exposed per gram of catalyst, deduced from TEM measurements (see Table 4.2). The calculated reaction rate correlates well with the Ni surface area exposed per gram of catalyst. For Ni_60, the existence of a high proportion of relatively large particles (Fig. 4.3), which contributes to a low extent to the metallic surface area, led to a lower reaction rate. In contrast, the highly-dispersed Ni_100 catalyst exposed the largest Ni surface area and thus afforded the highest reaction rate among the three catalysts. This reflects the significant effect of the aging temperature of SBA-15 on the catalyst preparation (Ni NPs dispersion and accessibility to the surface active sites) and thus on the catalyst activity. Remembering the confining of small particles in the walls of Ni_100, it also shows that CNA can access surface active sites without encountering significant internal diffusion limitations. Consequently, confining Ni NPs in secondary pores (micropores and small mesopores) ensures a large amount of accessible active sites due to a high dispersion of Ni NPs, and at the same time maintains the mesopores open for the effective diffusion of the reactants.^{17,46}



Scheme 4.3 Reaction pathway for the hydroconversion of HMF to value-added chemicals (BHMTHF, BHMTHF) and biofuels (DMF, DMTHF)

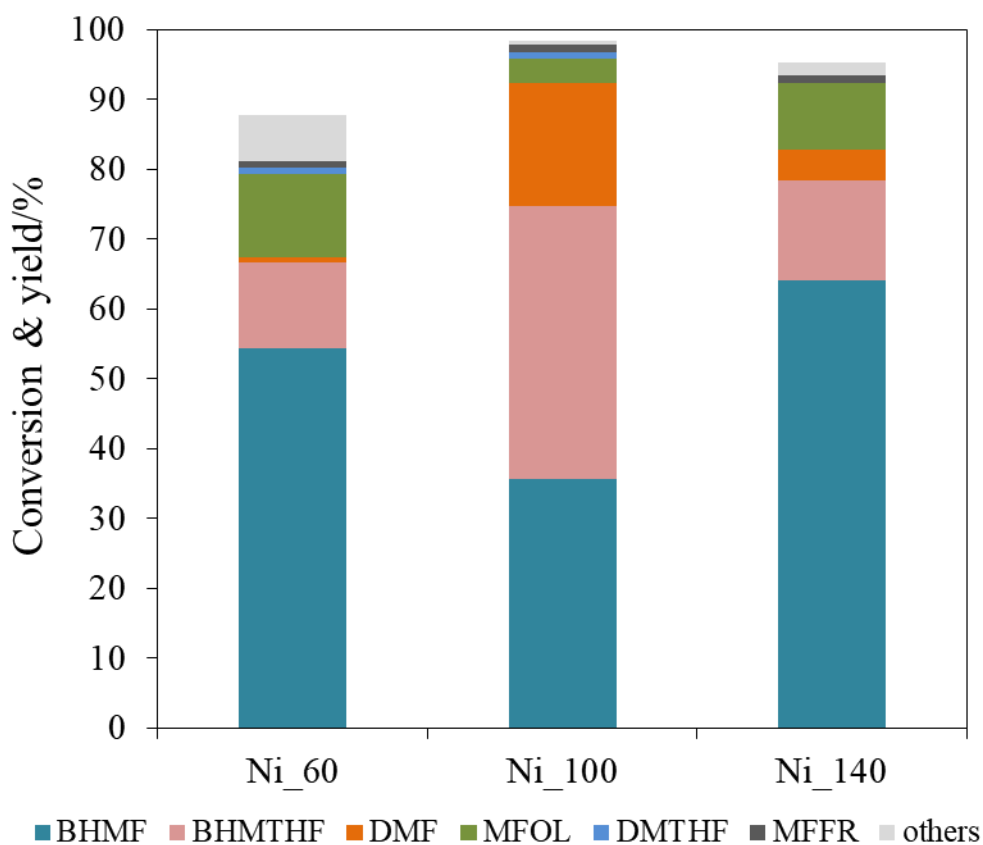


Figure 4.11 HMF conversion and product distributions over the MI-derived materials. Reaction conditions: 0.03 g HMF, 21.1 mg catalyst, 1.5 mL 1,4-dioxane, $P(\text{H}_2) = 15$ bar, $T = 130$ °C, reaction time = 1 h, stirring rate = 700 rpm.

Given the outstanding performance of the Ni_T catalysts in CNA hydrogenation, exploration of the efficiency of these MI-derived materials in the hydroconversion of HMF was also attempted. The evaluation of the catalytic performances of the Ni_T materials was performed in a SPR instrument at the Realcat platform in Lille. Considering the very high activity of these catalysts in the hydrogenation of CNA, a low reaction temperature (130 °C) and short reaction time (1 h) (as compared to the corresponding experimental parameters used for 15Ni/SBA-15_IWIMD in the previous chapter) were applied here in order to obtain differences in reactivity between the Ni_T materials. The results obtained here thus cannot be directly compared with the results obtained with 15Ni/SBA-15_IWIMD and presented in the previous chapter.

It has been well-established that the partial hydrogenation of HMF leads to the formation of BHMF, while the full hydrogenation gives BHMTHF (2,5-bis(hydroxymethyl)tetrahydrofuran) (Scheme 4.3), both of which are value-added chemicals serving as polymer precursors and solvents.^{47,48} The formation of BHMTHF involves the reduction of the furan ring, which generally requires relatively a high hydrogenation activity of the catalyst.⁴⁹ As seen in the previous chapter, the hydrogenolysis of the pendant groups leads to a valuable biofuel - DMF.⁵⁰

The conversions and product distributions obtained with Ni₆₀, Ni₁₀₀ and Ni₁₄₀ are reported in Fig. 4.11. Among the three MI-derived catalysts, Ni₁₀₀ exhibited the highest hydrogenation activity, affording a nearly complete conversion of HMF (98.5%). BHMF and BHMTHF were obtained as the main products, giving a combined yield of 75%. The heavily induced full hydrogenation of HMF over Ni₁₀₀ resulted in the formation of BHMTHF as the main product (39.1% yield). Notably, DMF (17% yield) and MFOL (3.5%) were also formed, suggesting some hydrogenolysis ability of this catalyst in these experimental conditions. The high combined yield of BHMF and BHMTHF, and the limited yield of MFOL indicate that the hydrogenation of HMF over Ni should primarily follow the route (1) (black line, HMF → BHMF → MFOL → DMF) (Scheme 4.3).

The limited hydrogenation activity of Ni₆₀ was reflected by the slower transformation of HMF along route (1), giving at a HMF conversion of 87 %, a higher BHMF yield (54.3%), a higher MFOL yield (11.9%), a much lower DMF yield (0.9%) and a lower BHMTHF yield (12.3%). With a higher dispersion of Ni NPs than Ni₆₀, Ni₁₄₀ exhibited an activity at an intermediate level between that of Ni₆₀ and Ni₁₀₀, leading to an increase of HMF

conversion up to 95 %, a BHMF yield of 64%, a MFOL yield of 9.7%, a DMF yield of 4.4% and a BHMTHF yield of 14.3%. Prolonging the reaction time and increasing conversion may lead to higher selectivities of the full hydrogenation product (BHMTHF) and of the fully hydrogenolyzed product (DMF) at the same levels as Ni₁₀₀.

The products distribution obtained here from the Ni_T materials (primarily producing BHMF and BHMTHF) is significantly different with that afforded by 15Ni/SBA-15_IWIMD (predominantly giving DMF and DMTHF). This can be attributed to the markedly different reaction conditions, especially the reaction temperature, which as aforementioned makes the comparison difficult. Indeed, the reaction temperature used here is relatively low (130 °C) and could hardly promote efficiently the hydrogenolysis of HMF over Ni_T catalysts. High reaction temperatures (≥ 180 °C) are generally required for Ni-based catalysts to afford high yields of DMF and DMTHF.⁵¹ Nevertheless, the results obtained here confirm the efficiency of the IWP-confined Ni NPs to reach high hydrogenation activities, and at the same time, indicate the potential of the Ni_T catalysts for the efficient production of valuable BHMF and BHMTHF from HMF, though the reaction conditions remain to be further optimized.

4.4 Conclusion

The secondary pore network of SBA-15 host materials plays an important role in determining the Ni(0) NPs size and localization when nickel is introduced by melt infiltration. The absence of a connection between adjacent pores through intra-wall porosity results in a poor diffusion of the precursor melt, which thus forms large extra-porous aggregates. Increasing the diameter of the IWP by increasing the aging temperature of SBA-15, and the presence of interconnected pores, both facilitate the formation of very small, pore-encapsulated Ni(0) NPs (around 2 nm in size for Ni₁₀₀). The catalytic activity of Ni MI-derived materials in the liquid-phase hydrogenation of cinnamaldehyde is shown to significantly increase when very small nickel particles are located in the silica intra-wall pores. Besides, MI-derived catalysts with finely dispersed nickel particles show a high potential in the reductive transformation of HMF to value-added BHMF and BHMTHF. This work provides new insight into how the microenvironment existing between the pore-occluded polymer and inorganic walls can be explored to stabilize highly dispersed metal (oxide) NPs, *in fine*, to produce excellent catalysts for hydrogenation reactions.

References

- (1) Singh, S.; Kumar, R.; Setiabudi, H. D.; Nanda, S.; Vo, D.-V. N. Advanced Synthesis Strategies of Mesoporous SBA-15 Supported Catalysts for Catalytic Reforming Applications: A State-of-the-Art Review. *Appl. Catal. Gen.* **2018**, *559*, 57–74. <https://doi.org/10.1016/j.apcata.2018.04.015>.
- (2) Tian, H.; Li, X.; Zeng, L.; Gong, J. Recent Advances on the Design of Group VIII Base-Metal Catalysts with Encapsulated Structures. *ACS Catal.* **2015**, *5* (8), 4959–4977. <https://doi.org/10.1021/acscatal.5b01221>.
- (3) Audemar, M.; Ciotonea, C.; De Oliveira Vigier, K.; Royer, S.; Ungureanu, A.; Dragoi, B.; Dumitriu, E.; Jérôme, F. Selective Hydrogenation of Furfural to Furfuryl Alcohol in the Presence of a Recyclable Cobalt/SBA-15 Catalyst. *ChemSusChem* **2015**, *8* (11), 1885–1891. <https://doi.org/10.1002/cssc.201403398>.
- (4) Chen, J.; Lu, F.; Zhang, J.; Yu, W.; Wang, F.; Gao, J.; Xu, J. Immobilized Ru Clusters in Nanosized Mesoporous Zirconium Silica for the Aqueous Hydrogenation of Furan Derivatives at Room Temperature. *ChemCatChem* **2013**, *5* (10), 2822–2826. <https://doi.org/10.1002/cctc.201300316>.
- (5) Yu, L.; He, L.; Chen, J.; Zheng, J.; Ye, L.; Lin, H.; Yuan, Y. Robust and Recyclable Nonprecious Bimetallic Nanoparticles on Carbon Nanotubes for the Hydrogenation and Hydrogenolysis of 5-Hydroxymethylfurfural. *ChemCatChem* **2015**, *7* (11), 1701–1707. <https://doi.org/10.1002/cctc.201500097>.
- (6) Ungureanu, A.; Dragoi, B.; Chiriac, A.; Royer, S.; Duprez, D.; Dumitriu, E. Synthesis of Highly Thermostable Copper-Nickel Nanoparticles Confined in the Channels of Ordered Mesoporous SBA-15 Silica. *J. Mater. Chem.* **2011**, *21* (33), 12529–12541. <https://doi.org/10.1039/C1JM10971E>.
- (7) Huwe, H.; Fröba, M. Synthesis and Characterization of Transition Metal and Metal Oxide Nanoparticles inside Mesoporous Carbon CMK-3. *Carbon* **2007**, *45* (2), 304–314. <https://doi.org/10.1016/j.carbon.2006.09.021>.
- (8) Wu, H.; Zhou, S.; Wu, Y.; Song, W. Ultrafine CuO Nanoparticles Isolated by Ordered Mesoporous Carbon for Catalysis and Electroanalysis. *J. Mater. Chem. A* **2013**, *1* (45),

14198–14205. <https://doi.org/10.1039/C3TA12927F>.

(9) Wang, Y. M.; Ying Wu, Z.; Zhu, J. H. Surface Functionalization of SBA-15 by the Solvent-Free Method. *J. Solid State Chem.* **2004**, *177* (10), 3815–3823. <https://doi.org/10.1016/j.jssc.2004.07.013>.

(10) Wang, Y. M.; Wu, Z. Y.; Wang, H. J.; Zhu, J. H. Fabrication of Metal Oxides Occluded in Ordered Mesoporous Hosts via a Solid-State Grinding Route: The Influence of Host–Guest Interactions. *Adv. Funct. Mater.* **2006**, *16* (18), 2374–2386. <https://doi.org/10.1002/adfm.200500613>.

(11) Tian, W. H.; Sun, L. B.; Song, X. L.; Liu, X. Q.; Yin, Y.; He, G. S. Adsorptive Desulfurization by Copper Species within Confined Space. *Langmuir* **2010**, *26* (22), 17398–17404. <https://doi.org/10.1021/la101856d>.

(12) Shon, J. K.; Kong, S. S.; Kim, Y. S.; Lee, J. H.; Park, W. K.; Park, S. C.; Kim, J. M. Solvent-Free Infiltration Method for Mesoporous SnO₂ Using Mesoporous Silica Templates. *Microporous Mesoporous Mater.* **2009**, *120* (3), 441–446. <https://doi.org/10.1016/j.micromeso.2008.12.022>.

(13) Zhou, C. F.; Wang, Y. M.; Cao, Y.; Zhuang, T. T.; Huang, W.; Chun, Y.; Zhu, J. H. Solvent-Free Surface Functionalized SBA-15 as a Versatile Trap of Nitrosamines. *J. Mater. Chem.* **2006**, *16* (16), 1520–1528. <https://doi.org/10.1039/B514317A>.

(14) Zheng, M.; Cao, J.; Liao, S.; Liu, J.; Chen, H.; Zhao, Y.; Dai, W.; Ji, G.; Cao, J.; Tao, J. Preparation of Mesoporous Co₃O₄ Nanoparticles via Solid–Liquid Route and Effects of Calcination Temperature and Textural Parameters on Their Electrochemical Capacitive Behaviors. *J. Phys. Chem. C* **2009**, *113* (9), 3887–3894. <https://doi.org/10.1021/jp810230d>.

(15) Jian, K.; Truong, T. C.; Hoffman, W. P.; Hurt, R. H. Mesoporous Carbons with Self-Assembled Surfaces of Defined Crystal Orientation. *Microporous Mesoporous Mater.* **2008**, *108* (1), 143–151. <https://doi.org/10.1016/j.micromeso.2007.04.055>.

(16) Ciotonea, C.; Dragoi, B.; Ungureanu, A.; Catrinescu, C.; Petit, S.; Alamdari, H.; Marceau, E.; Dumitriu, E.; Royer, S. Improved Dispersion of Transition Metals in Mesoporous Materials through a Polymer-Assisted Melt Infiltration Method. *Catal. Sci. Technol.* **2017**, *7* (22), 5448–5456. <https://doi.org/10.1039/C7CY00963A>.

(17) Ciotonea, C.; Mazilu, I.; Dragoi, B.; Catrinescu, C.; Dumitriu, E.; Ungureanu, A.; Alamdari, H.; Petit, S.; Royer, S. Confining for Stability: Heterogeneous Catalysis with Transition Metal (Oxide) Nanoparticles Confined in the Secondary Pore Network of Mesoporous Scaffolds. *ChemNanoMat* **2017**, *3* (4), 233–237. <https://doi.org/10.1002/cnma.201700014>.

(18) Zhang, Q.; Zhang, T.; Shi, Y.; Zhao, B.; Wang, M.; Liu, Q.; Wang, J.; Long, K.; Duan, Y.; Ning, P. A Sintering and Carbon-Resistant Ni-SBA-15 Catalyst Prepared by Solid-State Grinding Method for Dry Reforming of Methane. *J. CO₂ Util.* **2017**, *17*, 10–19. <https://doi.org/10.1016/j.jcou.2016.11.002>.

(19) Ning, X.; Lu, Y.; Fu, H.; Wan, H.; Xu, Z.; Zheng, S. Template-Mediated Ni(II) Dispersion in Mesoporous SiO₂ for Preparation of Highly Dispersed Ni Catalysts: Influence of Template Type. *ACS Appl. Mater. Interfaces* **2017**, *9* (22), 19335–19344. <https://doi.org/10.1021/acsami.7b04100>.

(20) Jongh, P. E. de; Eggenhuisen, T. M. Melt Infiltration: An Emerging Technique for the Preparation of Novel Functional Nanostructured Materials. *Adv. Mater.* **2013**, *25* (46), 6672–6690. <https://doi.org/10.1002/adma.201301912>.

(21) Yue; Zhou. Synthesis of Porous Single Crystals of Metal Oxides via a Solid–Liquid Route. *Chem. Mater.* **2007**, *19* (9), 2359–2363. <https://doi.org/10.1021/cm070124b>.

(22) Eggenhuisen, T. M.; Breejen, J. P. den; Verdoes, D.; Jongh, P. E. de; Jong, K. P. de. Fundamentals of Melt Infiltration for the Preparation of Supported Metal Catalysts. The Case of Co/SiO₂ for Fischer–Tropsch Synthesis. *J. Am. Chem. Soc.* **2010**, *132* (51), 18318–18325. <https://doi.org/10.1021/ja1080508>.

(23) Jiang, Q.; Wu, Z. Y.; Wang, Y. M.; Cao, Y.; Zhou, C. F.; Zhu, J. H. Fabrication of Photoluminescent ZnO/SBA-15 through Directly Dispersing Zinc Nitrate into the as-Prepared Mesoporous Silica Occluded with Template. *J. Mater. Chem.* **2006**, *16* (16), 1536–1542. <https://doi.org/10.1039/B516061H>.

(24) Galarneau, A.; Cambon, H.; Renzo, F. D.; Ryoo, R.; Choi, M.; Fajula, F. Microporosity and Connections between Pores in SBA-15 Mesostructured Silicas as a Function of the Temperature of Synthesis. *New J. Chem.* **2003**, *27* (1), 73–79.

<https://doi.org/10.1039/B207378C>.

(25) Kleitz, F.; Bérubé, F.; Guillet-Nicolas, R.; Yang, C.-M.; Thommes, M. Probing Adsorption, Pore Condensation, and Hysteresis Behavior of Pure Fluids in Three-Dimensional Cubic Mesoporous KIT-6 Silica. *J. Phys. Chem. C* **2010**, *114* (20), 9344–9355. <https://doi.org/10.1021/jp909836v>.

(26) Bérubé, F.; Khadhraoui, A.; Janicke, M. T.; Kleitz, F.; Kaliaguine, S. Optimizing Silica Synthesis for the Preparation of Mesoporous Ti-SBA-15 Epoxidation Catalysts. *Ind. Eng. Chem. Res.* **2010**, *49* (15), 6977–6985. <https://doi.org/10.1021/ie901659k>.

(27) Bérubé, F.; Khadhraoui, A.; Florek, J.; Kaliaguine, S.; Kleitz, F. A Generalized Method toward High Dispersion of Transition Metals in Large Pore Mesoporous Metal Oxide/Silica Hybrids. *J. Colloid Interface Sci.* **2015**, *449*, 102–114. <https://doi.org/10.1016/j.jcis.2014.12.001>.

(28) Zhao, D.; Feng, J.; Huo, Q.; Melosh, N.; Fredrickson, G. H.; Chmelka, B. F.; Stucky, G. D. Triblock Copolymer Syntheses of Mesoporous Silica with Periodic 50 to 300 Angstrom Pores. *Science* **1998**, *279* (5350), 548–552. <https://doi.org/10.1126/science.279.5350.548>.

(29) Zhao, D.; Sun, J.; Li, Q.; Stucky, G. D. Morphological Control of Highly Ordered Mesoporous Silica SBA-15. *Chem. Mater.* **2000**, *12* (2), 275–279. <https://doi.org/10.1021/cm9911363>.

(30) Cao, L.; Man, T.; Kruk, M. Synthesis of Ultra-Large-Pore SBA-15 Silica with Two-Dimensional Hexagonal Structure Using Triisopropylbenzene As Micelle Expander. *Chem. Mater.* **2009**, *21* (6), 1144–1153. <https://doi.org/10.1021/cm8012733>.

(31) Hoang, V. T.; Huang, Q.; Eic, M.; Do, T. O.; Kaliaguine, S. Effect of the Intrawall Microporosity on the Diffusion Characterization of Bi-porous SBA-15 Materials. In *Fluid Transport in Nanoporous Materials*; Conner, W. C., Fraissard, J., Eds.; NATO Science Series II: Mathematics Physics and Chemistry; Springer Netherlands, 2006; pp 591–602.

(32) Rasmussen, C. J.; Vishnyakov, A.; Thommes, M.; Smarsly, B. M.; Kleitz, F.; Neimark, A. V. Cavitation in Metastable Liquid Nitrogen Confined to Nanoscale Pores. *Langmuir* **2010**, *26* (12), 10147–10157. <https://doi.org/10.1021/la100268q>.

(33) Ungureanu, A.; Dragoi, B.; Chiriac, A.; Ciotonea, C.; Royer, S.; Duprez, D.; Mamede, A. S.; Dumitriu, E. Composition-Dependent Morphostructural Properties of Ni–Cu Oxide Nanoparticles Confined within the Channels of Ordered Mesoporous SBA-15 Silica. *ACS Appl. Mater. Interfaces* **2013**, *5* (8), 3010–3025. <https://doi.org/10.1021/am302733m>.

(34) Zhong, X.; Barbier, J.; Duprez, D.; Zhang, H.; Royer, S. Modulating the Copper Oxide Morphology and Accessibility by Using Micro-/Mesoporous SBA-15 Structures as Host Support: Effect on the Activity for the CWPO of Phenol Reaction. *Appl. Catal. B Environ.* **2012**, *121–122* (Supplement C), 123–134. <https://doi.org/10.1016/j.apcatb.2012.04.002>.

(35) He, C.; Li, Q.; Li, P.; Wang, Y.; Zhang, X.; Cheng, J.; Hao, Z. Templated Silica with Increased Surface Area and Expanded Microporosity: Synthesis, Characterization, and Catalytic Application. *Chem. Eng. J.* **2010**, *162* (3), 901–909. <https://doi.org/10.1016/j.cej.2010.06.037>.

(36) Wanka, G.; Hoffmann, H.; Ulbricht, W. Phase Diagrams and Aggregation Behavior of Poly(Oxyethylene)-Poly(Oxypropylene)-Poly(Oxyethylene) Triblock Copolymers in Aqueous Solutions. *Macromolecules* **1994**, *27* (15), 4145–4159. <https://doi.org/10.1021/ma00093a016>.

(37) Mayer, A. B. R. Colloidal Metal Nanoparticles Dispersed in Amphiphilic Polymers. *Polym. Adv. Technol.* **2001**, *12* (1–2), 96–106. [https://doi.org/10.1002/1099-1581\(200101/02\)12:1/2<96::AID-PAT943>3.0.CO;2-G](https://doi.org/10.1002/1099-1581(200101/02)12:1/2<96::AID-PAT943>3.0.CO;2-G).

(38) Ungureanu, A.; Dragoi, B.; Chiriac, A.; Royer, S.; Duprez, D.; Dumitriu, E. Synthesis of Highly Thermostable Copper-Nickel Nanoparticles Confined in the Channels of Ordered Mesoporous SBA-15 Silica. *J. Mater. Chem.* **2011**, *21* (33), 12529–12541. <https://doi.org/10.1039/C1JM10971E>.

(39) Ciotonea, C.; Dragoi, B.; Ungureanu, A.; Chiriac, A.; Petit, S.; Royer, S.; Dumitriu, E. Nanosized Transition Metals in Controlled Environments of Phyllosilicate–Mesoporous Silica Composites as Highly Thermostable and Active Catalysts. *Chem. Commun.* **2013**, *49* (69), 7665–7667. <https://doi.org/10.1039/C3CC43197E>.

(40) Galarneau, A.; Cambon, H.; Di Renzo, F.; Ryoo, R.; Choi, M.; Fajula, F.

Microporosity and Connections between Pores in SBA-15 Mesostructured Silicas as a Function of the Temperature of Synthesis. *New J. Chem.* **2003**, 27 (1), 73–79. <https://doi.org/10.1039/b207378c>.

(41) Marceau, E.; Löfberg, A.; Giraudon, J.-M.; Négrier, F.; Che, M.; Leclercq, L. From Al₂O₃-Supported Ni(II)–Ethylenediamine Complexes to CO Hydrogenation Catalysts: Characterization of the Surface Sites and Catalytic Properties. *Appl. Catal. Gen.* **2009**, 362 (1), 34–39. <https://doi.org/10.1016/j.apcata.2009.04.029>.

(42) Gil, A.; Díaz, A.; Gandía, L. M.; Montes, M. Influence of the Preparation Method and the Nature of the Support on the Stability of Nickel Catalysts. *Appl. Catal. Gen.* **1994**, 109 (2), 167–179. [https://doi.org/10.1016/0926-860X\(94\)80116-9](https://doi.org/10.1016/0926-860X(94)80116-9).

(43) Lin, W.; Cheng, H.; He, L.; Yu, Y.; Zhao, F. High Performance of Ir-Promoted Ni/TiO₂ Catalyst toward the Selective Hydrogenation of Cinnamaldehyde. *J. Catal.* **2013**, 303, 110–116. <https://doi.org/10.1016/j.jcat.2013.03.002>.

(44) Prakash, M. G.; Mahalakshmy, R.; Krishnamurthy, K. R.; Viswanathan, B. Studies on Ni–M (M=Cu, Ag, Au) Bimetallic Catalysts for Selective Hydrogenation of Cinnamaldehyde. *Catal. Today* **2016**, 263, 105–111. <https://doi.org/10.1016/j.cattod.2015.09.053>.

(45) Ashokkumar, S.; Ganesan, V.; Ramaswamy, K. K.; Balasubramanian, V. Bimetallic Co–Ni/TiO₂ Catalysts for Selective Hydrogenation of Cinnamaldehyde. *Res. Chem. Intermed.* **2018**, 44 (11), 6703–6720. <https://doi.org/10.1007/s11164-018-3517-7>.

(46) Ciotonea, C.; Dragoi, B.; Ungureanu, A.; Catrinescu, C.; Petit, S.; Alamdari, H.; Marceau, E.; Dumitriu, E.; Royer, S. Improved Dispersion of Transition Metals in Mesoporous Materials through a Polymer-Assisted Melt Infiltration Method. *Catal. Sci. Technol.* **2017**, 7 (22), 5448–5456. <https://doi.org/10.1039/C7CY00963A>.

(47) Scholz, D.; Aellig, C.; Hermans, I. Catalytic Transfer Hydrogenation/Hydrogenolysis for Reductive Upgrading of Furfural and 5-(Hydroxymethyl)Furfural. *ChemSusChem* **2014**, 7 (1), 268–275. <https://doi.org/10.1002/cssc.201300774>.

(48) Hu, L.; Lin, L.; Wu, Z.; Zhou, S.; Liu, S. Recent Advances in Catalytic Transformation of Biomass-Derived 5-Hydroxymethylfurfural into the Innovative Fuels and Chemicals. *Renew. Sustain. Energy Rev.* **2017**, 74, 230–257.

<https://doi.org/10.1016/j.rser.2017.02.042>.

(49) Tang, X.; Wei, J.; Ding, N.; Sun, Y.; Zeng, X.; Hu, L.; Liu, S.; Lei, T.; Lin, L. Chemoselective Hydrogenation of Biomass Derived 5-Hydroxymethylfurfural to Diols: Key Intermediates for Sustainable Chemicals, Materials and Fuels. *Renew. Sustain. Energy Rev.* **2017**, *77*, 287–296. <https://doi.org/10.1016/j.rser.2017.04.013>.

(50) Qian, Y.; Zhu, L.; Wang, Y.; Lu, X. Recent Progress in the Development of Biofuel 2,5-Dimethylfuran. *Renew. Sustain. Energy Rev.* **2015**, *41*, 633–646. <https://doi.org/10.1016/j.rser.2014.08.085>.

(51) Chen, S.; Wojcieszak, R.; Dumeignil, F.; Marceau, E.; Royer, S. How Catalysts and Experimental Conditions Determine the Selective Hydroconversion of Furfural and 5-Hydroxymethylfurfural. *Chem. Rev.* **2018**, *118* (22), 11023–11117. <https://doi.org/10.1021/acs.chemrev.8b00134>.

**CHAPTER 5: EFFECT OF METAL
DISPERSION ON THE CATALYTIC
PERFORMANCE OF MONOMETALLIC Cu/SBA-
15 CATALYSTS FOR THE SELECTIVE
HYDROGENOLYSIS OF HMF TO DMF**

5.1 Introduction

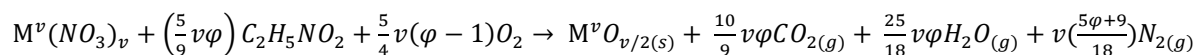
Chapters 3 and 4 have confirmed the performances of Ni-based catalysts in the hydrogenation of C=C and C=O bonds and in hydrogenolysis reactions. As shown in chapter 1, other common non-noble metals, e.g. Co, Fe and Cu, are also potential candidates for the selective hydroconversion of HMF. Among them, Cu-based catalysts stand out as a better choice, considering that Co is more expensive, whereas the activity of Fe is much lower than that of Cu and Co.¹

Concerning the hydroconversion of furanic compounds (i.e., HMF and furfural), Cu-based catalysts are generally characterized by: (i) a mild hydrogenation activity, derived from a relatively low activity for H₂ activation; (ii) the selective hydrogenation/hydrogenolysis of the pendant groups, due to the preferential vertical/tilted adsorption mode of furanic compounds. This enables Cu to minimize side transformations of HMF, such as decarbonylation and furan ring hydrogenation, while making Cu-based catalysts an ideal choice for the selective hydrogenation and hydrogenolysis of HMF to BHMF and DMF, as detailed in Chapter 1. However, on the one hand, it is rather bimetallic Cu-based catalysts that have been proposed in the literature as the main strategy to achieve high hydrogenation activities.^{2,3} Various formulations have been proposed, such as Cu-Pd, Cu-Ru, Cu-Zn, Cu-Fe, Cu-Co and Cu-Ni, to increase activity and/or selectivity, while undoubtedly increasing the cost and complexity of catalyst, especially when noble metals are added.^{4, 5, 6, 7, 8} On the other hand, a systematical study of the catalytic performances of monometallic Cu-based catalysts in the hydroconversion of HMF is still lacking.

Monometallic Cu-based catalysts prepared on an inert support could serve as an ideal system for fundamental study. An appealing inert support, as introduced in the previous chapters, is siliceous SBA-15 due to its high surface area, ordered mesoporous structure and high thermal stability. Like Ni-based catalysts, the catalytic properties of monometallic Cu-based catalysts also highly rely on the size of the metal particles, in other terms the dispersion of Cu NPs, which is strongly affected by the choice of the catalyst preparation procedure.⁹⁻¹⁶ For example, through classical impregnation it is generally difficult to disperse Cu NPs on SBA-15, because of the high mobility of copper precursors in the nanochannels of SBA-15 support during drying.¹⁷ The previous chapter shows that the melt infiltration method

facilitates the dispersion of Ni NPs in the SBA-15 support. This method could also afford well-dispersed Cu NPs on SBA-15 if the SBA-15 support was carefully prepared to be rich in surface silanol groups, or in residual Pluronic P123 (e.g. obtained by ethanol extraction).^{18,19} However, as compared to Ni/SBA-15 catalysts preparation, it is more difficult to apply this method to Cu/SBA-15 catalysts (especially with high Cu loadings) due to the lower water content in copper nitrates (maximum three moles of water per mole of copper nitrate, much lower than that of nickel nitrate hexahydrate) and a higher melting point of copper nitrate (114 °C of $\text{Cu}(\text{NO}_3)_2 \cdot 3\text{H}_2\text{O}$ vs. 56.7 °C of $\text{Ni}(\text{NO}_3)_2 \cdot 6\text{H}_2\text{O}$).

In contrast, the literature shows that the in-situ auto-combustion (ISAC) method could serve as a simple and efficient procedure to synthesize homogeneous and confined non-noble metal nanoparticles.²⁰⁻²³ This method is also based on impregnation, but it involves a non-mobile glycine-nitrate complex as a precursor. Impregnation is followed by heating the reactive solution continuously to 100 °C at which the evaporation of water (as solvent) takes place. Further heating of formed viscous gels to a critical temperature leads to vigorous initiation of the reactions (Equation 5.1) between metal nitrates (acting as oxidizers) and a fuel (glycine) along the whole volume of the media²⁴:

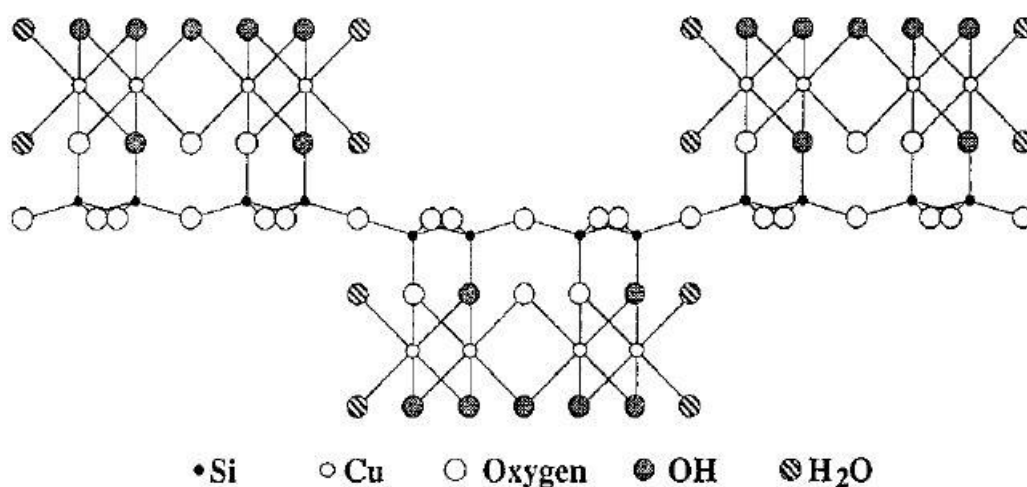


Equation 5.1

where v is the metal valence and φ , a tunable parameter, is the fuel-to-oxidizer ratio ($\varphi = 1$ implies that all oxygen required for complete combustion of fuel derives from the oxidizer, while $\varphi > 1$, or < 1 , implies fuel-rich, or lean, conditions).

It has been shown that the combustion of glycine by a metal nitrate at near stoichiometric and fuel-lean conditions ($\varphi \leq 1$) indeed facilitates the production of fine oxide powders, whereas an excess of glycine ($\varphi > 1$) leads to the formation of pure metal or alloy. The combustion reaction is completed within a short time, on the order of seconds, with maximum local temperatures reaching ~1500 °C. Such high temperatures facilitate the formation of crystalline phases. More importantly, the mixing of precursors at the molecular level and release of large quantities of gases (carbon dioxide, water, nitrogen, as shown in Equation (5.1)) result in the formation of nanoscale metal oxides and finely dispersed metal particles when inert supports are present (e.g., carbon nanotubes and SBA-15).^{23,25} In the

literature, the ISAC method has been applied to the synthesis of silica-supported catalysts, such as Fe/SBA-15 and LaCoO₃/SBA-15.^{22,26} However, the preparation of Cu/SBA-15 catalysts by the ISAC method has been rarely reported so far. In the only published work by Zhong et al., a series of Cu/SBA-15 catalysts with a Cu loading of 4 - 10 wt.% was prepared using this method, which successfully afforded SBA-15 mesopore confined Cu NPs in a particle size range of 6-11 nm (depending on the pore size of the SBA-15 support selected), suggesting the effectiveness of this method for the preparation of confined Cu/SBA-15 NPs.²⁰



Scheme 5.1 Representation of the structure of bulk chrysocolla²⁷

Another preparative procedure known for the synthesis of highly-dispersed catalysts is deposition-precipitation (DP).²⁸ In the DP method, the metal precursor is added to an aqueous suspension of the support and subsequently precipitated as a hydroxide or as a mixed phase (phyllosilicate, hydrotalcite) by raising the pH value. The surface of the support acts as a nucleating agent. The precipitation of copper ions on silica leads to the primary formation of chrysocolla, depicted in Scheme 5.1.²⁹⁻³² Chrysocolla is a copper silicate with a lamellar structure consisting of SiO₄ tetrahedra-based layers sandwiched between discontinuous CuO₆ octahedra-based layers.²⁷ The key factor of the DP method is to prevent the precipitation away from the support surface. The DP method developed by Geus et al. using urea (CO(NH₂)₂) as the precipitating base permits the gradual and homogeneous production of hydroxide ions throughout the whole solution via the following reaction carried out at 90 °C, CO(NH₂)₂ + 3H₂O → 2NH₄⁺ + HCO₃⁻ + OH⁻, and avoids a local increase of the pH value and the precipitation of metal hydroxide in solution.³³ In the literature, DP has been successfully

applied to a variety of well-dispersed catalysts, such as silica-supported Cu/Ni/Co catalysts and titania-supported Au/Cu catalysts.^{34–38} Finely dispersed Cu/SBA-15 NPs prepared by DP have been applied to the hydroconversion of HMF to 2,5-bis(hydroxymethyl)furan (BHMF) showing high catalytic selectivities.³⁹ However, no application of such catalysts in the production of DMF from HMF has been reported in the literature so far.

In this chapter, we apply the IWI (as a reference preparation method), ISAC and DP methods to prepare monometallic Cu/SBA-15 catalysts with a metal loading of 15 wt.% (denoted as 15Cu/SBA-15_IWI, 15Cu/SBA-15_ISAC and 15Cu/SBA-15_DP, respectively). We wish, for the first time, to check the catalytic performances of the resulting non-promoted 15Cu/SBA-15_ISAC and 15Cu/SBA-15_DP catalysts in the hydrogenolysis of HMF to DMF, and to study the effect of the Cu dispersion on HMF conversion as well as on DMF selectivity and yield. On the one hand, the catalyst structure will be characterized with different techniques such as nitrogen physisorption, X-ray diffraction (XRD), temperature programmed reduction by hydrogen (H₂-TPR) and transmission electron microscopy (TEM). On the other hand, the effects of different reaction parameters (*i.e.*, reaction temperature, reaction time, HMF/Cu molar ratio) on the catalyst reactivity will be studied, the reaction conditions will be optimized, and a kinetic study of the reaction will be proposed.

5.2. Catalyst preparation

The mesoporous SBA-15 support was prepared using the procedure described in Chapter 2. A reference Cu(15 wt.%)/SBA-15 catalyst was prepared by the same method as 15Ni/SBA-15_IWIMD as described in Chapter 3 and denoted as 15Cu/SBA-15_IWIMD.

For a typical ISAC preparation of 1 g of 15(wt.%)Cu/SBA-15, 50 mL of a copper nitrate aqueous solution ((0.048 mmol/mL Cu(NO₃)₂·2.5H₂O, 98%, Sigma-Aldrich)) and 50 mL of a glycine aqueous solution (0.448 mmol/mL NH₂CH₂COOH, 99%, Sigma-Aldrich) were prepared separately, and then mixed together by stirring for 12 h at room temperature. The resulting solution was dropwisely added and mixed to 0.85 g SBA-15 powder, and then aged for 12 h. The blue gel was heated at 100 °C until water was thoroughly evaporated. A white solid was obtained and combusted at 300 °C (with a fast ramp) for half an hour in an open vessel, in an oven, in static air conditions. Then the sample was calcined at 500 °C for 6 h in an open vessel in static air conditions (temperature increase rate = 1 °C min⁻¹). The calcined catalyst is noted as 15Cu/SBA-15_ISAC.

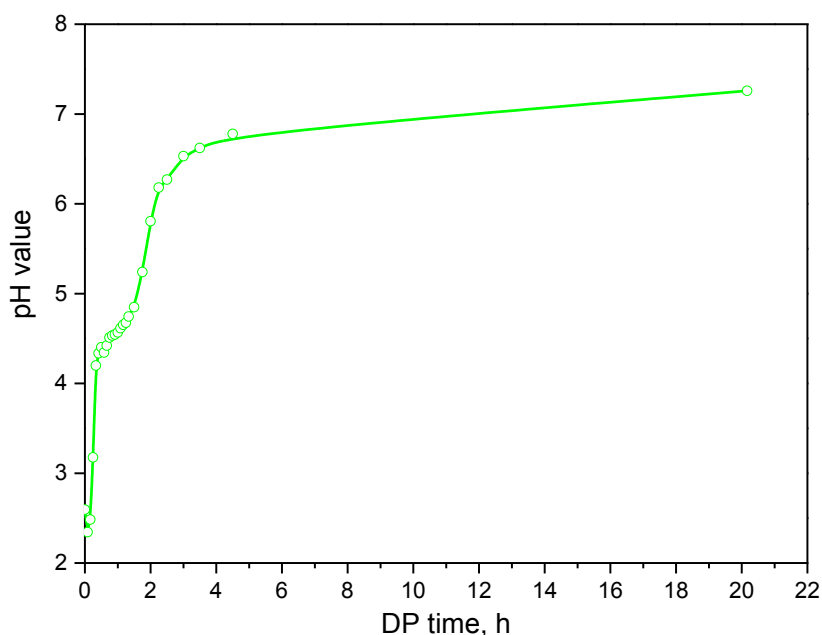


Fig. 5.1 pH evolution during the DP process for 15Cu/SBA-15 at 90 °C

For a typical DP preparation of 1 g of 15(wt.%)Cu/SBA-15, 0.85 g SBA-15 was added into 70 mL distilled water and stirred vigorously to disperse the support completely. 35 mL of copper nitrate aqueous solution (0.069 mmol/mL $\text{Cu}(\text{NO}_3)_2 \cdot 2.5\text{H}_2\text{O}$) was added into the SBA-15 suspension dropwisely. Then the temperature was increased to 90 °C. If necessary a few drops of nitric acid was added to tune the initial pH value of the solution to 2.0. Then 35 mL of urea (0.8 mmol/mL $\text{CO}(\text{NH}_2)_2$, 99%, Sigma-Aldrich) with a molar ratio of urea/copper nitrate equal to 3 was added to the slurry solution as a precipitating agent. The slurry was stirred for 24 h, cooled, filtered and washed. The precipitates were dried at 80 °C overnight and then calcined at 500 °C for 6 h with a ramp of 1.5 °C min^{-1} . The as-made catalysts (before calcination) are noted as 15Cu/SBA-15_DP_am. The calcined catalysts are noted as 15Cu/SBA-15_DP.

The deposition precipitation of copper onto the suspended SBA-15 support was monitored by pH-metry. As shown in Fig. 5.1, an initially rapid increase of pH occurred during the first hour, which was caused by the neutralization of nitric acid by the hydroxide ions generated by the hydrolysis of urea. Then at more elevated pH value (4-5), the rate of pH increase dropped for a number of reasons, such as the evaporation of ammonia, the CO_2 buffering effect, the ionization of silanol groups, the interaction between the precipitating Cu species

and the support, and the partial dissolution of SBA-15.⁴⁰⁻⁴³ The precipitation started from pH 4-5 and was completed at a pH value of 7.3 for 15Cu/SBA-15_DP. After calcination, the color of 15Cu/SBA-15_DP changed from bright blue to olive green. The bright blue color indicates the presence of hydrated octahedral Cu²⁺ ions in the as-made catalyst while the olive green color is usually attributed to the decomposed copper phyllosilicates.^{44,45}

5.3. Results and discussion

5.3.1 Characterization of the calcined catalysts

The XRD pattern at low angles for 15Cu/SBA-15_ISAC is depicted in Fig. 5.2. Diffractions in-between 0.5-2° indicates that despite the exothermic ISAC reaction, the organized pore structure is preserved. Additionally, the presence of the (210) and (300) reflections suggests an excellent long range ordering of the porosity. The decrease of the diffraction peak intensity may be related to the pore filling by CuO NPs which reduces the electron density contrast between the pores and silica walls as aforementioned in previous chapters.⁴⁶ Very small shifts of diffraction peak positions imply tiny changes in cell parameter values, which could be assigned to the fluctuation of experimental error. Nevertheless, the auto-combustion process does not result in the pore structure collapse of the SBA-15 support.

A significant difference in the low-angle X-ray diffraction pattern is observed for 15Cu/SBA-15_DP, as compared to 15Cu/SBA-15_ISAC and the SBA-15 support (Fig. 5.3). The (110), (200), (210) and (300) reflections disappear, suggesting a significant alteration of the ordered mesopore structure at long range and a poor uniformity for 15Cu/SBA-15_DP. The change in the meso-structural regularity could be assigned to the partial collapse of the ordered mesoporous structure of SBA-15 support due to the dissolution of silica walls by the harsh conditions, i.e. high pH value and high temperature, in the deposition precipitation process.^{42,47,48} The dissolution of SBA-15 in the basic medium and the reprecipitation of the silicate is the basis for the formation of the copper phyllosilicates, which at the same time also leads to a significant change in the structural characteristics of SBA-15, as indicated by the low-angle XRD characterization.

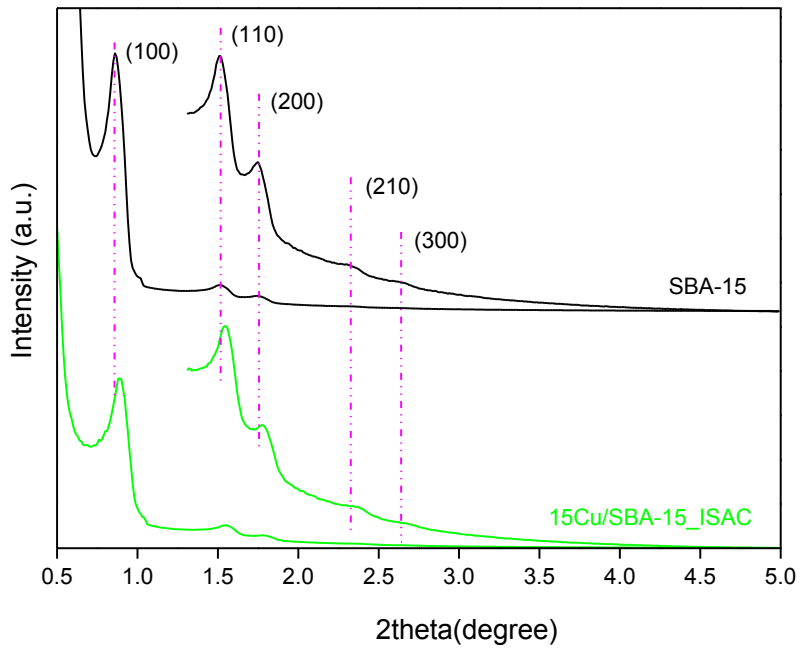


Fig. 5.2 Low angle XRD patterns for SBA-15 and 15Cu/SBA-15_ISAC

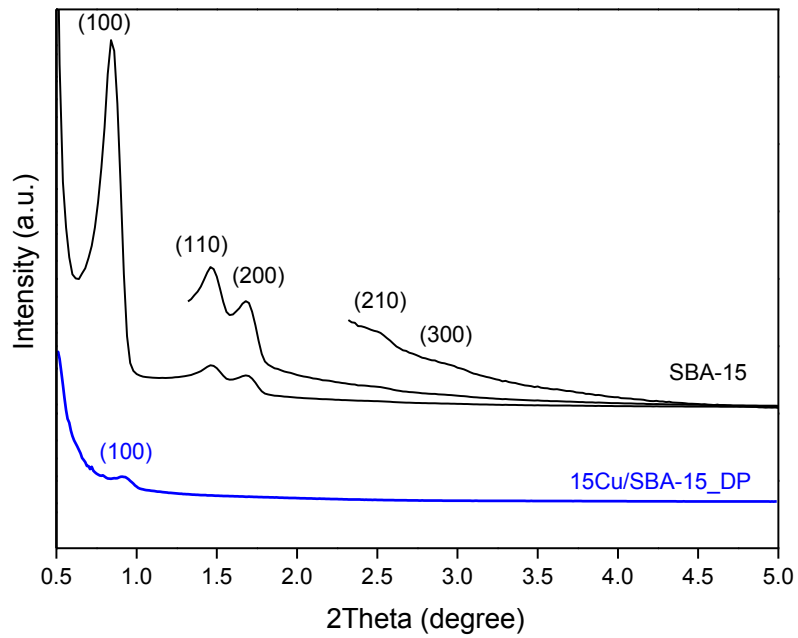


Fig. 5.3 Low angle XRD patterns for SBA-15 and 15Cu/SBA-15_DP sample

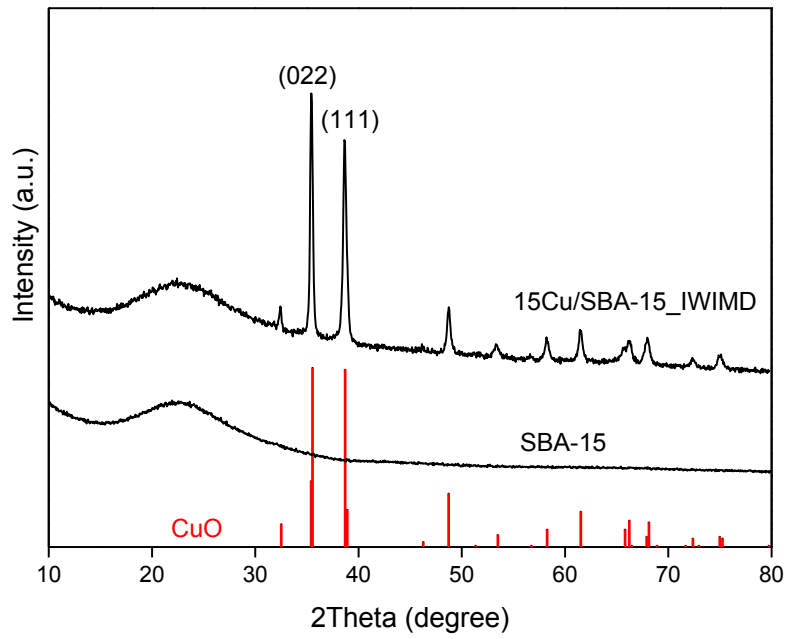


Fig. 5.4 High angle XRD pattern of the reference catalyst 15Cu/SBA-15_IWIMD

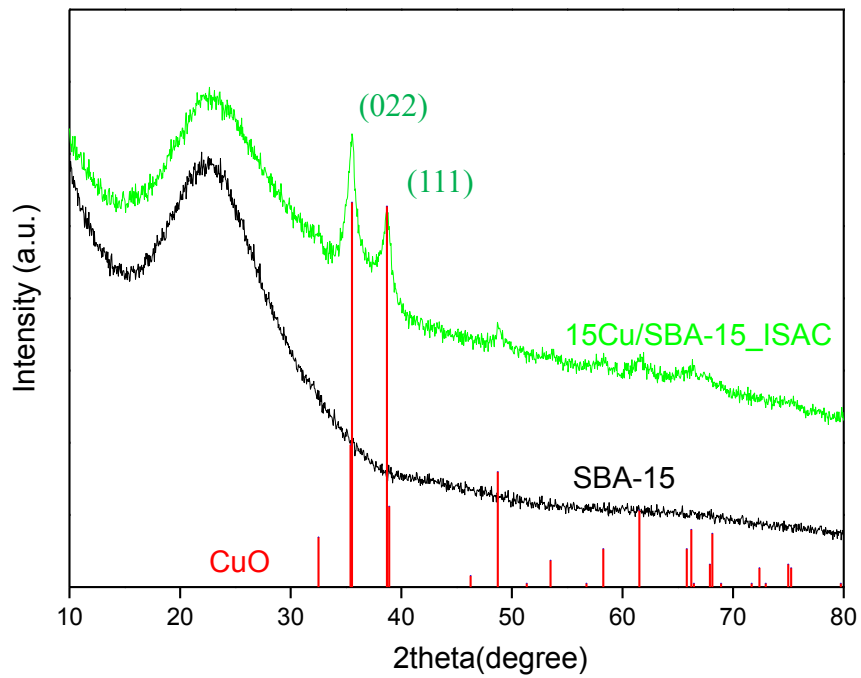


Fig. 5.5 High angle XRD patterns for SBA-15 and 15Cu/SBA-15_ISAC

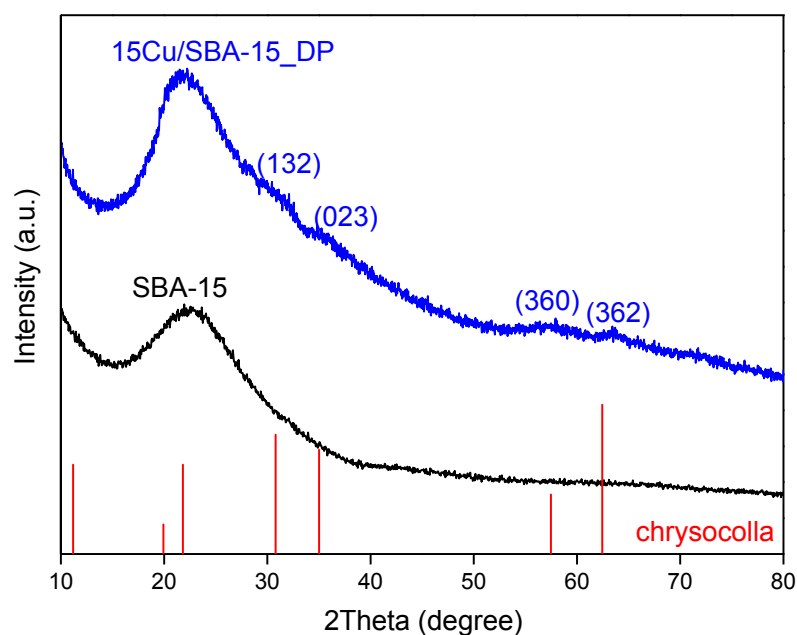


Fig. 5.6 High angle XRD patterns for SBA-15 and 15Cu/SBA-15_DP

The high-angle XRD patterns of 15Cu/SBA-15 catalysts are given in Fig. 5.4-5.6, with 15Cu/SBA-15_IWIMD used a reference. The diffraction peaks at 35.4° , 38.7° , 38.9° , 48.8° , 61.6° , 66.2° , 68.1° , recorded for 15Cu/SBA-15_IWIMD catalyst and 15Cu/SBA-15_ISAC, evidence the formation of crystalline CuO phases (JCPDS 056-0661). For 15Cu/SBA-15_IWIMD (Fig. 5.4), the sharp diffraction peaks indicate a large crystal size. The average size of CuO crystals calculated by the Scherrer equation is 64 nm. For 15Cu/SBA-15_ISAC (Fig. 5.5), the sharp end and the broad onset of the diffraction peaks indicate that both small and large CuO crystals may coexist in the sample. The average size of CuO crystals is thus smaller, which is 12.4 nm calculated by Scherrer equation, as compared to the reference catalyst. In contrast to 15Cu/SBA-15_IWIMD and for 15Cu/SBA-15_ISAC, no sharp diffraction peaks can be observed for 15Cu/SBA-15_DP (Fig. 5.6). Instead, a group of weak and broad diffraction peaks which could be indexed to copper phyllosilicate (chrysocolla, JCPDS 027-0188) is observed, implying that part of copper phyllosilicate formed during the DP process remains in the catalyst after the calcination process. However, it is difficult to calculate the size of the copper phyllosilicate crystals due to the low intensity and broadness of these peaks. In addition, in contrast to 15Cu/SBA-15_ISAC, CuO is not detected by XRD for 15Cu/SBA-15_DP. This might imply that CuO crystals, if existing, are highly dispersed over 15Cu/SBA-15_DP.

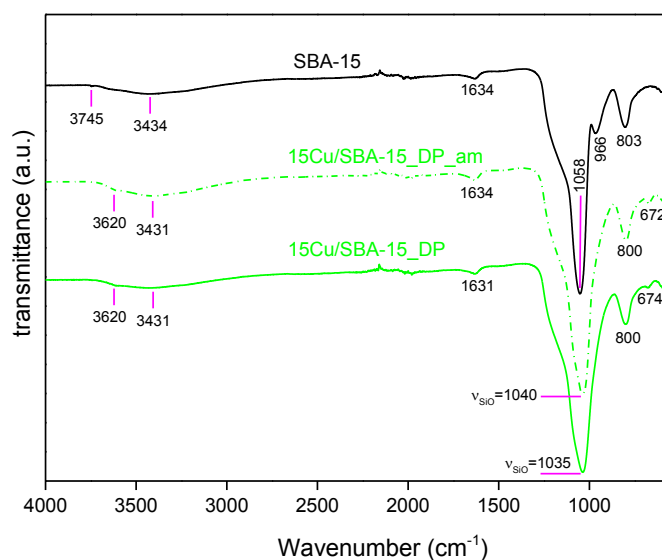


Fig. 5.7 IR spectra for 15Cu/SBA-15_DP and 15Cu/SBA-15_DP_am

The presence of the copper phyllosilicates in 15Cu/SBA-15_DP_am and 15Cu/SBA-15_DP was further checked by IR spectroscopy. Chrysocolla is characterized by the δ_{SiO_4} band of SiO_4 tetrahedra at 1024-1040 cm^{-1} , the ν_{OH} band of structural OH at 3620 cm^{-1} , and the δ_{OH} band of OH groups linked to 3 Cu^{2+} ions at 670-675 cm^{-1} .^{43,30,49} The absorption of SiO_4 tetrahedra is usually disturbed by the intense absorption peak of the ν_{SiO} band of amorphous silica at 1100-1000 cm^{-1} .⁵⁰ On Fig. 5.7, the broad bands at 3431-3434 cm^{-1} and 1631-1634 cm^{-1} are due to the H-O-H vibrations of adsorbed water, the absorption bands near 3745 and 966 cm^{-1} are assigned to the stretching and bending vibration of Si-OH; the bands near 1035-1058 cm^{-1} and 800-803 cm^{-1} are related to the Si-O bonds of amorphous silica.⁵⁰⁻⁵³ Compared to SBA-15, three changes can be observed for the DP solids. First, the disappearance of the Si-OH absorption bands near 3747 cm^{-1} and of the Si-OH absorption bands at 966 cm^{-1} for 15Cu/SBA-15_DP implies the consumption of the silanol groups by the formation of copper phyllosilicate. Second, an obvious red shift of the absorption band of SiO_4 tetrahedra from 1058 to 1040 cm^{-1} (for 15Cu/SBA-15_DP_am) implies that there is a relatively strong interaction between copper species and silica.⁴⁹ Third, in line with XRD, the absorption bands near 3620 cm^{-1} and 672-674 cm^{-1} observed for the two DP solids directly indicates the existence of copper phyllosilicates before and after calcination. Besides, the intensity of the absorption bands near 3620 and 672-674 cm^{-1} for the calcined sample is weaker than those of the as-made sample, which implies that some of the copper phyllosilicates are decomposed during calcination.

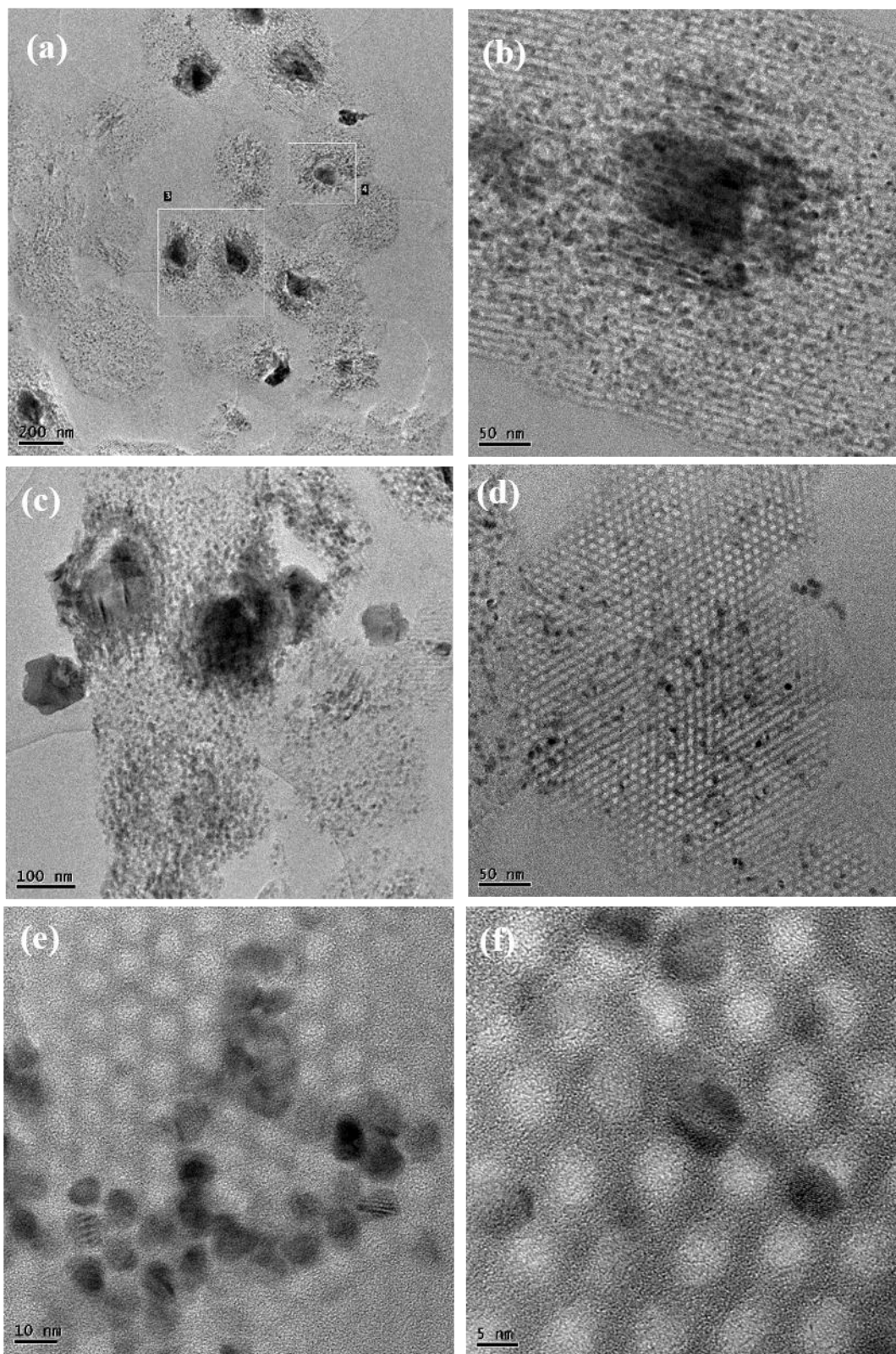


Fig. 5.8 Representative TEM images recorded for 15Cu/SBA-15_ISAC

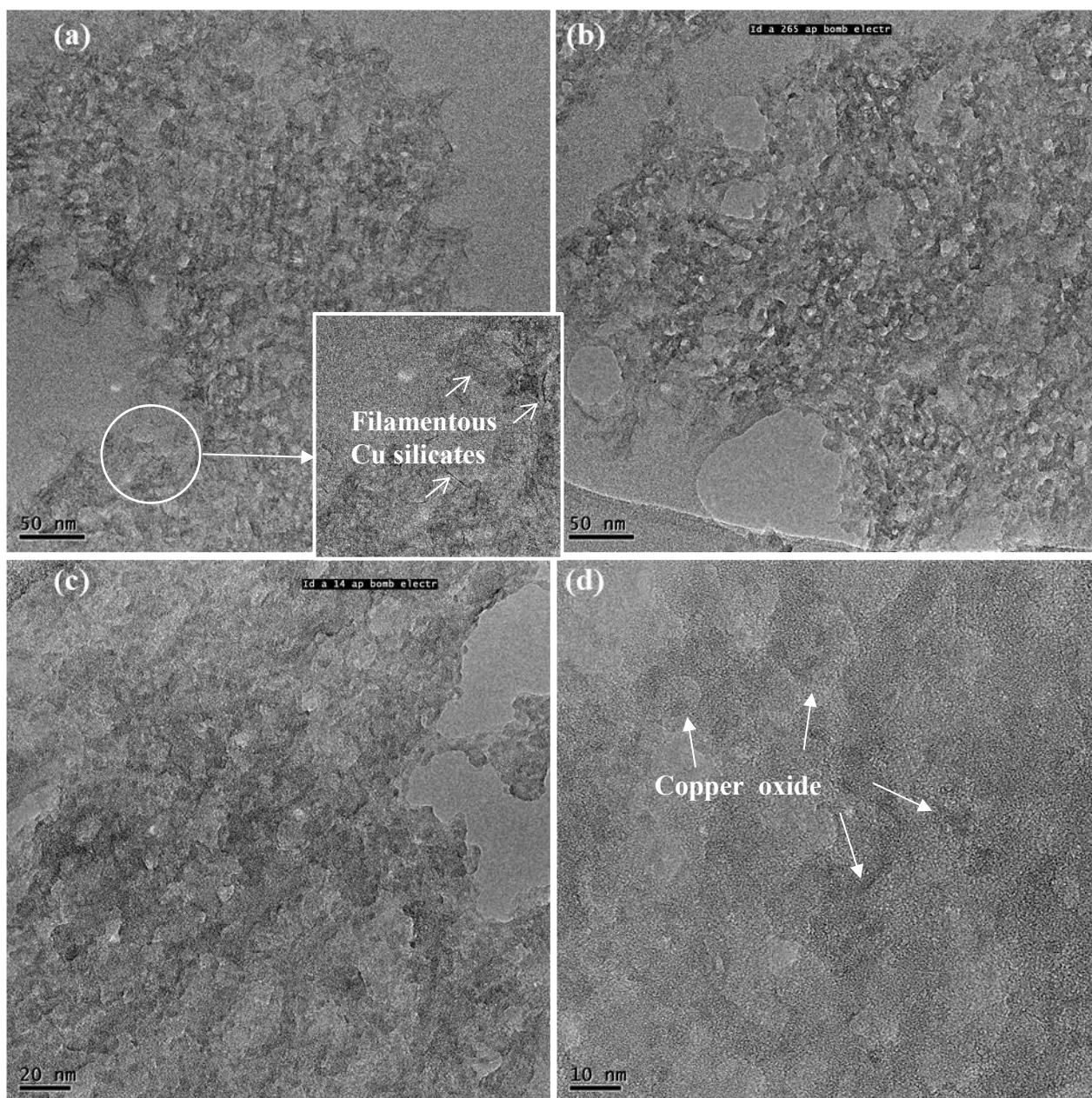


Fig. 5.9 Representative TEM images recorded for 15Cu/SBA-15_DP

The catalyst morphology was characterized by TEM. The microscopy images give direct evidence of the broad distribution of CuO particle sizes in 15Cu/SBA-15_ISAC as shown in Fig. 5.8. The solid shows the typical hexagonal SBA-15 mesoporous structure with a long-range order, confirming the results obtained by XRD at low angles. Besides, both open mesopores and blocked mesopores exist in the structure. Two types of metal oxide NPs with different morphologies can be observed. Part of copper oxide forms large aggregates at the mesopore openings at the edge of the SBA-15 grains, recrystallized out of the support

porosity (Fig. 5.8 a, c). Their size is quite large, up to 120 nm. Part of copper oxide is confined within the channels, generating nanorods (Fig. 5.8 b, d-f). Their diameter is about 8.0 nm, which is close to the pore size of the support, while their length is up to 50 nm. In some cases, the rod-like NPs have grown into adjacent mesopores and appear to be interconnected by the secondary porosity (Fig. 5.8 e). A careful observation reveals that the nanorods are actually aggregates of smaller CuO particles (Fig. 5.8 b). The microscopy characterization thus shows that the ISAC preparative procedure led to the formation of both external CuO aggregates and mesopore-confined smaller CuO particles.

As for 15Cu/SBA-15_DP, a very different catalyst morphology is observed as shown in Fig. 5.9. First, the typical long-range order of the mesoporous structure of SBA-15 cannot be observed any more. Instead, silica residues appear as full of irregular holes (Fig. 5.9 b), though the typical morphology of SBA-15 is partially preserved in some areas (Fig. 5.9 a). These results directly confirm the severe dissolution of the SBA-15 support during the DP process. Additionally, two types of nanoparticles with different morphologies can be observed. On the one hand, under high resolution conditions, very small and dark spots could be recognized in the dissolved silica zones (Fig. 5.9 c, d), which may be copper oxide particles issued from the partial decomposition of the Cu silicates during calcination. These particles are homogeneously and densely dispersed on the catalyst surface (Fig. 5.9 c) and are too small to be detected by XRD as supposed above. On the other hand, filamentous particles could also be observed (Fig. 5.9 a, inset). Most of these species exist as a single sheets and few of them as double sheets, which corresponds to the filamentous copper silicates. These results confirm that the deposition precipitation route leads to the stabilization of the transition metal in silicate phases, and to the formation of highly-dispersed CuO particles after calcination, which is consistent with the IR and XRD results.

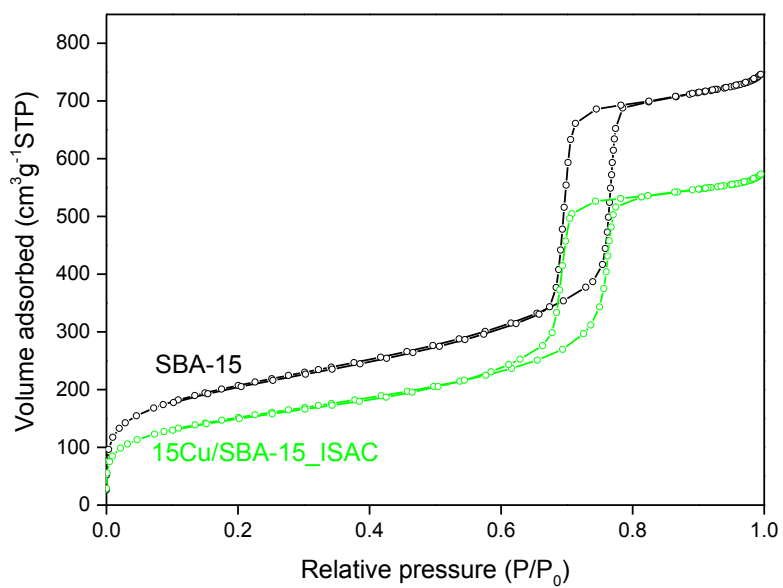


Fig. 5.10 N₂ physisorption isotherms for SBA-15 and 15Cu/SBA-15_ISAC

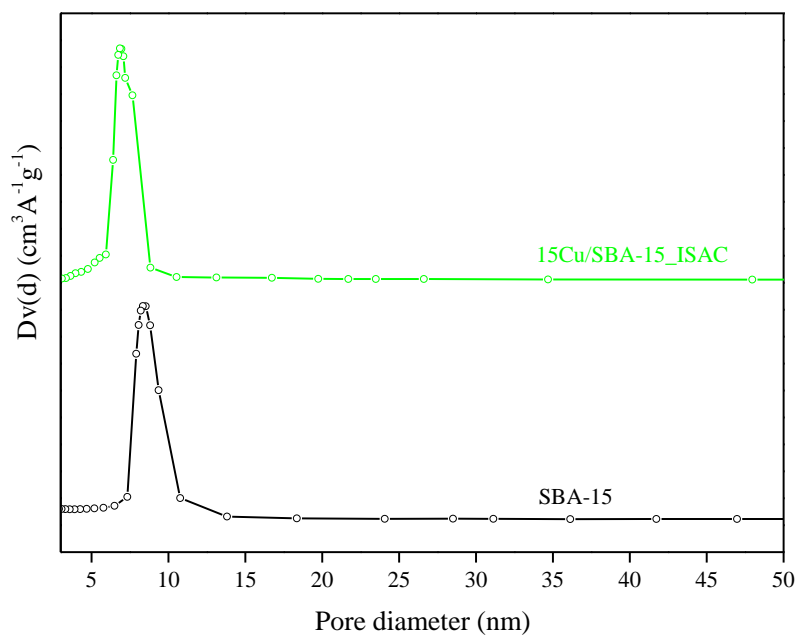


Fig. 5.11 Pore size distribution curves of SBA-15 and 15Cu/SBA-15_ISAC calculated using the B.J.H. model applied to the desorption branch

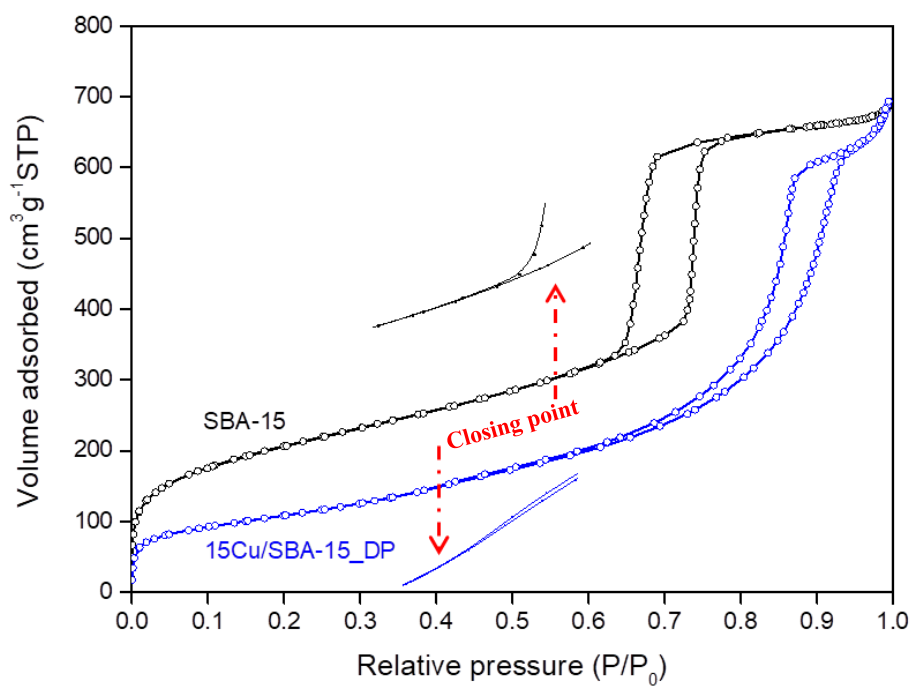


Fig. 5.12 N₂ physisorption isotherms for SBA-15 and 15Cu/SBA-15_DP

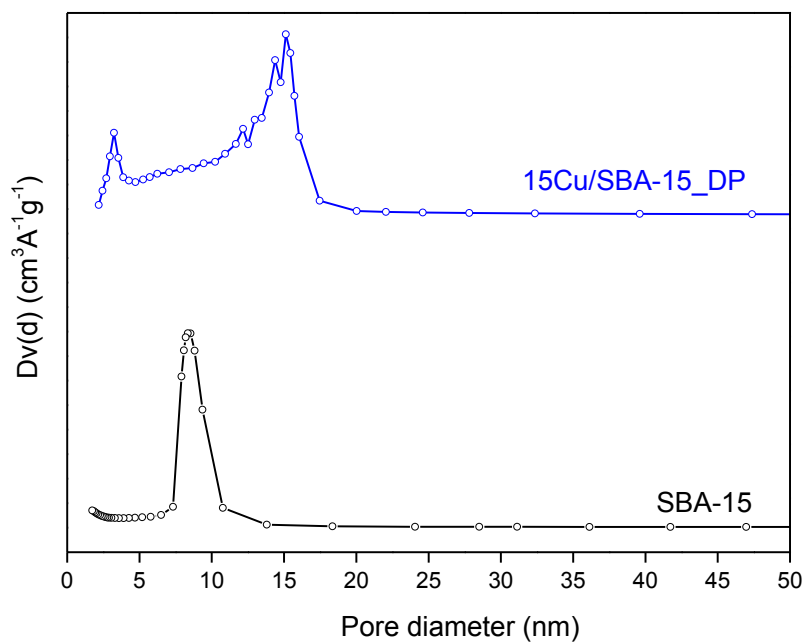


Fig. 5.13 Pore size distribution curves of SBA-15 and 15Cu/SBA-15_DP calculated using the B.J.H. model applied to the desorption branch

Table 5.1 Physico-chemical properties of 15Cu/SBA-15_ISAC and 15Cu/SBA-15_DP

Samples	S_{BET} , ^a m ² /g	V_t , ^b cm ³ /g	D_p , nm
SBA-15	732	1.2	8.3
15Cu/SBA-15_ISAC	632	0.9	6.8
15Cu/SBA-15_DP	331	0.9	3.2, 15.1

^a: B.E.T. surface area per gram of SBA-15 support; ^b: total pore volume per gram of SBA-15 support.

The textural properties of the support and of the 15Cu/SBA-15_ISAC and 15Cu/SBA-15_DP materials extracted from nitrogen physisorption experiments are gathered in Table 5.1 while the isotherms are presented in Fig 5.10-5.13. As for 15Cu/SBA-15_ISAC, the isotherm is of type IV with H1-type hysteresis loops (Fig. 5.10), which is typical of a mesoporous SBA-15 structure with a narrow pore size distribution of the cylindrical pores as aforementioned in previous chapters. The isotherm curve is observed to shift down along the y-axis, indicating a decrease of the pore volume, as shown in Table 5.1. This evolution arises as a result of the partial blocking of the primary mesopores with confined rod-like copper particles, which is consistent with the low-angle XRD and TEM results. As compared to the SBA-15 support, the closing of the hysteresis loop extends to a lower relative pressure value (from 0.67 to 0.54) due to the delayed capillary effect on the desorption branch, indicating the forming of ink-bottle mesopores. The B.J.H. pore diameter (Table 5.1) as well as the pore size distribution (as shown in Fig. 5.11) indeed displays a slight shift of the pore size to lower values after the introduction of CuO particles. In conclusion, after formation of copper oxide NPs by the ISAC method, the main characteristics of SBA-15 are retained while the confinement of the rod-like Cu NPs inside the porosity leads to the decrease of the surface area and of the pore volume.

For 15Cu/SBA-15_DP, the structure change caused by the deposition precipitation process is reflected by the nitrogen physisorption. As shown in Fig. 5.12, 15Cu/SBA-15_DP exhibits a type IV adsorption/desorption isotherm, but several significant difference could be observed between 15Cu/SBA-15_DP and SBA-15: (i) a marked shift of the hysteresis position to higher relative pressure (P/P_0), which indicates an increase in pore diameter; (ii) the delay in the closing of the desorption branch to 0.4 indicates the generation of small mesopores; (iii) a transformation of the hysteresis loop from H1 type (for SBA-15, massive uptake or desorption of N_2 at a given pressure) to H2 type-like, implying the lesser regularity of the catalyst structure, as well as the formation of slit-like pores, which is consistent with the formation of disordered, lamellar structures as reported in the literature.^{27,44,45} The lesser uniformity of the pores is directly reflected by the pore size distribution curve as shown in Fig. 5.13: a very wide pore size distribution with two visible maxima for 15Cu/SBA-15_DP, indicating that two distinct families of pores contribute to the overall pore volume. The first one shows up at 3.2 nm. The presence of this peak could be attributed to the formation of the slit-like pores. Similar features have also been observed by other authors in the pore size distribution of Cu/SBA-15 prepared by DP.^{31,42,54-56} The second one as the main peak shows up at 15.1 nm, which is larger than for SBA-15 at 8.3 nm. The shift of the most probable pore sizes of 15Cu/SBA-15_DP samples to higher values could be attributed to the formation of the larger pores generated by the dissolution of SBA-15 support. In summary, the porosity analysis suggests that the DP process resulted in a complete degradation of the structure of silica upon dissolution of SBA-15 and formation of lamellar phases, which led to lower surface area and larger (in average) and less uniform pores of 15Cu/SBA-15_DP as compared to the SBA-15 support as well as to 15Cu/SBA-15_ISAC.

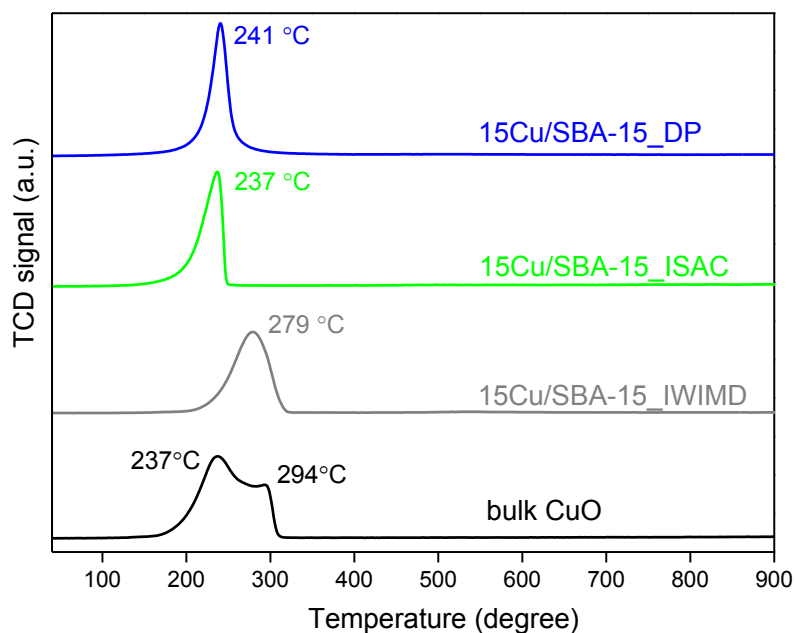


Fig. 5.14 H₂-TPR profile for calcined 15Cu/SBA-15 catalysts

The reducibility and speciation of the generated oxidic phases have been investigated by H₂-TPR, as shown in Fig. 5.14. Unsupported bulk CuO presents a broad reduction peak with a primary peak at 237 °C and a shoulder peak at 294 °C. According to the literature, the reduction temperature of CuO is highly dependent on the particle size, lower reduction temperatures being associated to smaller particles while higher reduction temperatures are related to large particles.⁵⁷⁻⁵⁹ Thus the broad reduction peak of bulk CuO is probably caused by a wide distribution of the particle sizes, with different kinetics of reduction. The reference catalyst 15Cu/SBA-15_IWIMD showed a reduction peak at 279 °C. In contrast, 15Cu/SBA-15_ISAC and 15Cu/SBA-15_DP were reduced at much lower temperatures (241 and 237 °C, respectively), implying a better dispersion of copper species in this two catalysts than the reference catalyst, which is consistent with the XRD and TEM results.

5.3.2 Characterization of the reduced catalysts

The existing state of copper species after reduction (300 °C, 2 h) and exposure to air was checked by high-angle XRD, as depicted in Fig. 5.15. For the reference 15Cu/SBA-15_IWIMD catalyst, the intense diffraction peaks at 50.7, 59.3 and 88.8°, corresponding to the reflection of the (111), (200) and (220) planes, respectively, indicated the presence of metallic copper crystals (JCPDS 04-0836). The sharp shape of these peaks implied a very large size of Cu NPs, which was evaluated as 60 nm through the Scherrer equation. For 15Cu/SBA-15_ISAC, diffraction by metallic Cu crystals was also detected. Peaks also exhibited shapes with sharp ends and broad onsets like the calcined sample, implying the existence of both large and small Cu NPs in the catalyst. The average size of the metallic Cu crystals was calculated as 23.9 nm. Besides, the diffraction peaks at 42.6 and 72.7°, indexed to the reflections of (111) and (220) planes, respectively, suggested the presence of Cu₂O (JCPDS 78-2076). The other characteristic peaks of Cu₂O at 34.5, 49.6 and 88.1° are superimposed with the diffraction peaks of silica and of metallic copper. The mean size of Cu₂O crystals given from the broad peaks by the Scherrer equation is 4.7 nm, much smaller than the metallic Cu crystals. According to the TPR profile of 15Cu/SBA-15_ISAC, CuO should be completely reduced at 280 °C after 2 h. It is thus likely that the smaller metallic Cu particles are easily oxidized once exposed to air during XRD characterization, and this group of Cu particles formed the Cu₂O phases. For 15Cu/SBA-15_DP, the broad diffraction peaks all corresponded to Cu₂O crystals. The average size of the Cu₂O crystals was 5 nm, which was close to the size of the Cu₂O crystals in 15Cu/SBA-15_ISAC. The Cu₂O crystals in 15Cu/SBA-15_DP should also derive from the exposure of small metallic Cu crystals to air during XRD characterization.

The morphology of reduced 15Cu/SBA-15 samples was characterized by TEM (Fig. 5.16-5.18). As expected, Cu particles in the reference 15Cu/SBA-15_IWIMD catalyst existed in large aggregates (Fig. 5.16).

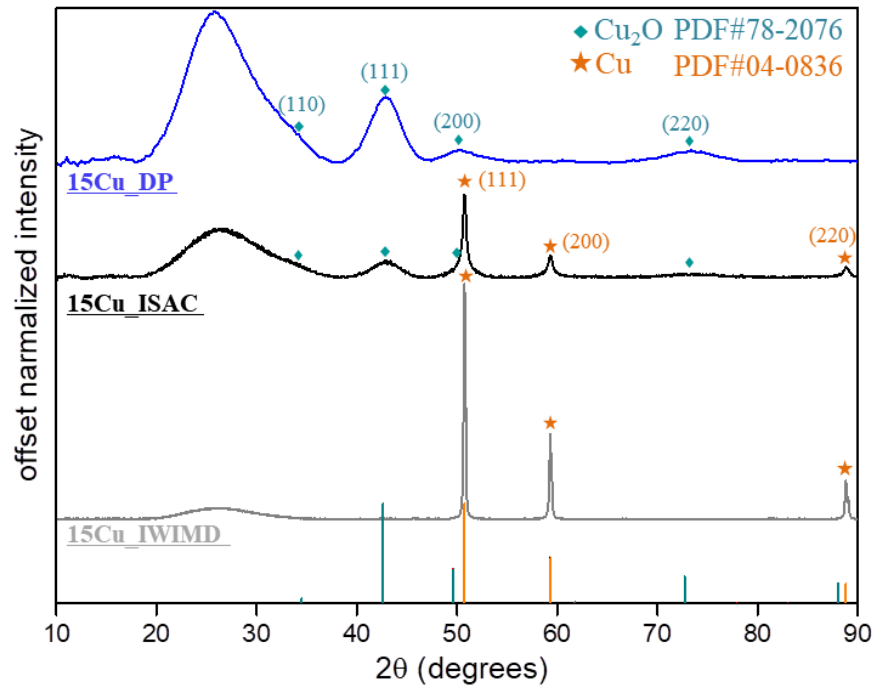


Fig. 5.15 High-angle XRD patterns of 15Cu/SBA-15 catalysts, reduced at 300 °C (Co K α source)

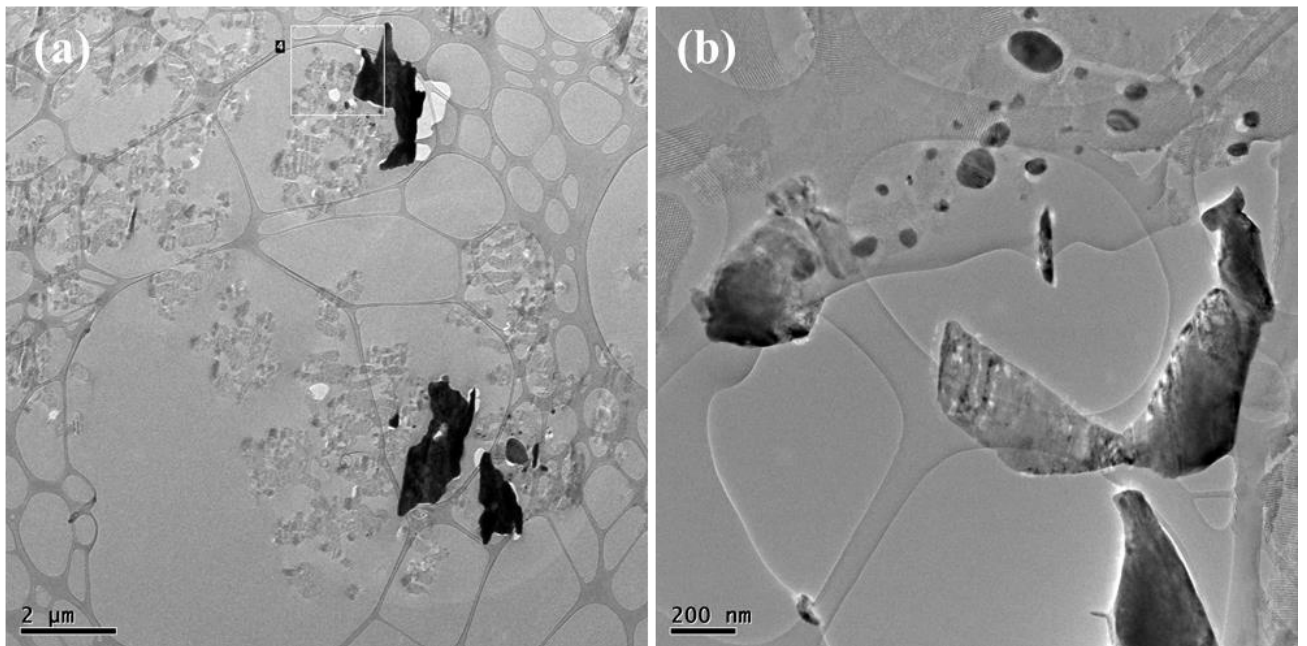


Fig. 5.16 Representative TEM images of reduced 15Cu/SBA-15_IWI

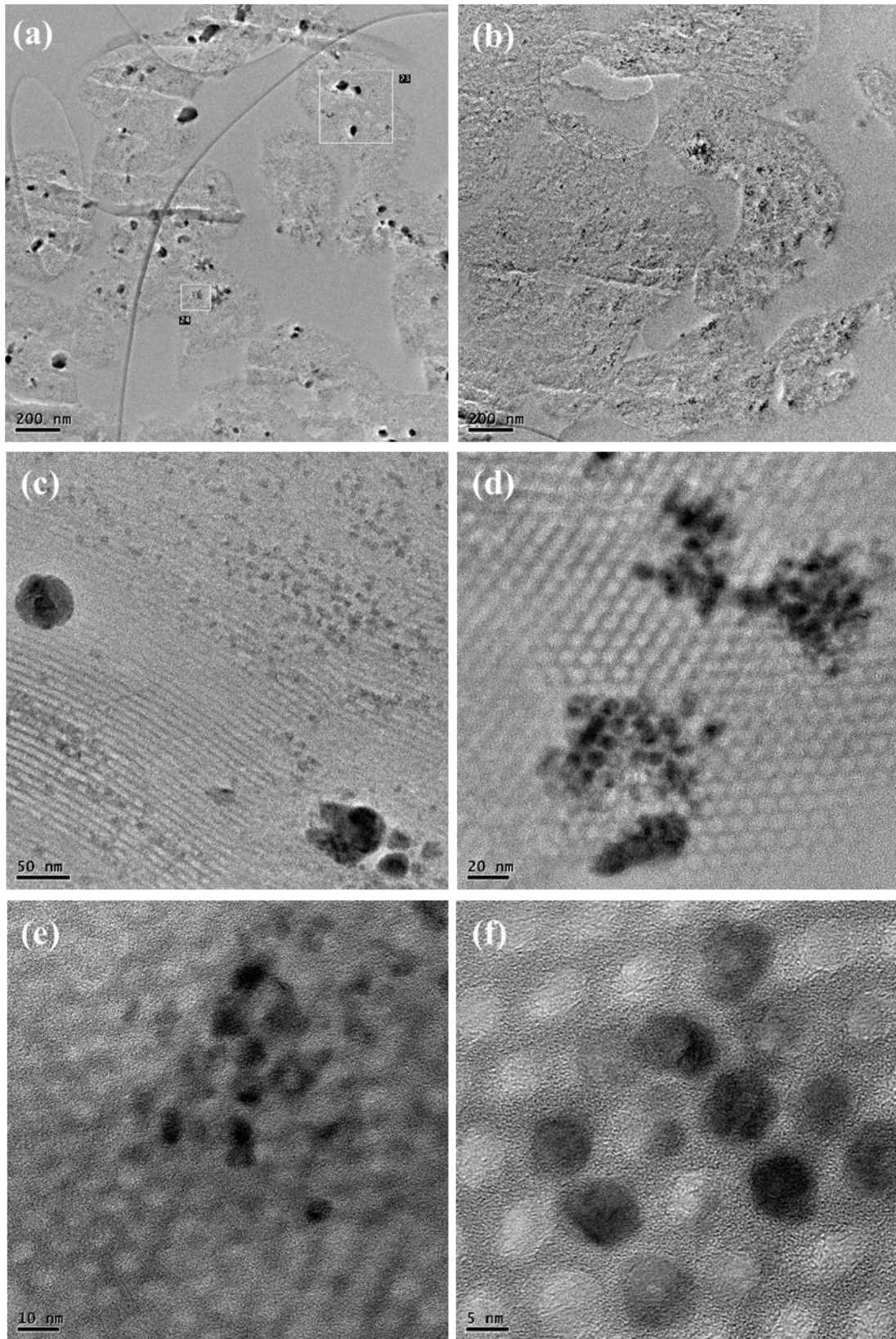


Fig. 5.17 Representative TEM images of reduced $^{15}\text{Cu}/\text{SBA-15}_{\text{ISAC}}$

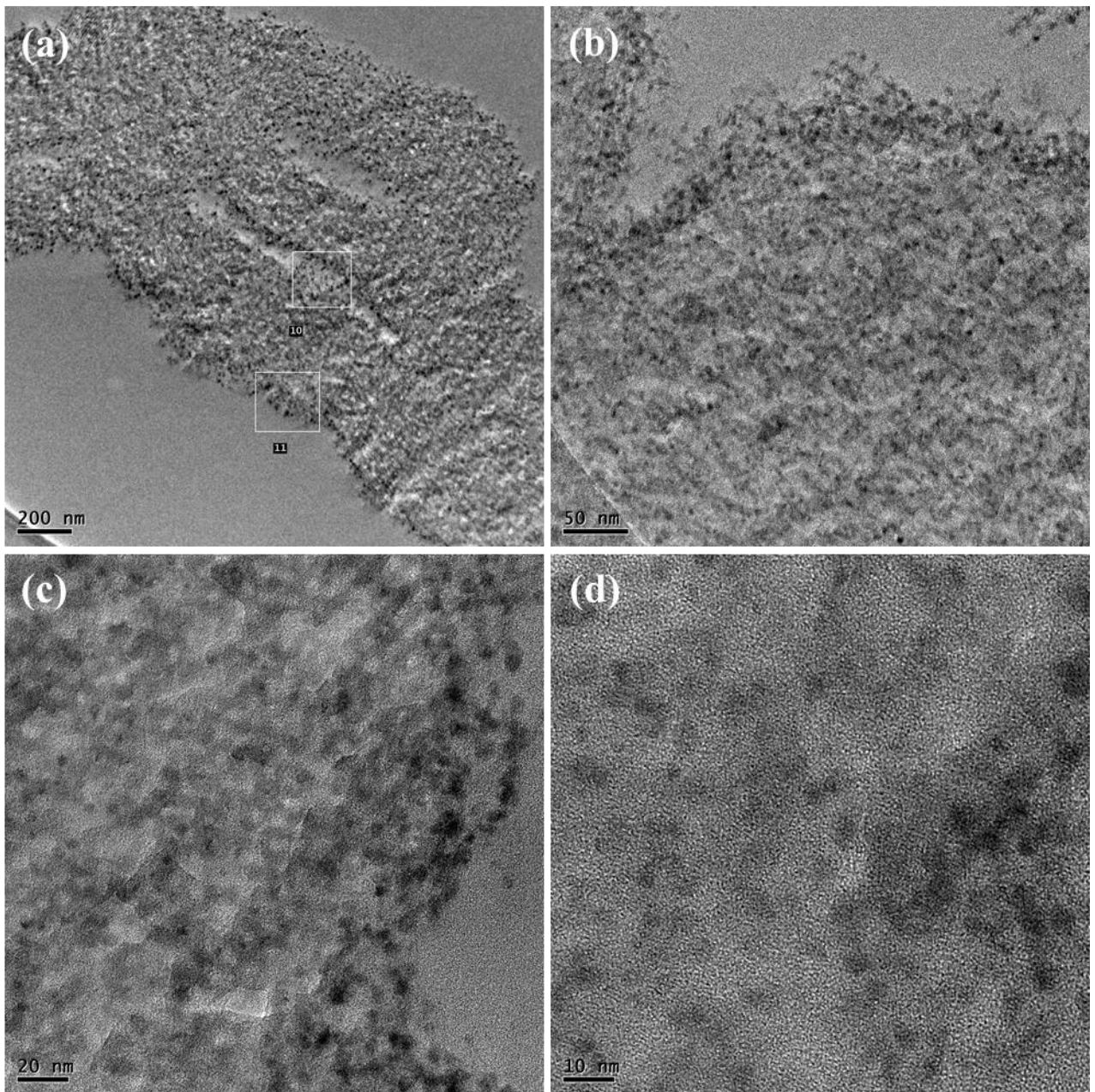


Fig. 5.18 Representative TEM images of reduced 15Cu/SBA-15_DP

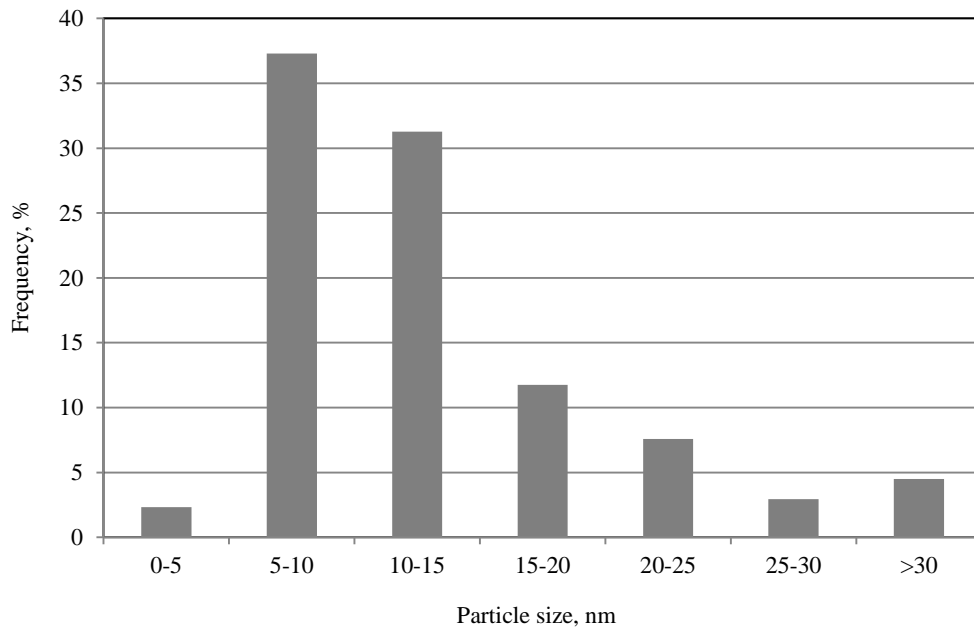


Fig. 5.19 Particle size distribution in 15Cu/SBA-15_ISAC

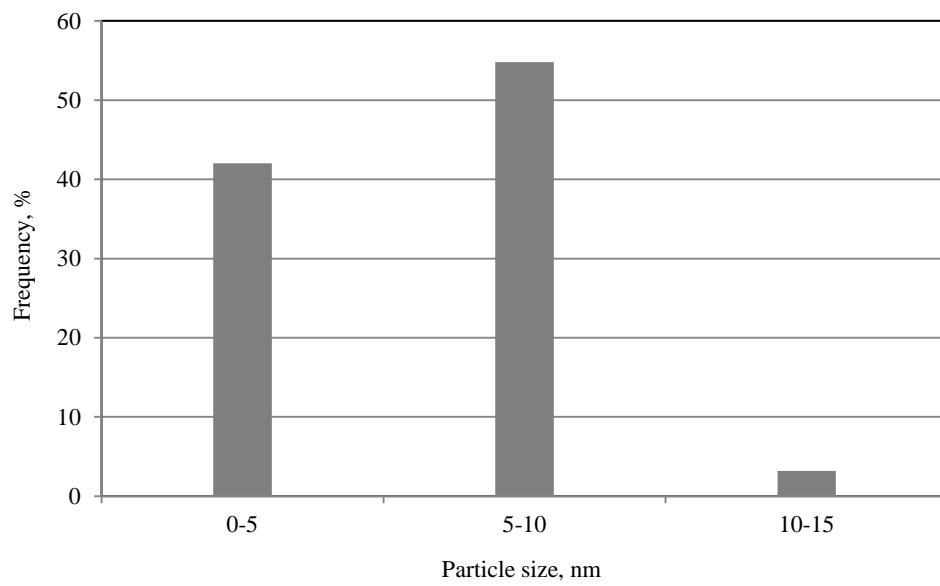


Fig. 5.20 Particle size distribution in 15Cu/SBA-15_DP

For 15Cu/SBA-15_ISAC, the catalyst morphology is similar to that of the calcined sample (Fig. 5.17). Three types of copper particles (Cu^0 and Cu_2O) remain in the catalyst: large Cu particles recrystallized out of the support porosity (Fig. 5.17 a, c); medium-sized Cu aggregates at the mesopore openings at the edge of the SBA-15 grains (Fig. 5.17 a, d); small copper particles, probably oxidized in air, confined within the support channels (Fig. 5.17 c-f). As indicated above, the mesopore-confined small particles should be Cu_2O particles. The particle size ranges from 3 to 50 nm, and around 40% of the particles (< 10 nm) are confined in the mesopores (Fig. 5.19). For 15Cu/SBA-15_DP, the catalyst reduction leads to the formation of small and homogeneously dispersed Cu_2O particles on the catalyst surface (Fig. 5.18). The filamentous particles observed in the clichés of the calcined sample are hardly observed here. The particle size histogram of 15Cu/SBA-15_DP in Fig. 5.20 shows that over 40% of the particles have a particle size smaller than 5 nm, and over 50% range between 5 and 10 nm. As compared to 15Cu/SBA-15_ISAC, applying the DP method leads to a marked enhancement of the dispersion of copper particles.

5.3.3 Preliminary exploration of reaction conditions

Due to its intermediate metal dispersion level among the three catalysts, anticipated to lead to an intermediate reactivity, 15Cu/SBA-15_ISAC was used to determine the reaction conditions that would lead to a significant production of DMF from HMF. The catalytic tests from a set of orthogonal experiments were performed in autoclaves from an Autoplant-Chemspeed instrument at the Realcat platform in Lille, as described in Chapter 2. 1,4-Dioxane was selected as the reaction medium, like in the previous chapters. The process parameters (i.e., reaction temperature, H_2 pressure and HMF/Cu molar ratio) and their values were selected on the basis of preliminary studies.¹ The same temperature (180-210-240 °C) and H_2 pressure range (15-30-45 bar) were chosen compared with 15Ni/SBA-15_IWIMD (section 3.2.3), but the HMF/Cu molar ratio was different, ranging from 5 to 100, covering the range of the ratios found in the literature. Once reaction parameters were determined, the design of experiments involving a L9 orthogonal array (3 levels ^ 3 factors: P, HMF/Cu molar ratio) was constructed in the same way as described in Chapter 3. The corresponding parameters, the catalytic results of HMF conversion and distribution of main products under the varying reaction conditions are summarized in Table 5.2.

Table 5.2 L9 orthogonal design for process parameters, and corresponding conversions and product distributions^a

Expt. no	T/°C	P/bar	HMF/Cu		conv./%	yield/%				carbon balance/%
			molar ratio	cat./g		DMF	BHMF	MFOL	MFFR	
1	180	15	100	0.016	4.2	0.8	0.0	0.7	0.0	97
2	180	30	5	0.338	94.7	43.1	5.3	11.3	0.7	54
3	180	45	50	0.034	33.0	4.5	8.0	0.0	0.9	80
4	210	15	5	0.338	100.0	59	0.0	1.2	1.6	61
5	210	30	50	0.034	44.8	5.4	10.0	0.0	1.1	72
6	210	45	100	0.016	37.1	4.6	23.5	0.0	1.8	90
7	240	15	50	0.034	83.0	12.5	58.0	0.0	3.4	89
8	240	30	100	0.016	21.8	1.6	10	2.1	0.0	92
9	240	45	5	0.338	100.0	54.5	0.0	0.0	1.2	56

^a: all the catalytic tests were performed in autoclaves from an Autoplant-Chemspeed instrument with 0.15 mmol/mL HMF in 25 mL 1,4-dioxane solution for 8 h.

These results show that: (i) DMF, BHMF, MFFR and MFOL were detected as products in these tests, with DMF and/or BHMF as the major products, and MFFR and MFOL as the minor products: both hydrogenation and hydrogenolysis of the C-OH bond can be favored by 15Cu/SBA-15_ISAC; (ii) low HMF/Cu molar ratios (≤ 50), in other terms large catalyst quantities (≥ 0.017 g), are required for an efficient conversion of HMF, indicating the limited activity of 15Cu/SBA-15_ISAC; (iii) however, a poor carbon balance occurred for low HMF/Cu molar ratios at each temperature level (Table 5.2, Entries 2, 4 and 9), possibly due to the polymerization of the intermediate products; (iv) HMF/Cu molar ratio (in other terms catalyst quantity) and temperature are the main factors influencing HMF conversion and the formation of BHMF and DMF, while H₂ pressure has a minor effect. As compared with 15Ni/SBA-15_IWIMD: (i) 15Cu/SBA-15_ISAC preferably catalyzes the hydrogenation/hydrogenolysis of the pendant groups of HMF; (ii) 15Cu/SBA-15_ISAC shows limited furan ring hydrogenation ability (no DMTHF detected).

One out of the nine tests is noteworthy. In Expt. No. 4, a DMF yield of 59% at 100% HMF conversion was obtained at 210 °C under 15 bar H₂ with a HMF/Cu molar ratio of 5, giving a maximum DMF selectivity (59%) among the selected range of reaction conditions, though the carbon balance under these reaction conditions is low. This test result reveals that the efficient hydrogenolysis of HMF over 15Cu/SBA-15_ISAC requires a relatively high

reaction temperature (210 °C) due to the high activation energy for C-O bond cleavage.⁶⁰ Besides, the low HMF/Cu molar ratio (5) used here indicates that a relatively high catalyst loading (0.338 g catalyst) is required for high DMF yields due to the low intrinsic activity of Cu. Nevertheless, this is an interesting result considering that there is neither active promoter nor active support used in the monometallic 15Cu/SBA-15_ISAC sample.

5.3.4 Effect of the HMF/Cu molar ratio

The effects of the HMF/Cu ratio on the catalytic reactivity of the 15Cu/SBA-15_ISAC sample were further studied in a Parr batch reactor at IC2MP, Poitiers. Since the reactor used here has a volume of half that of the batch reactor used in the previous tests, the solution volume was decreased to 12.5 mL, while keeping the other parameters unchanged. The detailed procedure of the catalytic tests is described in Chapter 2. The results are given in Fig. 5.21 (a-c).

Setting the HMF/Cu ratio to 5 (Fig. 5.21 (a)), HMF was completely converted in the first half hour, giving BHMF as the main product (52% yield) and the two products of successive hydrogenolysis, MFOL (18% yield) and DMF (26% yield) as secondary products. Only a slight amount of MFFR was detected. This indicated that during this period the selective hydrogenation of the C=O bond was the primary reaction. Prolonging the reaction time to 2 h resulted in the gradual decrease of BHMF yield to 23.1% and the increase of DMF yield and MFOL yield to 44.1% and 27%, respectively. Since BHMF could be converted into MFOL and DMF through selective cleavage of the C-O bond (as described in Scheme 3.1 in Chapter 3), the successive hydrogenolysis of BHMF to MFOL and of MFOL to DMF were dominant during this period. Further extending the reaction time to 6 h led to continuous decrease of BHMF yield to 5.6% and continuous increase of DMF yield to 68% and a decrease of MFOL yield to 9%. When the reaction time was extended to 8 h, the yields of the intermediate products further decreased, the carbon balance based on the identified products decreased, while a falling down of DMF yield occurred, suggesting that side reactions forming heavy products from BHMF and MFOL, as well as the ring opening of DMF, became the primary process during this process.^{61,62}

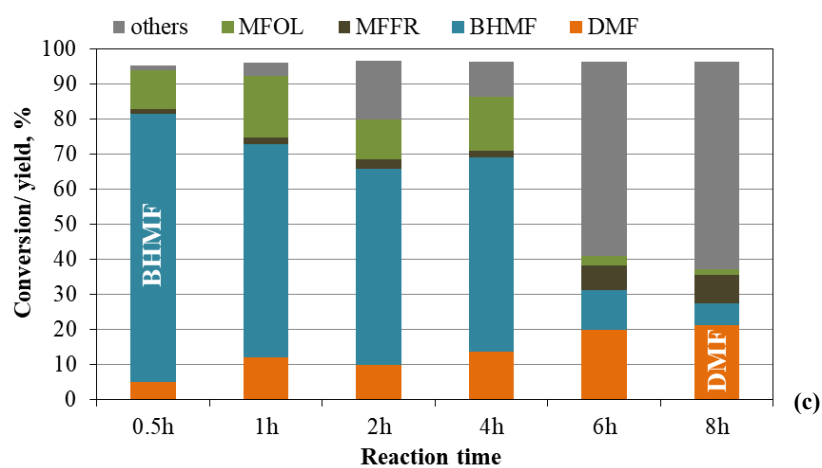
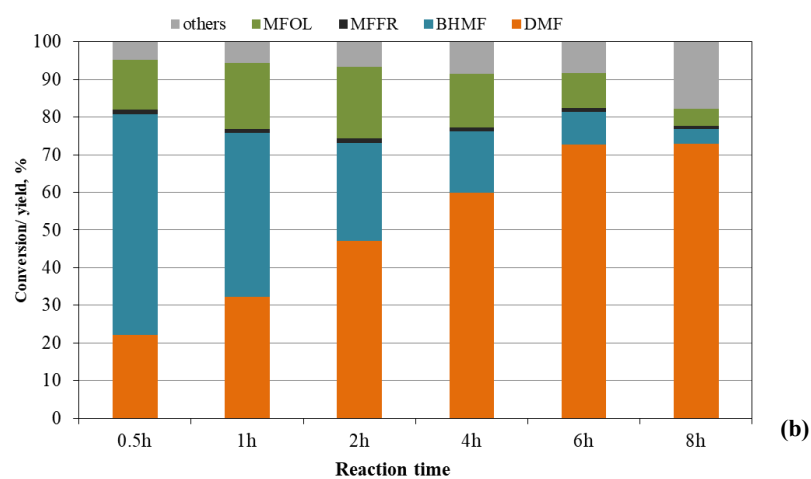
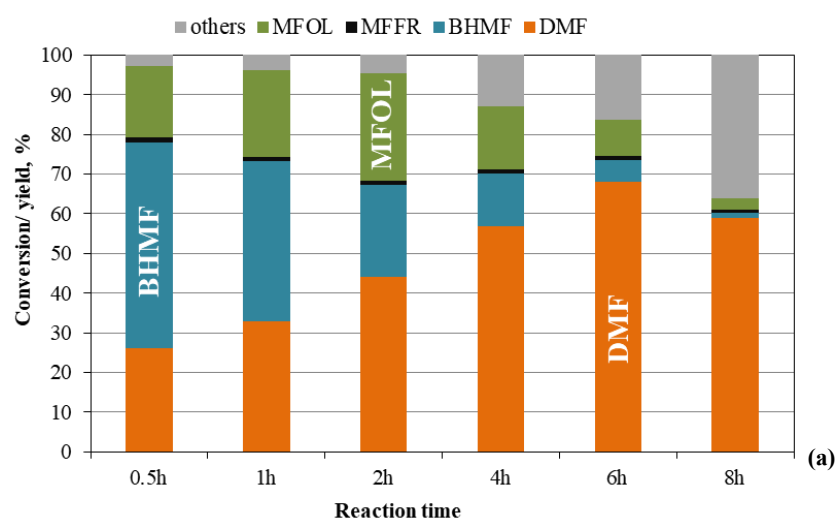


Fig. 5.21 Evolution of the product distributions with reaction time over 15Cu/SBA-15_ISAC using different HMF/Cu ratios (210 °C, 15 bar, 0.15 mmol/mL HMF in 12.5 mL 1,4-dioxane): (a) HMF/Cu ratio of 5; (b) HMF/Cu ratio of 10; (c) HMF/Cu ratio of 14

When increasing the HMF/Cu ratio to 10, the evolution of HMF conversion and the product distribution were similar to those obtained for a HMF/Cu ratio of 5 (Fig. 5.21 (b)). It is noteworthy that the yield of DMF at 6 h increased to 72.8% in this case, higher than that obtained for a HMF/Cu ratio of 5, indicating that changing the substrate loading could lead to a slight improvement. In addition, when the reaction time was prolonged to 8 h, the yield of DMF remained the same while the yields of unknown products were lower than those observed for a HMF/Cu ratio of 5, implying that during this period DMF was continuously produced from BHMF and MFOL though part of DMF was over-hydrogenated and part of BHMF and MFOL polymerized.

When further increasing the HMF/Cu ratio to 14, a marked change of the evolution of HMF conversion as well as product distribution was observed (Fig. 5.21 (c)). On the one hand, the conversion of HMF was lower than those for HMF/Cu ratios of 5 and of 10, only giving 96% even after 8 h, revealing that the catalyst quantity used here was not enough to support full HMF conversion. On the other hand, BHMF remained the primary product during the first 4 h and then its yield significantly decreased from 55.4% to 6.4% in the following 4 h, while the yields of DMF were kept low during the whole process (0-22% yield) and the carbon balance became very poor, demonstrating that a severe polymerization of BHMF occurred before its conversion to DMF due to the inadequate catalyst quantity.

Herein, the optimum HMF/Cu molar ratio (10 in this case) and reaction time (6 h in this case) are essential to obtain the maximum yield of DMF. In the subsequent experiments the HMF/Cu molar ratio was set to 10.

5.3.5 Effect of reaction temperature

With this HMF/Cu molar ratio fixed, the effect of another key parameter, the reaction temperature, on the catalytic reactivity of 15Cu/SBA-15_ISAC was investigated.

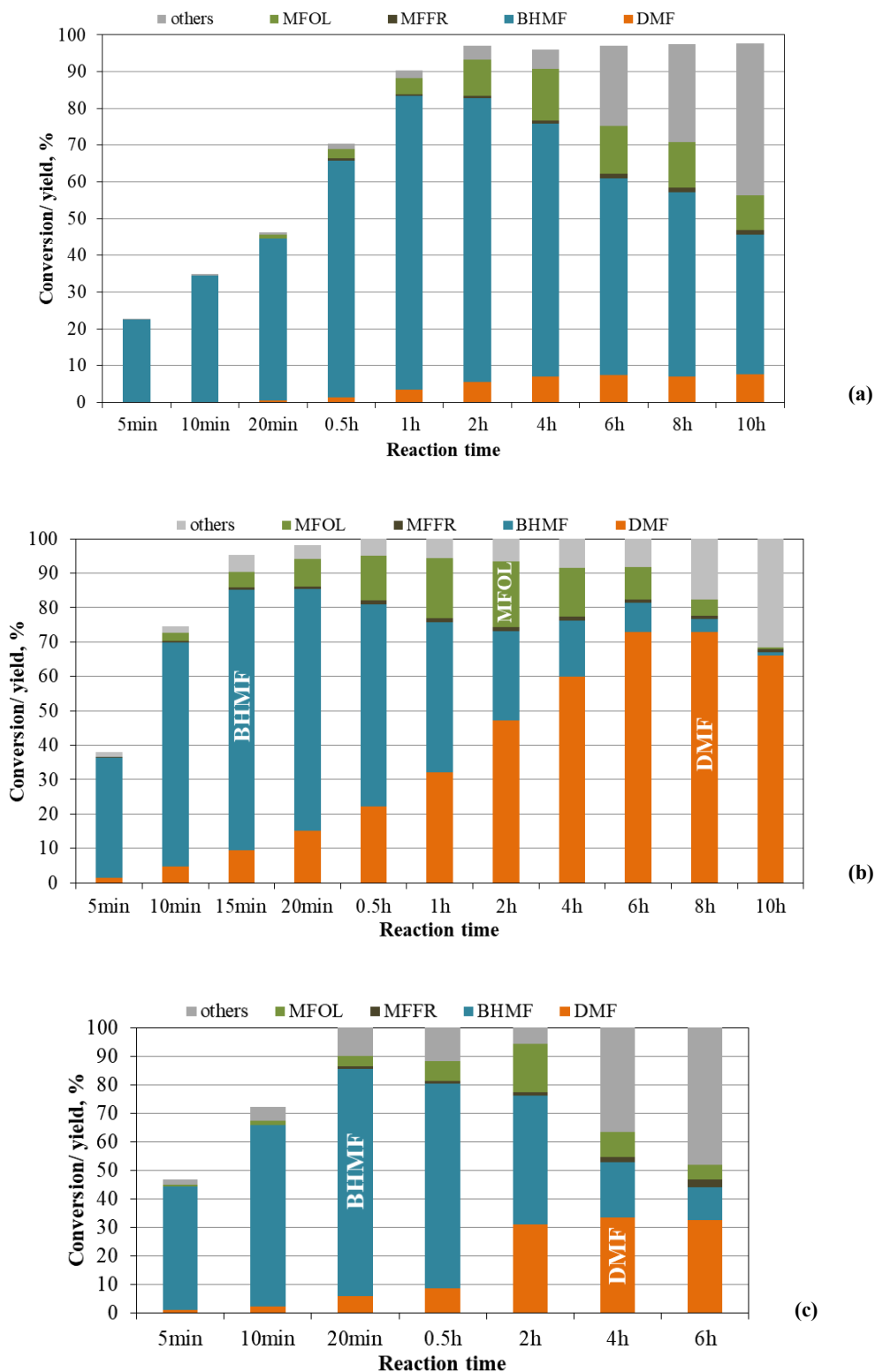


Fig. 5.22 Evolution of the product distributions with reaction time over 15Cu/SBA-15_ISAC at different temperatures (15 bar, HMF/Cu molar ratio of 10, 0.085 g catalyst, 0.15 mmol/mL HMF, 12.5 mL 1,4-dioxane):

(a) 180 °C; (b) 210 °C; (c) 220 °C

Fig. 5.22 summarizes the evolutions of HMF conversion and product distributions with time over 15Cu/SBA-15_ISAC at three different reaction temperatures (180, 210 and 220 °C). It could be confirmed that the hydrogenolysis activity was quite low at low reaction temperature (180 °C, Fig. 5.22 (a)): although the conversion of HMF reached 97.7%, the DMF yield was only 7.7%. Instead, BHMF was mainly produced, with a maximum yield of 80% reached at 1 h. The decrease of the carbon balance based on identified products may reveal a severe polymerization of BHMF at long reaction time, before it is converted to DMF. When the temperature was increased to 210 °C (Fig. 5.22 (b)), high yields of BHMF and DMF were produced at short and long reaction times, giving a BHMF yield of 75.8% at 95.2% HMF conversion at 15 min, and a DMF yield of 72.9% at full HMF conversion at 8 h, respectively. HMF conversion and products formation with time change as follows. After the shortest possible time of reaction using this catalytic device (5 min), the concentration of HMF rapidly decreased. It was almost exclusively converted to BHMF, giving a yield of 34.8% at 38% HMF conversion. The primary step of HMF conversion thus started with the partial hydrogenation of the side chain of -CHO to form -CH₂OH. Prolonging the reaction time to 15 min led to a gradual increase of concentrations of BHMF, MFOL and DMF and a continuously fast decrease of HMF concentration. BHMF yield of 75.8%, MFOL yield of 4.5% and DMF yield of 9.4% are obtained at 95.2% HMF conversion, which implied that the hydrogenation of the -CHO group remains the primary process during this period. Extending the reaction time to 0.5 h, DMF and MFOL were continuously produced at the cost of BHMF yield and the HMF concentration continuously decreased, giving a DMF yield of 22.1%, a MFOL yield of 13.1% and a BHMF yield of 58.7% at complete HMF conversion. The cleavage of the -CH₂OH groups of BHMF to MFOL and DMF started to dominate. Extending the reaction time to 2 h, the MFOL concentration reached its maximum value (19.1%) and started to decrease in the following hours, indicating that the hydrogenolysis of the second -CH₂OH group started to dominate. In the following hours, BHMF and MFOL were continuously consumed to produce DMF, giving a maximum DMF yield of 72.9% at 8 h. Extending the reaction time to 10 h resulted in over-hydrogenation of DMF and likely polymerization of the remaining BHMF and MFOL, leading to a decrease of DMF, BHMF and MFOL selectivities. During the whole process, only a small amount of MFFR was detected, indicating the transformation route with MFFR as an intermediate product was less favored. Moreover, it should be noted that the formation of DMF started at the very beginning of the reaction, indicating the high hydrogenolysis activity at this temperature.

Table 5.3 Catalytic performances of typical Cu-containing catalysts in the literature and in this work

Entry	Catalyst	Feed conditions	P (MPa)	T (°C)	t(h)	Conv. (%)	Yield (%)	ref
1	CuRu/C	5 wt.% HMF in 1-butanol	6.8	220	10	100	71	⁴
3	Cu20-PMO ^a	4 mmol HMF; 20 mL ethanol; 0.1 g catalyst	5	220	12	100	51.7	⁶³
4 ^b	Cu/AlO _x	0.2 mol/L HMF; 0.6 mol/L 1,4-butanediol; 1.5 g catalyst	1.6	220	0.5	100	72	⁶⁴
5	CuZn nanoalloy	13.6 mmol HMF; 20 mL CPME; 0.2 g catalyst	2	200	6	100	89.1	⁵
6	Cu/ZnO	11.9 mmol HMF; 35 mL 1,4-dioxane; 0.5 g catalyst	1.5	220	5	100	91.8	⁶⁵
7	CuCo/NGr/ α A ₂ O ₃	1 mmol HMF; 2 mL THF; 0.1 g catalyst	2	180	16	>99	>99	⁶
8	CuNi/A ₂ O ₃	1.6 mmol HMF; 20 mL THF; 0.5 g catalyst	3	200	6	100	56	⁶⁶
9	CuNi/TiO ₂	4 mmol HMF; 25 mL 1,4-dioxane; 0.3 g catalyst	2.5	200	8	100	84.3	⁶⁷
10	Cu ₃ Al oxide	1.2 mmol HMF; 15 mL methanol; 0.1 g catalyst	0.1 ^c	240	1.5	>99	96.7	⁶⁸
11	Raney Cu	11.9 mmol HMF; 35 mL 1,4-dioxane; 0.5 g catalyst	1.5	180	15	25	10.5	²
12	Cu/PMO	0.8 mmol HMF; 3 mL methanol; 0.1 mg catalyst	-	260	3	100	48	³
13	CuZrO _x	0.7 wt.% HMF in 1-butanol	1.5	200	2	99	60.6	⁶⁹
14	15Cu/SBA-15_IWIMD	3.75 mmol HMF; 12.5 ml 1,4-dioxane; 0.085 g catalyst	1.5	210	8	4.5	-	<i>refere- nce cataly- -st</i>
15	15Cu/SBA-15_ISAC	3.75 mmol HMF; 12.5 ml 1,4-dioxane; 0.085 g catalyst	1.5	210	8	100	72.9	<i>this work</i>

^a: Cu20-PMO, Cu_{0.59}Mg_{2.34}Al_{1.00}; ^b: combined 1,4-butanediol lactonization and transfer hydrogenation/hydrogenolysis of HMF under continuous flow conditions; ^c: CTH conversion of HMF from methanol under N₂ atmosphere.

When further increasing the temperature to 220 °C (Fig. 5.22 (c)), it is observed that the evolution of HMF conversion and product distribution are similar to those observed at 210 °C in the first 2 h. However, at longer reaction time (after 4 h) the carbon balance started to decrease due to the over-hydrogenation of the intermediate products as well as DMF, giving a slate of ring opening products (e.g., 2-hexanol, 1-butanol, 1,2-hexanediol, 1,2,6-hexanetriol) and ring hydrogenation products (e.g., 2-methyl-5-hydroxymethyl tetrahydrofuran, 2,5-dimethyltetrahydrofuran (DMTHF)).¹ On the one hand, this shows that 15Cu/SBA-15_ISAC is a potential catalyst to produce valuable ring opening products at high reaction temperature. On the other hand, it suggests that a temperature of 220 °C is too high for the selective formation of DMF. The investigation on the reaction temperature indicates that, within this limited range of 40 °C, temperature has an important impact on the product distribution, and a proper temperature (210 °C in this case) is necessary to afford the highest selectivity of DMF.

In conclusion, the catalytic study above suggests that the most suitable reaction conditions for the selective conversion of HMF to DMF on Cu could be set at 210 °C under 15 bar with a HMF/Cu molar ratio of 10. Under these reaction parameters, the 15Cu/SBA-15_ISAC sample could afford a DMF yield up to 72.9% at complete HMF conversion, while it was found that the reference 15Cu/SBA-15_IWIMD catalyst almost exhibited no activity (only 4.5% HMF conversion). In the literature, the most efficient Cu-based catalysts reported for the selective production of DMF from HMF are generally highly-dependent on the addition of other active elements (e.g. Ru, Zn, Ni, Co) or on the use of active supports (e.g. TiO₂, ZnO and NGr/Al₂O₃), as summarized in Table 5.3. Pure Cu-based catalysts scarcely afford high DMF yields (Table 5.3, Entry 11-13). Besides, no work has been reported so far on monometallic copper catalysts supported on an inert siliceous material for the conversion of HMF to DMF. We show here that the monometallic 15Cu/SBA-15_ISAC catalyst prepared by the simple ISAC method is able to give an activity comparable with the monometallic Cu-based catalysts reported in the literature. The relatively high hydrogenolysis reactivity of 15Cu/SBA-15_ISAC could be attributed to the existence of a population of well-confined Cu NPs (as confirmed by the characterization) and the advantageous structure of SBA-15 (i.e., high surface area and ordered mesopores).

5.3.6 Effect of metal dispersion on catalytic reactivity

Once the suitable reaction parameters determined, the catalytic performance of the highly dispersed 15Cu/SBA-15_DP catalyst was then investigated.

The evolution of HMF conversion and product distribution with reaction time over 15Cu/SBA-15_DP is depicted in Fig. 5.23. BHMF, MFOL, DMF and only a very small amount of MFFR were detected in the products, with BHMF and DMF as the main products at short and long reaction time, respectively, which is similar to what was observed over 15Cu/SBA-15_ISAC. A likewise product evolution with reaction time was also observed. At the initial time of the reaction (i.e., in the first 20 min), HMF predominantly experienced the partial hydrogenation reaction of the side chain, producing BHMF, whose yield gradually increased up to 89.1% at almost complete HMF conversion at 20 min. During this period, DMF and MFOL were only detected in small amounts, yielding 5.7 and 3.5%, respectively. Subsequently, BHMF was gradually converted to MFOL and DMF via the successive hydrogenolysis of the -CH₂OH groups. The DMF yield reached a maximum value, 95.4%, after 10 h.

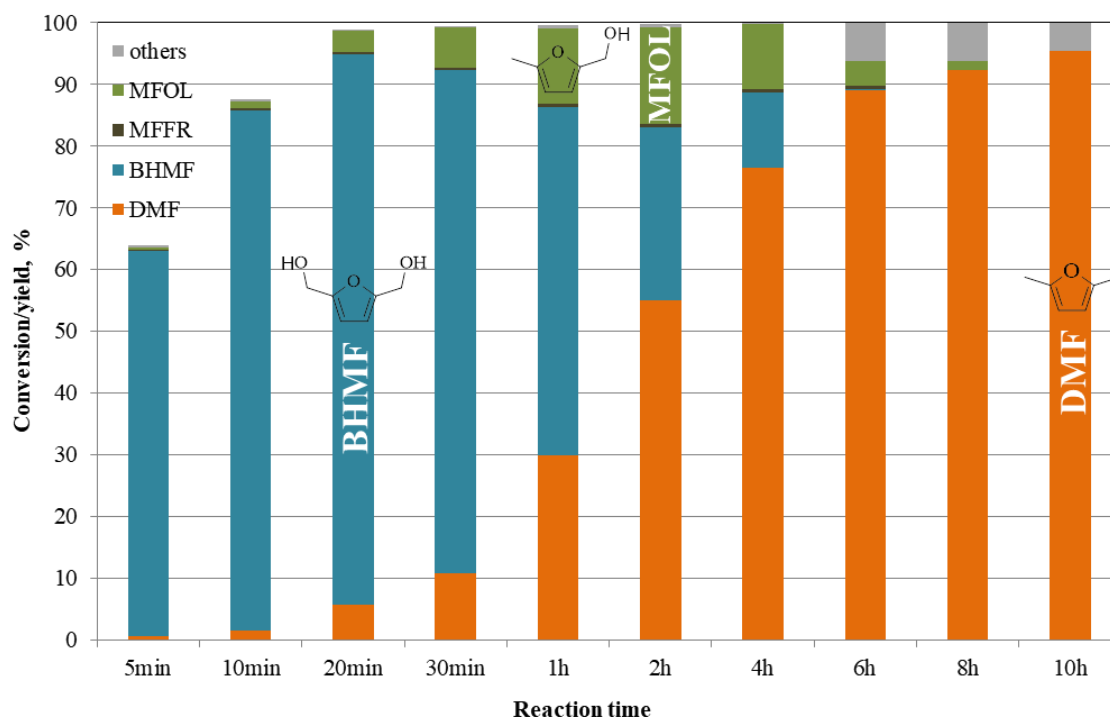


Fig. 5.23 Evolution of the product distribution with reaction time over 15Cu/SBA-15_DP

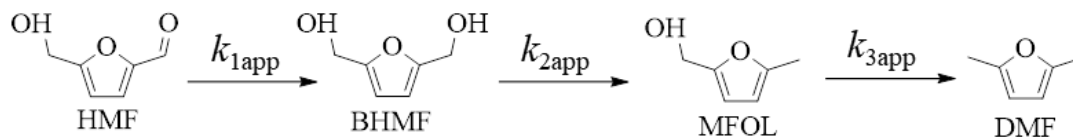
Reaction conditions: 210 °C, 15 bar, HMF/Cu ratio of 10, 0.084 g catalyst, 0.15 mmol/mL HMF in 12.5 mL 1,4-dioxane

As compared to 15Cu/SBA-15_IWIMD and 15Cu/SBA-15_ISAC, 15Cu/SBA-15_DP exhibited better catalytic performances for the selective production of DMF from HMF: a higher DMF yield with a higher carbon balance. The superior catalytic performance of 15Cu/SBA-15_DP could be primarily attributed to the higher dispersion of Cu NPs in this catalyst. In fact, according to the particle size histogram data, the fraction of exposed surface Cu atoms in 15Cu/SBA-15_DP is 31%, higher than that in 15Cu/SBA-15_ISAC (16%). As compared to the literature (Table 5.3), the DMF yield achieved by 15Cu/SBA-15_DP is at the top level among monometallic Cu-based catalysts, and is comparable to the best results obtained by bimetallic Cu-based catalysts, confirming the outstanding reactivity of this catalyst for the selective conversion of HMF to DMF.

5.3.6 Kinetic study

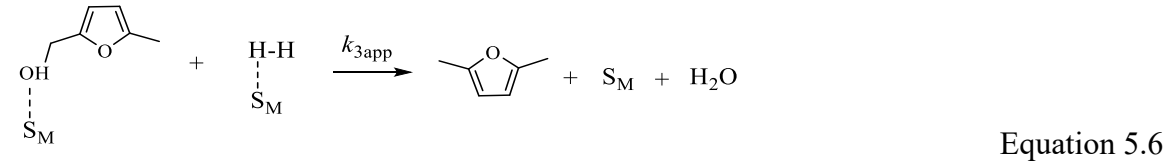
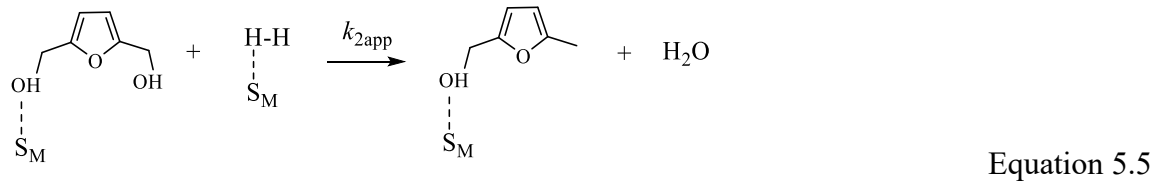
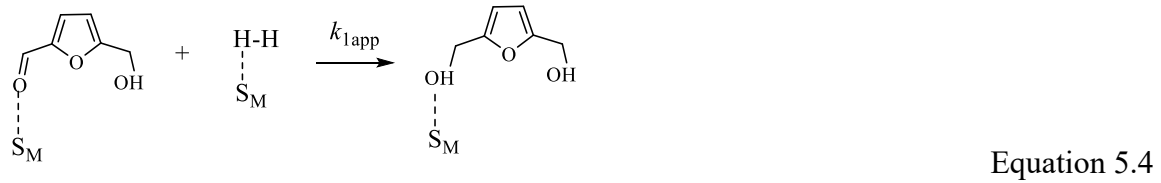
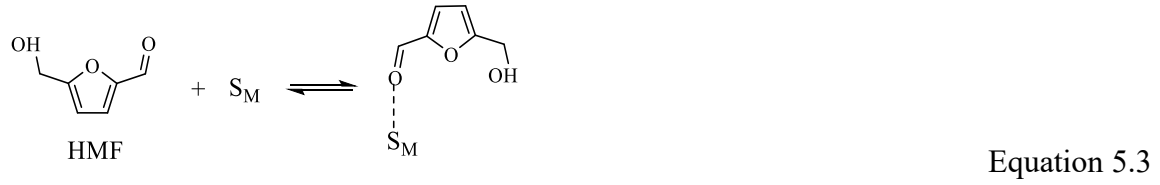
5.3.6.1 Kinetic modeling

In order to provide a more quantitative analysis of the catalysis results, a simplified kinetic model was defined, lying on the same hypotheses as described in Chapter 3.



Scheme 5.2 Simplified mechanism for the hydrogenolysis of HMF

As indicated above, MFFR is barely detected on 15Cu/SBA-15_ISAC, BHMF is detected in large amounts, and no DMTHF is formed, confirming the poor activity of Cu for the hydrogenation of furanic rings at 210 °C. On Cu, the hydro-deoxygenation of HMF to DMF primarily proceeds through the partial hydrogenation of the -CHO chain to form BHMF, which then experiences C-O hydrogenolysis to give MFOL and DMF. However, minor products that have not been identified may arise from the etherification of the alcohols, from the subsequent ring hydrogenation or from the ring opening of DMF. The direct formation of DMF from BHMF is possible but in most cases in the literature the stepwise route with MFOL as an intermediate is considered to be dominant.^{4,67,70-72} The sequence of reactions chosen for the kinetic model is depicted in Scheme 5.2, with three apparent rate constants to be optimized, respectively k_{1app} , k_{2app} and k_{3app} (Equations 5.2-5.6) and the rate laws for the conversion/production of the reactant/products are presented in Equations 5.7-5.10. It should be pointed out that, as proposed in Chapter 3, in this model, k_{app} contains three contributions, one corresponding to the adsorption of the reactant, one being the true kinetic constant and one related to a term containing the constant concentration of hydrogen (if the reaction order with respect to hydrogen is not 0).



Where S_M represents the surface active metal sites.

$$r_{\text{HMF}} = -k_{1app}[\text{HMF}] \quad \text{Equation 5.7}$$

$$r_{\text{BHMF}} = k_{1app}[\text{HMF}] - k_{2app}[\text{BHMF}] \quad \text{Equation 5.8}$$

$$r_{\text{MFOL}} = k_{2app}[\text{BHMF}] - k_{3app}[\text{MFOL}] \quad \text{Equation 5.9}$$

$$r_{\text{DMF}} = k_{3app}[\text{MFOL}] \quad \text{Equation 5.10}$$

Where r_i represents the rate of the consumption of species i , $[i]$ is the concentration of species i , and k_x ($x = 1, 2, 3$) is the apparent reaction rate constants for the corresponding reaction steps in Equation 5.4-5.6. Integrating Equation 5.7-5.10 using initial conditions, $[\text{HMF}] = [\text{HMF}]_0$ at $t = 0$ and $[\text{BHMF}] = [\text{MFOL}] = [\text{DMF}] = 0$ at $t = 0$, the analytical expressions for the temporal variation of the concentrations of HMF, BHMF, MFOL and DMF are obtained as Equation 5.11-5.14:

$$[HMF] = [HMF]_0 \exp(-k_{1app}t) \quad \text{Equation 5.11}$$

$$[BHMF] = \frac{k_{1app}[HMF]_0}{k_{2app} - k_{1app}} [\exp(-k_{1app}t) - \exp(-k_{2app}t)] \quad \text{Equation 5.12}$$

$$[MFOL] = (k_{1app} + k_{2app})[HMF]_0 \left[\frac{\exp(-k_{1app}t)}{(k_{2app} - k_{1app})(k_{3app} - k_{1app})} - \frac{\exp(-k_{2app}t)}{(k_{2app} - k_{1app})(k_{3app} - k_{2app})} + \frac{\exp(-k_{3app}t)}{(k_{3app} - k_{1app})(k_{3app} - k_{2app})} \right]$$

Equation 5.13

$$[DMF] = \frac{[HMF]_0 k_{2app} k_{3app}}{(k_{2app} - k_{1app})(k_{3app} - k_{1app})} (1 - \exp(-k_{1app}t)) + \frac{[HMF]_0 k_{1app} k_{3app}}{((k_{1app} - k_{2app})(k_{3app} - k_{2app}))} (1 - \exp(-k_{2app}t)) + \frac{[HMF]_0 k_{1app} k_{2app}}{((k_{1app} - k_{3app})(k_{2app} - k_{3app}))} (1 - \exp(-k_{3app}t)) - [unknowns]$$

Equation 5.14

As was done for the Ni catalyst in Chapter 3 to increase the quality of the fit, the production of DMF is fitted after subtraction of the concentrations of unknown products (Equation 5.14), deduced from the calculation of the carbon balance. This rough approximation implies that the unknown products are formed in the later stages of the reaction, by consumption of MFOL or DMF.

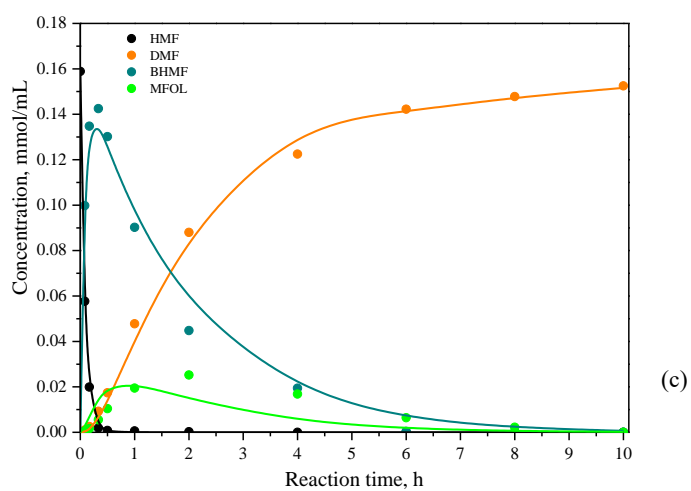
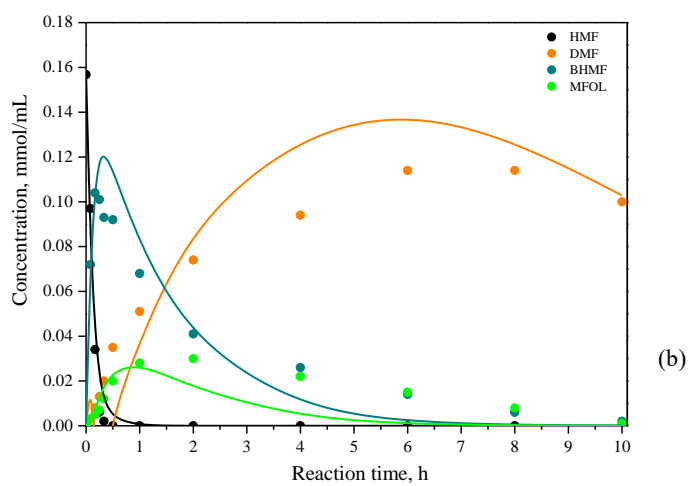
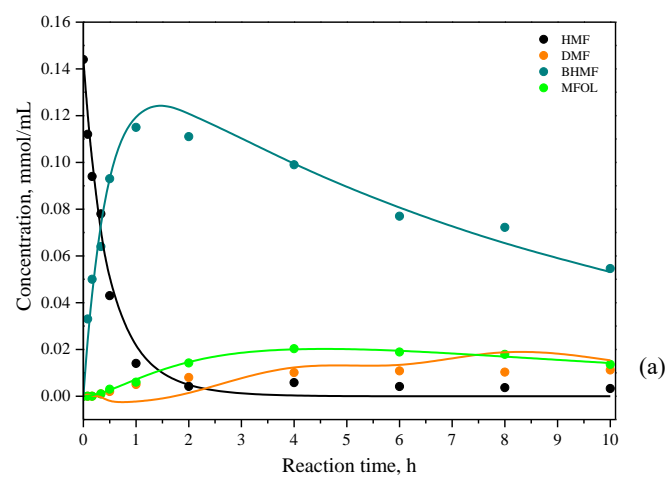


Fig. 5.24 Kinetic patterns of HMF conversion simulated using the Excel solver: (a) 15Cu/SBA-15_ISAC at 180 °C; (b) 15Cu/SBA-15_ISAC at 210 °C; (c) 15Cu/SBA-15_DP at 210 °C. Reaction conditions: 15 bar, HMF/Cu molar ratio of 10, 0.085 g catalyst, 0.15 mmol/mL HMF, 12.5 mL 1,4-dioxane.

Data points and solid lines represent experimental data and model, respectively

Table 5.4 Optimized apparent rate constants (k_{app}) for the modelling of HMF hydroconversion

T (°C), catalyst	k_{1app} (h ⁻¹)	k_{2app} (h ⁻¹)	k_{3app} (h ⁻¹)
180, 15Cu/SBA-15_ISAC	2.2	0.1	0.5
210, 15Cu/SBA-15_ISAC	7.8	0.8	2.4
210, Cu/SBA-15_DP	12.6	0.6	2.6

The fit by least-squares minimization was performed for 15Cu/SBA-15_ISAC catalyst tested at 180 and 210 °C (at 220 °C the production of unknown products is not negligible even at short reaction times, compromising the quality of the fit), and for the 15Cu/SBA-15_DP catalyst tested at 210 °C. The fitting curves are depicted in Fig. 5.24 (a-c).

The fits allow reproducing the consumption of HMF and the neat production of BHMF satisfactorily, even for longer reaction times. This should confirm that no inhibition term is required in the writing of the related rate equations, and that the unidentified products do not derive from the first stages of the reaction. But because of the rough correction carried out in the fit of DMF, modeled values for DMF exhibit more noise, though they appear in the correct order of magnitude at longer reaction times. Removing this correction leads to an even larger overestimation of the production of DMF. Probably for the same reason, the consumption of MFOL is overestimated at longer reaction times, especially for 15Cu/SBA-15_ISAC tested at 210 °C. Fits carried out for 15Cu/SBA-15_ISAC shows an increase of the three rate constants with reaction temperature (Table 5.4). In the three cases, and unlike the Ni catalyst, Cu systems primarily appear as hydrogenation catalysts. The rate constants associated to the hydrogenolysis steps are significantly lower than that those associated to C=O hydrogenation. The DP catalyst exhibits the highest value of k_{1app} , which can be linked to the largest number of surface Cu sites. However, the values of the two other rate constants are quite similar when one compares the ISAC and the DP catalysts at 210 °C. As was noted for Ni, the hydrogenolysis of MFOL presents a higher rate constant than that of BHMF. However, it must be recalled that the values of k_{3app} are probably overestimated, making any firm conclusion difficult.

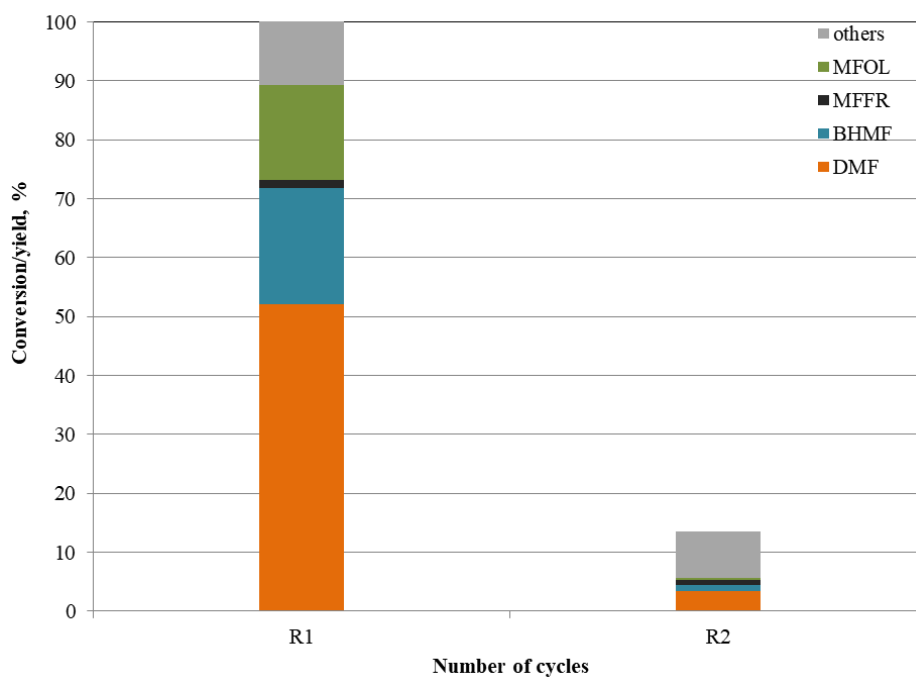


Fig. 5.25 HMF conversion and product yields as a function of the number of catalytic cycles for 15Cu/SBA-15_ISAC, without intermediate regeneration, reaction conditions: 3 h, 210 °C, 15 bar, HMF/Cu molar ratio of 10, 0.135 g catalyst, 0.15 mmol/mL HMF, 20 mL 1,4-dioxane.

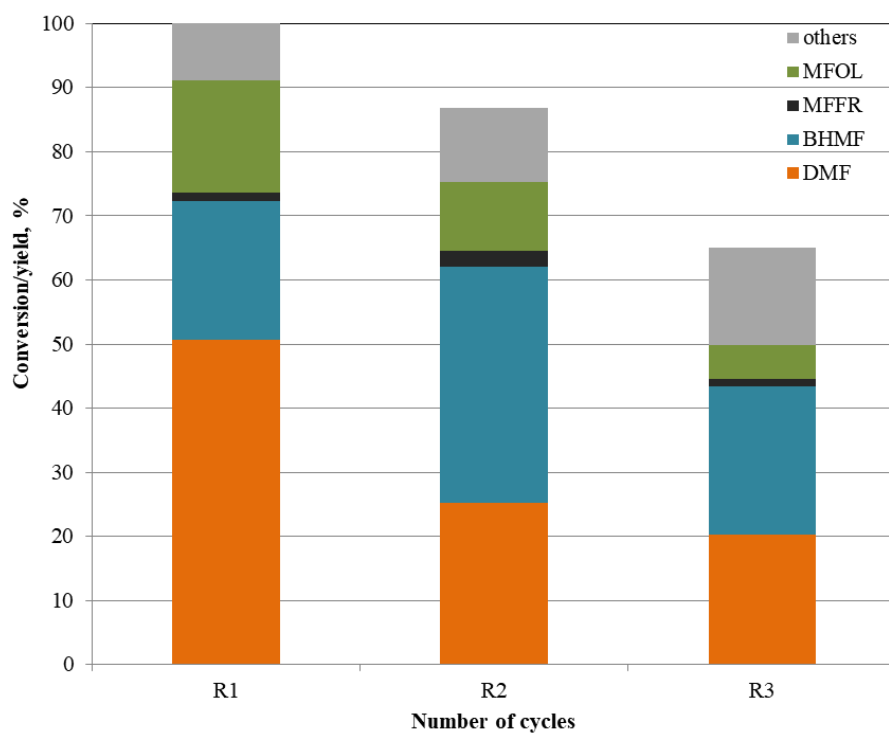


Fig. 5.26 HMF conversion and product yields as a function of the number of catalytic cycles for 15Cu/SBA-15_ISAC, with intermediate regeneration by calcination (500 °C for 6 h) and reduction (300 °C for 2 h), reaction conditions: 3 h, 210 °C, 15 bar, HMF/Cu molar ratio of 10, 0.135 g catalyst, 0.15 mmol/mL HMF, 20 mL 1,4-dioxane.

5.3.7 Recycling study

A limit previously identified in the literature for the application of Cu-based catalysts to HMF hydroconversion is the potential catalyst deactivation under the reaction conditions.^{1,63,65} Without regeneration processing between catalytic cycles, the 15Cu/SBA-15_ISAC catalyst was also troubled by a heavy deactivation problem, showing a considerable activity loss from 100% to 13.6%, as shown in Fig. 5.25. The possible causes for catalyst deactivation include Cu sintering, carbon deposition, Cu oxidation (the catalyst was exposed to air during the recovering process) and Cu leaching.¹ In order to improve the catalytic performance of the spent catalyst, a regeneration process was performed between the different cycles. The spent catalyst was calcined at 500 °C for 6 h and then reduced at 300 °C before the next use. The regeneration process was designed predominantly remove the carbonaceous deposits and reduce the copper oxides to metallic copper. As shown in Fig. 5.26, after two cycles, the HMF conversion decreased from 100 to 87%. At the same time, the DMF yield decreased by 25.5%, the MFOL yield decreased by 6.8% but the BHMF yield increased by 15.3%, indicating a loss of hydrogenolysis activity of the catalyst. After 3 cycles, the catalyst activity and the DMF yield continuously decreased, giving a DMF yield of 20.2% at 65% HMF conversion. As compared to the recycling tests without regeneration processing, the catalyst re-calcination and re-reduction marked improved the catalyst recyclability, suggesting that carbon deposition and Cu oxidation were causes of catalyst deactivation. The deactivation after regeneration was possibly caused by Cu sintering and Cu leaching. The characterization of the spent catalysts is currently been done in order to evidence the possible causes of catalyst deactivation.

5.4 Conclusion

A monometallic 15Cu/SBA-15_ISAC catalyst was prepared by the simple in-situ auto-combustion method involving glycine, and was able to present a promising reactivity (72.9% DMF yield) under optimized reaction conditions (210 °C, 15 bar, HMF/Cu molar ratio of 10, 8 h). A high HMF/Cu molar ratio (> 50) leads to a lower catalytic activity while a higher reaction temperature (≥ 210 °C) is necessary for the efficient cleavage of C-O bond. The use of the deposition-precipitation method led to a higher dispersion of copper NPs despite the destruction of the SBA-15 support, and a higher reactivity, giving a DMF yield of 95.4% after

10 h, which is at the top level in the literature reported for monometallic Cu-based catalysts. This result shows that it is possible to prepare monometallic Cu-based catalysts efficient for the selective conversion of HMF to DMF provided that Cu nanoparticles exhibit a high dispersion. The kinetic study showed that the formation of DMF from HMF primarily proceeded through the “HMF → BHMF → MFOL → DMF” route with the hydrogenolysis of the first C-O bond of BHMF as exhibiting the lowest value of apparent rate constant. The catalyst stability tests showed that the 15Cu/SBA-15_ISAC catalyst is not stable upon cycling. A significant part of the total deactivation originates from the reoxidation of copper between successive cycles. Applying a recovery process, involving intermediate calcination/reduction, leads to better stability, even if a decrease in hydrogenolysis activity is always observed.

References

- (1) Chen, S.; Wojcieszak, R.; Dumeignil, F.; Marceau, E.; Royer, S. How Catalysts and Experimental Conditions Determine the Selective Hydroconversion of Furfural and 5-Hydroxymethylfurfural. *Chem. Rev.* **2018**, *118* (22), 11023–11117. <https://doi.org/10.1021/acs.chemrev.8b00134>.
- (2) Kong, X.; Zhu, Y.; Zheng, H.; Dong, F.; Zhu, Y.; Li, Y.-W. Switchable Synthesis of 2,5-Dimethylfuran and 2,5-Dihydroxymethyltetrahydrofuran from 5-Hydroxymethylfurfural over Raney Ni Catalyst. *RSC Adv.* **2014**, *4* (105), 60467–60472. <https://doi.org/10.1039/C4RA09550B>.
- (3) Hansen, T. S.; Barta, K.; Anastas, P. T.; Ford, P. C.; Riisager, A. One-Pot Reduction of 5-Hydroxymethylfurfural via Hydrogen Transfer from Supercritical Methanol. *Green Chem.* **2012**, *14* (9), 2457–2461. <https://doi.org/10.1039/C2GC35667H>.
- (4) Román-Leshkov, Y.; Barrett, C. J.; Liu, Z. Y.; Dumesic, J. A. Production of Dimethylfuran for Liquid Fuels from Biomass-Derived Carbohydrates. *Nature* **2007**, *447* (7147), 982–985. <https://doi.org/10.1038/nature05923>.
- (5) Bottari, G.; Kumalaputri, A. J.; Krawczyk, K. K.; Feringa, B. L.; Heeres, H. J.; Barta, K. Copper–Zinc Alloy Nanopowder: A Robust Precious-Metal-Free Catalyst for the Conversion of 5-Hydroxymethylfurfural. *ChemSusChem* **2015**, *8* (8), 1323–1327. <https://doi.org/10.1002/cssc.201403453>.
- (6) Guo, W.; Liu, H.; Zhang, S.; Han, H.; Liu, H.; Jiang, T.; Han, B.; Wu, T. Efficient Hydrogenolysis of 5-Hydroxymethylfurfural to 2,5-Dimethylfuran over a Cobalt and Copper Bimetallic Catalyst on N-Graphene-Modified Al₂O₃. *Green Chem.* **2016**. <https://doi.org/10.1039/C6GC02630C>.
- (7) Luo, J.; Monai, M.; Wang, C.; Lee, J. D.; Duchoň, T.; Dvořák, F.; Matolín, V.; Murray, C. B.; Fornasiero, P.; Gorte, R. J. Unraveling the Surface State and Composition of Highly Selective Nanocrystalline Ni–Cu Alloy Catalysts for Hydrodeoxygenation of HMF. *Catal. Sci. Technol.* **2017**, *7* (8), 1735–1743. <https://doi.org/10.1039/C6CY02647H>.
- (8) Lessard, J.; Morin, J. F.; Wehrung, J. F.; Magnin, D.; Chornet, E. High Yield Conversion of Residual Pentoses into Furfural via Zeolite Catalysis and Catalytic

Hydrogenation of Furfural to 2-Methylfuran. *Top. Catal.* **2010**, *53* (15–18), 1231–1234. <https://doi.org/10.1007/s11244-010-9568-7>.

(9) Wu, J.; Shen, Y.; Liu, C.; Wang, H.; Geng, C.; Zhang, Z. Vapor Phase Hydrogenation of Furfural to Furfuryl Alcohol over Environmentally Friendly Cu–Ca/SiO₂ Catalyst. *Catal. Commun.* **2005**, *6* (9), 633–637. <https://doi.org/10.1016/j.catcom.2005.06.009>.

(10) Nagaraja, B. M.; Padmasri, A. H.; Seetharamulu, P.; Hari Prasad Reddy, K.; David Raju, B.; Rama Rao, K. S. A Highly Active Cu-MgO-Cr₂O₃ Catalyst for Simultaneous Synthesis of Furfuryl Alcohol and Cyclohexanone by a Novel Coupling Route—Combination of Furfural Hydrogenation and Cyclohexanol Dehydrogenation. *J. Mol. Catal. Chem.* **2007**, *278* (1–2), 29–37. <https://doi.org/10.1016/j.molcata.2007.07.045>.

(11) Villaverde, M. M.; Bertero, N. M.; Garetto, T. F.; Marchi, A. J. Selective Liquid-Phase Hydrogenation of Furfural to Furfuryl Alcohol over Cu-Based Catalysts. *Catal. Today* **2013**, *213*, 87–92. <https://doi.org/10.1016/j.cattod.2013.02.031>.

(12) Gong, W.; Chen, C.; Zhang, Y.; Zhou, H.; Wang, H.; Zhang, H.; Zhang, Y.; Wang, G.; Zhao, H. Efficient Synthesis of Furfuryl Alcohol from H₂-Hydrogenation/Transfer Hydrogenation of Furfural Using Sulfonate Group Modified Cu Catalyst. *ACS Sustain. Chem. Eng.* **2017**, *5* (3), 2172–2180. <https://doi.org/10.1021/acssuschemeng.6b02343>.

(13) Srivastava, S.; Mohanty, P.; Parikh, J. K.; Dalai, A. K.; Amritphale, S. S.; Khare, A. K. Cr-Free Co–Cu/SBA-15 Catalysts for Hydrogenation of Biomass-Derived α -, β -Unsaturated Aldehyde to Alcohol. *Chin. J. Catal.* **2015**, *36* (7), 933–942. [https://doi.org/10.1016/S1872-2067\(15\)60870-1](https://doi.org/10.1016/S1872-2067(15)60870-1).

(14) Pushkarev, V. V.; Musselwhite, N.; An, K.; Alayoglu, S.; Somorjai, G. A. High Structure Sensitivity of Vapor-Phase Furfural Decarbonylation/Hydrogenation Reaction Network as a Function of Size and Shape of Pt Nanoparticles. *Nano Lett.* **2012**, *12* (10), 5196–5201. <https://doi.org/10.1021/nl3023127>.

(15) Ohyama, J.; Esaki, A.; Koketsu, T.; Yamamoto, Y.; Arai, S.; Satsuma, A. Atomic-Scale Insight into the Structural Effect of a Supported Au Catalyst Based on a Size-Distribution Analysis Using Cs-STEM and Morphological Image-Processing. *J. Catal.* **2016**, *335*, 24–35. <https://doi.org/10.1016/j.jcat.2015.11.021>.

(16) Chen, L.F.; Guo, P. J.; Zhu, L. J.; Qiao, M. H.; Shen, W.; Xu, H. L.; Fan, K. N. Preparation of Cu/SBA-15 Catalysts by Different Methods for the Hydrogenolysis of Dimethyl Maleate to 1,4-Butanediol. *Appl. Catal. Gen.* **2009**, *356* (2), 129–136. <https://doi.org/10.1016/j.apcata.2008.12.029>.

(17) Ungureanu, A.; Dragoi, B.; Chiriac, A.; Royer, S.; Duprez, D.; Dumitriu, E. Synthesis of Highly Thermostable Copper-Nickel Nanoparticles Confined in the Channels of Ordered Mesoporous SBA-15 Silica. *J. Mater. Chem.* **2011**, *21* (33), 12529–12541. <https://doi.org/10.1039/C1JM10971E>.

(18) Zhou, C. F.; Wang, Y. M.; Cao, Y.; Zhuang, T. T.; Huang, W.; Chun, Y.; Zhu, J. H. Solvent-Free Surface Functionalized SBA-15 as a Versatile Trap of Nitrosamines. *J. Mater. Chem.* **2006**, *16* (16), 1520–1528. <https://doi.org/10.1039/B514317A>.

(19) Wang, Y. M.; Ying Wu, Z.; Zhu, J. H. Surface Functionalization of SBA-15 by the Solvent-Free Method. *J. Solid State Chem.* **2004**, *177* (10), 3815–3823. <https://doi.org/10.1016/j.jssc.2004.07.013>.

(20) Zhong, X.; Barbier, J.; Duprez, D.; Zhang, H.; Royer, S. Modulating the Copper Oxide Morphology and Accessibility by Using Micro-/Mesoporous SBA-15 Structures as Host Support: Effect on the Activity for the CWPO of Phenol Reaction. *Appl. Catal. B Environ.* **2012**, *121–122* (Supplement C), 123–134. <https://doi.org/10.1016/j.apcatb.2012.04.002>.

(21) Xiang, L.; Royer, S.; Zhang, H.; Tatibouët, J.-M.; Barrault, J.; Valange, S. Properties of Iron-Based Mesoporous Silica for the CWPO of Phenol: A Comparison between Impregnation and Co-Condensation Routes. *J. Hazard. Mater.* **2009**, *172* (2), 1175–1184. <https://doi.org/10.1016/j.jhazmat.2009.07.121>.

(22) Sellam, D.; Bonne, M.; Arrii-Clacens, S.; Lafaye, G.; Bion, N.; Tezkratt, S.; Royer, S.; Marécot, P.; Duprez, D. Simple Approach to Prepare Mesoporous Silica Supported Mixed-Oxide Nanoparticles by in Situ Autocombustion Procedure. *Catal. Today* **2010**, *157* (1), 131–136. <https://doi.org/10.1016/j.cattod.2010.03.008>.

(23) Groven, L. J.; Puszynski, J. A. Solution Combustion Synthesis of Carbon Nanotube Loaded Nickel Foams. *Mater. Lett.* **2012**, *73*, 126–128.

<https://doi.org/10.1016/j.matlet.2012.01.033>.

(24) Deshpande, K.; Mukasyan, A.; Varma, A. Direct Synthesis of Iron Oxide Nanopowders by the Combustion Approach: Reaction Mechanism and Properties. *Chem. Mater.* **2004**, *16* (24), 4896–4904. <https://doi.org/10.1021/cm040061m>.

(25) Manukyan, K. V.; Cross, A.; Roslyakov, S.; Rouvimov, S.; Rogachev, A. S.; Wolf, E. E.; Mukasyan, A. S. Solution Combustion Synthesis of Nano-Crystalline Metallic Materials: Mechanistic Studies. *J. Phys. Chem. C* **2013**, *117* (46), 24417–24427. <https://doi.org/10.1021/jp408260m>.

(26) Xiang, L.; Royer, S.; Zhang, H.; Tatibouët, J.-M.; Barrault, J.; Valange, S. Properties of Iron-Based Mesoporous Silica for the CWPO of Phenol: A Comparison between Impregnation and Co-Condensation Routes. *J. Hazard. Mater.* **2009**, *172* (2), 1175–1184. <https://doi.org/10.1016/j.jhazmat.2009.07.121>.

(27) Toupance, T.; Kermarec, M.; Lambert, J.-F.; Louis, C. Conditions of Formation of Copper Phyllosilicates in Silica-Supported Copper Catalysts Prepared by Selective Adsorption. *J. Phys. Chem. B* **2002**, *106* (9), 2277–2286. <https://doi.org/10.1021/jp013153x>.

(28) Geus, J. W.; van Dillen, A. J. Preparation of Supported Catalysts by Deposition–Precipitation. In *Handbook of Heterogeneous Catalysis*; Wiley-VCH Verlag GmbH & Co. KGaA, 2008. <https://doi.org/10.1002/9783527610044.hetc0021>.

(29) Toupance, T.; Kermarec, M.; Lambert, J.-F.; Louis, C. Conditions of Formation of Copper Phyllosilicates in Silica-Supported Copper Catalysts Prepared by Selective Adsorption. *J. Phys. Chem. B* **2002**, *106* (9), 2277–2286. <https://doi.org/10.1021/jp013153x>.

(30) Xiao, J.; Villemure, G. Preparation, Characterization and Electrochemistry of Synthetic Copper Clays. *Clays Clay Miner.* **1998**, *46* (2), 195–203.

(31) Di, W.; Cheng, J.; Tian, S.; Li, J.; Chen, J.; Sun, Q. Synthesis and Characterization of Supported Copper Phyllosilicate Catalysts for Acetic Ester Hydrogenation to Ethanol. *Appl. Catal. Gen.* **2016**, *510* (Supplement C), 244–259. <https://doi.org/10.1016/j.apcata.2015.10.026>.

(32) Yue, H.; Zhao, Y.; Zhao, S.; Wang, B.; Ma, X.; Gong, J. A Copper-Phyllosilicate Core-

Sheath Nanoreactor for Carbon–Oxygen Hydrogenolysis Reactions. *Nat. Commun.* **2013**, *4*, ncomms3339. <https://doi.org/10.1038/ncomms3339>.

(33) Hermans, L. A. M.; Geus, J. W. Interaction Of Nickel Ions With Silica Supports During Deposition-Precipitation. In *Studies in Surface Science and Catalysis*; Delmon, B., Grange, P., Jacobs, P., Poncelet, G., Eds.; Preparation of Catalysts II; Elsevier, 1979; Vol. 3, pp 113–130. [https://doi.org/10.1016/S0167-2991\(09\)60208-1](https://doi.org/10.1016/S0167-2991(09)60208-1).

(34) Zanella, R.; Giorgio, S.; Henry, C. R.; Louis, C. Alternative Methods for the Preparation of Gold Nanoparticles Supported on TiO₂. *J. Phys. Chem. B* **2002**, *106* (31), 7634–7642. <https://doi.org/10.1021/jp0144810>.

(35) Gong, J.; Yue, H.; Zhao, Y.; Zhao, S.; Zhao, L.; Lv, J.; Wang, S.; Ma, X. Synthesis of Ethanol via Syngas on Cu/SiO₂ Catalysts with Balanced Cu⁰–Cu⁺ Sites. *J. Am. Chem. Soc.* **2012**, *134* (34), 13922–13925. <https://doi.org/10.1021/ja3034153>.

(36) Van Der Grift, C. J. G.; Elberse, P. A.; Mulder, A.; Geus, J. W. Preparation of Silica-Supported Copper Catalysts by Means of Deposition-Precipitation. *Appl. Catal.* **1990**, *59* (1), 275–289. [https://doi.org/10.1016/S0166-9834\(00\)82204-6](https://doi.org/10.1016/S0166-9834(00)82204-6).

(37) Ciotonea, C.; Dragoi, B.; Ungureanu, A.; Chiriac, A.; Petit, S.; Royer, S.; Dumitriu, E. Nanosized Transition Metals in Controlled Environments of Phyllosilicate–Mesoporous Silica Composites as Highly Thermostable and Active Catalysts. *Chem. Commun.* **2013**, *49* (69), 7665–7667. <https://doi.org/10.1039/C3CC43197E>.

(38) Delannoy, L.; Thrimurthulu, G.; Reddy, P. S.; Méthivier, C.; Nelayah, J.; Reddy, B. M.; Ricolleau, C.; Louis, C. Selective Hydrogenation of Butadiene over TiO₂ Supported Copper, Gold and Gold–Copper Catalysts Prepared by Deposition–Precipitation. *Phys. Chem. Chem. Phys.* **2014**, *16* (48), 26514–26527. <https://doi.org/10.1039/C4CP02141J>.

(39) Zhu, Y.; Kong, X.; Yin, J.; You, R.; Zhang, B.; Zheng, H.; Wen, X.; Zhu, Y.; Li, Y.-W. Covalent-Bonding to Irreducible SiO₂ Leads to High-Loading and Atomically Dispersed Metal Catalysts. *J. Catal.* **2017**, *353*, 315–324. <https://doi.org/10.1016/j.jcat.2017.07.030>.

(40) Chytil, S.; Glomm, W. R.; Kvande, I.; Zhao, T.; Walmsley, J. C.; Blekkan, E. A. Platinum Incorporated into the SBA-15 Mesostructure via Deposition-Precipitation Method: Pt Nanoparticle Size Estimation and Catalytic Testing. *Top. Catal.* **2007**, *45* (1–4), 93–99.

<https://doi.org/10.1007/s11244-007-0246-3>.

(41) Jiao, L.; Regalbuto, J. R. The Synthesis of Highly Dispersed Noble and Base Metals on Silica via Strong Electrostatic Adsorption: II. Mesoporous Silica SBA-15. *J. Catal.* **2008**, *260* (2), 342–350. <https://doi.org/10.1016/j.jcat.2008.09.023>.

(42) Chen, L. F.; Guo, P. J.; Zhu, L. J.; Qiao, M. H.; Shen, W.; Xu, H. L.; Fan, K. N. Preparation of Cu/SBA-15 Catalysts by Different Methods for the Hydrogenolysis of Dimethyl Maleate to 1,4-Butanediol. *Appl. Catal. Gen.* **2009**, *356* (2), 129–136. <https://doi.org/10.1016/j.apcata.2008.12.029>.

(43) Toupance, T.; Kermarec, M.; Louis, C. Metal Particle Size in Silica-Supported Copper Catalysts. Influence of the Conditions of Preparation and of Thermal Pretreatments. *J. Phys. Chem. B* **2000**, *104* (5), 965–972. <https://doi.org/10.1021/jp993399q>.

(44) Van Der Grift, C. J. G.; Mulder, A.; Geus, J. W. Characterization of Silica-Supported Copper Catalysts by Means of Temperature-Programmed Reduction. *Appl. Catal.* **1990**, *60* (1), 181–192. [https://doi.org/10.1016/S0166-9834\(00\)82181-8](https://doi.org/10.1016/S0166-9834(00)82181-8).

(45) Van Der Grift, C. J. G.; Elberse, P. A.; Mulder, A.; Geus, J. W. Preparation of Silica-Supported Copper Catalysts by Means of Deposition-Precipitation. *Appl. Catal.* **1990**, *59* (1), 275–289. [https://doi.org/10.1016/S0166-9834\(00\)82204-6](https://doi.org/10.1016/S0166-9834(00)82204-6).

(46) Ungureanu, A.; Dragoi, B.; Chirieac, A.; Ciotonea, C.; Royer, S.; Duprez, D.; Mamede, A. S.; Dumitriu, E. Composition-Dependent Morphostructural Properties of Ni–Cu Oxide Nanoparticles Confined within the Channels of Ordered Mesoporous SBA-15 Silica. *ACS Appl. Mater. Interfaces* **2013**, *5* (8), 3010–3025. <https://doi.org/10.1021/am302733m>.

(47) Chytil, S.; Glomm, W. R.; Blekkan, E. A. Characterization of Pt/SBA-15 Prepared by the Deposition–Precipitation Method. *Catal. Today* **2009**, *147* (3), 217–223. <https://doi.org/10.1016/j.cattod.2008.09.003>.

(48) Chirieac, A.; Dragoi, B.; Ungureanu, A.; Ciotonea, C.; Mazilu, I.; Royer, S.; Mamede, A. S.; Rombi, E.; Ferino, I.; Dumitriu, E. Facile Synthesis of Highly Dispersed and Thermally Stable Copper-Based Nanoparticles Supported on SBA-15 Occluded with P123 Surfactant for Catalytic Applications. *J. Catal.* **2016**, *339*, 270–283. <https://doi.org/10.1016/j.jcat.2016.04.004>.

(49) Zhang, B.; Hui, S.; Zhang, S.; Ji, Y.; Li, W.; Fang, D. Effect of Copper Loading on Texture, Structure and Catalytic Performance of Cu/SiO₂ Catalyst for Hydrogenation of Dimethyl Oxalate to Ethylene Glycol. *J. Nat. Gas Chem.* **2012**, *21* (5), 563–570. [https://doi.org/10.1016/S1003-9953\(11\)60405-2](https://doi.org/10.1016/S1003-9953(11)60405-2).

(50) Wan, C.; Chen, B. Synthesis and Characterization of Biomimetic Hydroxyapatite/Sepiolite Nanocomposites. *Nanoscale* **2011**, *3* (2), 693–700. <https://doi.org/10.1039/C0NR00650E>.

(51) Frost, R. L.; Locos, O. B.; Ruan, H.; Klopogge, J. T. Near-Infrared and Mid-Infrared Spectroscopic Study of Sepiolites and Palygorskites. *Vib. Spectrosc.* **2001**, *27* (1), 1–13. [https://doi.org/10.1016/S0924-2031\(01\)00110-2](https://doi.org/10.1016/S0924-2031(01)00110-2).

(52) Wu, Z. Y.; Jiang, Q.; Wang, Y. M.; Wang, H. J.; Sun, L. B.; Shi, L. Y.; Xu, J. H.; Wang, Y.; Chun, Y.; Zhu, J. H. Generating Superbasic Sites on Mesoporous Silica SBA-15. *Chem. Mater.* **2006**, *18* (19), 4600–4608. <https://doi.org/10.1021/cm0608138>.

(53) Sun, L. B.; Kou, J. H.; Chun, Y.; Yang, J.; Gu, F. N.; Wang, Y.; Zhu, J. H.; Zou, Z. G. New Attempt at Directly Generating Superbasicity on Mesoporous Silica SBA-15. *Inorg. Chem.* **2008**, *47* (10), 4199–4208. <https://doi.org/10.1021/ic702223b>.

(54) Wang, S.; Guo, W.; Wang, H.; Zhu, L.; Yin, S.; Qiu, K. Effect of the Cu/SBA-15 Catalyst Preparation Method on Methyl Acetate Hydrogenation for Ethanol Production. *New J. Chem.* **2014**, *38* (7), 2792–2800. <https://doi.org/10.1039/C4NJ00134F>.

(55) Wang, S.; Li, X.; Yin, Q.; Zhu, L.; Luo, Z. Highly Active and Selective Cu/SiO₂ Catalysts Prepared by the Urea Hydrolysis Method in Dimethyl Oxalate Hydrogenation. *Catal. Commun.* **2011**, *12* (13), 1246–1250. <https://doi.org/10.1016/j.catcom.2011.04.019>.

(56) Dong, X.; Ma, X.; Xu, H.; Ge, Q. Comparative Study of Silica-Supported Copper Catalysts Prepared by Different Methods: Formation and Transition of Copper Phyllosilicate. *Catal. Sci. Technol.* **2016**, *6* (12), 4151–4158. <https://doi.org/10.1039/C5CY01965F>.

(57) Liu, Z.; Amiridis, M. D.; Chen, Y. Characterization of CuO Supported on Tetragonal ZrO₂ Catalysts for N₂O Decomposition to N₂. *J. Phys. Chem. B* **2005**, *109* (3), 1251–1255. <https://doi.org/10.1021/jp046368q>.

(58) Tu, C. H.; Wang, A. Q.; Zheng, M. Y.; Wang, X. D.; Zhang, T. Factors Influencing the Catalytic Activity of SBA-15-Supported Copper Nanoparticles in CO Oxidation. *Appl. Catal. Gen.* **2006**, *297* (1), 40–47. <https://doi.org/10.1016/j.apcata.2005.08.035>.

(59) Zheng, X. C.; Wu, S. H.; Wang, S. P.; Wang, S. R.; Zhang, S. M.; Huang, W. P. The Preparation and Catalytic Behavior of Copper–Cerium Oxide Catalysts for Low-Temperature Carbon Monoxide Oxidation. *Appl. Catal. Gen.* **2005**, *283* (1), 217–223. <https://doi.org/10.1016/j.apcata.2005.01.007>.

(60) Shi, Y.; Zhu, Y.; Yang, Y.; Li, Y. W.; Jiao, H. Exploring Furfural Catalytic Conversion on Cu(111) from Computation. *ACS Catal.* **2015**, *5* (7), 4020–4032. <https://doi.org/10.1021/acscatal.5b00303>.

(61) Li, J.; Liu, J.; Liu, H.; Xu, G.; Zhang, J.; Liu, J.; Zhou, G.; Li, Q.; Xu, Z.; Fu, Y. Selective Hydrodeoxygenation of 5-Hydroxymethylfurfural to 2,5-Dimethylfuran over Heterogeneous Iron Catalysts. *ChemSusChem* **2017**, n/a-n/a. <https://doi.org/10.1002/cssc.201700105>.

(62) Roylance, J. J.; Kim, T. W.; Choi, K. S. Efficient and Selective Electrochemical and Photoelectrochemical Reduction of 5-Hydroxymethylfurfural to 2,5-Bis(Hydroxymethyl)Furan Using Water as the Hydrogen Source. *ACS Catal.* **2016**, *6* (3), 1840–1847. <https://doi.org/10.1021/acscatal.5b02586>.

(63) Kumalaputri, A. J.; Bottari, G.; Erne, P. M.; Heeres, H. J.; Barta, K. Tunable and Selective Conversion of 5-HMF to 2,5-Furandimethanol and 2,5-Dimethylfuran over Copper-Doped Porous Metal Oxides. *ChemSusChem* **2014**, *7* (8), 2266–2275. <https://doi.org/10.1002/cssc.201402095>.

(64) Aellig, C.; Jenny, F.; Scholz, D.; Wolf, P.; Giovanazzo, I.; Kollhoff, F.; Hermans, I. Combined 1,4-Butanediol Lactonization and Transfer Hydrogenation/Hydrogenolysis of Furfural-Derivatives under Continuous Flow Conditions. *Catal. Sci. Technol.* **2014**, *4* (8), 2326–2331. <https://doi.org/10.1039/C4CY00213J>.

(65) Zhu, Y.; Kong, X.; Zheng, H.; Ding, G.; Zhu, Y.; Li, Y.-W. Efficient Synthesis of 2,5-Dihydroxymethylfuran and 2,5-Dimethylfuran from 5-Hydroxymethylfurfural Using Mineral-Derived Cu Catalysts as Versatile Catalysts. *Catal Sci Technol* **2015**, *5* (8), 4208–

4217. <https://doi.org/10.1039/C5CY00700C>.

(66) Srivastava, S.; Jadeja, G. C.; Parikh, J. Synergism Studies on Alumina-Supported Copper-Nickel Catalysts towards Furfural and 5-Hydroxymethylfurfural Hydrogenation. *J. Mol. Catal. Chem.* **2017**, *426*, Part A, 244–256. <https://doi.org/10.1016/j.molcata.2016.11.023>.

(67) Seemala, B.; Cai, C. M.; Wyman, C. E.; Christopher, P. Support Induced Control of Surface Composition in Cu–Ni/TiO₂ Catalysts Enables High Yield Co-Conversion of HMF and Furfural to Methylated Furans. *ACS Catal.* **2017**, 4070–4082. <https://doi.org/10.1021/acscatal.7b01095>.

(68) Zhang, Y. Catalytic Upgrading of Oxigenated Building Blocks in Lignocellulose-based Biorefineries. Tesi di dottorato, alma, 2017. [https://doi.org/Zhang, Yu \(2017\) Catalytic Upgrading of Oxigenated Building Blocks in Lignocellulose-based Biorefineries, \[Dissertation thesis\], Alma Mater Studiorum Università di Bologna. Dottorato di ricerca in Chimica <http://amsdottorato.unibo.it/view/dottorati/DOT498/>, 29 Ciclo. DOI 10.6092/unibo/amsdottorato/7797](https://doi.org/Zhang, Yu (2017) Catalytic Upgrading of Oxigenated Building Blocks in Lignocellulose-based Biorefineries, [Dissertation thesis], Alma Mater Studiorum Università di Bologna. Dottorato di ricerca in Chimica <http://amsdottorato.unibo.it/view/dottorati/DOT498/>, 29 Ciclo. DOI 10.6092/unibo/amsdottorato/7797).

(69) Iriondo, A.; Mendiguren, A.; Güemez, M. B.; Requies, J.; Cambra, J. F. 2,5-DMF Production through Hydrogenation of Real and Synthetic 5-HMF over Transition Metal Catalysts Supported on Carriers with Different Nature. *Catal. Today* **2016**. <https://doi.org/10.1016/j.cattod.2016.02.019>.

(70) Scholz, D.; Aellig, C.; Hermans, I. Catalytic Transfer Hydrogenation/Hydrogenolysis for Reductive Upgrading of Furfural and 5-(Hydroxymethyl)Furfural. *ChemSusChem* **2014**, *7* (1), 268–275. <https://doi.org/10.1002/cssc.201300774>.

(71) Nagpure, A. S.; Lucas, N.; Chilukuri, S. V. Efficient Preparation of Liquid Fuel 2,5-Dimethylfuran from Biomass-Derived 5-Hydroxymethylfurfural over Ru–NaY Catalyst. *ACS Sustain. Chem. Eng.* **2015**, *3* (11), 2909–2916. <https://doi.org/10.1021/acssuschemeng.5b00857>.

CHAPTER 6: GENERAL CONCLUSIONS AND PERSPECTIVES

The depletion of fossil carbon resources, huge energy demands, and environmental deterioration have encouraged the valorization of renewable biomass resources toward fuels and fine chemicals. 2,5-Dimethylfuran (DMF) and 2,5-dimethyltetrahydrofuran (DMTHF) have been identified as highly interesting biomass-derived liquid fuels with high energy densities and octane numbers, holding great potential as substitutes for petroleum-based gasoline. Production of DMF and DMTHF by hydroconversion of a biomass-derived platform molecule, 5-hydroxymethylfurfural (HMF), is a sustainable route. However, as a multifunctional compound, various other products, such as 2,5-bis(hydroxymethyl)furan (BHMF), 2,5-bis(hydroxymethyl)tetrahydrofuran (BHMTTHF), 5-methylfurfural (MFFR), 5-methylfurfuryl alcohol (MFOL), linear C₆ alcohols, and heavy polymers, can be formed from HMF during catalytic conversion under H₂. Achieving high selectivities to DMF and DMTHF from HMF is still a substantial challenge.

A number of noble metal-based catalysts (e.g. Ru, Pd, Pt and Au) have been designed to orient the HMF hydroconversion to DMF/DMTHF. They have exhibited a high intrinsic activity but suffer from a poor selectivity. Moreover, noble metals are limited resources and their cost is high and fluctuating. The development of alternative catalysts based on the first-row of transition metals, such as Ni and Cu, is of importance because of their relatively low cost. However, the catalytic performances of Ni- and Cu-based catalysts generally rely on the use of metal additives and/or active supports. In contrast, monometallic Ni- or Cu-based catalysts have been seldom reported as active and selective for the transformation of HMF, and the effect of the dispersion of Ni or Cu particles is not often discussed in the literature. In this context, the main focus of this thesis was to develop highly active and selective monometallic Ni- and Cu-based catalysts by controlling the dispersion of metal particles.

The following Ni- and Cu-based catalysts were prepared and tested in the hydroconversion of HMF to DMF or DMTHF:

- Monometallic Ni/SBA-15 catalysts prepared by the incipient wetness impregnation – mild drying (IWI-MD) method and by the melt infiltration (MI) method. The dispersion of Ni nanoparticles (NPs) was controlled by using a mesoporous siliceous SBA-15 support with different properties of intra-wall porosity.

- Monometallic Cu/SBA-15 catalysts prepared by the IWI-MD method, by the in-situ auto-combustion (ISAC) method and by the deposition-precipitation (DP) method. The dispersion of Cu NPs was controlled by using different preparative procedures.

The monometallic 15Ni/SBA-15_IWI-MD catalyst prepared by the IWI-MD method exhibited a wide distribution of nickel particle sizes (5-50 nm), bearing both aggregated nickel particles and a population of mesopore-confined nickel particles (~ 24%), giving an average particle size of 15 nm. A significant improvement of the dispersion of nickel particles was realized by controlling the secondary pore network of the SBA-15 host materials and by introducing nickel via the MI method. SBA-15 aged at 60°C lacked a connection between adjacent pores through intra-wall porosity. It resulted in a poor diffusion of the molten nickel precursor and thus in the formation of extra-porous metal aggregates. SBA-15 aged at higher temperatures (100, 140 °C) presented a larger diameter of the intra-wall pores and interconnected porosity which facilitated the formation of finely dispersed nickel particles (2.1, and 3.1 nm, respectively), indicating the important role of the secondary pore network of SBA-15 host materials in determining the nickel particle size when nickel is introduced by the MI method.

The effect of the dispersion of nickel particles was directly reflected by the catalytic reactivity for the hydroconversion of cinnamaldehyde (CNA) and HMF. The Ni/SBA-15 catalyst presenting the highest Ni surface area (particles confined in the intra-wall porosity) exhibited the highest hydrogenation rate for CNA hydroconversion. A complete conversion of CNA to hydrocinnamaldehyde (HCNA) was achieved in 1.5 h with an initial hydrogenation rate of $122.8 \text{ mmolCNA g}_{\text{cat}}^{-1}\text{h}^{-1}$, which is at the top level as compared to the results in the literature. It also led to a faster HMF hydroconversion under mild reaction conditions (130 °C, 15 bar, near complete HMF conversion at 1 h), and facilitated the full hydrogenation and hydrogenolysis of HMF (high yields of BHMTHF and DMF). Besides, the existence of a large population of mesopore-confined Ni particles was considered to be crucial for the fast hydrogenolysis and furan ring hydrogenation of HMF on 15Ni/SBA-15_IWI-MD under optimized reaction conditions (180 °C, 30 bar, HMF/Ni molar ratio of 3). A DMF yield of 70.5% was achieved after 0.5 h and a DMTHF yield of 96.6% after 10 h, which is one of the best results obtained with monometallic Ni-based catalysts reported in the literature.

The dispersion of Cu particles in monometallic Cu/SBA-15 catalysts is also a key factor affecting the catalyst reactivity, and was shown to be highly dependent on the preparative

procedures. Cu is a metal that is difficult to efficiently disperse by impregnation or melt infiltration, and the use of the classic IWI-MD method resulted in a poor dispersion of Cu particles (average particle size of 60 nm). In contrast, 15Cu/SBA-15_ISAC prepared by in-situ auto-combustion involving glycine displayed a higher Cu dispersion with a population of mesopore-confined Cu particles (< 5 nm in particle size). The use of the deposition-precipitation (DP) method allowed further enhancement of the Cu dispersion with an average Cu particle size of 5 nm, at the cost of severe destruction of the SBA-15 structure.

The dispersion of the Cu particles determined the catalytic performances of the catalyst. 15Cu/SBA-15_IWIMD showed almost no activity (4.5% HMF conversion). In contrast, the better dispersed particles of 15Cu/SBA-15_ISAC exhibited a much higher hydrogenation activity, giving a DMF yield of 66% at complete HMF conversion under optimized reaction conditions (210 °C, 15 bar, HMF/Cu molar ratio of 10, 10 h). The 15Cu/SBA-15_DP catalyst presenting the highest Cu dispersion showed excellent catalytic activity and selectivity, achieving a BHMF yield of 89.1% at near complete HMF conversion after 20 min and a DMF yield as high as 95% at full HMF conversion after 10 h under the same reaction conditions. The DMF yield obtained by 15Cu/SBA-15_DP is at the top level among the Cu-based catalysts reported in the literature.

A kinetic study built on a simple model (order 1 with respect to the organic reactant and intermediates, no inhibition term) revealed differences between Ni and Cu. The 15Ni/SBA-15_IWI-MD catalyst primarily appeared as a hydrogenolysis catalyst at 180°C. Both C=O hydrogenation and hydrogenolysis steps are fast compared to the hydrogenation of the furan ring. The conversion of HMF to DMTHF on Ni predominantly progressed via the “HMF → MFFR → MFOL → DMF → DMTHF” route. Unlike the Ni catalyst, a kinetic study based on the catalytic data of 15Cu/SBA-15_ISAC and 15Cu/SBA-15_DP obtained at 180 and 210°C showed that Cu systems primarily appear as hydrogenation catalysts, which preferably catalyze the C=O hydrogenation step compared to the hydrogenolysis steps, and are not able to catalyse the furan ring hydrogenation. The conversion of HMF to DMF on Cu predominantly progressed via the “HMF → BHMF → MFOL → DMF” route.

To summarize, this research work shows that controlling the metal dispersion through the pore characteristics of a mesoporous SBA-15 support, or through the suitable preparative procedure, can be the keys for the synthesis of non-precious monometallic Ni/SBA-15 and

Cu/SBA-15 catalysts that are both active and selective for the production of valuable DMF or DMTHF biofuels from the hydroconversion of HMF.

Based on the results obtained in this thesis, some perspectives can be proposed for future investigation on this project.

- Verifying the reusability of the Ni/SBA-15 and Cu/SBA-15 catalysts, identifying the causes for deactivation, and optimizing the regeneration procedures are necessary steps before moving to practical applications;
- The kinetic models built in this thesis could be further improved by using more comprehensive catalytic data in order to provide more precise results, and determining true kinetic constants through a micro kinetic model;
- The exploration of alternative supports such as mesoporous carbon materials, due to their exceptional textural characteristics and chemical stability, in replacement to SBA-15 will be interesting;
- The literature suggests that supports with basic functions potentially facilitate the active and selective transformation of furanic compounds, which also deserves more research interest;
- The study of solvent effects and the use of greener solvents such as alcohols will be interesting.